Understanding Degeneration and the Capacity for Reorganisation in the Adult Human Visual Cortex



Aislin Sheldon
Wellcome Centre for Integrative Neuroimaging
University of Oxford

Supervisors:
Professor Holly Bridge
Professor Susan Downes

A thesis submitted for the degree of
Doctor of Philosophy
Trinity 2022





NUFFIELD DEPARTMENT OF
CLINICAL NEUROSCIENCES



wellcome centre integrative neuroimaging



Abstract

Understanding Degeneration and the Capacity for Reorganisation in the Adult Human Visual Cortex

Aislin Alice Sheldon (they/them)
St John's College, The University of Oxford
A thesis submitted for the degree of *Doctor of Philosophy*
Trinity Term 2022
Word count: 47,839

Stargardt Macular Dystrophy (STGD1) causes degeneration of the photoreceptors, predominantly constrained to the cones within the central retina, which causes a loss of high acuity vision within the central visual field. Due to the topographic organisation of the primary visual cortex (V1), photoreceptor degeneration starting in the central retina projects to a focal region within posterior V1. There are treatments in development that aim to restore loss at the retina, however the majority of visual processing takes place in the visual cortex. Therefore, it is vital to determine if the visual cortex degenerates after a prolonged lack of input, as therapies that improve retinal function may not optimally restore vision if the visual cortex cannot respond to the new input. Previous research has shown that after a loss of visual input there are changes in the structure (Olivo et al., 2015, Burge et al., 2016; Hanson et al., 2019), function (Baseler et al., 2011) and neurochemistry (Bernabeu et al., 2009; Weaver et al., 2013) of the visual cortex.

The work presented in this thesis demonstrates the effects of vision loss on the adult visual cortex from a cohort with STGD1 compared to controls with healthy vision. I quantified the vision loss from STGD1 by measuring photoreceptor layer thickness, retinal sensitivity, and measures of visual function. I then used MRI measures of cortical structure, functional connectivity, and neurochemistry to investigate how vision loss affects the visual cortex.

Unsurprisingly, given the loss of cone photoreceptors in STGD1, these participants had reductions in retinal sensitivity, visual function, and photoreceptor layer thickness compared to controls. Firstly, using measures of cortical thickness, I found significant thinning of the grey matter within V1 in STGD1, suggesting that neuronal degeneration occurs after a loss of visual input. Furthermore, using resting state fMRI I found decreased functional connectivity between V1 and the LOC in STGD1. The LOC processes object recognition which requires high acuity vision. The visual loss in STGD1 is localised to the central visual field which is responsible for high acuity vision, and this is needed for object recognition. Connectivity from the region of projected loss (posterior V1) to the frontal cortex is also reduced in STGD1, suggesting a reduction in attentional modulation to the central part of the visual field. Finally, using MRSI, I found elevated *myo*-Ins levels, which are a marker for glial cell proliferation, within V1 in STGD1 compared to controls. This suggests that there is an increase in glial cells, which are responsible for repairing degenerating neurons within V1 from a loss of visual input in STGD1. Glutamate, which is a marker for neuronal function, was decreased within V1 in STGD1 compared to controls. This suggests a lack of functional activation within V1 due to a lack of input from vision loss in STGD1. GABA levels, which are a marker for neuronal inhibition, did not change in STGD1 compared to controls, however due to macromolecule contamination within the posterior visual cortex, this made accurate GABA quantification difficult.

This thesis demonstrates the effects of a loss of sensory input on the visual system by investigating degeneration and the capacity for reorganisation within the adult visual cortex. I found reduced functional connectivity, cortical thinning, elevated *myo*-Ins and reduced glutamate levels within V1, which are markers for cortical degeneration. In contrast markers for reorganisation (increased functional connectivity, increased glutamate, and decreased GABA) were not found. Therefore, I conclude that after a loss of visual input in adulthood, the visual cortex degenerates and has less of a capacity for reorganisation. These findings should be considered for treatments that aim to restore input at the retina, to optimally restore visual function, the treatment should be conducted as soon as possible after photoreceptor loss before cortical degeneration occurs.

Acknowledgements

Firstly, I would like to extend my gratitude to my two supervisors Professor Holly Bridge and Professor Susan Downes. To Susie thank you for welcoming me into your clinic; working with you and your team has given me an invaluable insight into the effects of eye disease, your dedication to helping patients living with these conditions is inspiring. To Holly, I am grateful for your constant support, guidance, and enthusiasm throughout my DPhil. Your input has been invaluable in improving my research skills, thank you for helping me develop into a better scientist.

Thank you to everyone in the vision group at WIN, Jasleen, Betina, Ivan, Juju and everyone in the ERGO research group, this project would not have been possible without your support. Lucy, thanks for all the laughs over coffee and fun times in Florida! To Hanna, for your support and friendship, particularly whilst we were the only people in the office in the pandemic. Watching our plant garden grow, helped when so many things were out of our control, thank you for welcoming me into your family, Pabbo and Fitzy have brought such joy to my life. To the wider office in the annexe, Camille, Magdalena, Patricia, Poly and Carl thank you for the kindness and humour throughout the time I was writing up. To Ioana, my mirrored lab/library desk buddy, your optimism and jokes broke through the stress even on the hardest of days. I would like to thank Serge Dumoulin for welcoming me into your group at Spinoza. Thank you to Carlien for teaching me mrVista and for being such a lovely friend, you and Jelle really made my time in the Netherlands special.

To my family, I love and appreciate you endlessly, my parents, Anne and Marc thank you for your support in my chosen life as an eternal student, I promise this is over now! To Deed, thank you for your constant positivity, it's something I carry with me not only throughout my DPhil but through my life. To Meem, thank you for all your check-ins and silliness, I have appreciated them so much. To my bros thanks for being such amazing, understanding, and hilarious friends - Iona, thank you for sharing your wealth of plant knowledge with me, Corrin, thank you for always providing cute updates

of Boris, Nuppy and Biscuit when I couldn't visit in the lockdowns. To Gran and Julie thank you for all your support and always making our picnics so much fun.

Thank you to my friends in St Johns, you have all made my time at Oxford truly unforgettable. Sammi, Carla and Alex you have made my life more vibrant. Hannah for your constant enthusiasm, developing the Womxn's Leadership Programme with you has inspired my life in so many ways. Izzy, thank you for being your wonderful self, I'm truly grateful for your advice and thoughtfulness. To Minying and Shahd thank you for your spousal support, you are both such wonderful humans. To Ben, for planting so many trees and for always being available for walks in nature, thank you for always checking in. To WOW! playing frisbee with you has been so much fun in my final years here. To Dale, Perisha, and Maya, my besties, you've brought endless happiness to the past 15 + years of my life, thank you for always being there for me throughout this journey and surprising me with the most special celebration at the end. Maya, I honestly don't know what I'd do without you, living with you has been perfect, thank you for helping me become the person I am today.

It's difficult to put into words how much this support has meant to me throughout my journey. I was always told the cliché that a PhD is like a rollercoaster, full of ups and downs, but what I didn't appreciate is the effect this has when it coincides with life events, until I was living it. Over the years of my DPhil, I aligned my actions with my morals by becoming vegan, I wrote my whole thesis through a global pandemic, which affected all of us, and, with the support of my queer circle I finally had the courage to come out. So, I want to thank you all for helping me safely get off this rollercoaster, whilst I flourished into the person I truly am, I'm grateful to you all, always and forever.

Finally, I dedicate this thesis to Christina Sheldon. Grannie, you always inspired me to follow my interests, no matter what they were. From a young age you instilled in me the belief that I was capable of achieving all my dreams. I especially wish you were here today to share this one dream with me.

For Christina MacDonald Fraser Sheldon

(1921 – 2008)

Contents

Abstract i

Acknowledgements iii

Contents iv

Abbreviations x

Specific chapter acknowledgements xii

COVID-19 impact statement xiii

Chapter 1: Introduction 1

1.1 Introduction to the healthy visual system 2

1.1.1 The retina 3

1.1.1.1 Retinal structure 3

1.1.1.2 Photoreceptors 4

1.1.2 The visual field 6

1.1.3 The primary visual cortex 7

1.2 Neuronal plasticity 9

1.2.1 Excitation and inhibition 9

1.2.2 Long-term potentiation and depression like plasticity 10

1.2.3. The critical period 11

1.3 Cortical degeneration 11

1.4 Macular dystrophy 12

1.4.1 1.4.1. Vision loss therapies 14

1.5 Cortical reorganisation after a loss of visual input 15

1.5.1 Non-human primate models of cortical reorganisation after vision loss 15

1.5.2 Neuronal reorganisation after vision loss in humans 15

1.5.3 Interpreting measures of GABA and glutamate from ^{1}H-MRS 17

1.5.4 GABA levels within the human visual cortex 18

1.6 Cortical degeneration after a loss of visual input 19

1.6.1 Non-human primate models of neuronal degeneration in vision loss 19

1.6.2 Neuronal degeneration after vision loss in humans 20

1.7 Synopsis of thesis 21

1.7.1 Aims of thesis 21

1.7.2 Thesis overview 22

Chapter 2: Methods and procedure 24

2.1 Introduction 25
2.2 Methods to assess retinal structure and visual function 25
2.2.1 Retinal Structure 25
2.2.2 Retinal Function 26
2.2.3 Relating retinal position to visual field location 27
2.2.4 Visual Acuity 28
2.2.5 Contrast Sensitivity 29
2.2.6 Colour Vision 30
2.3 Methods to assess cortical structure, function, and chemistry 32
2.3.1 Magnetic Resonance Imaging 33
2.3.2 Structural MRI 34
2.3.3 Functional MRI and the BOLD signal 35
2.3.3.1 Methods to assess functional connectivity 36
2.3.5 Methods to assess neurochemistry 37
2.3.5.1 Proton Magnetic Resonance Spectroscopy 37
2.3.5.2 Magnetic Resonance Spectroscopy Imaging 39
2.4 Procedure 40
2.4.1. Assessment of Stargardt Macular Dystrophy 40
2.4.2 Participants 42
2.4.3 Data collection 42
2.4.4 MRI Acquisition 43
2.4.5 Visual Testing Acquisition 44

Chapter 3: Measures of Visual Function
Functional changes in visual ability in Stargardt patients compared to controls 45
3.1 Abstract 45
3.2 Introduction 46
3.2.1 Vision loss caused by Stargardt Macular Dystrophy 46
3.2.2 Rationale 47
3.4 Methods 48
3.4.1 Participants 48
3.4.2 Retinal Sensitivity 48
3.4.3 Contrast Sensitivity 51
3.4.4 Visual Acuity 52
3.4.5 Colour Vision 53
3.4.6 Outlier detection 55
3.5 Results 55

3.5.1 Retinal sensitivity decreases in STGD1 55
3.5.2 Contrast sensitivity decreases in STGD1 58
3.5.3 Visual acuity decreases in STGD1 60
3.5.4 Colour vision decreases in STGD1 62
3.6 Discussion 66
3.6.1 Retinal sensitivity is reduced in STGD1 66
3.6.2 Contrast sensitivity is lower in STGD1 compared to controls 66
3.6.3 STGD1 have lower visual acuity due to central loss 67
3.6.4 Colour vision discrimination decreases across all axes of colour space in STGD1 67
3.6.5 Limitations and future research directions 67
3.6.6 Chapter conclusion 68

Chapter 4: Structure
Structural Changes in the Visual System in Stargardt patients compared to Controls 69
4.1 Abstract 69
4.2 Introduction 70
4.2.1 Rationale 71
4.3 Methods 71
4.3.1 Participants 71
4.3.2 Acquisition 72
4.3.3 Analysis 72
4.3.3.1 Optical Coherence Tomography 72
4.3.3.2 Magnetic Resonance Imaging 73
4.3.4 Statistical Analysis 75
4.4 Results 76
4.4.1 STGD1 have thinner photoreceptor layers than controls 76
4.4.2 STGD1 have thinner nerve fibre layers than controls 76
4.4.3 Grey matter density does not change between STGD1 and controls 77
4.4.4 Cortical thickness is reduced within V1 in STGD1 79
4.4.5 Cortical thickness correlates with photoreceptor layer thickness 80
4.4.6 Cortical thickness correlates with retinal sensitivity 82
4.5 Discussion 82
4.5.1 STGD1 have a thinner retina than controls 82
4.5.2 Grey matter density does not change in STGD1 83
4.5.3 Cortical thickness decreases within V1 in STGD1 83
4.5.4 Limitations and future directions 84

4.5.5 Chapter Conclusion 84

Chapter 5: Functional connectivity

Functional Connectivity Changes in the Visual System between Stargardt patients and Controls 85

5.1 Abstract 85

5.2 Introduction 86

5.2.1 Rationale 87

5.3 Methods 87

5.3.1 Participants 87

5.3.2 Functional Magnetic Resonance Imaging acquisition 87

5.3.2.1 Stimulus presentation 88

5.3.2.2 Eye Movements 88

5.3.3 Rs-fMRI Analysis 88

5.3.3.1 Pre-processing 88

5.3.3.2 Dual Regression 89

5.3.3.3 Correlation with disease severity 90

5.3.3.4 ROI connectivity to the whole brain 91

5.3.3.5 ROI connectivity within the visual cortex 92

5.3.3.5 Statistical analysis 92

5.5 Results 93

5.5.1 Functional connectivity decreases within the visual cortex in STGD1 93

5.5.2 Functional connectivity within RSNs does not vary with disease severity 96

5.5.3 Functional connectivity from the LGN to the remaining cortex does not change in STGD1 98

5.5.4 Functional connectivity from V1 to the remaining cortex is reduced in STGD1 98

5.5.5 Functional connectivity between visual areas correlates with disease Severity 101

5.6 Discussion 103

5.6.1 Functional connectivity decreases within the visual cortex in STGD1 103

5.6.2 Posterior V1 connectivity to the frontal pole and the medial frontal cortex decreases in STGD1 104

5.6.3 Posterior V1 connectivity to the LGN and hMT+ correlates with disease severity 104

5.6.4 Limitations and future directions 105

5.6.5 Chapter conclusion 105

Chapter 6: Neurochemical validation 106
6.1 Abstract 106
6.2 Introduction 107
6.2.1 Single Voxel Magnetic Resonance Spectroscopy 107
6.2.2 Magnetic resonance spectroscopy imaging 108
6.2.3 Neurochemicals of interest 109
6.3 Measures of spectral quality 110
6.3.1 Spectral linewidth 110
6.3.2 Signal-to-noise 110
6.3.3 Cramér-Rao lower bounds 111
6.3.4 Coefficients of variance 111
6.3.5 Importance of avoiding contamination 111
6.3.6 Metabolite reference 112
6.4 Methods 113
6.4.1 Participants 113
6.4.2 Magnetic Resonance Spectroscopy Imaging 113
6.4.3 Measure of spectral quality 115
6.4.4 Statistical Analysis for validation 115
6.5 Measures of spectral quality 116
6.5.1 Cramér-Rao Lower Bounds 116
6.5.2 Grey matter fractions 116
6.5.2.1 Glutamate 117
6.5.2.2 N-Acetylaspartate 117
6.5.2.3 Myo-Inositol 118
6.5.2.4 Gamma-Aminobutyric Acid 119
6.6 Discussion 120
6.6.1 Spectral quality of occipital slab placement 120
6.6.2 Limitations and future directions 121
6.6.3 Chapter Conclusion 121

Chapter 7: Neurochemical
Neurochemical Changes in the Visual Cortex between Stargardt patients compared to Controls 122
7.1 Abstract 122
7.2 Introduction 123
7.2.1 Rationale 124
7.3 Methods 124
7.3.1 Participants 124

7.3.2 MRSI acquisition 124
7.3.3 Analysis 125
7.3.3.1 Correction for grey matter fractions 126
7.3.3.2 Statistical Analysis 126
7.4 Results 127
7.4.1 N-Acetylaspartate concentrations do not change within V1 in STGD1 127
7.4.2 Myo-inositol concentrations increase within V1 in STGD1 128
7.4.3 Glutamate concentrations decrease within V1 in STGD1 129
7.4.4 GABA concentrations do not change within V1 in STGD1 130
7.4.5 Neurochemical markers for cortical degeneration correlate with disease severity 131
7.5 Discussion 136
7.5.1 Myo-inositol levels are elevated within V1 in STGD1 136
7.5.2 NAA levels correlate with disease severity in STGD1 136
7.5.3 Reduced glutamate levels within V1 in STGD1 136
7.5.4 GABA levels do not change within V1 in STGD1 compared to controls 137
7.5.5 Limitations and future directions 137
7.5.6 Chapter Conclusion 138

Chapter 8: General discussion
Measuring degeneration and the capacity for reorganisation in the adult human visual cortex 139
8.1 Thesis overview 140
8.2 Summary of key findings 141
8.2.1 Understanding cortical degeneration in the adult human visual cortex after vision loss 142
8.2.2 Understanding the capacity for reorganisation in the adult human visual cortex after vision loss 142
8.3 General limitations 142
8.4 Future research directions and open questions 143
8.5 Final conclusions 145

References 146

Abbreviations

ABCA4	ATP binding cassette subfamily A member 4
ANOVA	Analysis of variance
BET	Brain extraction tool
BOLD	Blood-oxygenated-level-dependent
CRLB	Cramér-Rao lower bound
CSF	Corticospinal fluid
COV	Coefficients of variance
EPI	Echo-planar imaging
FLIRT	FMRIB's linear registration tool
fMRI	Functional MRI
FMRIB	Oxford centre for functional MRI of the brain
FNIRT	FMRIB's non-linear registration tool
FSL	FMRIB's software library, www.fmrib.ox.ac.uk/fsl
FID	free induction decay
FD	frequency domain
GABA	Gamma-aminobutyric acid
Glu	Glutamate
GM	Grey matter
GRESHIM	Gradient Echo Shimming
^{1}H-MRS	Proton Magnetic Resonance Spectroscopy (MRS)
LPZ	Lesion projection zone
LOC	Lateral occipital complex
MRS(I)	Magnetic resonance spectroscopy (imagining)
myo-Ins	Myo-inositol
MRI	Magnetic resonance imaging
NMR	Nuclear magnetic resonance
NAA	N-Acetylaspartate
OCT	Optical coherence tomography
ppm	Parts per million
rs-fMRI	Resting state fMRI
RF	Radio frequency
ROI	Region of interest
STGD1	Stargardt Disease
SD	Standard deviation
SNR	Signal to noise ratio

TR	Repetition time
TE	Echo time
TD	Time domain
V1	Primary visual cortex
VBM	Voxel-based morphometry
VOI	Voxel of interest
pRF	Population receptive field mapping
WM	White matter

Research acknowledgements

I would like to extend my gratitude to all participants who gave their time to take part in the research presented in this thesis, thank you for your patience in the long and tiring testing days, and for helping forward the research within this area of science. Thank you to all the clinical staff in the Oxford Eye hospital, who enabled this project by aiding with patient recruitment, data collection and room bookings. With thanks to the radiographers and core staff at WIN who helped make this project run smoothly.

Specific chapter acknowledgements

Chapter 3 – Vision Measures

With many thanks to Dr Jasleen Jolly, who taught me the clinical vision tests in this chapter and contributed to the analysis programme for the microperimetry with Amandeep Singh Josan. Many thanks to Sophie Templer (Final Honours Scheme Research Student) who created the Python code for the colour vision analysis and created figure 39.

Chapter 4 – Structure

With many thanks to Dr Jasleen Jolly and Aran Johal (Final Honours Scheme Research Student) who segmented the OCT data. Thank you to the team who created Brainlife.io and Dr Jasleen Jolly who analysed the cortical thickness eccentricity data.

Chapter 6 – Neurochemical Validation

With many thanks to Dr William Clarke, Professor Saad Jbabdi and Professor Charlotte Stagg for their valuable advice on MRSI analysis and the development of the FSL MRS tool. Thank you to Dr Betina Ip and Dr Ioana-Florentina Grigoras for your many helpful discussions on MRS and GABA interpretation.

I would like to thank all the funding bodies who contributed to my DPhil. To NDCN and the MRC for funding my DPhil studentship, to Eurofins Scientific and St John's College for funding my covid-19 extensions, and to the Guarantors of Brain for funding my talk at the Vision Sciences Society Conference.

COVID-19 impact statement

The COVID-19 pandemic has had a profound impact on the work contained within this thesis. The pandemic coincided with my 3rd year of my DPhil when I was in the middle of data analysis. The Wellcome Centre for Integrative Imaging (WIN), FMRIB building was closed between the 17th March 2020 until the 17th of July 2020. The first stages of re-opening had limited access, I returned in September 2020, after nearly 7 months without access. From the 17th July the working hours were significantly limited from 9:00am – 7:00pm. In addition to the limited working space in my department the libraries were also closed for a similar time frame and had limited slots for working in. These normally consisted of 2-hour timeslot separated 2 hours apart for covid disinfection. This was severely disruptive for my ability to work on my thesis. This period of my DPhil was originally planned for analysis, but I had many delays in fixing analysis pipelines as all communication went online and made trouble shooting with others in the department more difficult. Since restrictions started to lift this significantly improved data analysis, allowing me to write up my thesis.

1 Introduction

1.1 Introduction to the healthy visual system

Vision is the dominant sense in humans and is used to help navigate the world and facilitate social interactions. Light waves enter the eyes and are detected by the light sensitive cells in the retina called the photoreceptors. This signal is organised from the nasal and temporal halves of the retina which process the left (blue in figure 1) and right (pink in figure 1) visual field. These signals project along the optic nerve, the nasal retinal fibres then cross at the optic chiasm, this separates the information from the left and right visual field along the optic tract to the lateral geniculate nucleus (LGN). This information is then passed from the LGN along the optic radiations to the visual cortex (Maunsell and Newsome, 1987) (figure 1). Visual information from the left visual field (blue in figure 1) projects to the right hemisphere and vice versa.

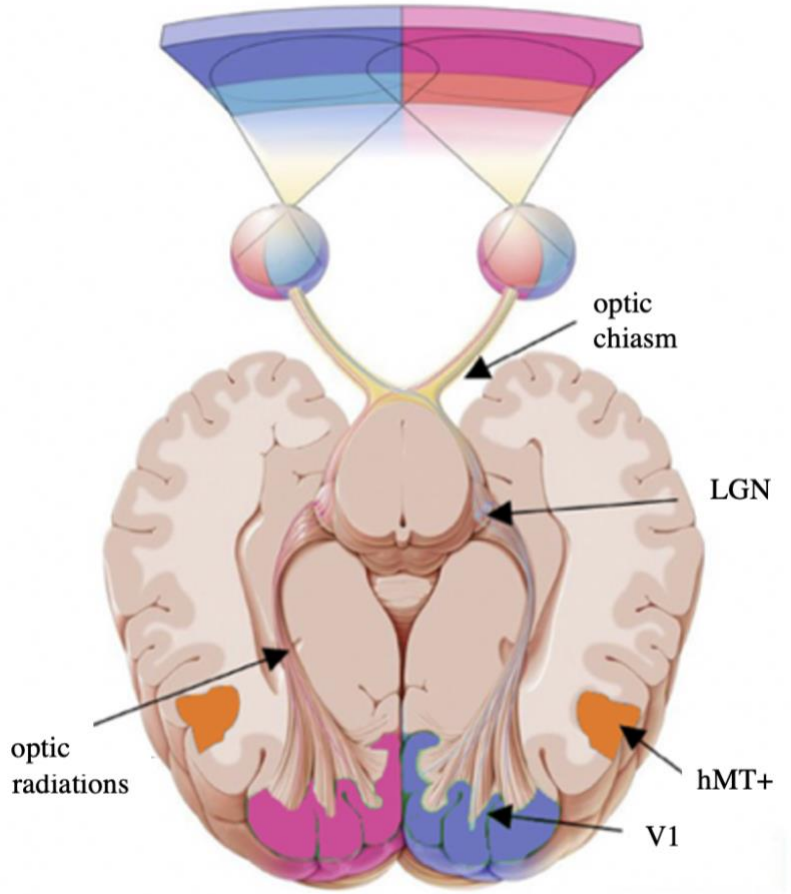


Figure 1: The major visual pathway showing the projections from the retina to the visual cortex. V1 blue). Image adapted from source: https://www.kenhub.com/en/library/anatomy/the-visual-pathway: optic_nerve_and_visual_pathway.jpg

1.1.1 The retina

1.1.1.1 Retinal structure

The retina is the complex light-sensitive structure at the back of the eye, comprised of multiple layers with different functions (figure 2). Photons of light enter and pass through the inner retinal layers until they are detected by the photoreceptors (rods and cones) in the outer retinal layer. Light photon energy is converted into electrical activity via phototransduction, and these electrical signals are sent from the photoreceptors, through the synapses of the bipolar cells to the ganglion cells. There are three major classes of ganglion cells (over 30 in total), and their axons create the nerve fibre layer, which exits the eye at the optic nerve and synapses in the LGN. The retinal pigment epithelium (RPE) provides metabolic energy for the photoreceptors, and the pigment absorbs the remaining light photons to reduce light scatter. The macula has a high density of photoreceptors spanning the central 5° of the visual field and is responsible for our central vision. The fovea is a small depression within the macula and occupies the central 1° of the visual field; this is the fixation point in the healthy retina and has the highest visual acuity.

In the healthy retina, vitamin A (retinol) is the precursor to the metabolite retinal. Retinal combines with opsins to create visual pigments such as rhodopsin (in rods) and photopsins (in cones). When light is absorbed by the visual pigments, it initiates the process of phototransduction (Bavik et al., 2015). The *ABCA4* gene encodes a transmembrane protein (ABCR) localised on the photoreceptors (Papermaster et al., 1978). The by-product from phototransduction, fluorophore A2E (the major component in lipofuscin), is removed from the RPE by ABC transporter proteins coded by *ABCA4*.

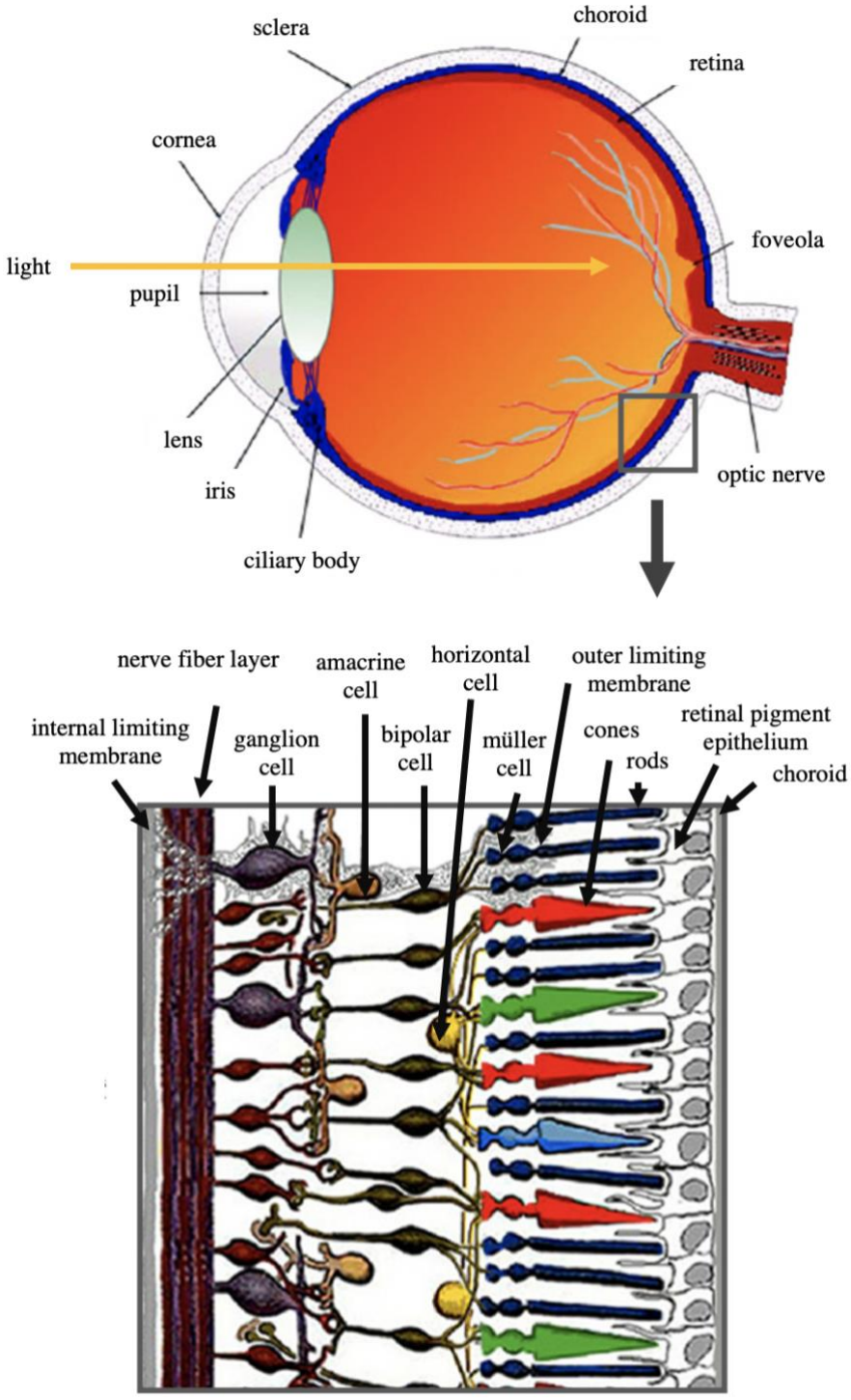


Figure 2: Schematic shows how light enters the eye through the pupil and reaches the retina (top), which is made up of a complex number of cells (bottom). Image adapted from (Macgillivray et al., 2014)

1.1.1.2 Photoreceptors

The human visual system can distinguish between a range of wavelengths of light. The two types of photoreceptors in the retina are rods and cones, which are sensitive to different wavelengths and therefore active under varying light conditions. Cones are active under photopic conditions (figure 3), whilst rods are active under scotopic conditions (figure 3), and both are active under mesopic conditions. Rods and cones have varying functions and spatial distributions which are explained further below.

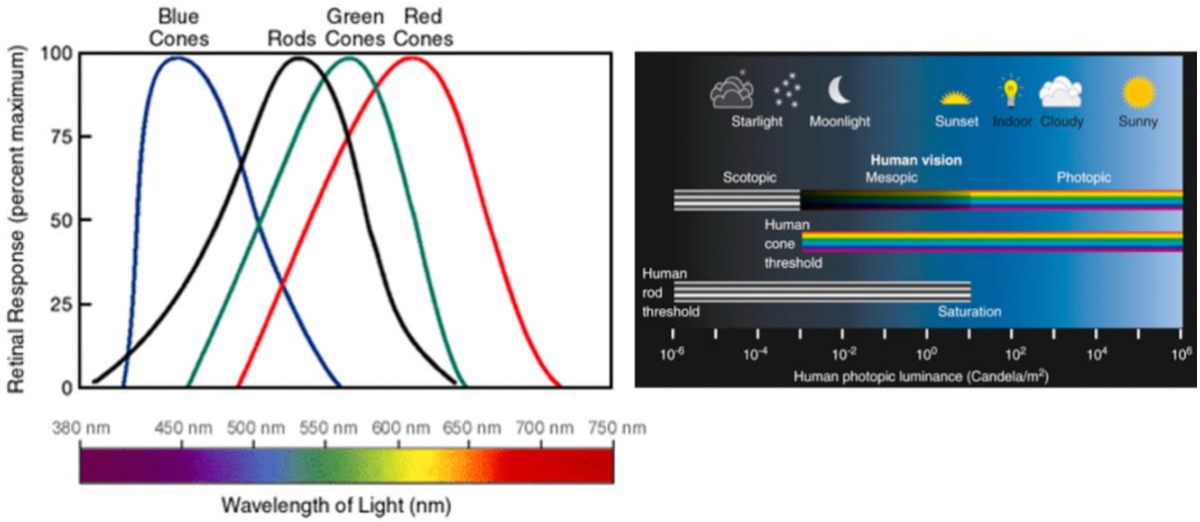


Figure 3: The spectral sensitivity of rods (black line) and cones (blue, green, and red lines) in the human retina, plotted against wavelength of light (nm) (image from Al-Bahadly et al, 2010) (right). The human retinal luminance (cd/m^2) thresholds of cones and rods under scotopic, mesopic and photopic conditions (image adapted from (Kelber, 2018).

Cones:

Cones are active under high levels of luminance and are responsible for processing both high acuity vision and colour vision. The cones are concentrated in the central retina, and this corresponds to processing the central visual field. Colour vision is the ability to distinguish between various wavelengths of light, independent of the relative light intensity (Hilbert, 1992). There are three types of cone classes, and each have a different peak frequency at either short, medium, or long

wavelengths of light. These differences in cone wavelength sensitivity relate to different axes of opponent colour space. L-cones process wavelengths of light associated with the red part of the electromagnetic spectrum, M-cones process those associated with the green part of the spectrum and S-cones process those associated with the blue part of the spectrum (figure 3). M-cones and L-cones are densely distributed in the macula, whilst S-cones have a lower distribution that is absent within the central 0.33° of the macula (Curcio et al., 1991) (figure 4).

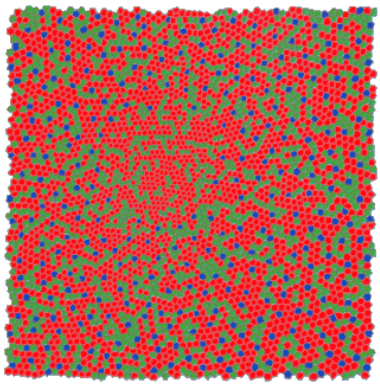


Figure 4: Cone mosaic of the human fovea showing the distribution of the three cone classes, S-cones (blue), M-cones (green) and L-cones (red). Source: https://www.cis.rit.edu/people/faculty/montag/vandplite/pages/chap_9/ch9p1.html: mosaic.gif.

Rods:

The rods are concentrated in the outer edges of the retina, and these process the peripheral visual field. Compared to cones, rods are active under low light levels, as only a few photons of light are needed to activate them. Rods are responsible for processing night vision, which is the ability to see in the dark and this is in grayscale as the rods do not process colour vision

1.1.2 The visual field

When the eye is fixated on a point in space, the visual field is the total area that is visible. The visual field is divided into the right and left hemifields, which are partly processed by both eyes with an overlapping representation in the midline. Each eye has a single eye field (orange and purple in figure

5), where the nasal retina (from the fovea to the nose) processes the medial part of the visual field (0 – 60°), and the temporal retina (from the fovea to the temples) processes the lateral part of the visual field (0 – 90°). The overlapping representation at the midline is viewed by both eyes, and this provides binocular vision (figure 5).

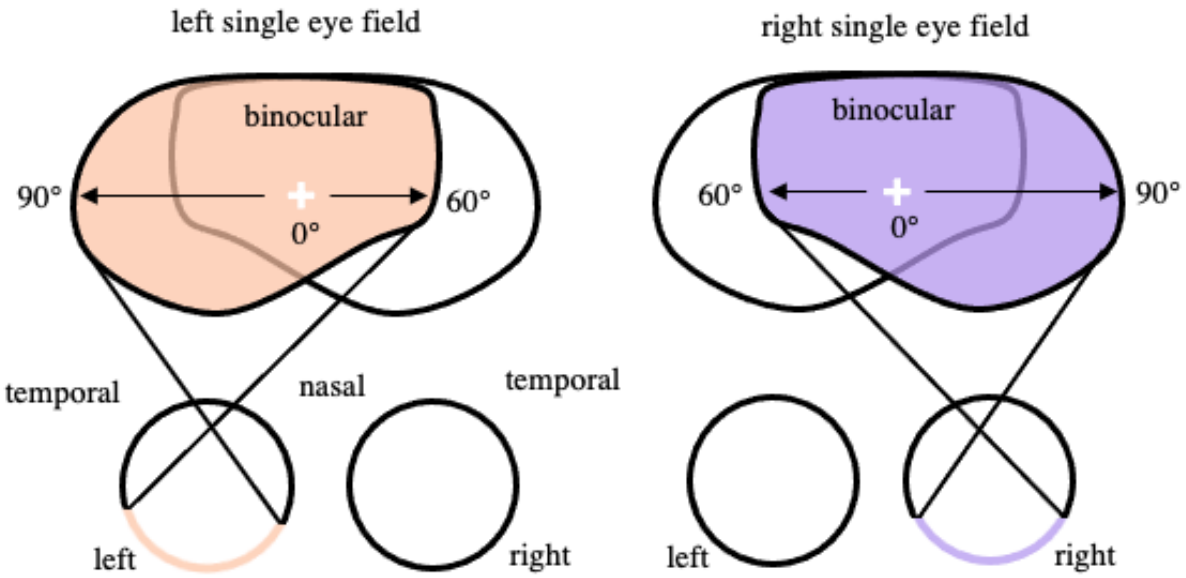


Figure 5: The visual field split into the single eye fields processed by the left (orange) and right (purple) retina. Fixation shown by the white cross. The overlapping representation provides binocular vision.

1.1.3 The primary visual cortex

The visual cortex performs the majority of visual processing by turning the electrical signals from the retina into our rich visual percept of the world. The visual cortex is organised into a visual hierarchy, where the primary visual cortex (V1), located along the calcarine sulcus (red line in figure 6) is the first area of the cerebral cortex to receive input from the optic radiations.

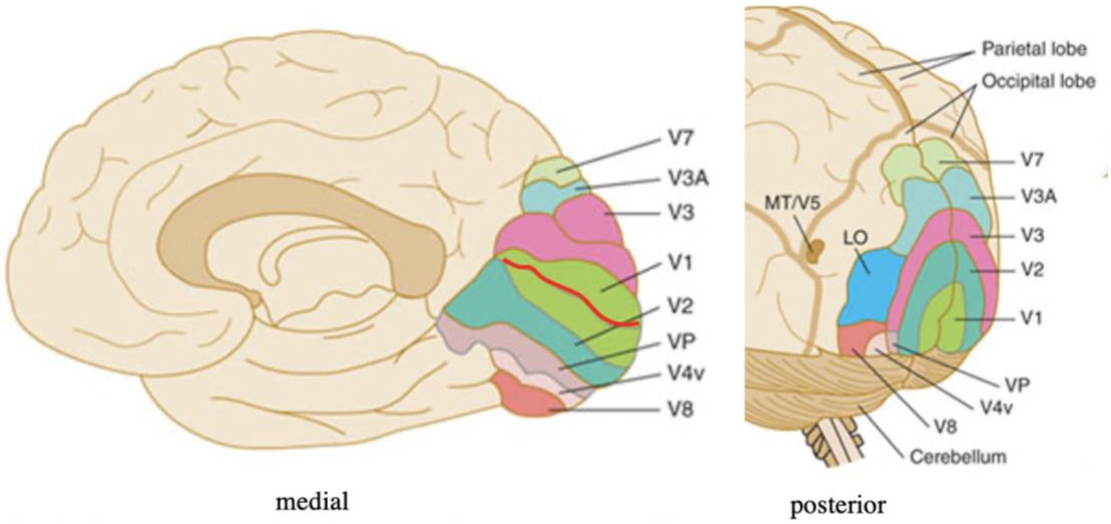


Figure 6: Visual areas within the occipital lobe, adapted from (Barrett et al, 2016). The medial view (left) depicts the early visual areas that contain topographic maps of the visual world, the calcarine sulcus within V1 is represented by the red line. The posterior view (right) shows the higher visual areas V4 where colour is processed, lateral occipital complex (LOC) where form is processed and hMT+ where visual motion is processed.

A receptive field (RF) is a region in sensory space that when stimulated elicits a neuronal response (Hartline, 1938). Within the visual cortex neurons activate when a stimulus falls within their RF in visual space. V1 contains a topographic representation of the visual field. This means adjacent RFs that process corresponding points in visual space are represented by adjacent neurons (Wandell et al., 2007). This topographic organisation is called retinotopy and can be mapped by moving a stimulus across the visual field which activates adjacent neurons within V1 (Hubel and Wiesel, 1968). Figure 7 shows retinotopy where the cortical neurons are stimulated by a flickering checkerboard in the visual field. The central visual field (red - yellow) is projected to the posterior end of V1 (occipital pole), as stimulation moves into the peripheral visual field (blue - pink) this is represented towards the anterior end of V1.

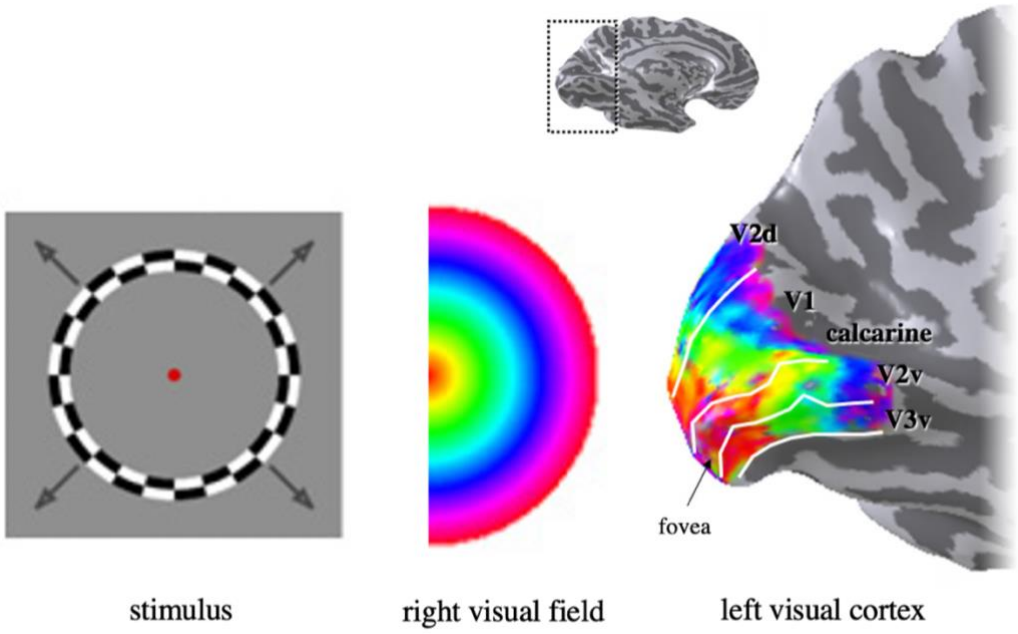


Figure 7: Retinotopic map projected onto the inflated right hemisphere of the visual cortex, adapted from (Brewer et al., 2005). Expanding ring high contrast checkerboard stimuli (right) activate the cortical central representation of the visual field (red) out to the peripheral (blue). Boundaries between visual areas are represented by white lines.

V1 is the largest of the visual areas, and occupies ~1470mm^2 of cortical space in humans (Dougherty et al., 2003). Within the retina the fovea contains the highest density of cones, and this encompasses a disproportionately large area within V1. The fovea requires a larger amount of cortex compared to peripheral regions of the retina; this overrepresentation of the fovea is called cortical magnification. The neurons in V1 that represent the fovea have smaller RF sizes than those that represent peripheral parts of the retina, and this underpins the higher visual acuity within the central visual field. Figure 7 shows the overrepresentation of the central visual field (red in visual field), with a proportionally larger amount of the cortex dedicated to processing it (red in visual cortex).

1.2 Neuronal plasticity

Neuroplasticity refers to changes in synaptic signalling between neurons that can facilitate behavioural change such as skill acquisition or improve recovery after stroke (Hallett, 2001; Karni et al., 1995). The changes in synaptic signalling can occur due to a variety of factors including

modifications in dendritic spines, changes in the number of receptors and increased transmitter release.

1.2.1 Excitation and inhibition

Neuronal activity is controlled by the relative contribution of excitation and inhibition. Excitatory synaptic inputs contribute towards neuronal firing whereas inhibitory synaptic inputs make the neuron less able to respond to an action potential. Two neurotransmitters that change the neuronal charge are Gamma-aminobutyric acid (GABA), the dominant inhibitory neurotransmitter, and glutamate, the major excitatory neurotransmitter (Petroff, 2002). There are two ionotropic glutamate receptors: α-amino-3-hydroxy-5-methyl-4-isoxazolepropionic acid (AMPA) and N-Methyl-D-aspartate (NMDA) and these are located on the postsynaptic neurons. The highest concentration of glutamate is found in the pre-synaptic vesicles (Zhou and Danbolt, 2014). Levels of glutamate are maintained at low concentrations in the extra-synaptic space to avoid glutamate hypertoxicity which can lead to cell death.

When an action potential arrives at the presynaptic axon terminal it depolarises the membrane and opens the voltage gated Ca^{2+} channels, this influx of Ca^{2+} causes glutamate to be released from the pre-synaptic glutamatergic neuron. The glutamate binds to the AMPA receptors ($AMPA_r$) on the post-synaptic neuron (Figure 8A). This allows an influx of Na+ into the cell which depolarises the neuron and makes the postsynaptic neuron more able to respond to action potentials.

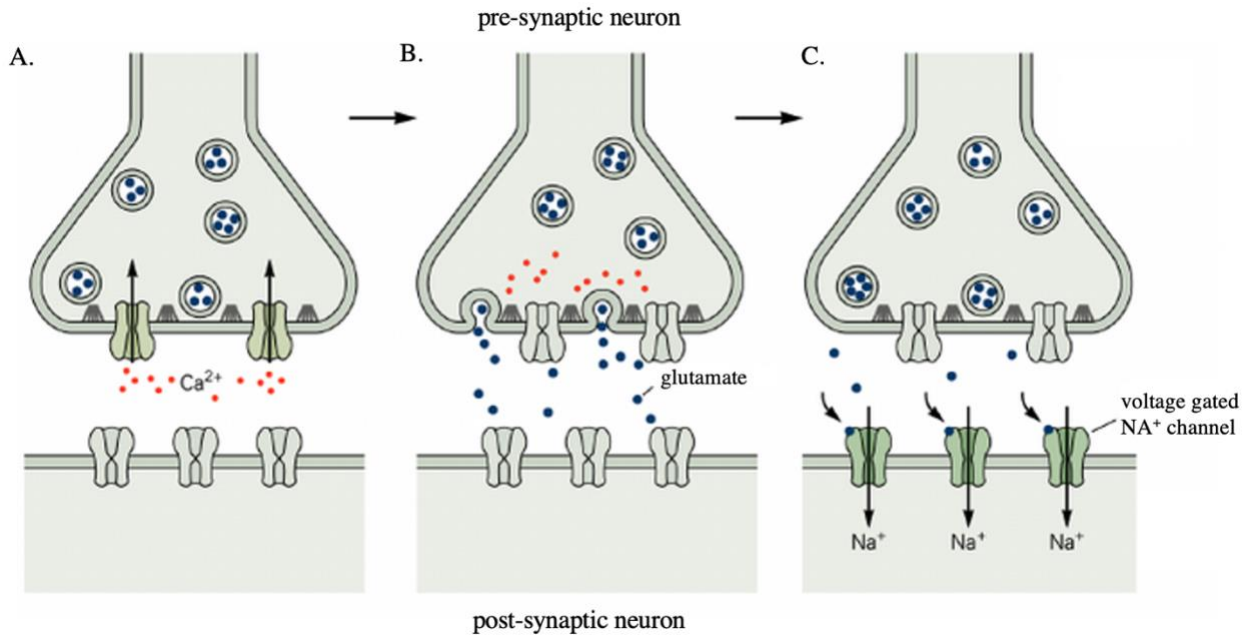


Figure 8: Schematic showing the glutamatergic synaptic transmission, adapted from (Kandel et al, 2000). A) Action potential opens the calcium channels on the presynaptic terminal, causing an influx of Ca^{2+}. B) This increase in positive charge causes the vesicles containing glutamate to fuse on the presynaptic membrane and release glutamate into the synaptic cleft. C) Glutamate binds with receptors on the post-synaptic neuron which allows an influx of Na^{+}.

There are two major pools of GABA within neurons, cytoplasmic GABA and vesicular GABA. Cytoplasmic GABA is synthesised from the precursor glutamate and is thought to be involved in neuronal activity through metabolism (Martin and Rimvall, 1993) from Stagg et al (2011c)). Vesicular GABA is present in the pre-synaptic boutons and is involved in synaptic inhibition (Martin and Rimvall, 1993) from Stagg et al (2011c)). The GAD receptors for cytoplasmic GABA are tonic (GAD_{67}) and have a high and persistent affinity for GABA, whilst the GAD receptors for vesicular GABA are phasic (GAD_{65}) and have a low affinity for GABA that is able to change rapidly (Lee and Maguire, 2014).

In the cortex there are two major GABA receptor subtypes, $GABA_A$ and $GABA_B$ receptors. $GABA_A$ receptors produce rapid inhibitory signals to hyperpolarise the postsynaptic membrane (Vithlani et al., 2011). Whilst $GABA_B$ receptors create prolonged inhibitory signals and are thought to regulate

synaptic plasticity (Bettler et al., 2004; Nguyen and Woo, 2003). In addition to the phasic inhibition from synaptic $GABA_A$ receptors, extra-synaptic $GABA_A$ receptors are thought to be involved in tonic inhibition from free extracellular GABA (Belelli et al., 2009).

1.2.2 Long-term potentiation and depression like plasticity

Repeated neuronal stimulation causes synapses to strengthen over time, and this long-lasting repeated strengthening in signal transmission is called long-term potentiation (LTP). The NMDA receptors ($NMDA_r$) allow glutamate to bind when the depolarisation of the cell causes the displacement of Mg^{2+}. This can occur from repeated stimulation of the post-synaptic neuron forcing the Mg^{2+} out of the NMDA receptor which causes a brief and high magnitude increase in Ca^{2+} entering the neuron (Yang et al., 1999). This increase in Ca^{2+} triggers an increase in AMPA receptors mediated synaptic transmission through an increase in the number and/or conductance of the active channels on the post-synaptic membrane (Benke et al., 1998) (Shi et al., 1999) (Park et al., 2021). This increase in AMPA receptor function therefore allows more glutamate to flow into the cell, increasing the cells excitatory response.

Long-term depression (LTD) in contrast, is the long-term weakening of synaptic connections. The NMDA receptors are also involved in LTD. When Ca^{2+} enters the post-synaptic neuron for a prolonged time at a low concentration this causes a decrease in AMPA receptors on the cell membrane. Therefore less glutamate flows into the cell, decreasing the cells excitatory response (Yang et al., 1999).

Both LTP and LTD have been well studied in the hippocampus (Bliss et al., 2003). In the neocortex plasticity with similar mechanisms to LTP has been reported, this is referred to as LTP-like plasticity and has been found in the visual cortex. In the rodent visual cortex, LTP-like plasticity can be induced using theta-burst stimulation (Wang and Daw, 2003). In the human visual cortex, LTP-like plasticity has been demonstrated using visually evoked potentials (VEPs) when viewing reversing checkerboards (Elvsashagen et al., 2012). This is described as “LTP-like” plasticity as there are some

similarities in the mechanisms with LTP but not all are shared when investigated at the cellular level (Koppel et al., 2015). For instance LTP-like plasticity is partly dependent on GABAergic interneurons and has been demonstrated in the rodent neocortex when combining a stimulation electrode with the $GABA_A$ agonist, diazepam, which blocked LTP-like processes (Trepel and Racine, 2000).

1.2.3. The critical period

The critical period is the time frame where the brain undergoes an intense period of neural development and is particularly influenced by the surrounding environment. In the human visual system, this stage is from birth until puberty, around the age of 12 (Poizner et al., 1990). The maturation of GABAergic circuits is caused by internal chloride levels changing over development and this maturation triggers the onset of the critical period (Hensch, 2005).

After the critical period, the visual cortex is considered to be less able to adapt to change from the environment. This has been shown from studies that investigate restoration of visual input after the critical period but find a lack of improvement in visual function (Lewis and Maurer, 2009; Maurer et al., 2007). Therefore the visual cortex is less able to adapt to a change of input in adulthood. As the maturation of GABAergic circuits triggers the critical period, GABA is an important neurochemical that could be used to increase the extent of neuroplasticity within the visual cortex.

1.3 Cortical degeneration

Neuronal death can occur via two processes: apoptosis or necrosis. Necrosis occurs via damage from external sources, whereas apoptosis occurs from programmed cell death. A lack of synaptic input causing the neurons to die occurs via apoptosis. In necrosis, there is an increase in the number of DNases, which are enzymes that destroy the DNA within the nucleus of the neuron. This causes the cell to condense and fragment, which is followed by phagocytosis from macrophages (Fricker et al., 2018). N-Acetylaspartate (NAA) is one of the most abundant metabolites in the human brain and is almost exclusively localised within the neurons and provides acetate for myelin synthesis (Shannon et al., 2016). NAA concentrations have been found to correlate with neuronal integrity (Moffett et al.,

2007). Therefore, NAA levels are an accepted marker for neuronal health or dysfunction (Rigotti et al., 2007). NAA is localised almost exclusively within neurons, and therefore neuronal degeneration reduces the amount of NAA present in the brain. High levels of NAA represent neuronal integrity, whilst lower levels are a marker for neuronal loss.

Glial cells support neurons through axonal myelination, removing debris in the extracellular space and releasing inflammatory biomarkers (Jakel and Dimou, 2017; Wolf et al., 2017). Neuronal degeneration can cause an increase in glial cell proliferation to repair the damage caused. Therefore, an increase in glial cell number is a sign of cortical degeneration. Myo-inositol (*myo*-Ins) is another abundant metabolite in the human brain and is concentrated in the glial cells. Glial cells support neurons through myelinating the axons and cleaning debris in the extracellular space (Jakel and Dimou, 2017). Neuronal degeneration can cause an increase in glial cell proliferation which could reflect an increase in inflammation or to remove debris in the extracellular space. Therefore, an increase in glial cell number is a sign of cortical degeneration. *Myo*-Ins is concentrated within glial cells and therefore an increase in this is linked to neuronal death.

1.4 Macular dystrophy

Inherited retinal degenerations are the leading cause of acquired early-onset vision loss in the developed world (Francis, 2006; Liew et al., 2014). Stargardt macular dystrophy (STGD1) is one of the more common types of retinal disease with a prevalence of 1 in 8 - 10,000 people (Michaelides et al., 2003). STGD1 is a juvenile inherited form of macular dystrophy, it is an autosomal recessive condition and associated with pathogenic variants in the *ABCA4* gene (Kjellstrom, 2015). This mutation disrupts the production of the ABC transporter protein coded by this gene. When these proteins are defective the vitamin A dependent fluorophore (A2E) is not broken down effectively and therefore not removed efficiently (Kennedy et al., 1995). A2E builds up in the RPE to create lipofuscin which clumps to form fatty deposits that increase over time and occlude central vision (figure 9C) (Kennedy et al., 1995). These deposits are toxic to the retina and lead to disrupted RPE metabolism and RPE cell death (Molday, 2007), with secondary loss of photoreceptor cells (Weng et

al., 1999), which is currently irreversible. The nerve fibre layer (ganglion and bipolar cells) is also affected in STGD1 but it is unclear whether this is due to a knock on effect of degeneration from the other retinal layers or from anterograde trans-neuronal degeneration (Reich et al., 2021).

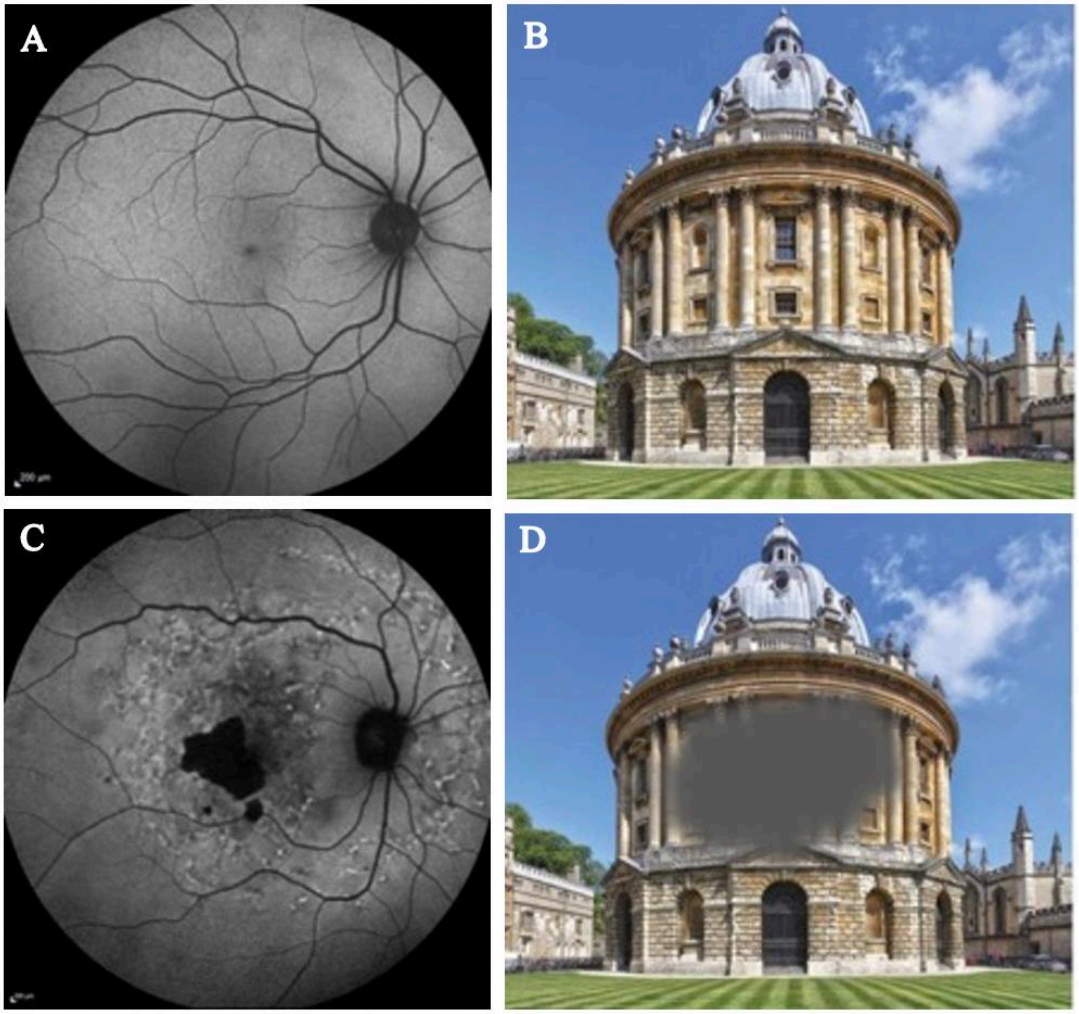


Figure 9: (A) Example fundus autofluorescence image of a healthy retina (B) with corresponding expected vision. (C) Example fundus autofluorescence image in STGD1 (D) with corresponding simulated visual field loss. Fundus autofluorescence images collected from a STGD1 patient and a control with a healthy visual system in the Low Vision Clinic, Oxford Eye Hospital, Oxford University Hospitals NHS Foundation Trust.

In STGD1 the RPE and photoreceptor loss predominantly affects the macular region of the retina. The macula has a high density of cones which enable high acuity vision, and therefore this loss leads to a

scotoma (area of vision loss) within the central visual field. The nerve fibre layer is thicker at the central macula in STGD1 due to inflammation and thinner at the peripheral macula (Reich et al., 2021). There are variable phenotypes in retinopathies associated with *ABCA4* variants, ranging from STGD1 macular dystrophy to chorioretinal atrophy with rod and cone dysfunction, mimicking retinitis pigmentosa (RP) (Al-Khuzaei et al., 2021a). These phenotypes have variable levels of severity, with differing ages of onset and rates of progression (Starace et al., 2021). This leads to individual differences in the degree to which the retinal structure is affected (Fishman et al., 1999; McBain et al., 2012; Westeneng-van Haaften et al., 2012). In "typical" STGD1 there is central retinal atrophy with foveal photoreceptor damage accompanied by flecks (Gomes et al., 2009). Only patients with phenotypes "typical" for macular STGD1 were included in this thesis to ensure the vision loss was confined to the central visual field. There is consensus in the literature that structural loss is correlated with functional loss, so the greater the loss of the photoreceptor layers, the larger the loss of functional vision (Testa et al., 2012). The symptoms of vision loss tend to first present in early adulthood, after the end of the critical period and this degeneration continues over the lifespan.

1.4.1. Vision loss therapies

The current therapeutic advice for those suffering with STGD1 is to wear tinted eyewear when in bright light, avoid vitamin A supplements and if necessary be assessed for low vision aids. Currently, there are no clinically approved therapies to restore vision in STGD1, although there are treatments in development. These therapies range from trying to slow or halt the degeneration, to replacing the lost photoreceptors. A synthetic form of vitamin A has been developed to slow the build-up of lipofuscin and therefore reduce the rate of vision loss (Issa et al., 2015). Gene therapy aims to stabilise the degeneration by replacing the defective form of the *ABCA4* gene and therefore halt further vision loss (Binley et al., 2013).

The most promising therapy for restoration of vision is through stem cells with the aim of replacing the degenerated retinal pigment epithelial cells and/or photoreceptors in retinal disease (West et al., 2020). Predominantly, photoreceptor replacement therapies have focused on replacing the rods. While

improvements in vision have been reported but it is unclear if this is from within the replaced cells themselves or from new synaptic connections with the remaining cells (Reh, 2016). There is less research into cone photoreceptor replacement, but the results so far are promising. A mouse model of achromatopsia with stem cell therapy to replace the cones found that an increase in synaptic connections between the replaced cells and the original cells occurred (Ribeiro et al., 2021). The mice retinas showed an increase in electrophysiology light responses and in their light avoidant behaviour. These results show a promising behavioural improvement in light sensitivity of the replaced cones in congenital vision loss; however, stem cell treatment has not been successfully performed in an adult group with vision loss after the critical period.

To summarise, STGD1 causes photoreceptor degeneration that creates vision loss within the central visual field. There are currently a range of treatments in development to restore function at the retina. The most promising therapies for sight restoration are based on stem cell implantation, however these have yet to be investigated in an adult population with vision loss, like STGD1.

1.5 Cortical reorganisation after a loss of visual input

The brain has a remarkable capacity to adapt to an altered sensory input early in life, however, much less is known about how the adult brain processes a loss of input. Vision loss in STGD1 predominantly starts after the closing of the critical period of development, therefore the brain may be unable to adapt to a loss of sensory input.

1.5.1 Non-human primate models of cortical reorganisation after vision loss

Non-human primates have a visual system that is most similar to the human visual system, as unlike many species, they possess a macula. This is important because it is the region predominantly affected in STGD1. Therefore, findings from studies using non-human primates are more applicable to what we would expect to happen in the human visual cortex after vision loss. Due to the topographic organisation of the visual cortex, an area of focal loss in the retina, projects to a localised region of the visual cortex; this is called the lesion projection zone (LPZ) (Shao et al., 2013). Metabolic signals,

were measured with cytochrome oxidase staining, in the LPZ of macaques indicated a permanent reduction of signal up to 9 months post retinal lesion (Horton and Hocking, 1998). This suggests that reorganisation is not occurring in the cortex, however the vision loss was only monocular in these groups and therefore the input to the visual cortex from the remaining eye may have prevented reorganisation.

Keliris and colleagues (2022) used retinotopic mapping to investigate whether cortical reorganisation occurred in the LPZ of adult macaques with retinal lesions. They found activation of voxels inside the LPZ that respond to the foveal border of the scotoma that became present two weeks post lesion and suggests the neurons inside the LPZ are reorganising to process the spared input. They found the mean modulation activation strength of these voxels within the LPZ remained stable up to five months post lesion. This suggests that after initial vision loss the neurons inside the LPZ start to respond to regions at the borders of the scotoma, whether this response stays stable after five months is unclear.

1.5.2 Neuronal reorganisation after vision loss in humans

In humans with retinal degeneration, the LPZ can be functionally mapped in the visual cortex using fMRI (Baseler et al., 2011; Ritter et al., 2019; Silson et al., 2018). Photoreceptor degeneration within the central retina, resulting in a loss of the central visual field can be mapped to the posterior section of V1 (Baseler et al., 2011). In an adult patient group with macular degeneration the LPZ was measured using retinotopic mapping in fMRI (Baseler et al., 2011). Functional activation was absent within the LPZ and the authors concluded this did not show evidence of remapping within the LPZ (Baseler et al., 2011). Vision loss occurred after the critical period in these patients, therefore these results suggest neuronal reorganisation is limited if vision loss occurs in adulthood.

(Liu et al., 2010) used retinotopic mapping to investigate whether cortical reorganisation occurred in humans with AMD and JMD. They found that stimuli that activated the PRL caused activation in the

foveal cortical projection, but this did not extend to the posterior occipital pole. They suggested this showed an incomplete reorganisation of the LPZ after vision loss.

Resting state fMRI (rs-fMRI) provides a measure of functional connectivity between regions across the cortex. This can be investigated in patient groups with vision loss to measure whether connectivity changes between regions within the visual cortex or between those regions and the rest of the brain. In adults with vision loss from glaucoma, reduced functional connectivity was found between the early visual areas (V1 and V2), whilst increased connectivity was found between V1 and the right inferior parietal lobule and basal ganglia (Li et al., 2017). These finding suggest that that lack of input in adulthood increases the communication from the visual cortex to the rest of the brain to promote reorganisation. However, in another patient group with glaucoma, functional connectivity between V1 and regions outside of the early visual areas (fusiform gyrus, bilateral cuneus, left precuneus) were found to decrease (Wu et al., 2020). These contrasting results may be due to glaucoma causing both degeneration at the retina and in the brain (Lawlor et al., 2018; You et al., 2021). Therefore, the changes in the visual cortex may be due to separate degenerative processes in the brain, rather than the loss of input from the retina causing degeneration in the visual cortex. Therefore, this should be considered when interpreting whether the degeneration in the cortex is due to a loss of input at the retina from glaucoma.

In a patient group with peripheral loss from RP, decreased functional connectivity was found between the bilateral calcarine and cortical regions outside the visual cortex (post central gyrus and superior parietal lobule (SPL)) (Huang et al., 2019). The authors suggested the reduction in connectivity to the SPL may be due to the loss of peripheral vision which reduces motion discrimination. The end point of the dorsal visual stream is located in the SPL and is responsible for the integration of visuomotor signals; the authors suggested this would reflect reductions in the visuomotor coordination in RP. Additionally, they found significantly lower functionally connectivity within the calcarine sulcus in RP patients. However, they did find increased functional connectivity between the calcarine and the sub-cortical regions of the thalamus and caudate in the RP group. A follow up paper with the same

participant cohort found that the functional connectivity also varied with disease length in RP (Dan et al., 2019). The functional connectivity within the bilateral lingual gyrus correlated with both disease length (negative correlation) and visual acuity (positive correlation). Therefore, as disease severity increases the functional connectivity within the lingual gyrus decreases. These results show that a loss of visual input from retinal disease reduces functional connectivity both within the visual cortex and between the visual cortex and to regions in the rest of the brain.

In a study comparing STGD1 to controls, increased functional connectivity was found from the central early visual cortex (EVC) (the region of projected loss in STGD1) to the cuneus, intraparietal sulcus but decreased connectivity to the central anterior cingulate cortex and the middle temporal gyri (Sabbah et al., 2017). In contrast, the peripheral EVC showed increased connectivity to the right lateral occipital complex (LOC), lingual gyri and the fusiform gyrus, but decreased connectivity to the cuneus and left dorsal anterior cingulate (Sabbah et al., 2017). However, they did not find a correlation between functional connectivity and disease severity, measured by duration of visual deficit. These mixed results may have been due to the ROI definition, as the ROI locations were limited to the screen size used for retinotopic mapping, therefore the peripheral EVC is still close to the central visual field and may also encapsulate part of the vision loss in STGD1 and not the RP loss. The authors suggested that the increases in functional connectivity indicated that reorganisation was occurring in the cortex after a loss of visual input. However, the results show both increases and decreases in functional connectivity which do not correlate with disease severity, and therefore should be interpreted with that in mind.

Overall, the research investigating functional connectivity changes after a loss of visual input find inconsistent results. Both increases and decreases in functional connectivity have been found within the visual cortex and between visual regions and the remaining cortex after vision loss.

1.5.3 Interpreting measures of GABA and glutamate from ^{1}H-MRS

The cortex is an interconnected circuit of a variety of cell types that communicate with each other through action potentials and chemical signalling. Measures of neurochemistry can provide a valuable insight into the processes that occur at a particular point in time, within a specific region of the cortex. Cortical measurements *in vivo* can be measured at different spatial and temporal resolutions depending on the invasiveness of the technique used. In humans, Magnetic Resonance Spectroscopy (^{1}H-MRS) is a non-invasive technique that can measure neurochemical concentrations *in vivo*. Each ^{1}H-MRS voxel contains thousands of neurons; therefore, it is not possible to measure the neurotransmitter level in each neuron individually with this technique. Synaptic activity occurs on the level of milliseconds, whereas ^{1}H-MRS has an acquisition time in the order of minutes and therefore ^{1}H-MRS measures do not directly infer synaptic activity.

Glutamate levels are involved in cortical plasticity and GABA is fundamental in modulating cortical inhibition by regulating membrane potential. Glutamate levels measured with ^{1}H-MRS are not thought to reflect glutamatergic excitation and therefore should not be used as a measure for neuronal plasticity. As glutamate-related plasticity is generally reflected in changes in the density and sensitivity of receptors, and therefore undetectable by ^{1}H-MRS (Stagg, 2014). This view is supported by a lack of glutamate after administration of ketamine (an NMDA-receptor antagonist) which should increase glutamatergic excitation, however no changes in glutamate levels were found, suggesting glutamatergic excitation is invisible to ^{1}H-MRS (Taylor et al., 2012). However, further research is needed using animal models to disambiguate the glutamate signal ^{1}H-MRS measures in order to confirm that this signal is not from glutamate-related plasticity. Instead, glutamate levels measured with ^{1}H-MRS are thought to reflect the metabolic glutamate signal. This has been shown in elderly participants with lower neuronal mitochondrial metabolism which correlated with reductions in glutamate measured ^{1}H-MRS (Boumezbeur et al., 2010). Elevated glutamate levels have been found to correlate with increased functional activation within the visual cortex, measured with simultaneous BOLD-fMRI and ^{1}H-MRS (Ip et al., 2017). Therefore ^{1}H-MRS measured glutamate can be interpreted as a measure of functional activity within the cortex.

Around 20% of cortical neurons are GABAergic, they are widespread throughout the cortex and have extensive connectivity. Due to this range of interconnectivity, GABAergic neurons have both a role in regulating circuit excitability and are able to drive broad network synchronisations (Griffen and Maffei, 2014). Strong evidence using tDCS has shown that ^{1}H-MRS measured GABA concentrations reflect the pool of GABA in extra-cellular space rather than a measure of intracellular metabolic activity (Stagg et al 2011a). However this has not been replicated using TMS (Dyke et al., 2017), although this difference in results may be due to the different brain stimulation techniques used. Therefore, a measured increase in GABA concentrations is thought to reflect tonic inhibitory activity that affects local neuronal excitability (Stagg et al, 2011 a, b, c). Both studies investigated GABA levels within the motor cortex, however it is unclear if the same effect is present within the visual cortex. The plasticity boost in the motor cortex using tDCS has not been replicated in the visual cortex, where behavioural performance was not found to improve (Larcombe et al., 2019). This suggests that the visual cortex may be less plastic than the motor cortex. Overall, a decrease in GABA levels in the brain would suggest an increase in activation which may lead to cortical plasticity.

Additionally, when interpreting ^{1}H-MRS measured GABA and glutamate concentrations, they should be considered in conjunction with concentrations of the other neurochemicals. Neuronal death may push other neurochemicals into the extracellular space. Therefore, it is important to measure if there is a marked increase across all neurochemicals or only the neurochemicals of interest, as neuronal death would cause a change in concentration across many neurochemical measures.

1.5.4 GABA levels within the human visual cortex

It has been shown there is a role for GABA in the visual cortex in learning (Frangou et al., 2018) and a reduction in GABA after monocular deprivation (Lunghi et al., 2015). This shows how a short-term change in visual input can decrease GABA levels, which would cause a decrease in neuronal inhibition. The monocular deprivation was over a time period of 150 minutes, whereas the loss from

STGD1 progresses slowly over years, therefore it is unclear if vision loss in STGD1 would affect GABA levels in the same way long term.

Vision loss early in life have shown variable results in GABA measurements within the visual cortex. (Weaver et al., 2013) found indications of lower GABA levels, suggesting that the visual cortex may reorganise to take on another function through a decrease in inhibition early in life. In addition, (Coullon et al., 2015) found a wide variability in GABA concentrations within the visual cortex, suggesting a change in GABA concentrations does follow visual loss. At the time of these studies the techniques to measure GABA were not as sensitive as the techniques used now, which would have made GABA difficult to measure. Both studies investigated vision loss within the critical period; therefore, it is unclear if the GABA concentrations would also change in vision loss in adulthood.

To summarise, the brain is developing throughout the critical period, where the synaptic strength between neurons is easily altered and therefore more readily able to respond to a change of input. The research stated supports the view that GABA is linked to long term plasticity, with a reduction in GABA leading to a reduction in neuronal inhibition that can influence the potential for reorganisation in the visual cortex. Whether this happens within the visual cortex of patients with vision loss after the critical period is currently unknown.

1.6 Cortical degeneration after a loss of visual input

It is unclear how the visual cortex processes a loss of visual input in adulthood, since, the neurons may be unable to form new connections and instead degenerate.

1.6.1 Non-human primate models of neuronal degeneration in vision loss

In non-human primates with peripheral vision loss caused by glaucoma, a reduction in the size of the lateral geniculate nucleus (LGN) has been found, and this loss was four times greater in the magnocellular than the parvocellular layers (Weber et al., 2000). The magnocellular layers process visual stimuli with a high temporal frequency such as movement of large objects, whereas the

parvocellular layers process visual stimuli with a high spatial resolution such as small, detailed objects. As glaucoma effects the peripheral visual field and causes a reduction in detection of large object movement, it is understandable that these magnocellular layers degenerate to a greater extent in glaucoma. VBM allows measurement of global grey matter density in the brain. Marmosets with retinal degeneration in glaucoma had a reduction in V1 volume shown with voxel-based morphometry (VBM) using 7T MRI. This reduction in V1 was confirmed with histology, where a reduction in cell number was found in layer 4 of V1 in glaucoma compared to controls (Noro et al., 2019). These findings suggest that a loss of input from the retina causes neuronal degeneration in the regions that process this input.

The animal literature shows that degeneration of the retina is associated with degeneration across the visual pathway including the LGN and V1. However, these studies predominantly use glaucoma as a model of vision loss and as stated previously glaucoma is also a neurodegenerative disease (Lawlor et al., 2018). Therefore, the changes in the visual cortex may be due to genetically determined degeneration, rather than from a loss of visual input.

NAA levels are an accepted marker for neuronal health or dysfunction (Rigotti et al., 2007). Neurochemical markers for degeneration have been found after binocular enucleation in two macaques (Wu et al., 2013). ^{1}H-MRS was performed 16 months post-enucleation and NAA levels were found to decrease, suggesting degeneration was occurring within the neurons. Levels of *myo*-Ins, which are considered a marker for glial cell proliferation, were found to increase (Haris et al., 2011). As previously stated, an increase in glial cell number is a sign of cortical degeneration, as glial cells repair damage within the neuron.

1.6.2 Neuronal degeneration after vision loss in humans

Structural markers of degeneration:

Studies investigating VBM changes in IRDs have shown a reduction in visual cortex volume in RP (Machado et al., 2017), glaucoma (Boucard et al., 2009; Zikou et al., 2012), and macular degeneration

(Boucard et al., 2009; Hernowo et al., 2014). Specifically in a patient cohort with STGD1 a reduction in grey matter volume was found in the visual cortex using VBM (Olivo et al., 2015). Due to the topographic organisation of the visual cortex, the LPZ from a loss of input at the retina is projected to posterior V1. In patients with macular degeneration, a reduction in grey matter density has been found at posterior V1, where the central lesion zone of the visual field is represented (Plank et al., 2011).

VBM provides a measure of grey matter density across the brain, whereas measures of cortical thickness can investigate grey matter thickness within specific regions of the visual cortex. A direct measure of cortical thickness *in vivo* is not possible in the human brain; therefore, structural MRI can give an indirect quantification of grey matter thickness. Cortical thickness is measured by the shortest difference between the edge of the white matter to the pial surface of the brain. This varies considerably across the brain, where the thinnest area is the visual cortex which varies from 1.5 mm to 2.5 mm (Alvarez et al., 2019). Cortical thickness has been shown to be altered after a loss of visual input from conditions such as congenital blindness and albinism (Bridge et al., 2009; Bridge et al., 2014).

Cortical thickness has been compared within the grey matter between the anterior and posterior V1 in patient cohorts with vision loss. Due to the topographic organisation, a focal point of loss in the visual field, projects to a specific point in the visual cortex. A thinner posterior V1, which represents the central visual field (and thus where the loss is processed) has been found in patients with macular degeneration using Freesurfer measures of cortical thickness (Burge et al., 2016; Hanson et al., 2019), suggesting a loss of input causes degeneration in the cortex. However a thinner V1 was not found in patients with vision loss from RP compared to controls (Ferreira et al., 2017), suggesting degeneration was not occurring. This study used a different analysis tool (BrainVoyager), therefore it is unclear whether these contrasting results are due to differences between the analysis software or variabilities between the patients' phenotypes. Whether cortical degeneration occurs after vision loss remains to be determined.

Neurochemical markers of degeneration:

Using ^{1}H-MRS, Boucard and colleagues (2009) did not find any difference in NAA concentrations within the visual cortex between patients with vision loss and matched control participants. This may have reflected the large voxel size or lack of accounting for tissue segmentation, leading to highly variable NAA levels even within the control population. In a similar study investigating neurochemical changes with ^{1}H-MRS in the visual cortex of patients with glaucoma, a reduction in NAA in the visual cortex was found (Zhang et al., 2013). The authors suggested this may be due to neuronal degeneration after a loss of visual input due to glaucoma.

In a patient cohort with vision loss due to a variety of causes (RP, optic neuritis, optic nerve lesion) and varying ages of onset (before and after the critical period), ^{1}H-MRS was used to measure multiple neurochemical concentrations in the visual cortex (Bernabeu et al., 2009). They found elevated *myo*-Ins levels in the visual cortex which they suggested could be due to inflammation or glial cell proliferation, to counteract the neuronal degeneration from a loss of visual input.

To summarise, the literature in non-human primate models of vision loss in adulthood suggests that neurons degenerate after a loss of visual input. As non-human primates share a similar visual system to humans, similar degeneration processes would be expected to occur in the adult human visual cortex after vision loss. In the human literature, the large voxel sizes in ^{1}H-MRS make it unclear whether cortical degeneration occurs after vision loss in adulthood. Therefore, currently very little is known about how the human visual cortex responds to a loss of input in adulthood.

1.7 Synopsis of thesis

1.7.1 Aims of thesis

This thesis investigates whether reorganisation or degeneration occurs in the adult visual cortex after vision loss due to STGD1. Currently there are treatments in development to restore input at the retinal level, however the majority of visual processing takes place in the visual cortex. Therefore it is vital to confirm if the visual cortex degenerates after a prolonged lack of input, as therapies that improve

retinal function may not optimally restore vision if the visual cortex cannot respond to the new input. Ultimately, a stable LPZ ready to respond to the restored input, regardless of the length of time since the onset of the scotoma would be the ideal scenario for recovering sight loss. However, there is not a consensus in the literature on how the adult visual cortex responds after a loss of sensory input. Therefore this thesis aims to answer this question by investigating whether changes in structure, function, and neurochemistry occur in the visual system after photoceptor loss from STGD1.

This thesis has two primary aims:

1. To understand if degeneration occurs after a loss of input to the adult visual cortex.

If degeneration occurs, then the neurons that process the lost input would cease to fire, and therefore degenerate, this will create cortical thinning in the area that processes the vision loss. This loss would reflect a functional change in decreased connectivity within the visual cortex and between the visual cortex and the surrounding brain areas due to neuronal loss. Degeneration would be reflected in a decrease in NAA due to neuronal loss and an elevation of *myo*-Ins concentrations to reflect glial cell proliferation.

2. To investigate the capacity for reorganisation in the adult visual cortex after vision loss.

If reorganisation occurs, then the neurons that process the lost input would start to make new connections to surrounding neurons. These new connections would be reflected in a change in the neurochemicals of GABA and glutamate. For this thesis GABA was used as a measure to infer plasticity, as glutamate-related plasticity is generally reflected in changes in the density and sensitivity of receptors, and therefore undetectable by ^{1}H-MRS (Stagg, 2014). A decrease in GABA concentration would create a reduction in inhibition and therefore an increase in the potential for neuronal reorganisation. If the neurons reorganise rather than degenerate, then the visual cortex should be structurally similar between controls and STGD1. A change in neuronal function would follow a neurochemical change therefore this would present as an increase in functional connectivity

within the visual cortex and between the visual cortex and the surrounding brain areas, in order to promote reorganisation.

1.7.2 Thesis overview

The first experimental chapter (Chapter 3 – Vision Measures) presents the STGD1 patients' visual function and quantifies the individual vision loss in each of the STGD1 patients to provide an indication of disease severity. This chapter includes measures of retinal sensitivity, colour vision and contrast sensitivity. Vision measurements from participants with a healthy visual system were used to generate a baseline for comparison with the STGD1 participants.

In the second experimental chapter (Chapter 4 – Structural) the structure of the retina was investigated to measure cellular loss in the photoreceptor and nerve fibre layers. To understand whether a loss of structure at the retina causes degeneration in the visual cortex, measures of grey matter volume and thickness were investigated. Measures of grey matter volume were first used to investigate global changes at a voxel wise level, then cortical thickness measures were used to investigate grey matter thickness across V1.

In the third experiment chapter (Chapter 5 – Functional), resting state fMRI was used to investigate how the loss of visual input from STGD1 affects the neural connectivity. Functional connectivity both within the visual cortex and between regions of the visual cortex and the rest of the brain was investigated.

In Chapter 6 (Neurochemical Validation) the Magnetic resonance spectroscopy imaging (MRSI) technique was validated to ensure it accurately measured neurochemical concentrations, as the research presented in this thesis is the first to use this technique within the visual cortex. In the final experimental chapter (Chapter 7 – Neurochemical), MRSI was used to investigate neurochemical concentrations within V1 in STGD1. Markers for neuronal reorganisation and degeneration were

investigated and this allowed a comparison of neurochemical concentrations inside and outside the area of projected loss in STGD1.

2 Methods and Procedure

This chapter provides an overview of the methods and procedure for the experiments described in this thesis. The choice of methods used to assess visual function and structure of the retina are first described, followed by a description of the different Magnetic Resonance Imaging (MRI) methods used to investigate the structure, function, and neurochemistry of the cortex. It finally describes the procedure for the data collection testing day and includes demographics of the participant cohort including how STGD1 was assessed.

2.1 Introduction

STGD1 causes progressive degeneration of the photoreceptors in the retina, and predominantly affects the central macula. This degeneration causes a loss of vision in the central visual field, and this particularly affects colour vision discrimination and high acuity vision. To understand how the visual system is affected after vision loss caused by photoreceptor death in STGD1, we used techniques that measure retinal structure, alongside behavioural measurements of visual function. These give a valuable insight into an individual's perception and can be used to measure the extent of vision loss after retinal damage. As a loss of input at the retina is expected to impact on brain structure and function, we measured the visual cortex with MRI, these included structural, functional, and neurochemical measures.

As STGD1 is progressive, there are a range of disease severities due to differing rates of degeneration occurring at the level of the retina. Therefore, the methods used in this thesis were chosen to encapsulate the different amounts of vision loss between patients with STGD1 compared to controls with a healthy visual system.

2.2 Methods to assess retinal structure and visual function

2.2.1 Retinal Structure

The retina is comprised of multiple layers with specific cell types; these work in collaboration to process the light signals that enter the eye. The retinal structure can be imaged non-invasively using Optical Coherence Tomography (OCT) (Spectralis® HRA+OCT imaging system, Heidelberg Engineering, Heidelberg, Germany). This technique uses near-infrared light waves to echo off the tissue structure in the retina and using a Michelson interferometer enables the time delay to be measured from the reflection of the light at different depths. The receiver contains a spectrometer that uses Fourier analysis of the reflected light spectrum to create high resolution (10 μm) 3D, cross-sectional images of the retina.

OCT images enable visualisation of highly detailed differentiation between the layers such as the nerve fibre layer, RPE and photoreceptor layers which are structures that are affected by IRDs (figure 10). The thinnest point at the centre of the retina is the fovea (figure 10), which is particularly vulnerable to retinal damage caused by STGD1. Focal changes within one retinal layer may be observed, and the extent and type of cell affected depends on the type of IRD, in STGD1 these are the RPE and photoreceptor cells. This focal damage can cause subsequent degeneration to surrounding layers of the retina. Therefore, OCT can be used to measure the extent of damage in the retina within specific layers.

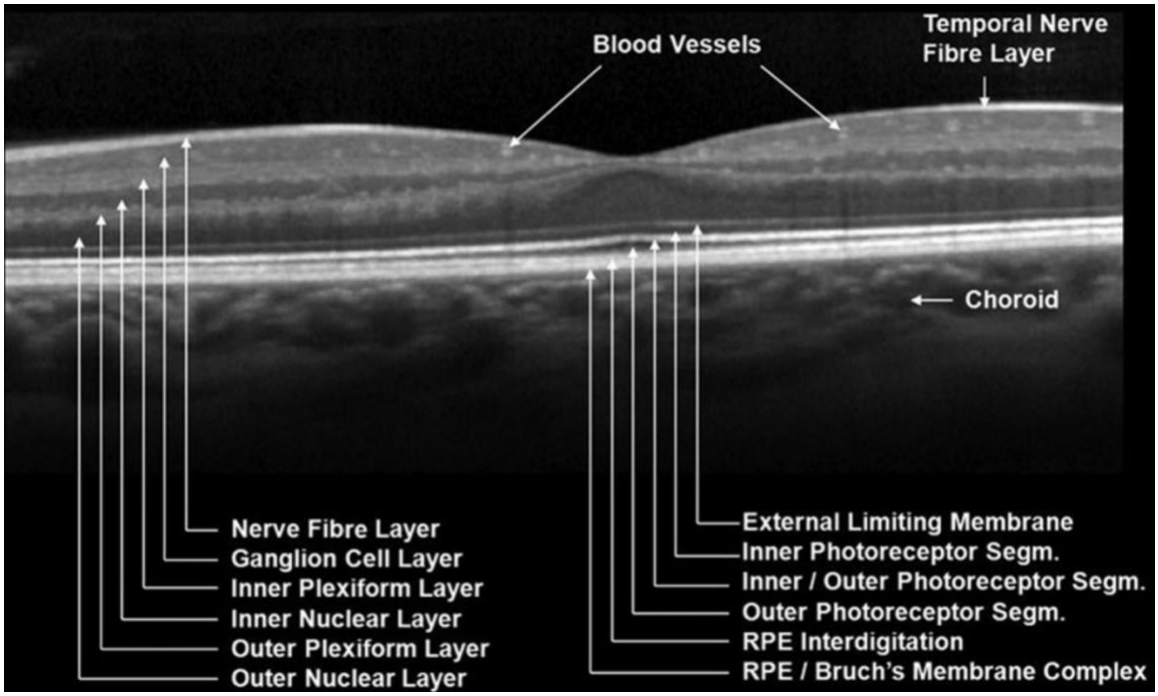


Figure 10: Optical Coherence Tomography cross-section of a healthy human retina. Individual retina layers are labelled. The thinnest point at the centre of the retina is the fovea. Image from (Putnam, 2017).

2.2.2 Retinal Function

Perimetry is a non-invasive procedure that measures visual function across a section of the participant's visual field. This technique can map the extent of a visual field deficit from damage to the visual system. Perimetry produces plots of the participants visual field, and this technique can map

regions of vision loss if they are located within the area measured. There are two main forms of perimetry, static and kinetic. The first is static perimetry is where a participant fixates on a target in the centre of a bowl, a static light is projected onto the surface and the participant responds if they see this light. The second is kinetic perimetry where the participant fixates in the centre of the bowl but has to detect a moving target instead. Static perimetry is more accurate at detecting scotomas compared to kinetic perimetry. This thesis used a form of static perimetry called microperimetry (MAIA system, Centervue, Padova, Italy).

Microperimetry measures the sensitivity of the retina to light. The participant fixates on a cross in the centre of the visual field, lights of varying luminance levels (dB) are displayed and received by retina, and a response is recorded if they are seen by the participant (green in figure 11). In individuals with vision loss microperimetry can be used to map regions of functional loss reflected by the location of reduced retinal sensitivity (red/black in figure 11). The image of the visual field is inverted and left-right reversed on the retina, due to the crossing of light rays at the pupil, thus the inferior retina responds to the superior visual field and vice-versa. This should be adjusted for when interpreting visual field loss from retinal sensitivity plots.

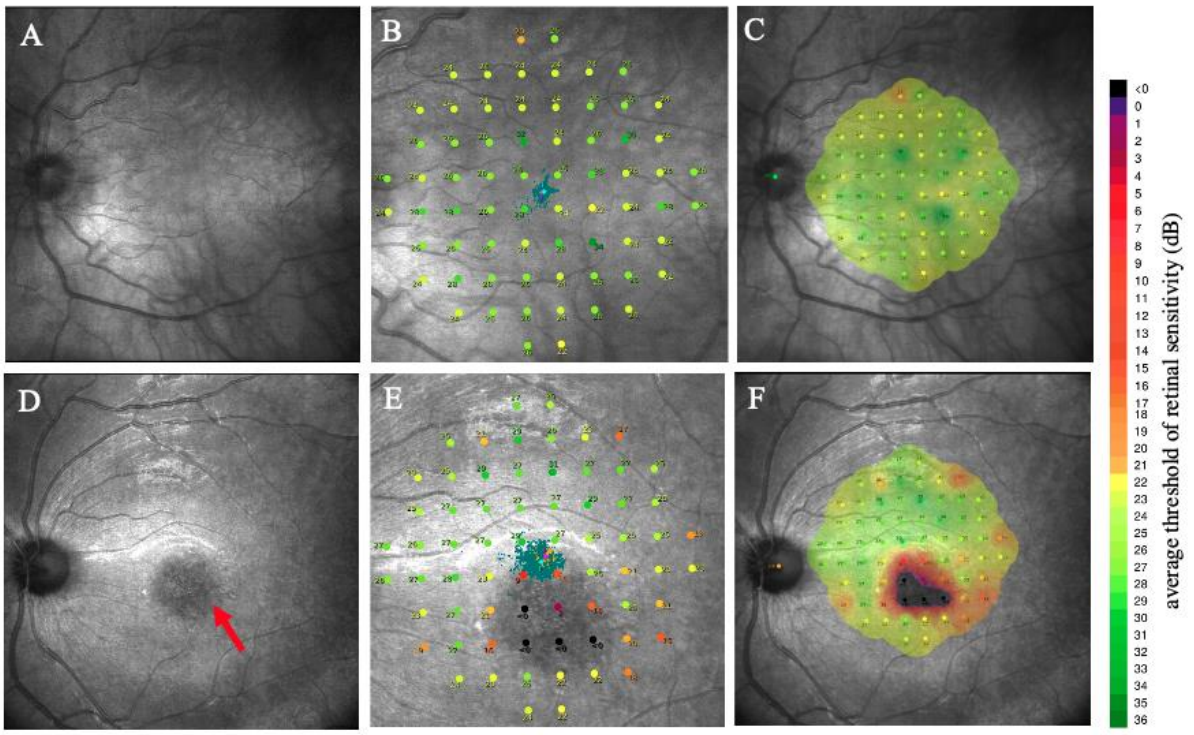


Figure 11: Infrared image of the left retina of a control with healthy vision (A) with the retinal sensitivities (dB) of light points shone onto retina (B) and corresponding interpolated retinal sensitivity map (C). Fundus autofluorescence image of the left retina of a patient with STGD1 (D), red arrow points to scotoma. Retinal sensitivities (dB) of light points shone onto retina (E) and corresponding interpolated retinal sensitivity map (F). The retinal sensitivities (dB) show light stimulus seen (green) to unseen (black) with the corresponding retinal sensitivity colour bar on the right. Fixation points are shown in turquoise.

2.2.3 Relating retinal position to visual field location

In this thesis retinal position is compared to locations within the visual field, as the projected visual field is used as a measure to sub-divide V1 (°). The central visual field loss in STGD1 is projected to the posterior visual cortex and, due to cortical magnification, this region of loss is overrepresented in V1. Therefore, this section explains how visual field location (°) relates to the position on the retina (mm). The foveola (the region of highest acuity vision) and used for fixation in the healthy visual system occupies the central ~ 0.35mm of the retina which relates to 1.5° of the visual field (figure 12). The fovea extends to the central~ 1.5mm and this relates to central 7° of the visual field, whilst the

diameter of the macula is more variable around ~ 3 – 5 mm of the retina and up to the central 18° of the visual field (Polyak, 1972). The size of an object's image on the retina is proportional to the distance it is viewed at, and this is measured in visual angle (minutes of arc). The visual field extends 90° laterally to the temporal edge and this is represented at the most anterior position of V1. For this thesis, microperimetry measured up to the central 20° of the retina and the OCT measured the central 18° of the retina.

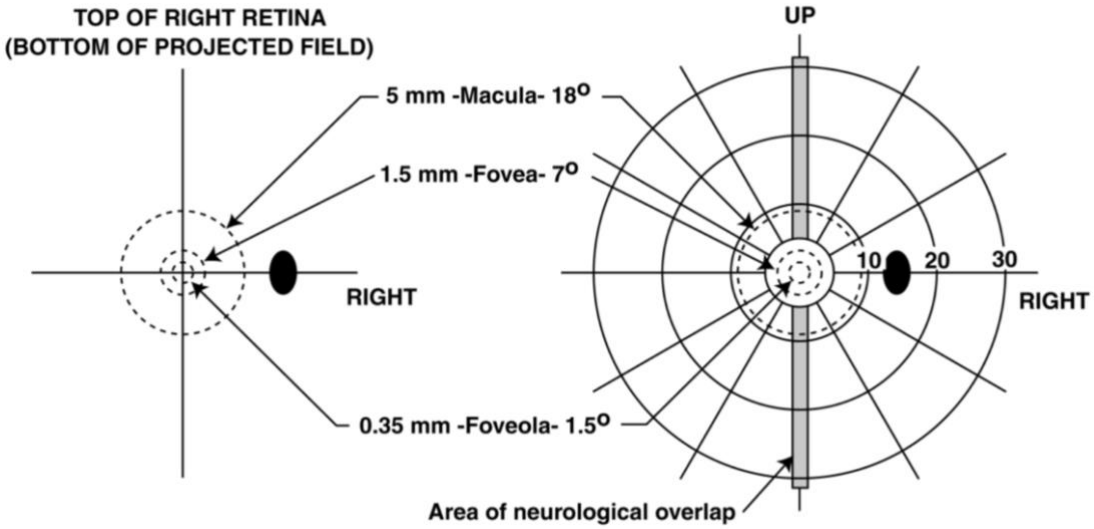


Figure 12: Retinal position related to visual field location. Black disc is the optic nerve (left image) which creates a blind spot (right image) in the visual field. Image from source: https://neuronresearch.net/vision/clinical/macular_foveola_sparing.htm: retina&visualfields.jpg

2.2.4 Visual Acuity

Visual acuity is the ability to spatially resolve fine detail within the visual field and is higher in the central visual field due to the high-density cone pure region of the fovea, compared to the peripheral visual field. It can be measured by presenting optotypes, which are high contrast letters and asking the individual to resolve them. Visual acuity is measured on a logarithm of the minimum angle of resolution (logMAR) chart (figure 13), the optotype size decreases as the individual reads down the chart. This reduction in size means the optotypes are presented in finer detail and therefore higher acuity vision is needed to resolve them. The point at which the letters can no longer be resolved relates to the individual's visual acuity. The chart is viewed at a set distance, and this is used to

calculate visual acuity. Visual acuity provides an insight into the individuals visual function and in vision loss can measure how the damage affects central, fine detailed vision.

The Electronic Visual Acuity (EVA) tester (Emmes Corporation) is a computerised version of the standard charts. The EVA was chosen for this study as it provides a more accurate measure of visual acuity in participants with visual field loss compared to standard charts (Jolly et al., 2020). The is due to central vision loss affecting fixation and therefore, they find it difficult to maintain fixation over the large VA charts, compared to a smaller computerised screen (Jolly et al., 2020).



J Optom. 2013;6:18–24

Figure 13: A logarithmic visual acuity chart to measure visual function. Optotypes decrease in size as the participant reads down the chart. The participant responds verbally from left to right; this continues until no further optotypes can be read. The point the optotypes can no longer be resolved provides a measure of visual acuity.

2.2.5 Contrast Sensitivity

Spatial resolution refers to the ability to resolve a luminance-defined stimulus and provides a measure of visual acuity. The luminance profile of sine-wave gratings are examples of spatial stimuli, and these sinusoidal gratings can be varied for spatial frequency (cycles/°) and contrast. Spatial frequency determines the distance between the gratings, where a high spatial frequency has gratings that are closer together than gratings from a lower spatial frequency. Contrast (%) refers to the difference in luminance that makes a stimulus visible compared to its background.

The spatial contrast sensitivity function (CSF) detects the amount of contrast needed to discriminate patterns across varying spatial scales (Campbell, 1990). The Cambridge Spatial Achromatic Contrast Sensitivity Function is an automated, computerised test that measures an individual's CSF. It presents varying spatial frequencies of sinusoidal gratings at differing contrasts and measures the contrast sensitivity detection threshold for each spatial frequency. The CSF is determined as the lowest level of contrast that can be detected for each sinusoidal grating presented and is plotted as contrast sensitivity against different spatial frequencies of the gratings (figure 14). The area under the curve (red in figure 14) represents the visible contrasts seen and the area above the curve are unseen. The maximum sensitivity of the CSF in humans with healthy spatial vision is approximately at 4 cycles/°. The contrast sensitivity decreases at either side of the peak and at higher spatial frequencies there is a high frequency cut-off where a grating is no longer visible at 100% contrast. This high frequency CSF cut-off is equivalent to the point where the optotypes are no longer resolved in visual acuity charts.

As high acuity vision is processed in the central visual field, damage to this area would be reflected in the CSF. High spatial frequencies require high acuity vision to resolve them, therefore loss of the central visual field would be reflected in lower contrast sensitivity thresholds at higher spatial frequencies.

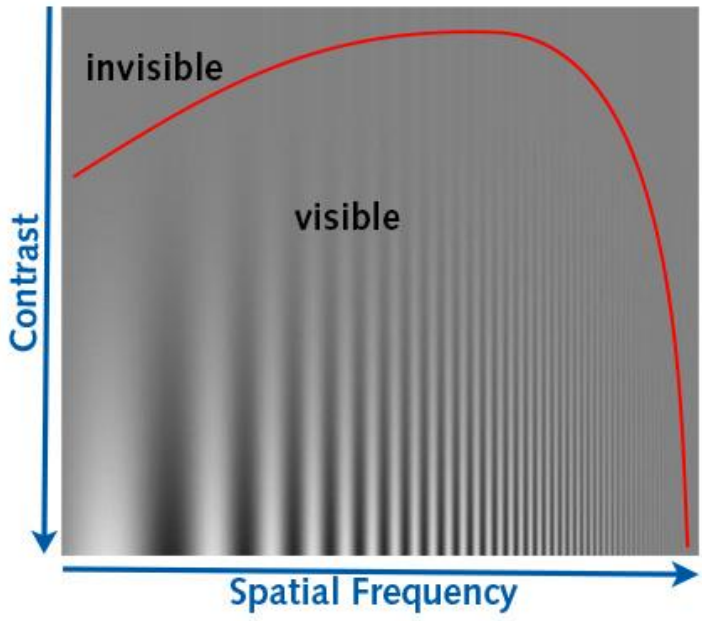


Figure 14: A contrast sensitivity function (red line) from a control with normal spatial vision, measured using the Cambridge Spatial Achromatic Contrast Sensitivity Function, Metropsis, the area under the curve is visible, whilst above the curve is not visible. (Source: Psychophysics UK: typical-contrast-sensitivity-function.jpeg from https://www.psychophysics.uk/spatial-contrast-sensitivity//).

2.2.6 Colour Vision

Colour vision is the ability to distinguish between various wavelengths of light, independent of the relative light intensity (Hilbert, 1992). As explained in the introductory chapter, the cones are sensitive to specific wavelengths of light, and these correspond to different axes of opponent colour space. Tests of colour vision measure the participants ability to identify different colours. A deficiency in colour vision means a person finds it difficult to distinguish between certain colours and can provide a measure of cone function.

Our perception of colour comprises hue, saturation, and brightness. The perception of hue is related to wavelength of light, a wavelength between 495 - 570 nm is perceived to have a hue of green, whereas wavelengths between 450 - 495 nm are perceived to have a hue of blue. Brightness depends on luminance and saturation depends on the intensity of the stimulus and these both influence the

perceived colour. For tests of colour vision, the screen luminance is kept constant to ensure the perceived hue is due to the wavelength of light used.

The Cambridge colour test (CCT) is an automated computerised test which presents Landolt-C stimuli with differing chromaticity from the background. The programme presents the stimuli with varying hues along the colour confusion lines of the protan, deutan and tritan axes. These presented hues measure the sensitivity of the L-, M- and S-cones. The participant distinguishes the orientation of the Landolt-C and the CCT determines their hue detection threshold using a descending staircase procedure. These results are plotted in a trivector colour space (figure 15), a deficiency along one of the colour axes would be presented as an elongation of that axes.

The CCT was developed to assess colour vision deficiency and has been modified for participants with vision loss; this version is called the low vision CCT (lvCCT) (Simunovic and Moore, 1998). The lvCCT uses larger disc shaped stimuli with a uniform hue rather than the Landolt-C shape. The discrimination threshold is determined by the detection of the disc that contains chromaticity compared to discs of a neutral hue. To indicate cone function, the lvCCT was used for the colour vision measures described in this thesis due to the STGD1 patients' low vision.

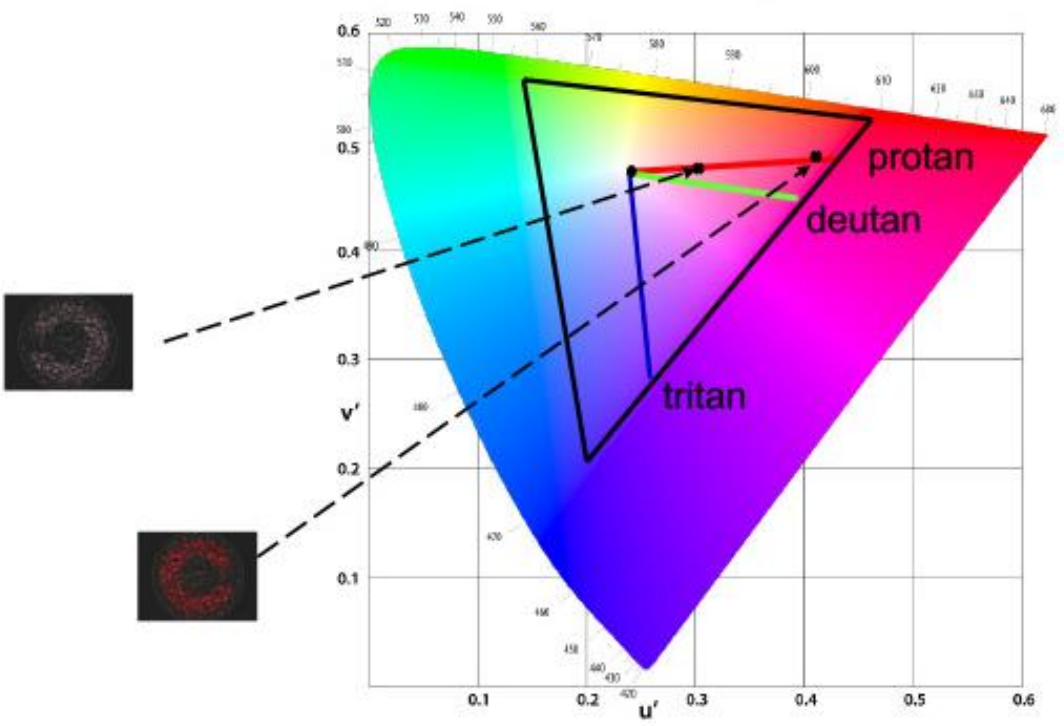


Figure 15: Trivector colour space plot from the Cambridge Colour Test for a control with normal colour vision. It determines the minimum hue needed to determine the orientation of the Landolt-C gap along the colour confusion lines of the protan, deutan and tritan axes (Source: Psychophysics UK: Figure-3-CCT-CIELUV-diagram.jpeg from https://www.psychophysics.uk/colour-discrimination/).

2.3 Methods to assess cortical structure, function, and chemistry

There are a multitude of techniques used to assess brain structure and function. Techniques that measure brain structure create detailed images of brain anatomy with high spatial resolutions that distinguish between different tissue types. The techniques that measure neuronal activity do this in two main ways, firstly, through the electrical level of the neuronal action potentials and, secondly, through the chemical level via the neurotransmitter messages between cells and the overall metabolic system of the brain network. This neuronal activity can be measured both directly and indirectly, with techniques such as blood oxygenation level dependent (BOLD) imaging using levels of blood oxygenation as an indirect measure for neuronal activity.

The techniques that assess structure and function vary in terms of the level of invasiveness, temporal, and spatial resolution and, therefore, have intrinsic advantages and limitations. The techniques used in animal models have higher spatial and temporal resolutions compared to techniques used in humans, due to the level of invasiveness ethically allowed (figure 16). In humans, techniques such as electroencephalogram (EEG) can infer neuronal activity by measuring the electrical activity on the surface of the scalp, this has a high temporal resolution but lower spatial resolution. In contrast, MRI can measure localised activation with a higher spatial resolution but with a lower temporal resolution. Transcranial magnetic stimulation (TMS) can be used to disrupt neuronal activation with the affects measured in behaviour. Figure 16 shows the trade-off between temporal and spatial resolution for these techniques. The study described in this thesis uses MRI as it is sufficient to measure our hypotheses.

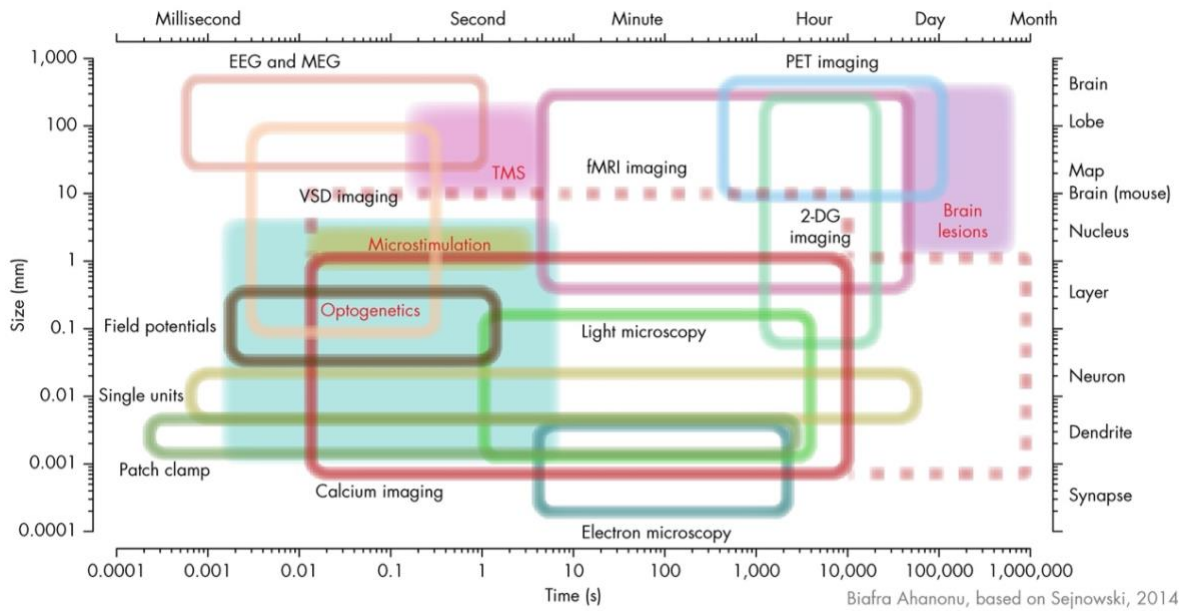


Figure 16: Spatiotemporal graph of neuroscience methods, showing the spatial and temporal resolution of different neuroimaging techniques. The techniques used for human neuroimaging are at the top of the graph as they are mainly non-invasive and due to this are measure over lower spatial resolutions. This is adapted by Biafra Ahanonu from (Sejnowski et al., 2014).

2.3.1 Magnetic Resonance Imaging

MRI was invented in 1977 when physicists developed the use of nuclear magnetic resonance (NMR) to create an in-vivo image of the human body (Altman, 1997). Clinically, MRI is used to image abnormalities in the body and this aids in the diagnosis of disease. In research it is used to aid in the understanding of the human body and also in the development of treatments for disorders. Since the development of MRI, neuroscientists have used it to investigate the human brain in a multitude of ways. It can be used to generate an image of the structure of the brain, to measure blood oxygenation levels in order to infer neuronal activation, to track white matter connections and to quantify brain metabolite concentrations. MRI scanners have a range of field strengths, with 1 Tesla (T) typical for clinical imaging, whilst 3 T and 7 T (+) being common for research imaging. Research into ultra-high field MRI is pushing boundaries with the current maximum for human imaging at 10.5 T. The higher the field strength means the increased sensitivity to detect signal, and therefore the higher the spatial resolution, pushing MRI to lower down the resolution scale in figure 16. The limits of MRI image detail are continually being pushed by physicists who are improving MR scan sequences and computer scientists who are developing analysis programmes to gain a better spatial resolution of the images such as by using modelling with histology (Morawski et al., 2018).

2.3.2 Structural MRI

Structural MRI creates high resolution images of the human brain enabling the definition of cortical structures and differentiation between tissue types (figure 17). As previously stated, the contrast between different tissue types can be varied by changing the parameters of the pulse sequence.

T1-weighted imaging

The study in this thesis used T1-weighted (T1w) imaging. As previously mentioned, this is generated by measuring the magnetisation gain in the longitudinal axis and shows different contrasts in different tissues. In T1w images the white matter (WM) is lightest, the grey matter (GM) is darker, and the cerebrospinal fluid (CSF) is the darkest contrast (figure 17). Protons within these tissue types, such as grey, white matter and CSF all have varying magnetism relaxation times (figure 17). On average T1w

images have short TE and TR times compared to T2w images and they take around 6 minutes to acquire.

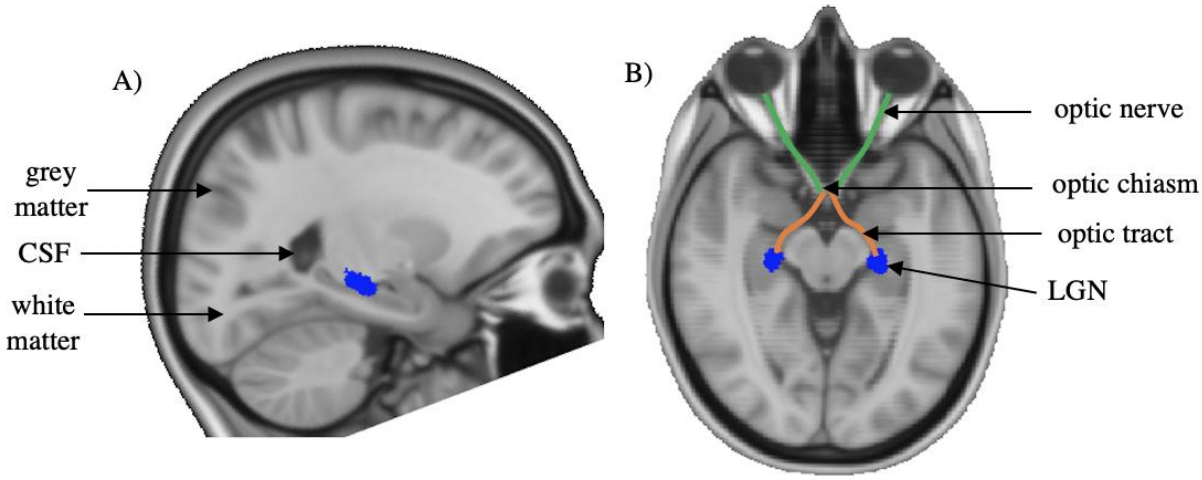


Figure 17: MNI standard T1w image of the human brain with 1mm^3 voxel size displayed in sagittal (A) and axial (B) views. The contrast changes from white matter (lightest) to grey matter, then cerebrospinal fluid (CSF) (darkest) (A). Structures of the visual system displayed are the optic nerve (green), where the fibres cross at the optic chiasm and then along the optic tract (orange) to the lateral geniculate nucleus (LGN) (blue) (B). The LGN is defined by the Juelich histological atlas (Amunts et al., 2005) (Eickhoff et al., 2005) (Eickhoff et al., 2006).

An advantage of structural MRI is the high spatial resolution which can be improved at increased magnetic field strength, at 3T the standard voxel size is 1mm^3. As these scans take around 6 minutes to acquire, a limitation of this method is the susceptibility to motion. Motion is difficult to correct for in post-processing as movement creates a blocky shift in the image, therefore if the participant moves then the scan is usually repeated.

2.3.3 Functional MRI and the BOLD signal

Functional MRI (fMRI) is a non-invasive technique which measures changes in regional blood flow as an indirect measure of neuronal activity. In 1992, fMRI was first used in humans to detect visual cortex activation whilst stimulating the visual field (Ogawa et al., 1992). Blood oxygenation level

dependent (BOLD) imaging is the most common method in fMRI. The brain has a high energy consumption, where it consumes ~20% of total energy despite equating for only < 2% of body weight (Raichle et al., 2001). GM consumes between three to four times more oxygen than the white matter (Pantano et al., 1984) and therefore the BOLD response is primarily a measurement of activity in the GM (Logothetis, 2002).

The premise of the BOLD response is that when neurons produce action potentials, they use oxygen, and this causes an increase in deoxyhaemoglobin (Hb) in that region. Hb is paramagnetic and creates local distortions in the magnetic field, which cause an initial decrease in the MR signal. This lasts between 2-4 seconds but is too short to be adequately imaged with fMRI (Logothetis, 2003). There is an increase in cerebral blood flow (CBF) to the activated region and this increases the amount of oxyhaemoglobin ($Hb0_2$) to exceed initial levels around 6 seconds (figure 18). This therefore decreases the ratio of Hb present leading to an increase in the MR signal which lasts between 6-12 seconds. The MR signal then decreases to return to baseline with an initial undershoot.

The predicted changes in regional blood flow between oxygenated and de-oxygenated blood are used to calculate the BOLD response, this is called the haemodynamic response function (HRF) (figure 18). Experimental paradigms use a stimulus with set onset presentation times that are convolved with the HRF. This then shows areas of the brain with the predicted response that were activated when the stimulus was present.

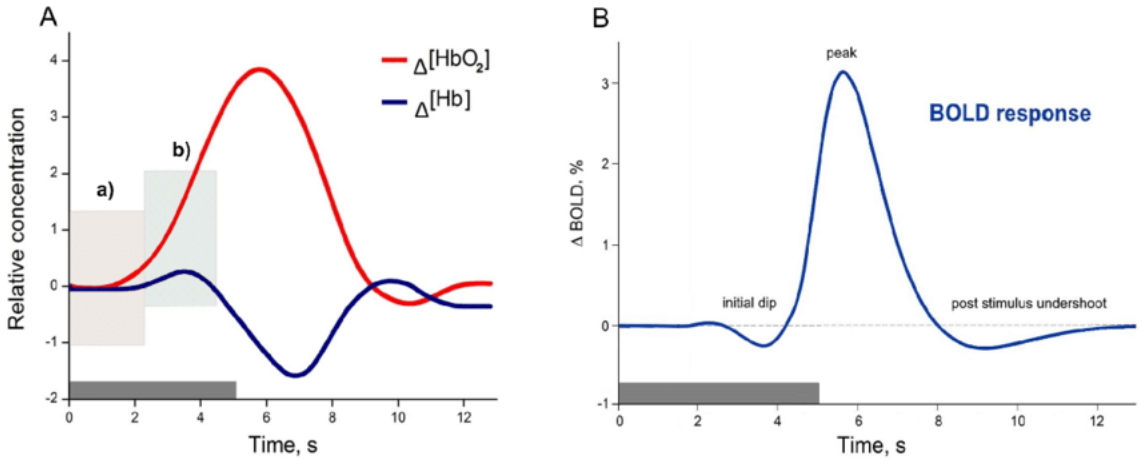


Figure 18: (A) An example of a canonical haemodynamic response, where the concentrations of haemoglobin ($Hb0_2$) and deoxyhaemoglobin (Hb) change in the area activated, a) shows the small increase in Hb and b) shows the larger increase in $Hb0_2$. (B) The haemodynamic response function showing the initial dip of BOLD signal at ~4 seconds, a peak at 6 seconds, then the return back to baseline at 12 seconds. Image from (Cinciute, 2019).

2.3.3.1 Methods to assess functional connectivity

Of the total energy consumption of the brain ~ 50% supports the functionality of synaptic transmission at baseline levels (Gusnard and Raichle, 2001; Logothetis et al., 2001). Therefore, investigating the functional connectivity at baseline should reflect the general connectivity strength across the cortex.

Rs-fMRI measures spontaneous low-frequency fluctuations in the BOLD signal and then compares the synchronicity of the BOLD signal across regions as a measure of their connectivity. Rs-fMRI has two main approaches, the model based and the model free approach. The work in this thesis uses analysis methods from both approaches and is presented in chapter 5. Model free analyses are used for more exploratory hypotheses, an example of this is independent component analysis (ICA). In group-ICA resting state networks (RSNs) are differentiated from within the group signal (an example of which is shown in figure 19). Then for the RSNs of interest the functional connectivity within that network is investigated dependent on the hypothesis. Model-based analyses can be used to investigate

a specific hypothesis about functional connectivity strength between specific ROIs and the rest of the cortex. This is calculated using the BOLD signal timeseries from within that ROI and then this is correlated with the BOLD signal from the rest of the cortex.

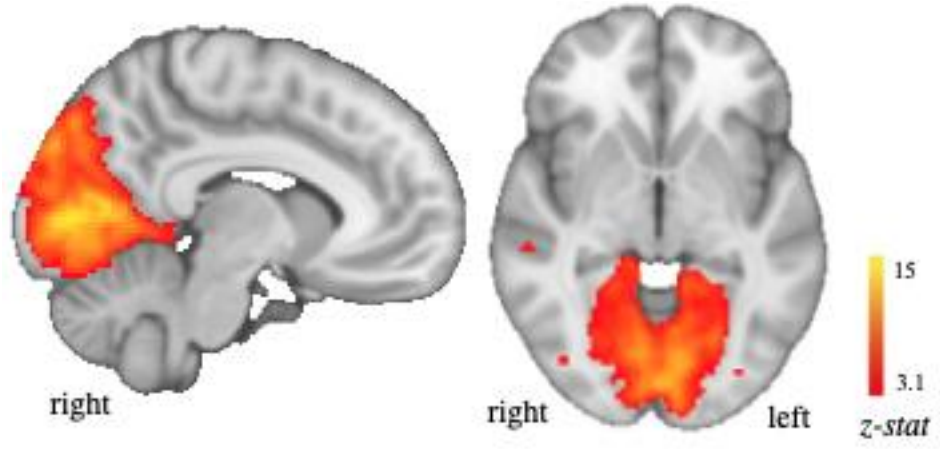


Figure 19: Resting state network z statistic image thresholded at 3.1 (red – yellow colour bar) within the visual cortex overlaid on the MNI152 standard brain.

2.3.5 Methods to assess neurochemistry

The chemical level of brain activity reflects the neurotransmitter messages between cells and the overall metabolic system of the brain network. The neurotransmitters are the messages between neurons that control whether an action potential is propagated through the system, or silenced.

2.3.5.1 Proton Magnetic Resonance Spectroscopy

Magnetic resonance spectroscopy (MRS) is a technique that can non-invasively measure neurometabolites *in vivo*. In structural imaging the hydrogen protons are detected from the large H^2O signal, whereas in proton magnetic resonance spectroscopy (^{1}H-MRS) the protons of interest are from the other metabolites present in the brain. Metabolites are chemicals involved in metabolism and have low concentrations at millimolar levels, the concentrations are around 1000x smaller in comparison to water. For this reason, water suppression is needed to accurately measure metabolites. As the metabolites have low concentrations, ^{1}H-MRS requires large voxel sizes (~8cm^3), with long acquisition times to gain an adequate signal to noise ratio (SNR). The spatial resolution of MRS is

lower than MRI and fMRI, however these techniques are constantly being developed to acquire data in smaller voxels sizes. The temporal resolution of MRS is debated, with the consensus in papers using acquisition times of minutes rather than seconds.

Nuclear Magnetic Resonance (NMR) Spectroscopy is a technique commonly used in analytical chemistry to identify molecules in a sample. The sample is placed in a magnetic field, and a radio frequency wave is applied to cause the protons to resonate at their specific frequencies. This process outputs a spectrum of the individual molecules in the sample. This has been developed to measure the human brain in vivo with ^{1}H-MRS which I will refer to as MRS for the duration of this thesis. Each type of metabolite has a unique Larmor frequency, and this is measured in MRS using chemical shift imaging. Therefore, when the B0 field is applied, this causes electrons in these molecules to shift away from the hydrogen proton (figure 20). The larger the shift means the smaller the chemical shielding and therefore the higher the protons resonate frequency. The signal is recorded by measuring free induction decay (FID) in the time domain (TD) and this then has a Fourier transform applied to be plotted in the frequency domain (FD) (figure 20).

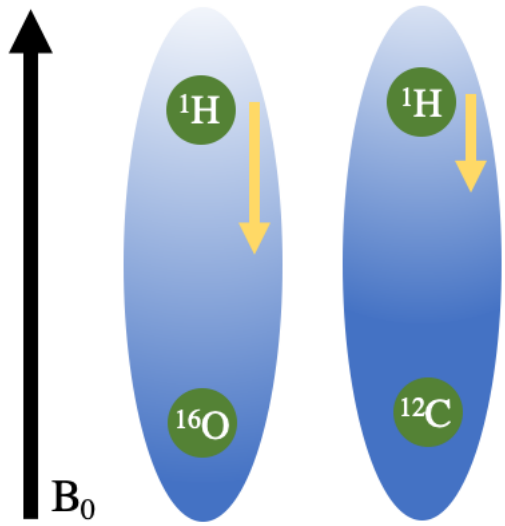


Figure 20: A schematic of the B_0 field (black up arrow) and two molecules containing hydrogen. Electrons move away from the hydrogen proton when the B_0 field is applied, this is called chemical

shift. The molecule with the ^{16}O has the largest chemical shift (yellow arrow) due to the larger pull on the electrons and therefore the hydrogen atom has less chemical shielding.

The chemical shift of the hydrogen atom is the frequency it undergoes resonance at. This is represented in parts per million (ppm), plotted against frequency. The ppm scale is a dimensionless unit calculated to normalise magnetic field strength, as the location in hertz (cycles/sec) varies as field strength changes (Tognarelli et al., 2015). The units 'per million' refer to the strength of the magnetic field being in the order of 10^6 Hz (Cecil, 2013). The molecular structure of metabolites contains hydrogen atoms bound into different chemical groups. If a metabolite contains multiple protons, then these are broken down into separate peaks across the spectrum, as each proton resonates at a different frequency depending on the amount of chemical shielding (figure 21). The output for MRS is a chemical shift spectrum for each voxel (figure 21) rather than in structural or functional MRI where an image of the brain is produced. The spectrum shows the intensity of the signal at each resonant frequency (figure 21). The x axis represents the position of the metabolite peaks depending on the amount of chemical shielding in ppm and the y axis is the signal intensity (proportional to the relative number of resonating protons) (Cecil, 2013).

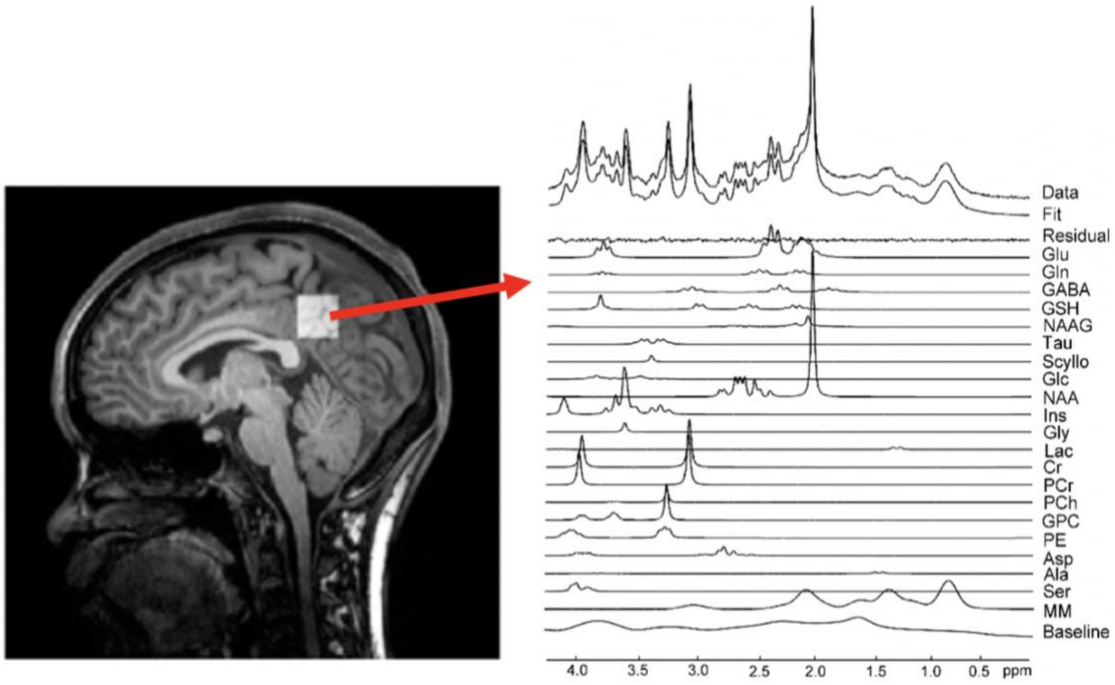


Figure 21: Example MRS spectrum of a voxel in the human brain showing the raw data, fit, residuals

and baseline. The individual predicted metabolite spectra are shown in between the residual and baseline. The x axis represents the amount of shielding on the proton in parts per million (ppm) and the y axis represents the signal intensity. The peaks show the resonance frequency of the protons in the hydrogen atoms, with some molecules having multiple hydrogen atoms and therefore multiple peaks. Figure from (Takado et al., 2019).

2.3.5.2 Magnetic Resonance Spectroscopy Imaging

The single voxel ^{1}H-MRS technique described measures metabolite concentrations in one large voxel in the human brain, whereas, Magnetic Resonance Spectroscopy Imaging (MRSI) can measure metabolite concentrations across a high resolution (5x5x10mm) cortical section in vivo (Steel et al., 2018). The advantage of MRSI over conventional single-voxel MRS is that multiple voxels can be acquired at the same time, permitting a comparison of neurochemical concentrations in different regions in the brain. Each MRSI voxel contains thousands of neurons and therefore it is not possible to measure the neurotransmitter level in each neuron individually in the human brain. The work presented in chapters 6 and 7 uses MRSI to measure across multiple points across the visual cortex. Figure 22 shows example metabolite ratio maps of tNAA, Glx and tCho standardised to total creatine. The concentrations of these metabolites vary between GM and WM, such as Glx (glutamate and glutamine) where the concentration is lower in the WM and higher in the GM.

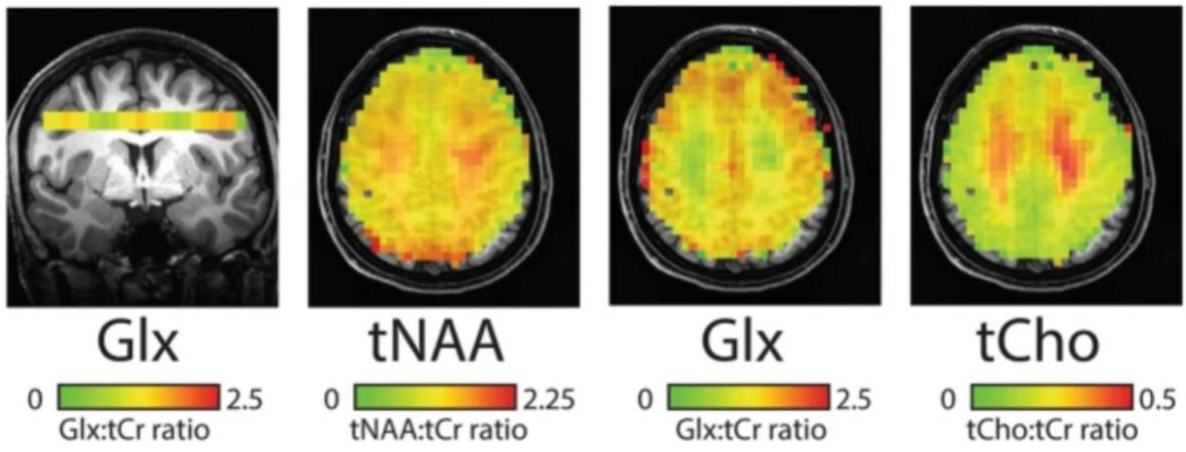


Figure 22: MRSI image showing a 5 × 5 × 10mm voxel placement with metabolite ratio maps of tNAA, Glx and tCho standardised to total creatine in the axial view. The coronal view shows the slab position and thickness of 10mm. The colour bars show where the concentration of the metabolites are low (green) to high (red). These MRSI maps are overlaid on a T1w image. Image from (Steel et al., 2018).

2.4 Procedure

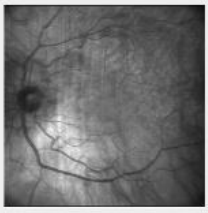
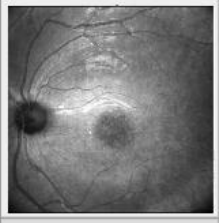
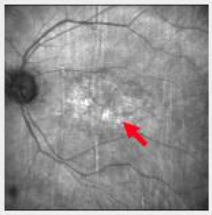
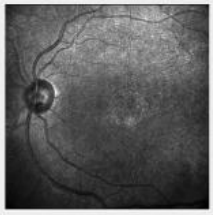
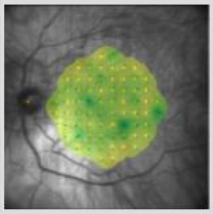
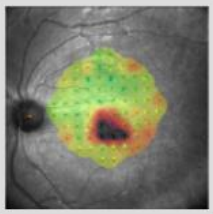
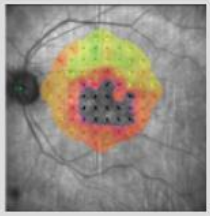
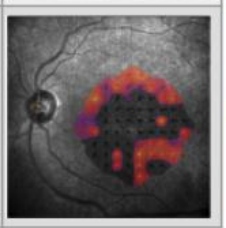
2.4.1. Assessment of Stargardt Macular Dystrophy

As stated in the chapter 1, Stargardt Disease is associated with pathogenic variants in the *ABCA4* gene (Al-Khuzaei et al., 2021a). These phenotypes have variable levels of severity, with different ages of onset and rates of progression (Starace et al., 2021) and the term *ABCA4* retinopathy is often used to describe the different phenotypes associated with variants in the gene (Al-Khuzaei et al., 2021b). This leads to individual differences in the degree to which the retinal structure is affected (Fishman et al., 1999; McBain et al., 2012; Westeneng-van Haaften et al., 2012). In "typical" STGD1 there is central retinal atrophy with foveal photoreceptor damage accompanied by flecks (Gomes et al., 2009). The patients screened for inclusion had Stargardt Macular Dystrophy with an autosomal recessive inheritance pattern and ABCA4 pathogenic variants.

Only patients with phenotypes "typical" for macular STGD1 were included in this thesis to ensure that the vision loss was confined to the central visual field. Retinal sensitivity (dB) measured by microperimetry was used to indicate functional vision loss. Patients were included if they had localised bilateral functional loss inside the central 20° of their retinae (chapter 3). As STGD1 causes a progressive degeneration, there are a range of disease severities due to differing rates of degeneration occurring at the retina, therefore the group of participants included in this thesis is non-homogeneous. Table 1 provides an account of participant age, gender identity and disease severity. Disease severity was quantified by the area of the scotoma (°) (outlined in chapter 3) and then further categorised into three ordinal groups: mild, moderate, and severe (Table 2).

Participant number	Gender identity	Age	Disease length	Disease severity
002	F	25	9	mild
003	M	21	15	moderate
009	M	24	12	severe
010	F	41	24	mild
013	F	47	16	severe
014	M	56	24	severe
023	F	62	20	moderate
028	M	34	21	severe
030	F	24	8	severe
037	M	61	n/a	moderate
048	F	54	24	severe
055	M	23	9	severe
057	M	19	6	moderate
059	F	17	9	moderate
060	M	49	6	mild
062	F	31	21	moderate
064	F	18	7	severe

Table 1: Details of the seventeen patients with STGD1 who participated in this study, showing age, gender identity, disease length and disease severity categorised by retinal sensitivity (dB) (mild, moderate, and severe).

Participant Number	001 Control	002 STGD1	023 STGD1	055 STGD1
Disease Severity	N/A	Mild	Moderate	Severe
Fundus Autofluorescence				
Retinal Sensitivity				

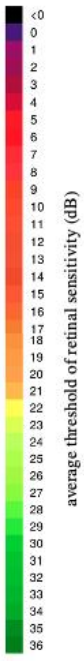


Table 2: Examples of fundus autofluorescence images of the left retina of patients with STGD1 (002, 023, 055) in the three categorised disease severities (mild, moderate, and severe) and a healthy retina

(001) for comparison. The patient's scotomas are the darker localised areas in the macula, some contain the white flecks characteristic of STGD1 disease (shown by the red arrow). The corresponding retinal sensitivities (dB) show light stimulus seen (green) to unseen (black) with the corresponding retinal sensitivity colour bar on the right.

2.4.2 Participants

Seventeen participants with STGD1 (9 females, mean age 35.6 ± 16.2 SD) and seventeen comparison participants (7 females, mean age 38.7 ± 14.9 SD), with healthy vision participated in the study presented in this thesis. The study was conducted under ethical approval from the NHS London – Bromley Research Ethics Committee (IRAS Ref: 226399) and all participants provided informed written consent. Participants with STGD1 were recruited from the low vision clinics where they are under the care of Professor Susan Downes at the Oxford Eye Hospital, Oxford University Hospitals NHS Foundation Trust, John Radcliffe Hospital. The age-matched controls were recruited mainly from friends and family of the patient cohort and through word of mouth at the University of Oxford. Those selected met the safety requirements for 3T MRI by not having ferromagnetic objects in their body and not having history of claustrophobia or epilepsy. Each participant was reimbursed for their travel expenses, overnight stay in accommodation if needed and paid £35 for their time.

2.4.3 Data collection

Participants attended a single day of testing with the outline shown in figure 23. Participants arrived in the morning of the day of testing. They gave written informed consent and then underwent MR safety screening separately by the investigator and then the radiographer. The study visit consisted of an MRI scan session (approximately 90 minutes) in the morning at FMRIB (Oxford Centre for Functional Magnetic Resonance Imaging of the Brain), followed by vision measurements (approximately 3 hours) at the Oxford Eye Hospital, Oxford University Hospitals NHS Foundation Trust, John Radcliffe Hospital (chapter 3). Figure 23 shows the order of the day, this visit ended with an opportunity for participants to ask any final questions and they were given contact details if they have any further enquiries.

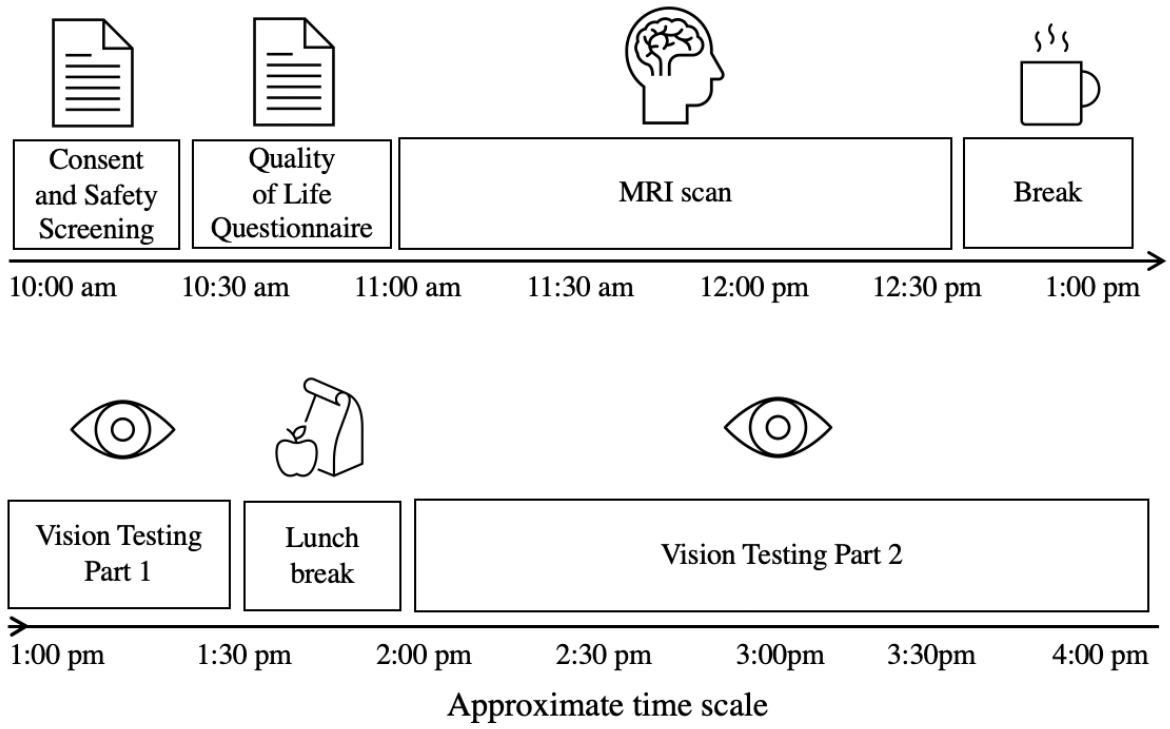


Figure 23: Outline of the testing day, starting with consent and MR safety screening, followed by the MRI scan and then the vision tests.

2.4.4 MRI Acquisition

Once written informed consent was provided and they were cleared for MRI safety, the participants were given a description of what to expect in the scan. They were advised that they could press the buzzer at any point if they felt uncomfortable and could leave the scan at any time. They were shown an example of the stimuli shown in the prf-fMRI scan and that they should respond with a button press for the fixation task. The importance of fixation and minimal movement was emphasised. The participants changed into pocketless scrubs to ensure metallic objects were not brought into the scan room. They then entered the scan control room and if applicable were fitted with MR safe glasses that correct for refractive error. The participants were fitted with earplugs by the radiographer to ensure hearing was protected, they then lay down with their head padded into the head coil in order to reduce participant movement. They were given the buzzer and the button box in separate hands, and then covered with a blanket to prevent them from getting cold.

The scans were carried out on the 3T Prisma MRI scanner (Siemens Healthcare, Erlangen, Germany), using a 64-channel head coil. The scan session is outlined in figure 24 and took around 75 minutes. The scan slot was 90 minutes to allow for radiographer safety screening, set up and ear plug fitting. The order of the MRI scans is outlined in figure 24, these started with a T1-w structural image and followed by the diffusion-weighted-imaging (DWI) sequence. The MRSI slab was placed whilst the DWI was acquired to utilise scan time and the T1-w image was used to place the MRSI slab in the preferred position. Four pRF-fMRI runs were acquired, followed by a field map scan. The acquisition ended with 10 minutes of resting state fMRI (rs-fMRI), note the DWI and pRF-fMRI scans were not included in this thesis.

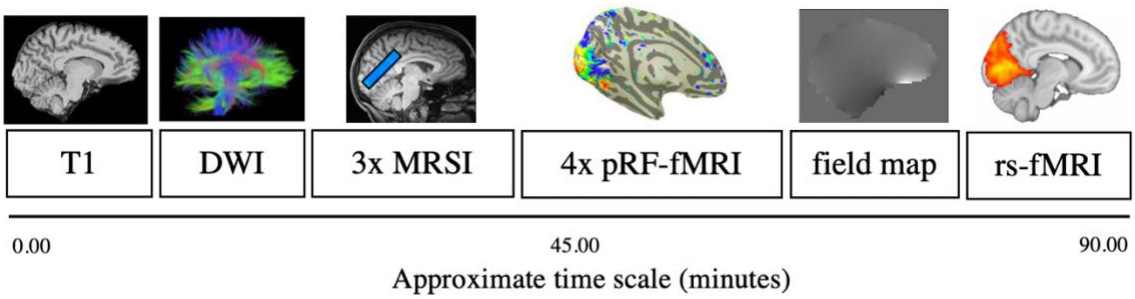


Figure 24: Schematic outlining the scan protocol with numbers of scan repeats which took around 90 minutes. Note that the diffusion-weighted-imaging *(DWI) and population receptive field mapping (pRF-fMRI) scans were not included in this thesis.*

2.4.5 Visual Testing Acquisition

After the MRI scan the participants were given a short break before the vision testing. This was important to give their eyes a rest due to the large amount of fixation required in the MRI scan. The participants were taken to the Eye Hospital and the OCT imagining was completed first (around 1pm). This then was followed by a 30-minute lunch break, the participants then returned to the Eye Hospital and had microperimetry, visual acuity, colour vision and contrast sensitivity measured, the order of

the day is shown in figure 25. These were completed in randomised orders due to machine availabilities. Pupil dilation was not required for the vision testing protocols.

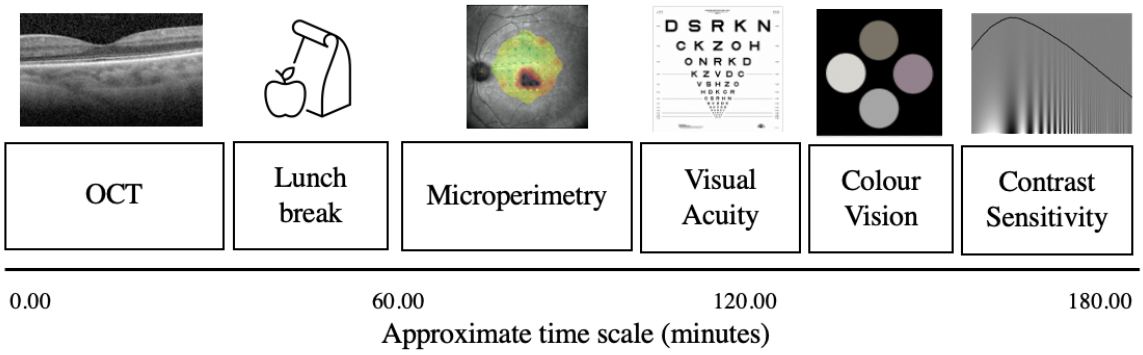


Figure 25: Schematic outlining the order of vision testing which took around 3 hours. Optical coherence tomography (OCT) was carried out first then the participants had a lunch break, followed by the remainder of the vision testing.

3 Measures of Visual Function

Functional changes in visual ability in Stargardt patients compared to controls

3.1 Abstract

Stargardt macular dystrophy (STGD1) causes progressive degeneration of the photoreceptors in the retina, and predominantly affects the central macula. This degeneration causes a loss of vision in the central field and particularly reduces colour vision discrimination and high acuity vision. As STGD1 is progressive, there are a range of disease severities and rates of degeneration occurring at the level of the retina. This chapter demonstrates the extent of functional vision loss in the STGD1 group and how this loss was used to define disease severity.

This chapter presents measurements of visual function in the STGD1 patient cohort and compares them to controls with a healthy visual system. I found that STGD1 patients had large reductions in high acuity vision, measured by contrast sensitivity and visual acuity. Given the loss of cones in STGD1, reductions in colour vision across all three opponent colour axes were also found. Retinal sensitivity was measured with microperimetry and STGD1 showed a range of functional loss restricted to the macula. Retinal sensitivity was used to infer disease severity, and we found that the magnitude of loss at the retina correlated with reduced visual acuity, contrast sensitivity and colour vision discrimination. These findings demonstrate that a loss of cones in the retina causes a deficit in high acuity and colour vision.

3.2 Introduction

3.2.1 Vision loss caused by Stargardt Macular Dystrophy

STGD1 is a genetic disorder caused by a defective ABCA4 gene and this leads to progressive degeneration of the retinal pigment epithelium (Molday, 2007) causing secondary loss of photoreceptors (Weng et al., 1999). In STGD1 the loss of photoreceptors is predominantly constrained to the macula causing progressive loss to central vision. Central vision is processed by the cone photoreceptors which are responsible for high acuity and colour vision, whereas the rods process peripheral and night vision, which is less affected in STGD1.

Structural degeneration of the retina due to STGD1, reduces the sensitivity of the retina to light within those regions. An increase in atrophic lesions in the photoreceptor layer of the macula measured by biomicroscopy were found to significantly correlate with lower retinal sensitivities measured by microperimetry (Testa et al., 2012). This shows how a loss of photoreceptors in the macula reduces the ability of the retina to detect light and this therefore would cause a loss of vision to the central visual field. The rates of degeneration have been compared longitudinally in STGD1. In STGD1 the lesion area in the RPE has been found to increase at a rate of $0.282mm^2$ per year, which causes a loss of retinal function of 1.19dB per year (Testa et al (2015). This shows how loss of the RPE cells, which are the first retinal cells to degenerate in STGD1, causes a reduction in retinal sensitivity.

High acuity vision is processed by the cones in the retina; therefore, degeneration of the central retina would show a reduction in visual acuity. Best-corrected visual acuity (BCVA) significantly correlates with lesion magnitude at the fovea, where a larger scotoma caused a decrease in BCVA (Kong et al., 2017). This shows that greater retinal degeneration causes a reduction in visual acuity. A reduction in the sensitivity of the central retina to light would be expected to affect high acuity vision. Visual acuity measured by the Snellen chart was found to correlate with retinal sensitivity measure by microperimetry (Testa et al., 2012). They found that a greater reduction in retinal sensitivity significantly correlated with a reduction in the ability to discriminate letters on the Snellen chart

(Testa et al., 2012). This shows that a loss of function at the central retina reduces the ability to discriminate objects in fine detail.

The contrast sensitivity function provides a measure of how well a person can distinguish both fine detail and lower acuity vision. Due to central vision loss in STGD1, affecting high acuity vision, a larger amount of contrast is needed to resolve gratings at higher spatial frequencies compared to lower spatial frequencies (Alahmadi et al., 2018). This shows that damage at the central retina causes a larger deficit in high, compared to low acuity vision.

A loss of cones in the central retina reduces the ability to discriminate colour. The central ~0.34° of the foveae contains only M/L-cones and is S-cone free. The central fovea is the first area of the retina to degenerate in STGD1 and therefore M/L-cones are affected first. This has been shown by a larger deficit in red/green discrimination compared to blue/yellow discrimination in STGD1 patients (Vandenbroucke et al., 2015). As the central cones process M-/L- wavelengths, STGD1 patients show a higher deficit in the colour axes processed by L-cones (red) and M-cones (green) compared to S-cones (blue), due to the loss being constrained there.

Measures of visual function can provide a valuable insight into how degeneration at the retina affects visual perception. The research presented in this thesis uses measures of retinal sensitivity, contrast sensitivity, visual acuity, and colour vision to measure the extent of STGD1 patient's functional vision loss. The previous chapter (Methods and Procedure, Chapter 2) introduced the four tests of visual function presented here, and this chapter presents the methods and results.

3.2.2 Rationale

Investigating visual function after photoreceptor damage

A localised loss of photoreceptors in the retina creates a focal scotoma in the visual field. The loss of cones would cause a reduction in visual function. In this chapter, measures of visual function are used to investigate if there are differences between STGD1 and controls in retinal sensitivity, visual acuity,

contrast sensitivity and colour vision. Retinal sensitivity was used to infer disease severity, and these were correlated with the other visual function measures.

Hypothesis 1: Retinal sensitivity will be lower in STGD1 compared to controls, and this will be localised within the central retina.

Hypothesis 2: STGD1 will have lower contrast sensitivity (therefore higher contrast thresholds) than controls, particularly at higher spatial frequencies reflecting the deficits in fine detailed vision.

Hypothesis 3: Visual acuity will be reduced in STGD1 compared to controls, reflecting the deficits in fine detailed vision.

Hypothesis 4: STGD1 will show a deficit in colour vision, and this deficit will be larger along the red-green (protan/deutan) axes reflecting the central loss that affects M-/L- cones more than S-cones.

Hypothesis 5: Contrast sensitivity, visual acuity and colour vision will correlate with disease severity as measured by retinal sensitivity.

3.4 Methods

3.4.1 Participants

The research presented in this chapter includes 17 participants with STGD1 (9 females, 8 males, mean age 35.6 ± 16.2 SD) and 17 comparison controls with healthy eyes and normal vision (7 females, 10 males, mean age 38.7 ± 14.9 SD). All the participants completed the tests of visual function.

3.4.2 Retinal Sensitivity

Acquisition:

Microperimetry was measured using the Macular Integrity Assessment (MAIA) microperimeter (Centervue, Padova, Italy) with a protocol developed using testing results from low vision patients in

the Oxford Eye Hospital (John Radcliffe Hospital). The MAIA measures retinal sensitivity with real time fixation loss correction, without requiring pupil dilation. It uses a confocal scanning laser ophthalmoscope (SLO) to create fundus images of the retina in order to position the area of acquisition. The participants dark adapted for five minutes under mesopic conditions (room illuminance below 2 lux) prior to testing. Their chin and forehead were positioned against the rest, and they were told to fixate on the central red ring (2° diameter) within the MAIA's internal screen. If this was not visible due to vision loss, then a larger white cross was used at the patients preferred retinal location (PRL). If this was still invisible, then the patient was verbally guided by the examiner, the guided location was based on the position of the fundal image. Therefore, this ensured the centre of the macula was positioned over the red ring throughout the test.

A radial 20° grid with 2° spacing and 68 points specified the retinal position the light was directed on (Figure 26). Lights of varying luminance (1 – 36 dB) were flashed onto the retina with a 4 - 2 staircase procedure to obtain threshold estimates of retinal sensitivity at each point. The participants pressed a button if they saw a flash of light and eye tracking measured their fixation (turquoise), if the fixation loss was ≤ 15% then the test was repeated. If the participant had not completed microperimetry in the past 12 months, then a trial test was first conducted so the participant could get used to the testing procedure. Testing was conducted monocularly (right then left) without corrective lenses. To map the scotoma boundary more accurately, a second grid with 1° spacing was placed over the scotoma (figure 26C).

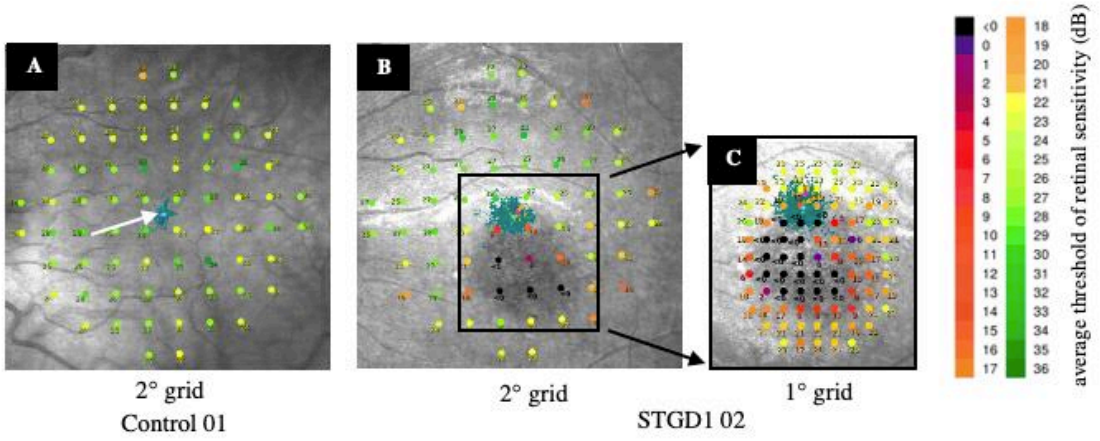


Figure 26: The microperimetry 20° grid overlaid on the fundus image of the left retina for control 01 (A) and STGD1 02 (B), with a second 1° spaced grid overlaid on the scotoma (C). This shows the functional sensitivity of the retina with points seen (green) through to unseen (black), a black cluster of points in STGD1 shows the functional loss from the scotoma. Fixation (white arrow) is measured throughout the test and shown in turquoise.

Analysis:

Binocular retinal sensitivities were combined using the microperimetry 2D analysis tool (Josan et al., 2021) in the programme R (v3.6.3). For controls with healthy vision, the monocular retinal sensitivity plots (figure 27A/B) were centred over the foveal fixation point (white arrow figure 27A/B) and combined to create binocular plots (figure 27C). Due to the scotoma within the STGD1 patients' retinae, their fixation points are at the PRL rather than their anatomical fovea (figure 28A/B/C/D). The 2° grids were placed over the anatomical fovea at data acquisition; therefore, the positions of these grids were used to adjust the monocular retinal sensitivity plots by using the location of the anatomical fovea. These recentred monocular plots were overlaid to combine the 1° and 2° grids and then combined to make binocular retinal sensitivity plots (Figure 28E). Interpolation was used to model the values between the individual points to generate heat maps (figure 27D and 28F). The thin plate splines interpolation technique was performed using the *fields* package (version 10.3) and the maps were displayed using the *ggplot2* package in R (version 3.31) (Josan et al., 2021).

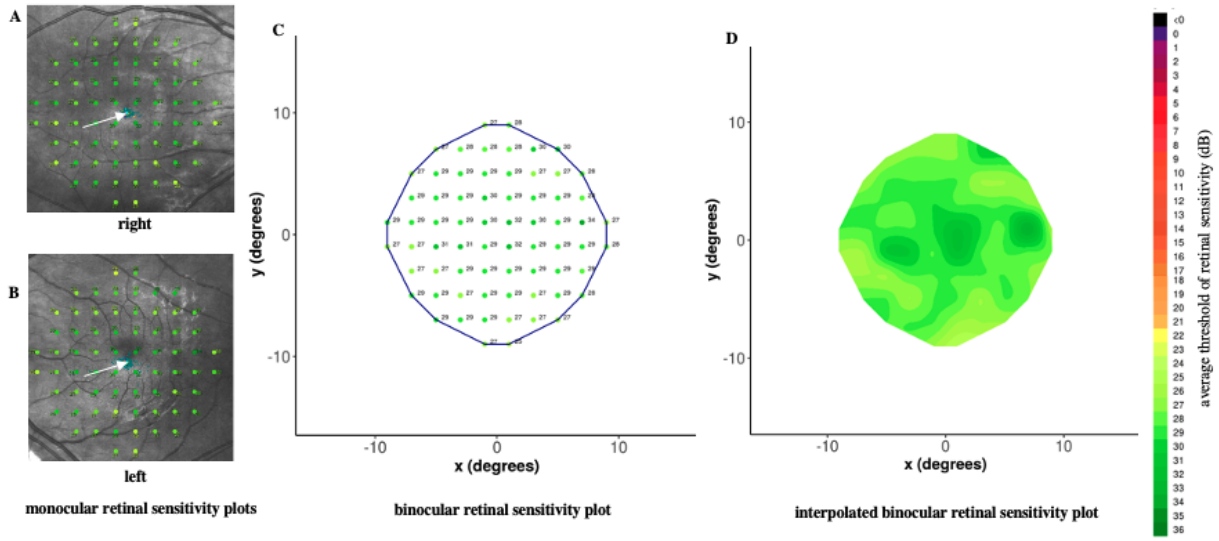


Figure 27: Monocular retinal sensitivity grids (A/B) for a control with healthy vision overlaid on the fundus image. These were combined using the fixation point (white arrows) to generate binocular plots (C), that are then interpolated to create heat maps (D) This shows the functional sensitivity of the retina with points seen (green) through to unseen (black).

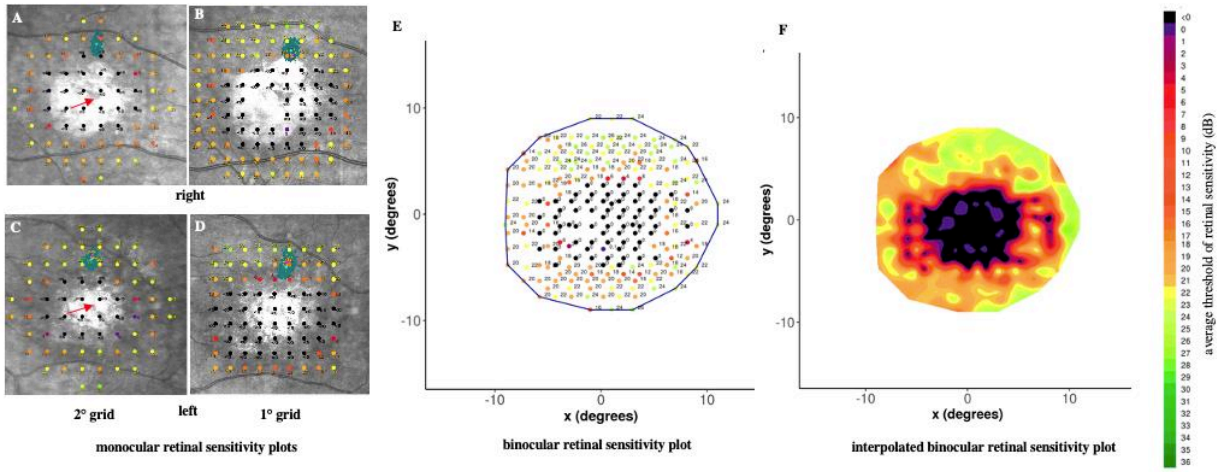


Figure 28: Monocular retinal sensitivity 2° (A/C) and 1° (B/D) grids from a STGD1 retina, overlaid on the fundus image. These were combined using the anatomical fovea (red arrows) to generate binocular plots (C), that are then interpolated to create heat maps (D) This shows the functional sensitivity of the retina with points seen (green) through to unseen (black).

Statistical analysis:

The binocular retinal sensitivity plots were split into eccentric retinal locations (0 - 1°, 1 - 3°, 3 - 5°, 5 – 7° and 7 – 9°) and the mean sensitivity was calculated per location (°). Two-way Analysis of Variance (ANOVA) was performed with main effects of group (STGD1 vs control) and retinal location (°) to determine differences in retinal sensitivity (dB). Tukey post-hoc analysis was used to investigate whether there was a statistically significant difference in retinal sensitivity (dB) between groups within the individual retinal locations (°). All statistical analyses in this chapter were performed using GraphPad Prism (version 9.0).

3.4.3 Contrast Sensitivity

Acquisition:

Contrast Sensitivity was assessed using the computerised Cambridge Spatial Achromatic Contrast Sensitivity Function test (Cambridge Research Systems Ltd (2012)). This displays gratings at varying contrasts to detect the minimum level they are visible to the observer, and this provides a measure of the individuals contrast sensitivity function. This test was conducted in a darkened room, with the participant seated 1.5m from the screen. The participant was corrected for optimal refractive error if needed and the test was conducted binocularly. The screen resolution was 1920 × 1080 (32 bits 60 Hz), with a 26.18 × 14.90° FOV. Contrast sensitivity was measured across five spatial frequencies (1°, 2°, 4°, 8°, 10°) of sinusoidal gratings. For each spatial frequency the test determined the lowest contrast needed to discriminate the grating from a grey background. Each trial randomly presented the gratings in a vertical or a horizontal orientation and the participant responded with a keyboard press to indicate the orientation of the gratings (figure 29).

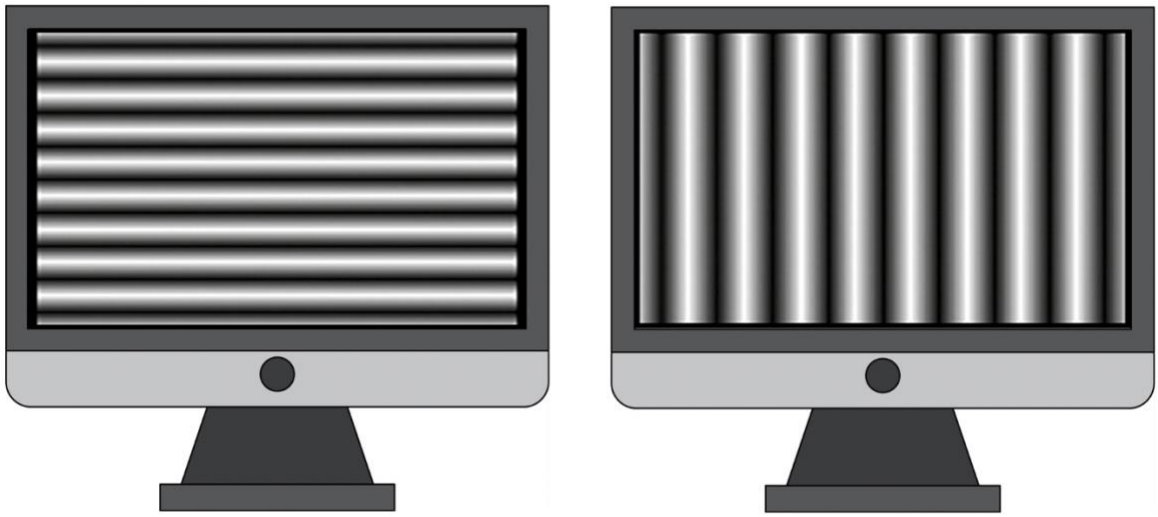


Figure 29: Grating stimuli shown on the monitor screen for the CSF test. The left screen shows horizontal gratings, and the right screen shows vertical gratings which were displayed randomly at different contrasts and spatial frequencies.

Statistical analysis:

The contrast sensitivity function was calculated as 1/contrast-threshold at each spatial frequency and logarithmically transformed (base 10). An ANOVA was performed with main effects of group (STGD1 vs control) and spatial frequency (cpd) to determine differences in the contrast sensitivity. Fisher's LSD post-hoc analysis was used to investigate whether there was a statistically significant difference in contrast sensitivity between groups within individual spatial frequencies (cpd). Due to the range of disease severities in the STGD1 patient cohort, a larger amount of vision loss was expected to correlate with a decrease in CSF. Therefore, Pearson's R was used to investigate whether there were significant correlations between the extent of vision loss and the amount of contrast needed to detect the spatial frequency of a grating.

3.4.4 Visual Acuity

Acquisition:

The Electronic Visual Acuity (EVA) Tester by EMMES Corporation was used to measure visual acuity (VA). The EVA was used as it as it provides a more accurate measure of visual acuity in

participants with visual field loss compared to standard charts (Jolly et al., 2020). The single line presentation was used as this has been found to be favourable over single letter presentation in patients with vision loss (Jolly et al., 2020).

Participants wore optimal refractive correction and sat three meters from the EVA screen, with their line of sight in the middle of the screen and in a darkened room. A string of five letters in the centre of a computer screen were presented and the participant read these out loud from left to right (Figure 30). The letters were first presented at size 20/200 and the size of these letters decreased if the participant gave a successful verbal response to at least one letter on the line above. This size decreased until size 5/200. If the participants were unable to give a successful response to one letter at 20/200 then the size increased. A mid-range size (20/200) was chosen to being with as most participants could successfully identify sizes 20/200 and larger. Therefore, only sizes 20/200 and above were used to detect the visual acuity threshold for those with who were unable to identify the small letter sizes (< 20/200). The eyes were measured binocularly, then monocularly (right then left) with an occluder over the fellow eye. This process was continued until the participant had responded to all the letters presented, with a maximum of 100 letters shown.



Figure 30: The EVA screen containing the single line array of five letters. The participant discriminated the letters from left to right, and this was used to define individual visual acuity.

Statistical analysis:

The number of letters detected for binocular, right and left eyes were compared to the total number of letters presented (100) and converted to a percentage (%). To determine differences in VA, an independent samples t-test was performed to investigate the effects of group (STGD1 vs control) on total letters read (%). Due to the range of disease severities in the STGD1 patient cohort, a larger amount of vision loss was expected to correlate with a decrease in VA. Therefore, Pearson's R was used to investigate whether there were significant correlations between the extent of vision loss and VA.

3.4.5 Colour Vision

Acquisition:

Colour vision was assessed using the computerised low vision Cambridge Colour Test (lvCCT). The lvCCT measures discrimination thresholds of chromatic sensitivity along protan, deutan and tritan axes (Simunovic et al., 1998). The low vision version was used to ensure the differences were due to colour vision deficit rather than errors in visual search (Simunovic et al., 1998). This test was conducted in a darkened room, performed binocularly with best corrected refractive error. The participant sat 1.5m from the screen with a FOV of 26.18°x14.90°. The white point is a set of chromaticity coordinates used to define the colour "white". The white point was set at the standard illumination of D65 (6500 kelvin) with the conditions on the Azimuth colour system set with values of 0.0667, 4.8382 and 5.9852 to represent L, M & S-cone responses. Four discs with a radius of 2° were displayed at +/-4.3° from the centre of the screen to the edge of the disc in horizontal and vertical directions on a dark screen. Three discs contain varying shades of grey and one disc is saturated with colour, and all varied in luminance (figure 31). The participant responded with a

keyboard press. The order of the testing was randomised, with three trials per block and a staircase procedure was used to determine saturation threshold discrimination.

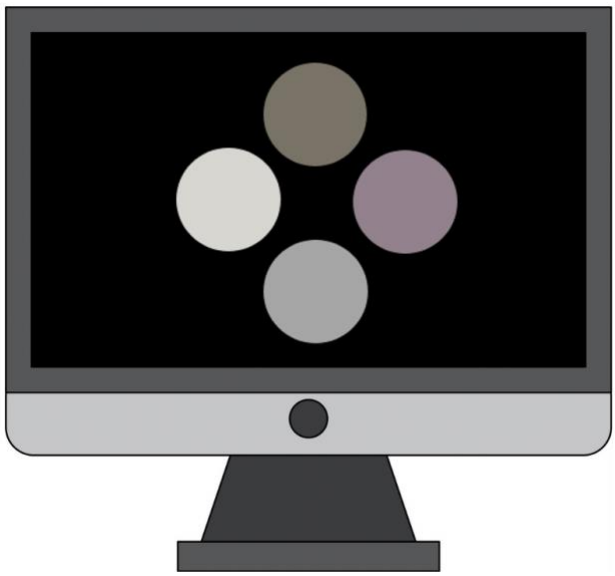


Figure 31: The lvCCT screen containing three discs varying in shades of grey and one disc saturated with colour (middle right). The participant discriminated the disc that contained colour, and this was used to define individual thresholds of colour discrimination.

Analysis:

The lvCCT provides a saturation threshold for the protan, deutan and tritan axes where a higher threshold relates to a greater deficit in a particular colour perception, and therefore, dysfunction in the corresponding cone class. The magnitudes from the lvCTT were converted by subtracting 100 for the statistical analyses, so lower discrimination thresholds represented a greater deficit in colour vision. An ANOVA was performed with main effects of group (STGD1 vs control) and colour axes to determine differences in colour vision discrimination thresholds. Fisher's LSD post-hoc analysis was used to investigate whether there was a statistically significant difference in the magnitude of colour vision deficit between groups within the colour axes. Due to the range of disease severities in the STGD1 patient cohort, a larger amount of vision loss was expected to correlate with a decrease in colour discrimination thresholds, particularly in the deutan and protan axes. Therefore, Pearson's R

was used to investigate whether there were significant correlations between the extent of vision loss and colour vision discrimination.

To visualise the deficit in colour vision the results were plotted as 3D vectors of colour discrimination in colour space. The length of the vector corresponds to the magnitude of colour deficit and the angle of the vector corresponds to the colour axes with the largest deficit. These were generated in python which used the angle of deviation and magnitude of vectors from controls with a healthy visual system and normal colour vision to generate a baseline vector. The angle of deviation and magnitude from the colour discrimination thresholds measured by the lvCCT were then plotted for each participant compared to the average vector of colour discrimination.

3.4.6 Outlier detection

For all analyses described in this section, outlier detection was calculated using the robust regression and outlier removal (ROUT) method in GraphPad Prism (version 9.0) (Benjamini and Hochberg, 1995) (Benjamini and Yekutieli, 2001). This method is based on the false discovery rate (FDR) and considers both multiple comparisons and the distribution of p-values within the data (Motulsky and Brown, 2006). The FDR is chosen by the Q percentage which decides the distance from the predicted model that a point should be considered an outlier. Q = 1% was chosen for the results presented in this section, therefore > 1% of the statistically significant findings were false positives. Outliers are shown in the graphs shaded in orange but were removed from the subsequent statistical analyses.

3.5 Results

3.5.1 Retinal sensitivity decreases in STGD1

As there is localised degeneration of the retina in STGD1, this reduces light sensitivity at specific regions of the retina. Due to photoreceptor loss in the central retina in STGD1, I predicted that this area would have a reduced response to light and therefore lower retinal sensitivities than controls. Figure 32 shows binocular retinal sensitivity maps from example controls (A, B, C) and STGD1 patients (D, E, F). Those participants with lower retinal sensitivities particularly in the central retina,

were classified as having lower visual function and therefore a higher disease severity. The patients were categorised into disease severities (mild, moderate, and severe) based on the mean retinal sensitivity from the binocular grids (Table 3). Patients were categorised as mild if their average retinal sensitivities were > 20 dB (n = 3), moderate if they were between 10 – 20 dB (n = 6) and severe if they were < 10 dB (n = 8).

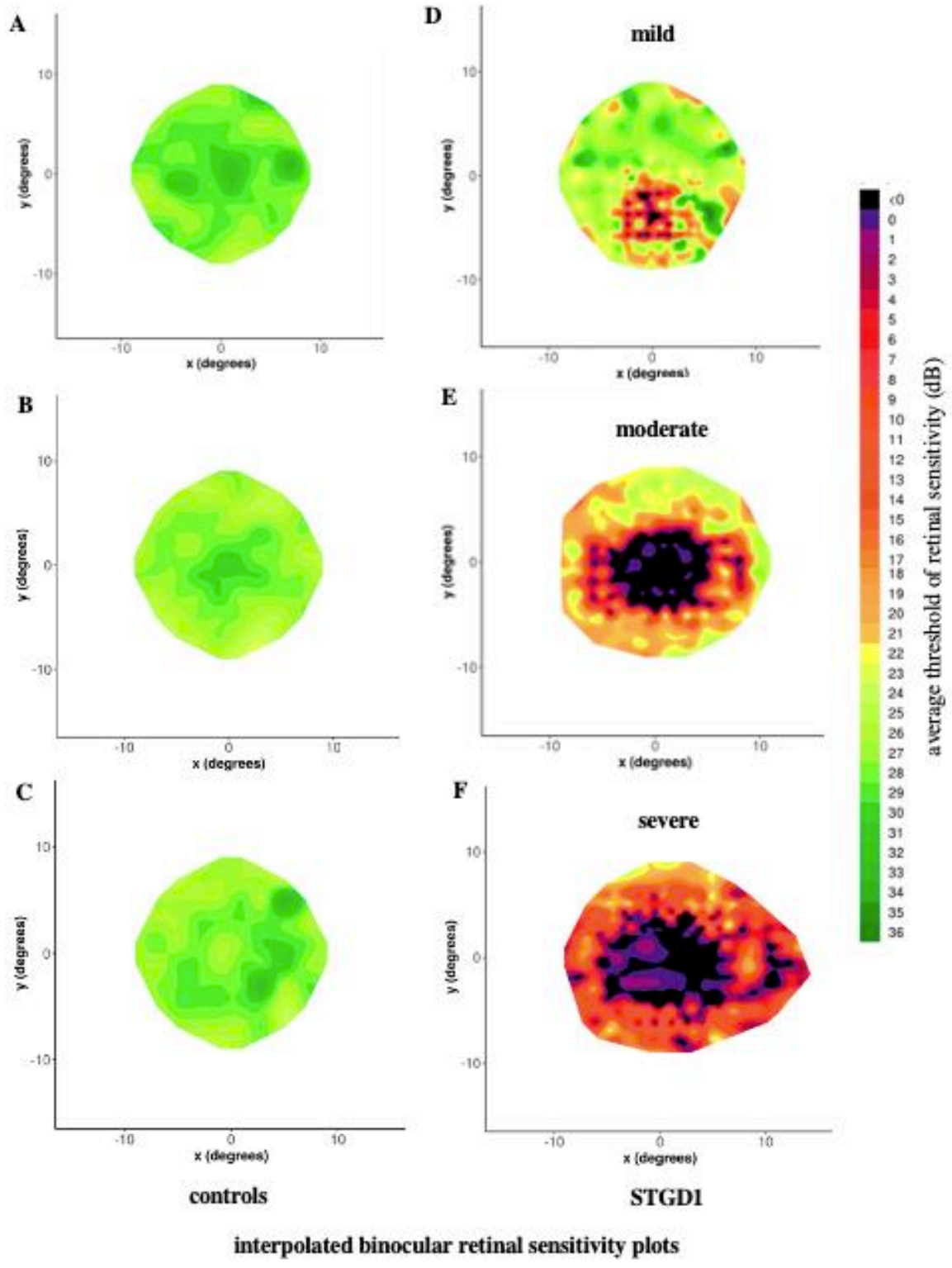


Figure 32: Binocular retinal sensitivity maps for three controls (A – C) and three STGD1 (D – F) participants (with mild, moderate, and severe vision loss). This shows the functional sensitivity of the retina with points seen (green) through to unseen (black).

Participant number	*Retinal sensitivity (dB)*	*Disease severity*
002	20.5	mild
003	15.6	moderate
009	6.7	severe
010	22.0	mild
013	5.9	severe
014	9.8	severe
023	13.8	moderate
028	7.6	severe
030	8.3	severe
037	17.8	moderate
048	6.2	severe
055	2.2	severe
057	13.0	moderate
059	14.2	moderate
060	23.8	mild
062	12.1	moderate
064	9.1	severe

Table 3: STGD1 patients mean retinal sensitivities (dB) calculated from the binocular plots, categorised into disease severities (mild, moderate, and severe).

STGD1 had lower overall retinal sensitivities than controls across the central 0 – 9° of the retinae and this is shown in figure 33. Participants with STGD1 showed lower retinal sensitivities than control participants, indicated by a significant effect of group in a 2-way ANOVA ($F(1, 160) = 416.4$, $p < 0.001$). There was no main effect of retinal position across the STGD1 and controls groups ($F(4, 160) = 2.257$, $p = 0.065$). However, the effect of retinal position differed significantly in the two groups, shown by the significant interaction ($F(4, 160) = 5.619$, $p < 0.001$). This was driven by the increase in function with eccentricity in the STGD1 group and slight decrease in the control group. Nonetheless, the STGD1 group showed loss of retinal sensitivity across all locations, shown by a significant effect at 1° ($p < .001$), 3° ($p < .001$), 5° ($p < .001$), 7° ($p < .001$) and 9° ($p < 0.001$) across the retina. This

shows that the central photoreceptor degeneration in STGD1 causes a reduction in function across the central 9° of the retinae.

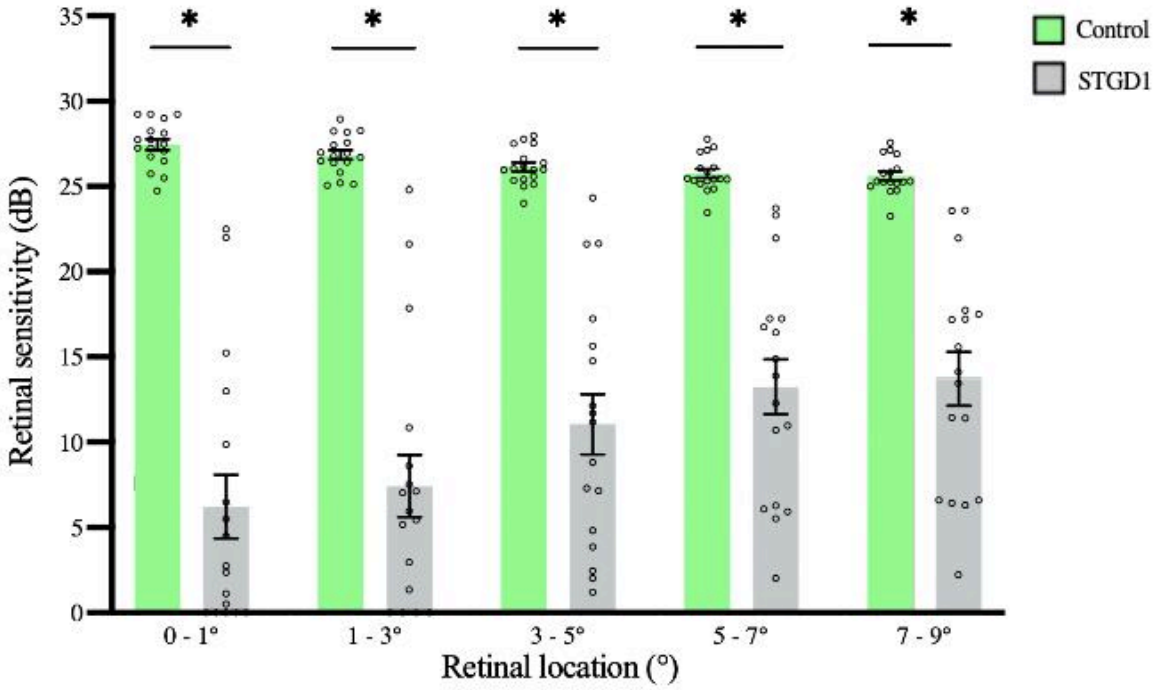


Figure 33: Retinal (left and right retina averaged) sensitivities (dB) between controls with healthy vision (green) and STGD1 (grey) across the central 9 ° of the retina. Individual data points are shown with circles (black) and error bars show standard deviation. Bars show significance at p ≤ 0.05 (*), p ≤ 0.01 (**) or p ≤ 0.001 (***) or non-significance of p > 0.05 (ns).

3.5.2 Contrast sensitivity decreases in STGD1

STGD1 had overall lower contrast sensitivities than controls across the five spatial frequencies measured (figure 34). Unsurprisingly given the loss of cones and therefore loss of central vision, we found a reduction in high acuity vision. Participants with STGD1 showed lower contrast sensitivities than control participants, indicated by a significant effect of group in a 2-way ANOVA ($F(1, 80) = 8.645$, $p = 0.004$). The contrast sensitivity required to resolve a grating did not vary depending on the spatial frequency, shown by a non-significant effect of spatial frequency ($F(4, 80) = 1.874$, $p =$

0.123). The contrast sensitivity required to resolve a grating did not vary in STGD1 compared to controls across spatial frequencies, indicated by a non-significant interaction between group and position on retinal sensitivity ($F(4, 80) = 1.183$, $p = 0.325$). Fisher's LSD post-hoc tests only showed a significant difference between STGD1 and controls at 4° (p = 0.002) but no difference at 1° (p = 0.671), 2° (p = 0.195) 8° (p = 0.361) and 10° (p = 0.456), indicating those with STGD1 need higher contrast to distinguish gratings at 4 cpd.

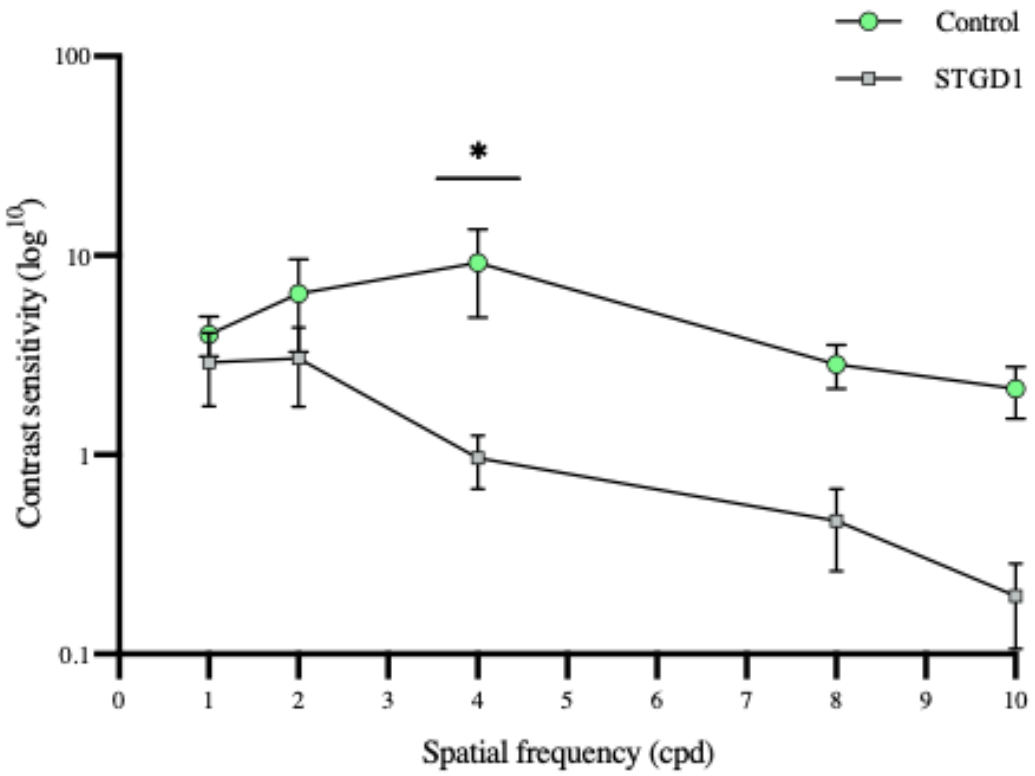


Figure 34: Contrast sensitivity (log^{10}) at varying spatial frequencies (cpd) between patients with STGD1 (grey square) and controls (green circle) with standard error (SE). Bars show significance at $p \leq 0.05$ (*), $p \leq 0.01$ (**) or $p \leq 0.001$ (***) or non-significance of $p > 0.05$ (ns).

Greater disease severity does not correlate with lower contrast sensitivity

To investigate the effect of disease severity on the ability to resolve gratings at differing spatial frequencies (1, 2, 4, 8, 10 cpd), Pearson's R correlation was conducted to compare the mean contrast required to resolve the gratings and plotted against retinal sensitivity (0 - 9°) (dB) (figure 35).

Contrast sensitivity thresholds were not correlated with retinal sensitivities (dB) ($r(15) = -.18$, $p < 0.513$). This is demonstrated in figure 35 where STGD1 (grey squares) with lower retinal sensitives did not require higher contrasts to resolve gratings of higher spatial frequencies. These results do not suggest that a larger amount of functional loss at the retina, does not correlate with the amount of contrast needed to resolve gratings of higher spatial frequencies.

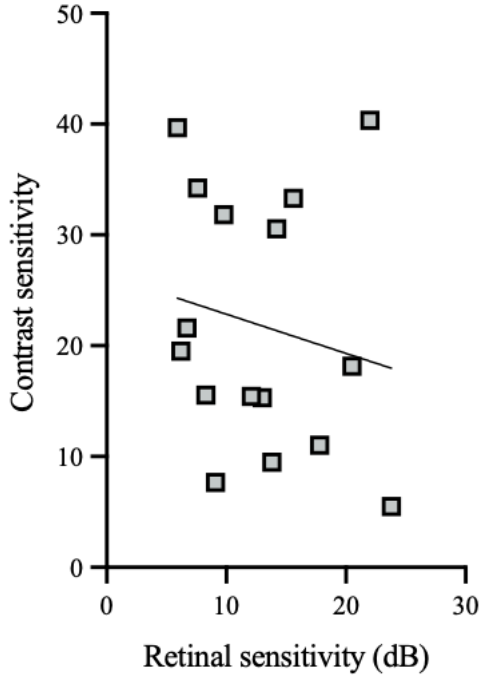


Figure 35: The average contrast sensitivity required to distinguish gratings at five spatial frequencies (1, 2, 4, 8, 10 cpd) correlated with mean retinal sensitivity (dB) for STGD1 (grey squares) are plotted with lines of best fit.

3.5.3 Visual acuity decreases in STGD1

Due to the central vision loss in STGD1 which leads to a deficit in fine detail vision, I predicted that STGD1 will have a lower visual acuity than controls. As the patients have bilateral central scotomas visual acuity would be expected to be similar across eyes. STGD1 had an overall lower visual acuity, and this is shown in figure 36. The STGD1 group ($M = 56.12$, $SD = 21.14$) had lower binocular VAs than controls ($M = 93.35$, $SD = 2.62$) indicated by a significant difference in an independent samples

t-test ($t(7.207) = p < 0.001$). These results show that due to the loss of central vision in STGD1 they have a reduction in visual acuity.

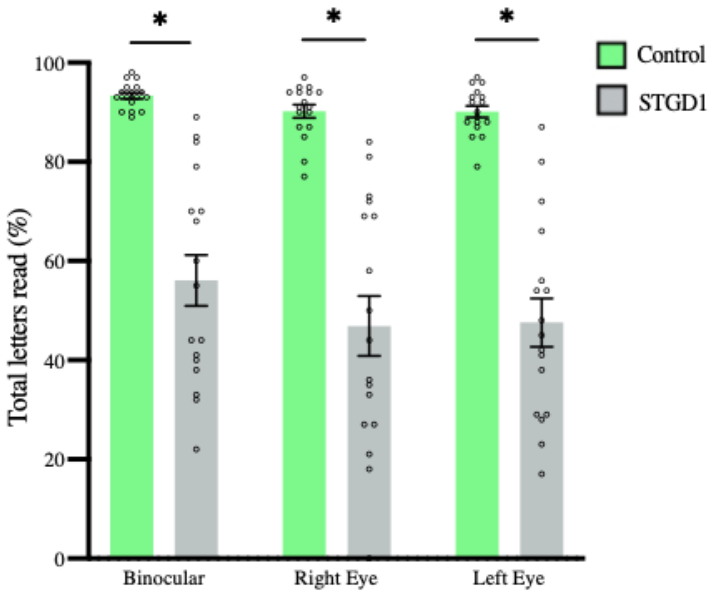


Figure 36: Visual acuity (binocular and monocular) measured by the EVA test between controls with healthy vision (green) and STGD1 (grey). Individual data points are shown with circles (black) and error bars show standard deviation. Bars show significance at $p \leq 0.05$ (*), $p \leq 0.01$ (**) or $p \leq 0.001$ (***) or non-significance of $p > 0.05$ (ns).

Greater disease severity does not with a reduction in visual acuity

To investigate the effect of disease severity on visual acuity, Pearson's R correlation was conducted to compare binocular visual acuity and plotted against retinal sensitivity (0 - 9°) (dB) (figure 37). More letters rad and therefore higher visual acuity correlated with higher retinal sensitivities (dB) ($r(16) = .41$, $p < 0.107$). This is demonstrated in figure 37 where STGD1 patients (grey squares) who have lower retinal sensitives did not have a significantly different percentage of the total letters read. These results do not suggest that a larger amount of functional loss at the retina causes a larger reduction in visual acuity discrimination.

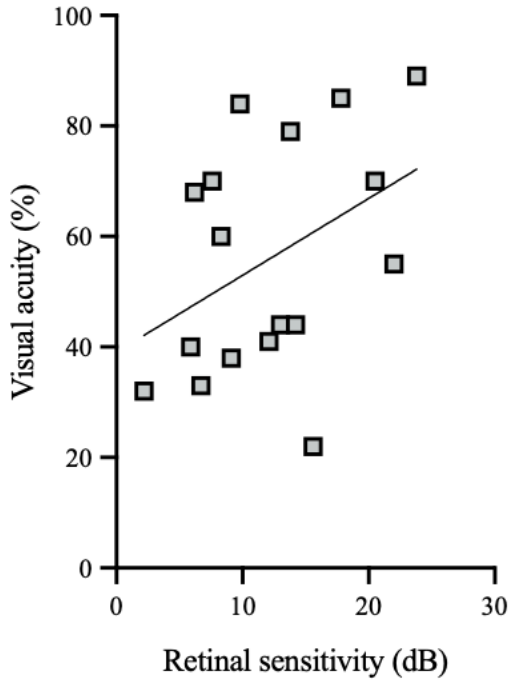


Figure 37: Binocular visual acuity (% of total letters read) correlated with mean retinal sensitivity (dB) for STGD1 (grey squares), are plotted with lines of best fit.

3.5.4 Colour vision decreases in STGD1

A loss of cone photoreceptors in the central retina leads to a reduced ability to discriminate colour. I predicted an overall colour vision deficit in STGD1 compared to controls. This colour deficit is expected to be larger in some axes than others, as the central 0.34° of the foveae is S-cone free and the loss in STGD1 is largest here, therefore they should show a higher deficit in the colour axes processed by L-cones and M-cones compared to S-cones. However, as all patients have scotomas larger than 0.34° this difference may not be detectable.

Unsurprisingly given the loss of cones, STGD1 had higher discrimination thresholds for the individual protan, deutan and tritan colour axes compared to controls, shown in figure 38. Participants with STGD1 showed higher discrimination thresholds than control participants, indicated by a significant effect of group in a 2-way ANOVA ($F(1, 93) = 51.39$, $p < 0.001$). Discrimination thresholds did not change across axes of colour space, shown by a non-significant effect of colour axes ($F(2, 93) = 3.004$, $p = 0.054$). However, discrimination thresholds did not vary in STGD1

compared to controls across colour axes, indicated by a non-significant interaction between group and colour axes ($F(2, 93) = 0.001$, $p = 0.999$). The STGD1 group showed an increase in discrimination thresholds across all colour axes, shown by a significant effect in protan ($p < 0.001$), deutan ($p = 0.001$) and tritan ($p < 0.001$) colour axes. An individual colour axes was not significantly more affected in STGD, in protan compared to deutan ($p = 0.889$), in tritan compared to protan ($p = 0.125$) and in deutan compared to tritan ($p = 0.162$). Figure 39 shows the colour discrimination vectors plotted in colour space for individual controls (A) and STGD1 (B) and the average for each group (C). These graphs show that STGD1 have a greater magnitude of loss (larger vector length) than controls and these are not particularly shifted to one axis in colour space (shown by vector angle). Due to the large amount of functional loss in the majority of the STGD1 patient cohort it is unsurprising that they have reduced colour vision discrimination across all three axes of colour space.

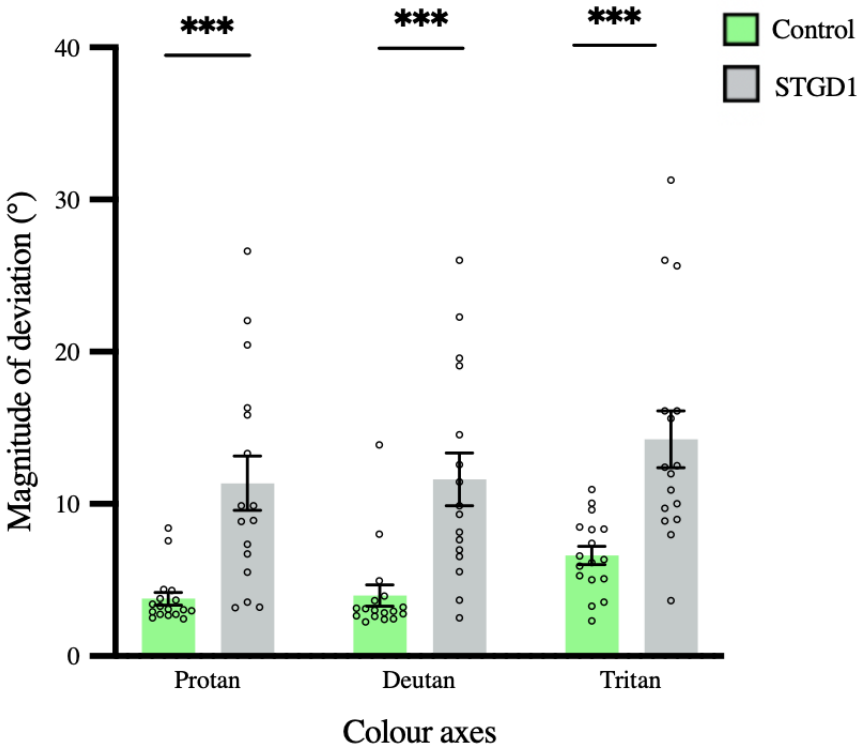


Figure 38: Colour vision discrimination (binocular) for protan, deutan and tritan axes, calculated by the magnitude of the vector in colour space and measured by the Cambridge Colour Test between controls with healthy vision (green) and STGD1 (grey). Individual data points are shown with circles

(black) and error bars show standard deviation. Bars show significance at p ≤ 0.05 (*), p ≤ 0.01 (**) or p ≤ 0.001 (***) or non-significance of p > 0.05 (ns).

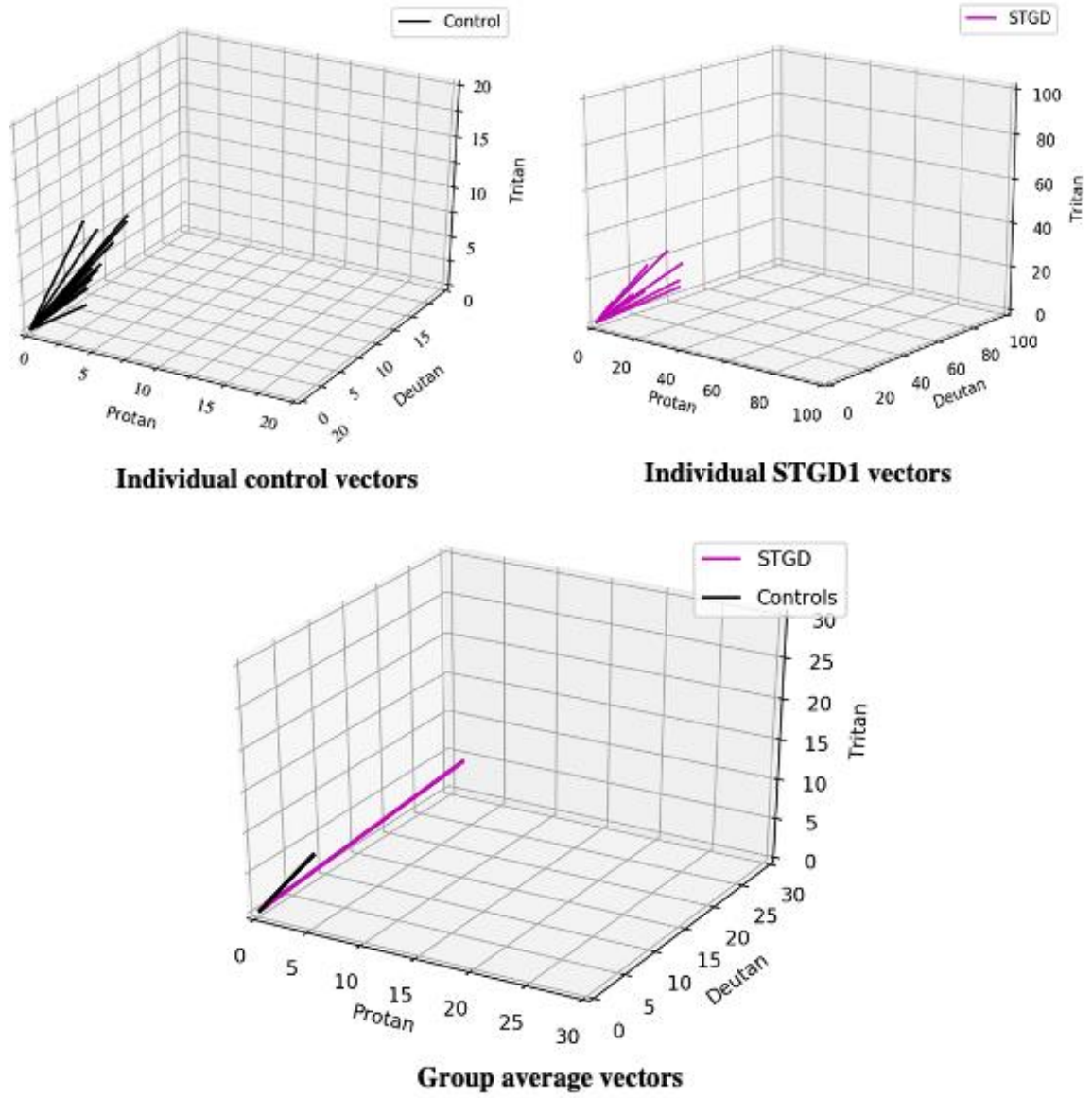


Figure 39: Colour discrimination vectors plotted in colour space for individual controls (A) (black) and STGD1 (B) (purple) and the average for each group (C). Vectors are plotted in colour space (protan, deutan and tritan axes), where the magnitude of the vector represents the amount of loss in that discrimination threshold and the angle of the vector represents in which axes of colour space the discrimination is most affected in.

Larger deficits in colour vision do not correlate with a greater disease severity

To investigate the effect of disease severity on colour vision, Pearson's R correlation was calculated to compare colour vision discrimination along the three colour axes (protan, deutan and tritan) and plotted against retinal sensitivity (0 - 9°) (dB) (figure 40). Colour vision discrimination measured as the average vector threshold was not significantly correlated with increased retinal sensitivity (dB) ($r(15) = .22$, $p = 0.418$). To investigate if a deficit along one axis was driving this significant effect, the discrimination thresholds for the individual colour axes were correlated with disease severity. Colour vision discrimination did not significantly correlate with higher retinal sensitivities (dB) along the protan ($r(15) = .13$, $p = 0.624$), deutan ($r(15) = .28$, $p = 0.285$) and the tritan ($r(15) = .15$, $p = 0.569$) axes. This is demonstrated in figure 40 where STGD1 patients (grey squares) who have lower retinal sensitivities did not have significantly different colour vision discrimination thresholds along the protan (A), deutan (B), tritan (C) and mean colour axes (D). These results do not suggest that a larger amount of functional loss at the retina causes a reduction in colour vision discrimination.

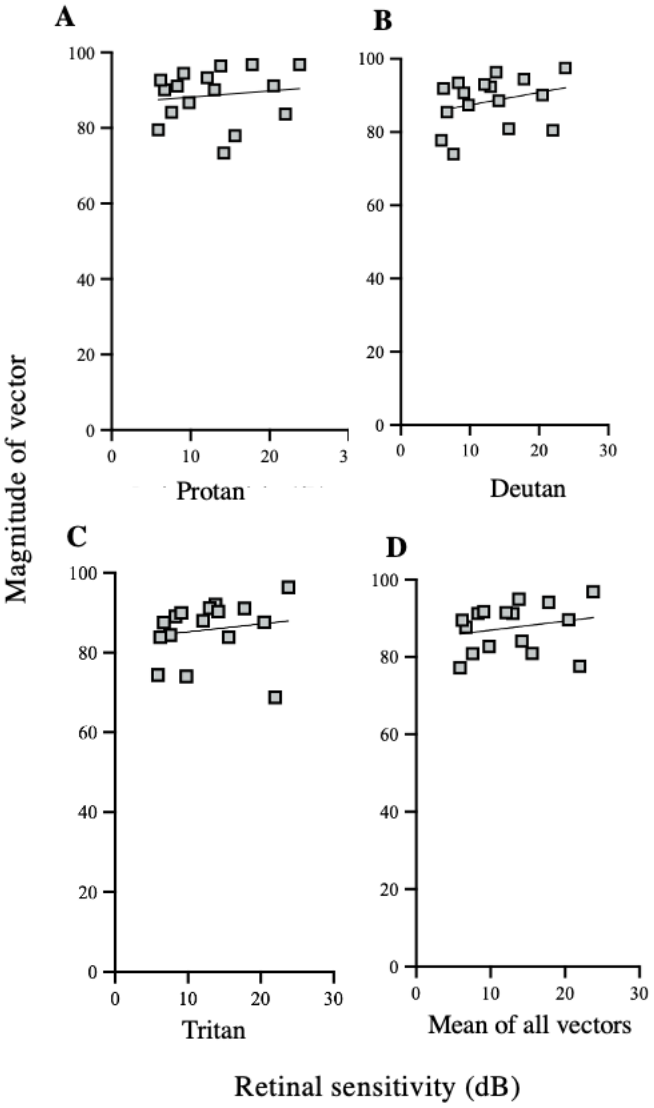


Figure 40: Discrimination along the protan (A), deutan (B), tritan (C) and mean (D) colour axes correlated with mean retinal sensitivity (dB) for STGD1 (grey squares), are plotted with lines of best fit.

3.6 Discussion

This chapter aimed to investigate if damage at the retina in STGD1 causes a reduction in visual function. Visual function was measured using retinal sensitivity, contrast sensitivity, visual acuity, and colour vision discrimination. Retinal sensitivity was first used to decide whether the patient met the inclusion criteria for this study (bilateral loss within the central 20° of the retina) and then used to categorise patients into disease severities. I found that STGD1 had deficits across all measures of

visual function compared to controls. As the STGD1 cohort had a variety of disease severities this was expected to correlate with visual function. I found that a larger loss measured by retinal sensitivity correlated with reductions in visual acuity, contrast detection and colour vision discrimination.

3.6.1 Retinal sensitivity is reduced in STGD1

As predicted, the retinal sensitivities in STGD1 are significantly reduced compared to controls across the central 20° of the retinae and this reduction is larger within central positions of the macula. This shows how the loss of photoreceptors in STGD1 reduces the ability to discriminate light projected onto the retina. Retinal sensitivity was used as measure of disease severity, as a greater reduction in retinal sensitivity correlates with reduced visual acuity (Testa et al., 2012).

3.6.2 Contrast sensitivity is lower in STGD1 compared to controls

A lower contrast sensitivity indicates a larger amount of contrast needed to distinguish between two points in visual space. I found that STGD1 have lower contrast sensitivities than controls shown by a significant effect of group. This demonstrates that the loss of cones in central vision reduces high acuity vision in STGD1. Previous research has found that the loss in STGD1 causes a larger deficit in gratings of higher spatial frequencies (Alahmadi et al., 2018), however this was not what we found. A statistically significant difference was only found between STGD1 and controls at 4 cpd and not at higher spatial frequencies like in Alahmadi et al (2018). The CSF peak is around ~4 cpd in healthy controls so this may reflect why the significant effect was found here and not at higher spatial frequencies. This test measured 5 spatial frequencies spread out over 10 cpd, therefore this could have been improved by testing at 3 and 5 cpd to investigate if STGD1 also had significantly lower contrast sensitivities around 4 cpd. This shows that a loss of cones in STGD1 reduces high acuity vision, where a greater contrast is needed to distinguish between two points in visual space.

3.6.3 STGD1 have lower visual acuity due to central loss

Unsurprisingly given the loss of cones and therefore loss of central vision, we find a reduction in high acuity vision in STGD1. As predicted, patients with STGD1 had a reduced ability to discriminate letters at smaller sizes due to their deficit in discriminating fine detail. Increased disease severity measured by lower retinal sensitivities did not significantly correlate with a reduction in visual acuity, which is in contrast with previous research (Testa et al., 2012). This shows how a loss of cones in the retina reduces the ability to discriminate fine detail vision.

3.6.4 Colour vision discrimination decreases across all axes of colour space in STGD1

A loss of cone photoreceptors in the central retina reduces the ability to discriminate colour. As the central ~0.34° of the fovea contains only M/L-cones and is S-cone free previous research in STGD1 has shown a greater deficit in the colour axes that are processed by L-/ M-cones (red/green) compared to S-cones (blue) (Vandenbroucke et al., 2015). The STGD1 patients recruited for this project have scotomas larger than 0.34°, therefore a deficit in colour discrimination was expected across the three axes of colour space measured. We found that all three colour axes were equally affected in STGD1, however lower colour vision discrimination thresholds did not correlate with greater disease severity. This shows how a loss of cone photoreceptors reduces colour vision discrimination.

3.6.5 Limitations and future research directions

Within the testing day there was a trade-off between length of testing and the amount of data that was able to be collected. Participant comfort was the most important factor in deciding the amount of time taken for each vision test, therefore some measures were limited in the amount of data that was able to be collected. If an additional testing day was added the length of tests could have been increased, such as collecting more than five cpd in contrast sensitivity to better understand which spatial frequencies are most affected in STGD1.

Colour vision discrimination was significantly affected across all three axes of colour space and this loss correlated with disease severity. This contrasts with the results from Vandenbrouck and colleagues (2015) who found a larger deficit in red/green discrimination compared to blue/yellow

discrimination in STGD1 patients. This likely reflects the greater loss within the s-cone free region at the fovea. This difference in results may be due to the size of the colour stimuli used, as due to the STGD1 participants scotoma size, this may have shifted the amount of the screen they were able to view due to the location of their PRL. The patients with larger scotoma sizes would have seen less of the screen and therefore be unable to detect part of the colour stimuli locations which would have biased the results.

If more testing time was permitted, then more sensitive techniques for cone measurements could have been used. Adaptive optics can image cross-sections of the human retina *in vivo* which show individual cone cells. This could be used to quantify the amount of L-, M- and S-wavelength cones present in the macula, and therefore provide a more accurate measure of the amount of loss between the cone classes. This measure of cone loss could be used as a better value for the predicted deficits across the axes of colour space.

The microperimeter measured retinal sensitivity within the central 20° of the retinae, however this technique is unable to measure whether vision loss is present in the periphery of the visual field. Wider field perimetry (20° - 90°/180°) was collected for this project using the Octopus perimeter. Further analysis should be completed to confirm that the vision loss in the STGD1 participants is constrained within the 20° of the retinae and is not present in the periphery. This is required to confirm that peripheral visual field loss is not present, as this would cause a reduced input to the peripheral representation of the visual field in V1, and therefore this region could not be used as a comparison region that would be unexpected to change between STGD1 and controls.

Machines that measure microperimetry are expensive and are not generally available in clinics to measure vision loss. Tests that provide a measure or visual acuity like the EVA and the Cambridge Spatial Achromatic Contrast Sensitivity Function test are more affordable. The research presented in this chapter shows that for patients with STGD1 measures of visual acuity correlate with retinal sensitivity. Therefore, these measures of visual acuity can be used to predict the amount of loss at the

retina, and this can be used as a more affordable way to measure the rate of vision loss over time in STGD1.

3.6.6 Chapter conclusion

This chapter demonstrates the effect of STGD1 disease on visual function compared to controls with a healthy retina. The cone photoreceptors located in the centre of the retina process colour and high acuity vision. As STGD1 damages the central retina these patients therefore have deficits in fine detail vision, as demonstrated by the performance on the tests of visual acuity and contrast sensitivity. As cones process colour vision STGD1 patients also show deficits in colour vision discrimination across all three axes of colour space.

4 Structure

Structural Changes in the Visual System in Stargardt patients compared to Controls

4.1 Abstract

Degeneration of the retina in STGD1 causes thinning of the RPE and photoreceptor layers (Cai et al., 2018). This causes a lack of visual input to the visual cortex. If the cortex has been secondarily affected, this may have a negative impact on potential treatments aimed at restoring retinal function, rendering them ineffective. Reductions in grey matter volume have been found in patients with central vision loss from STGD1 (Olivo et al., 2015) and macular degeneration (Plank et al., 2011). Additionally, cortical thinning localised to the region of projected vision loss within V1 has been found in cohorts with macular degeneration (Burge et al., 2016; Hanson et al., 2019). These findings suggest that a loss of visual input causes degeneration within the visual cortex.

Degeneration at the retina was investigated using Optical Coherence Tomography allowing assessment of the photoreceptor and the nerve fibre layers. To determine whether degeneration at the retina leads to degeneration in the visual cortex, cortical structure was measured using Voxel Based Morphometry to assess changes in grey matter volume compared to control participants. Cortical thickness was then used to measure more localised changes in V1 representing different eccentricities of the visual field. I found that the photoreceptor layers were thinner in the retinae of patients with STGD1 compared to controls, and this thinning was more apparent across the central retinae. The nerve fibre layer was thinner in STGD1 than controls except for the central 2° where it was thicker, possibly due to inflammation. In the primary visual cortex, there was significant thinning in STGD1 compared to controls, but this was not greater at the posterior V1 where the vision loss is projected. These results indicate that degeneration in the retina causes cortical thinning within V1 which may reflect neuronal degeneration after a loss of input.

4.2 Introduction

The primary visual cortex (V1) has a topographic organisation, meaning a region in visual space is processed by adjacent populations of neurons. Localised damage to the retina, is projected into a focal region of V1. Since the topographic organisation is maintained throughout the visual cortex, the neurons that normally process that region of the visual field, now have a loss of input. These neurons could cease to fire and become dormant, or they could make new connections to other neurons, or they could degenerate. The fate of these neurons has implications for the viability of treatments that aim to halt the damage at the retina and restore vision. If the neurons are dormant then they will be ready to accept any potential restored input at the retina. However, if the neurons were to degenerate or reorganise, they may be unable to process the restored input at the retina and this would act as a barrier for recovery of vision. Therefore, it is vital to understand if degeneration or reorganisation has occurred in the visual cortex and if so, the extent of these changes.

In STGD1 the RPE and photoreceptor loss predominantly affects the macula region of the retina, the macula has a high density of cones which enable high acuity vision, and therefore this loss leads to central vision loss. STGD1 causes degeneration to the RPE and the photoreceptor layers and these degenerate at a rate of 0.33 ± 0.38 mm^2/year for the RPE and 0.31 ± 0.31 mm^2/year for the photoreceptor layers (Cai et al., 2018). The nerve fibre layer is thicker at the central macula in STGD1 due to inflammation and thinner at the peripheral macula (Reich et al., 2021). There is consensus in the literature that structural loss is correlated with functional loss, so the larger the loss within the photoreceptor layers, the larger the loss of functional vision (Testa et al., 2012).

Non-human primate models of retinal degeneration have shown that loss at the retina correlates with loss along the visual pathway. Glaucoma causes localised retinal degeneration like STGD1; however, the loss is constrained to the peripheral visual field. Additionally in glaucoma the retinal nerve fiber layer which projects to the cortex is directly affected. In STGD1 the nerve fibre layer it is secondarily affected after RPE and photoreceptor loss, therefore glaucoma is a different model to investigate a loss of visual input, and this should be considered when interpreting how these results may relate to

STGD1. Reductions in V1 volume have been found in marmosets with glaucoma shown with voxel-based morphometry (VBM) at 7T MRI. This reduction in V1 was confirmed with histology, where a reduction in cell number was found in layer 4 of V1 in glaucoma compared to controls (Noro et al., 2019).

Voxel based morphometry (VBM) allows measurement of global changes in the brain, specifically the density of grey matter. Studies investigating VBM changes in RDs have shown a reduction in visual cortex volume in RP (Machado et al., 2017), glaucoma (Boucard et al., 2009; Zikou et al., 2012), age related and juvenile macular degeneration (Boucard et al., 2009; Hernowo et al., 2014). Specifically in a patient cohort with STGD1 a reduction in GM volume was found in the visual cortex using VBM (Olivo et al., 2015). A reduction in GM density in patients with macular degeneration has been found at the posterior visual cortex where vision loss is projected (Plank et al., 2011). As VBM allows us to measure global changes in the brain, cortical thickness can then be used to investigate grey matter thickness within a localised region of the cortex. Cortical thickness varies considerable across the brain and the thinnest area is the visual cortex which varies from 1.5 mm to 2.5 mm (Alvarez et al., 2019). Cortical thickness depends on participant age as cortical thickness changes with brain maturation (Fjell et al., 2015) and has been shown to be altered in conditions such as congenital blindness and albinism (Bridge et al., 2009; Bridge et al., 2014).

Cortical thinning localised to the region of projected vision loss within V1 has been found in cohorts with macular degeneration using Freesurfer measures of cortical thickness (Burge et al., 2016; Hanson et al., 2019). These findings suggest that a loss of visual input causes degeneration within the visual cortex. However, in a cohort with peripheral loss from RP, no changes in cortical thickness were observed within V1 measured using BrainVoyager (Ferreira et al., 2017). Whether these contrasting results in cortical thickness after vision loss are due to the disease or differences between the analysis software is not yet clear.

4.2.1 Rationale

As shown in the previous chapter (Chapter 3 – Vision Measures) patients with STGD1 have extensive central vision loss. As the build-up of lipofuscin in STGD1 disease causes photoreceptor death, retinal structure was investigated to measure the extent of degeneration at the inner and outer layers. VBM and cortical thickness were used as measures to provide an indication of whether degeneration occurs in the cortex after a loss of visual input.

Hypothesis 1: Due to the loss of cones in STGD1 there should be thinning of the inner and outer layers of the retina compared to controls.

Hypothesis 2: There will be a localised region of reduced grey matter density in the STGD1 visual cortex, and this reduction will be localised to the posterior calcarine, reflecting the location of vision loss.

Hypothesis 3: There will be cortical thinning within V1 in STGD1 and this thinning will be greatest in the area of the cortex that responds to the central representations of the visual field.

4.3 Methods

4.3.1 Participants

The work in this chapter includes the full set of participants with STGD1 (9 females, 8 males, mean age 35.6 ± 16.2 SD) and comparison controls with healthy eyes and normal vision (7 females, 10 males, mean age 38.7 ± 14.9 SD). No participants were excluded from the subsequent analyses.

4.3.2 Acquisition

Optical Coherence Tomography:

OCT imaging was performed using the spectral domain OCT system (Spectralis® HRA+OCT imaging system, Heidelberg Engineering, Heidelberg, Germany). OCT uses infrared light to image the individual layers of the retina at high resolution (10 μm). This technique can show structural loss across the retina and if localised damage occurs within a specific layer. This creates high resolution

3D structural images of the patient's retina. The participant was positioned with their chin placed on the chinrest and their forehead against the bar. The chinrest height was adjusted optimally for each participant. The participants were asked to maintain this position throughout the scan. The participant fixated on a central target, or if this was difficult due to central vision loss then a target was placed in their preferred retinal location (PRL). If fixation was lost, the experimenter verbally guided the participant back to the fixation point. The scans were centred over the fovea, covered 20° × 20° and consisted of 49 individual scan layers. The experimenter monitored the scans throughout with verbal feedback, to ensure stable fixation. The OCT machine scored the quality of the image, if this number fell below 20 and part of the image of the retina was missing then the scan was repeated. The OCT scans were performed monocularly, first with the right eye and then the left.

Magnetic Resonance Imaging:

T1-weighted structural MR images were acquired with a 3T Prisma MRI scanner (Siemens Healthcare, Erlangen, Germany), at the Functional Magnetic Resonance Imaging Centre of the Brain (FMRIB, University of Oxford). T1-weighted (T1w) whole head (including nose) anatomical images were acquired axially, using a 64-channel head coil (MP-RAGE, TR = 1900 ms, TE = 3.97 ms, T1 = 904 ms, flip angle = 8°, slices = 192, resolution = $1mm^3$) for all participants. The T1w scans were used to anatomically localise the functional and neurochemical data, to measure grey matter density (with VBM) and to reconstruct the cortical surface (with Freesurfer) to measure cortical thickness.

4.3.3 Analysis

4.3.3.1 Optical Coherence Tomography

The OCT segmentations were completed using the Orion Advanced OCR Analysis (Voxeleron) segmentation software. The segmentations were manually checked and if required were manually segmented to ensure the retinal layers were accurately distinguished. The segmentation data was processed in MATLAB to split the individual layer thicknesses along the 0 – 8° of the retinae and averaged over the left and right retina (figure 41). Figure 41 shows the position (A) of the cross section (B) through a healthy retina. In this cross section the photoreceptor complex (2) is intact

across the retinal image. A STGD1 retina is shown in (C) with the damage occurring in the central macula region, the retinal cross section is shown in D. In the STGD1 retina the inner retinal thickness is thinner than that in controls and the photoreceptor complex (2) is thinner in the central retina (in between red lines) due to photoreceptor loss.

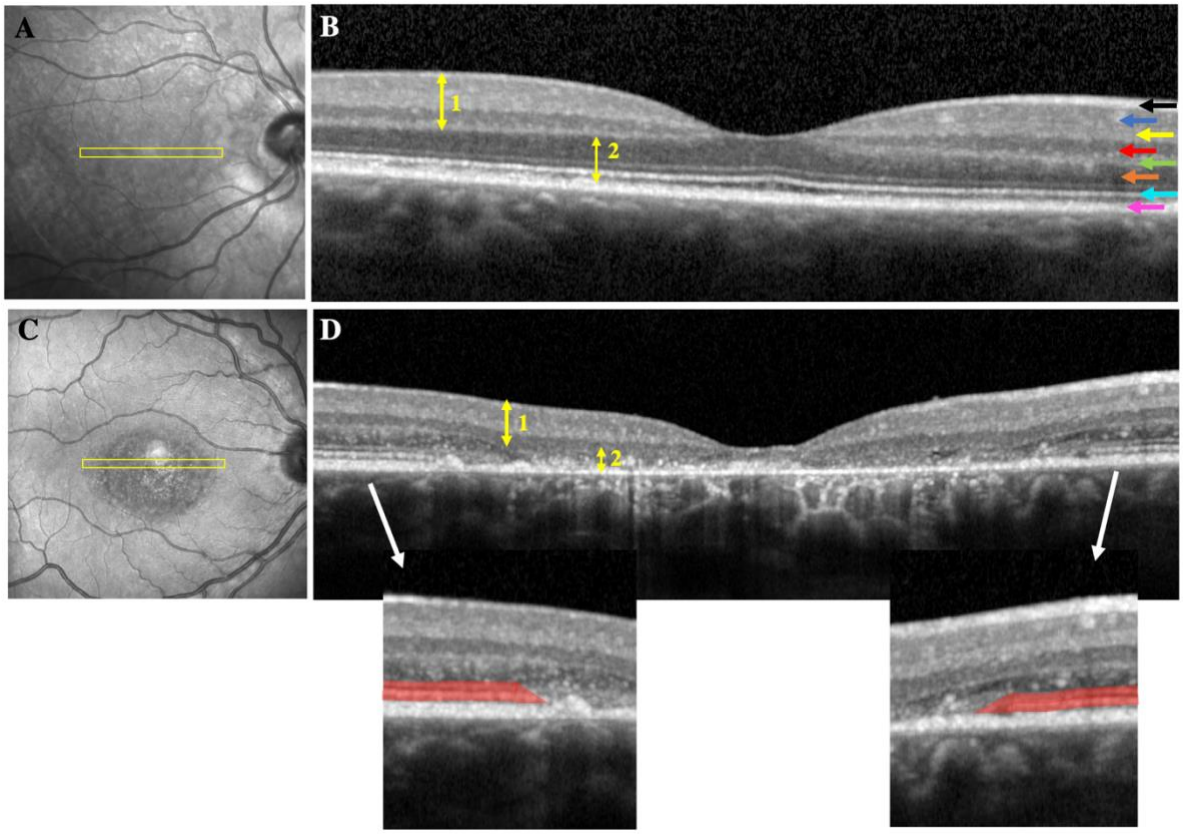


Figure 41: Structural images of the right retina measured with optical coherence tomography. Images from a healthy retina (A/B) and a retina with structural loss due to STGD1 disease (C/D). A/C show a fundus autofluorescence image of the retina with the optic disc at the right and the macula at the centre, note the damage at the macula in C due to STGD, the yellow rectangle shows the cross-section position of the corresponding images B/D. In B/D 1 = inner retinal thickness, and 2 = photoreceptor complex. In B, the healthy retina arrows point towards each layer, black = retinal nerve fibre layer, blue = ganglion cell layer, yellow = inner plexiform layer, red = inner nuclear layer, green = outer plexiform layer, orange = outer nuclear layer, turquoise = photoreceptor layers, pink = retinal pigment epithelium. In D, the STGD1 retina, red highlights the preserved ellipsoid zone which stops abruptly at the red edge.

4.3.3.2 Magnetic Resonance Imaging

Voxel Based Morphometry

The T1w MPRAGE structural images (1mm^3) were processed using FSL-VBM (FMRIB Software Library) version 1.1 (Douaud et al., 2007), with FSL tools (Smith et al., 2004) and an optimised protocol (Good et al., 2001). Structural images were first brain extracted using the FSL brain extraction tool, then segmented into different tissue types (GM, WM, and CSF) before being non-linear registered to standard space (MNI 152) (Andersson et al., 2007). The individual structural images were then averaged to create a grey matter template specific for the studied population (controls and STGD1). The structural images were then non-linearly registered to the template and smoothed with an isotropic Gaussian kernel with a sigma of 3mm. Finally, an occipital lobe mask was used to restrict the voxelwise general linear model (GLM) analysis to the visual cortex, as this is where any effects were predicted to occur. In order to investigate the effects of vision loss to reflect the varying levels of retinal damage and functional vision loss in the STGD1 patients who had different disease severities, VBM was repeated to investigate how grey matter density correlated with the amount of vision loss (structural from the outer retinal layer (μm) and functional form retinal sensitivity(dB)).

To determine significant differences, the voxelwise GLM (threshold-free cluster enhancement) was applied using permutation-based non-parametric testing (5000 permutations), corrected for multiple comparisons across space ($p < 00.05$).

Cortical thickness:

As VBM allows us to measure global changes in the brain, cortical thickness can then be used to investigate grey matter thickness within a localised region of the cortex. Cortical thickness is investigated at a voxel-wise level and is calculated by the shortest difference between the edge of the white matter and the pial surface of the brain. The T1w MPRAGE structural images (1mm^3) were first

pre-processed with the *fsl_anat* function from FMRIB Software Library (FSL). This consisted of reorientation to AC-PC space, bias field corrected and non-linearly aligned to the MNI-152 ($0.7mm^3$) standard template using *fnirt* (Jenkinson et al., 2002). The pre-processed T1's were then reconstructed using the *recon-all* tool in Freesurfer (v 6.0.0) (Dale et al., 1999). This reconstructs the cortical surface and registers it to a standardised space (MNI305) (Fischl and Dale, 2000). Segmentations of the pial (GM) and white matter (WM) surfaces were created and the distance between these edges was calculated to generate measures of cortical thickness.

To measure cortical thickness across different eccentricities of the visual field represented in the visual cortex, V1 was defined from the standard Benson retinotopy atlas and fitted to the cortical surfaces generated in Freesurfer (Benson et al., 2014; Benson et al., 2012) (figure 42). The individual T1w images were registered to the MNI152 standard brain. Smoothing of 10 mm width was applied to the statistical maps. V1 was divided along eccentricity from 0°- 90° of the visual field (0 - 1°, 1 - 2°, 2 - 3°, 3 - 4°, 4 - 5°, 5 - 6°, 7 - 15°, 16 - 30°, 40 – 90°). Cortical thickness was then averaged for each eccentricity region of interest (ROI) to generate a value per hemisphere. This analysis was automated on the open source platform brainlife.io (Avesani et al., 2019).

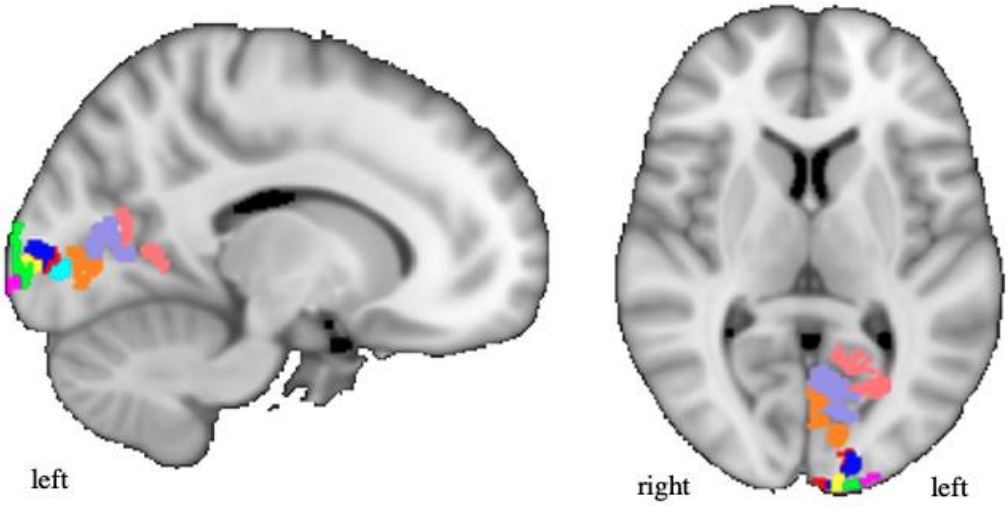


Figure 42: Regions of interest along V1 of the left hemisphere that respond to 0 - 90° of the visual field (0 - 1° = hot pink, 1 - 2°= green, 2 - 3° = yellow, 3 - 4° = dark blue, 4 - 5° = red, 5 - 6° = light

blue, 7 - 15° = orange, 16 - 30° = purple, 40 - 90° = light pink) eccentricity generated from functional retinotopy in the Benson atlas, used to measure cortical thickness, overlaid over the standard brain (MNI152).

In order to investigate the effects of vision loss to reflect the varying levels of retinal damage and functional vision loss in the STGD1 patients who had different disease severities, cortical thickness was correlated with the amount of vision loss (structural from the outer retinal layer and functional form retinal sensitivity). Cluster correction was applied in Freesurfer and only clusters that passed the significance level of $p < 0.05$ were included in this chapter.

4.3.4 Statistical Analysis

Statistical analyses were performed using GraphPad Prism (version 9.0). Analysis of variance (ANOVA) tests were performed to determine if there was a difference between STGD1 and controls across eccentricities of the retinae in the outer retinal layer thickness and the inner retinal thickness. An ANOVA was also performed to compare between the two groups across eccentricities of the visual field represented in V1 of the visual cortex. Results were considered statistically significant at $p < 0.05$.

Due to the range of disease severities in the STGD1 patient cohort, cortical thickness was correlated with extent of vision loss. Pearson's R was used to calculate correlations between vision loss and cortical thickness. Results were considered statistically significant at $p < 0.05$.

4.4 Results

4.4.1 STGD1 have thinner outer retinal layers than controls

Participants with STGD1 had thinner outer retinal layers than control participants, indicated by a significant effect of group in a 2-way ANOVA ($F(1, 253) = 560.5$, $p < 0.001$). Outer retinal layer thickness changes across retinal eccentricity, indicated by a significant effect of retinal position ($F(7, 253) = 2.106$, $p < 0.043$). While thickness decreases across eccentricity in the healthy retina, it

increases in STGD1 reflecting the increase degeneration at the central retina. This is shown by the significant interaction between group and eccentricity ($F(7, 253) = 12.28$, $p < 0.001$). STGD1 had significantly thinner outer retinal layers at all eccentricities across the retina, than controls. The graph in figure 43 shows a thinning across the 0 - 8° of the outer retinal layer in STGD1 and unsurprisingly this thinning is greatest in the central retina, which is where the damage is greatest in STGD1.

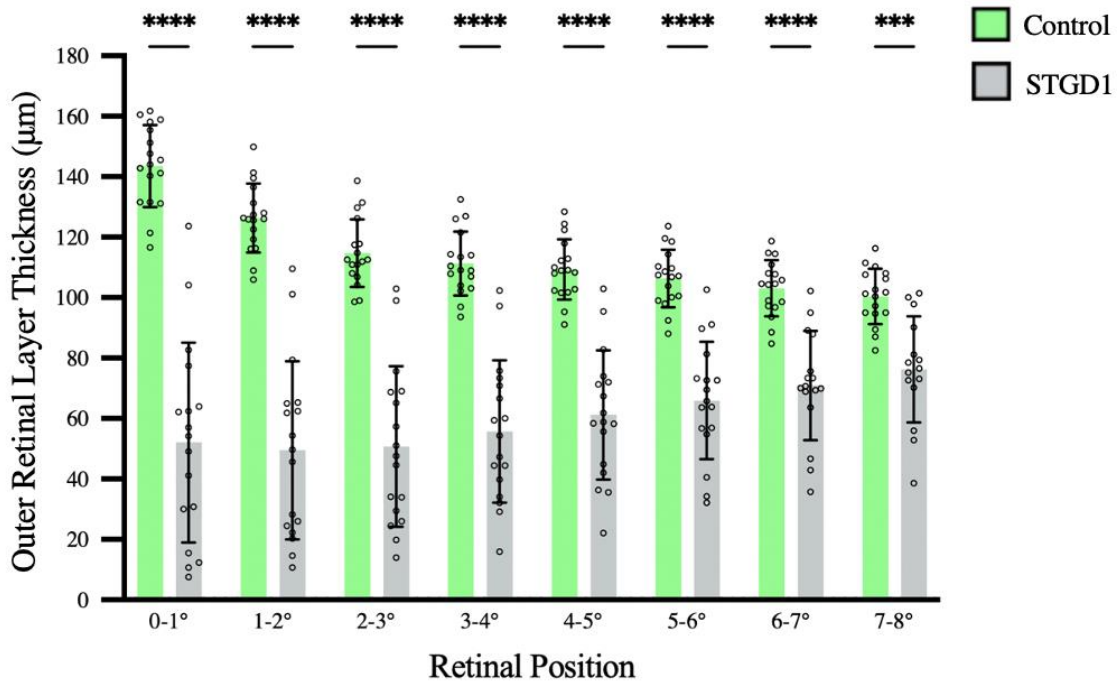


Figure 43: Outer retinal thickness (µm) between controls with healthy vision (green) and STGD1 (grey) across eccentric positions (°) of the retinae (left and right eyes averaged). Individual data points are shown with circles (black) and error bars show standard deviation. Bars show significance at $p \leq 0.05$ (*), $p \leq 0.01$ (**) or $p \leq 0.001$ (***) or non-significance of $p > 0.05$ (ns).

4.4.2 STGD1 have thinner inner retinal layers than controls

Participants with STGD1 had different inner retinal layer thickness (ganglion, bipolar and nuclear layers) than control participants, indicated by a significant effect of group in a 2-way ANOVA ($F(1, 253) = 96.19$, $p < 0.001$). The inner retinal thickness changes across retinal eccentricity, indicated by a significant effect of retinal position ($F(7, 253) = 87.10$, $p < 0.001$). While thickness increases

across eccentricity in the healthy retina, it varies across eccentric positions in STGD1. This is shown by the significant interaction between group and eccentricity ($F(7, 253) = 23.32$, $p < 0.001$). This interaction reflects the finding that the nerve fibre thickness was significantly thicker in STGD1 than controls at 0 - 1° ($p < 0.001$), but not significantly different at 1° - 2° ($p = 0.193$) and then significantly thinner at all higher eccentricities (2°- 3°: $p < 0.001$, 3°- 4°: $p < 0.001$, 4°- 5°: $p < 0.001$, 5°- 6°: $p < 0.001$; 6° - 7°: $p < 0.001$, 7° - 8°: $p = 0.004$). The graph in figure 44 shows there is thinning from 2 - 8° which may reflect from the loss of input from the RPE and photoreceptor degeneration, the lack of thinning in the 0 - 2° may reflect inflammation from the toxic build-up of lipofuscin in the central retina this causes the inner retinal layer to appear thicker.

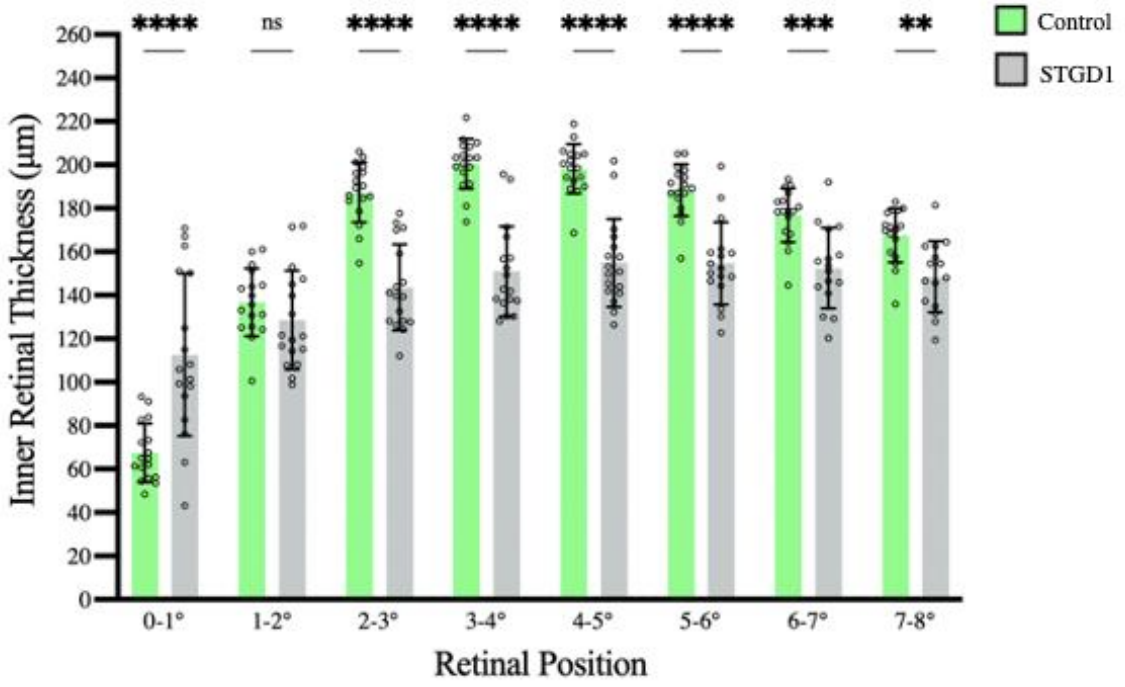


Figure 44: Inner retinal thickness (µm) between controls with healthy vision (green) and STGD1 (grey) across eccentric positions (°) of the retinae (left and right eyes averaged). Individual data points are shown with circles (black) and error bars show standard deviation. Bars show significance at p ≤ 0.05 (*), p ≤ 0.01 (**) or p ≤ 0.001 (***) or non-significance of p > 0.05 (ns).

4.4.3 Grey matter density does not change between STGD1 and controls

Even given the large structural degeneration at the retina, no significant differences in grey matter volume were found between STGD1 and controls ($p < 0.05$) using VBM. STGD1 showed decreased grey matter density along the calcarine (red - yellow in figure 45). These results were significant at $p = 0.035$ but were uncorrected for multiple comparisons.

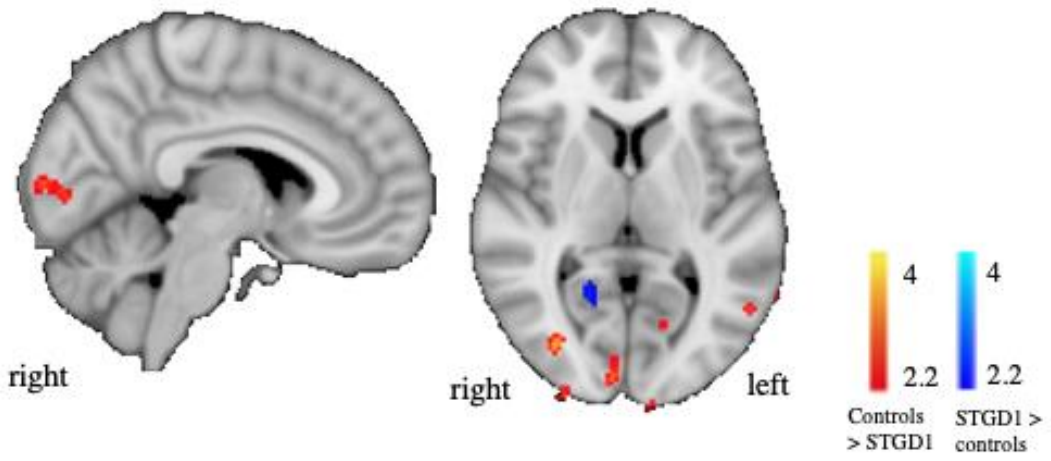


Figure 45: Regions of decreased grey matter density for controls > STGD1 (red - yellow) and STGD1 > controls (light – dark blue) with a significance threshold of p = 0.035, uncorrected for multiple comparisons, overlaid over the standard brain (MNI152).

As there are a variety of disease severities in the STGD1 group, the VBM analysis was correlated with two types of vision loss regressors. The first was retinal structure, calculated as the overall thickness of the photoceptor layer (µm) (0 - 3°) from OCT. There was no significant difference in grey matter volume when correlated with outer retinal layer thickness ($p < 0.05$) using VBM. When uncorrected for multiple comparisons, decreased outer retinal layer thickness correlated with decreased grey matter density along the calcarine ($p = 0.035$) (red - yellow in figure 46).

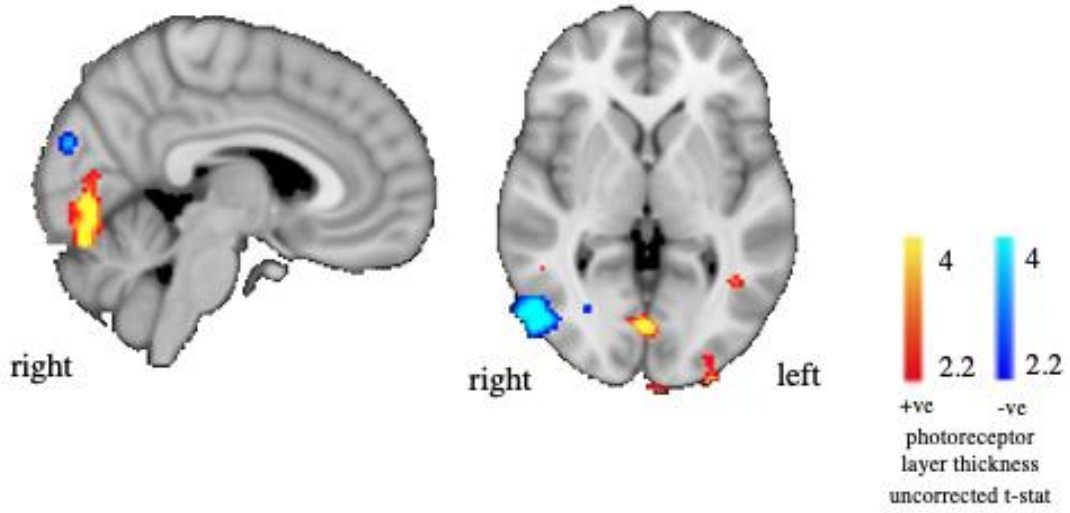


Figure 46: Regions of decreased grey matter density correlated with increased (red – yellow) and decreased (dark – light blue) outer retinal layer thickness (μm) in the central 0-3° of the retina, with a significance threshold of p = 0.035, uncorrected for multiple comparisons, overlaid on the MNI152 standard brain.

The second vision loss regressor was retinal sensitivity, calculated by the overall retinal sensitivity measured from microperimetry (dB). There were no significant differences in grey matter volume when correlated with retinal sensitivity ($p < 0.05$) using VBM. When uncorrected for multiple comparisons, decreased retinal sensitivity correlated with decreased grey matter density along the calcarine ($p = 0.035$) (red - yellow in figure 47).

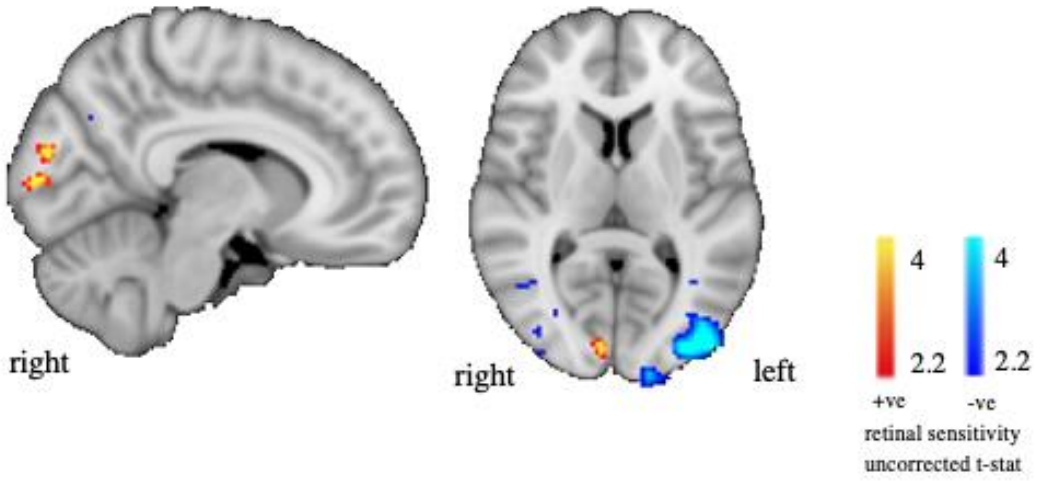


Figure 47: Regions of decreased grey matter density correlated with increased (red – yellow) and decreased (dark – light blue) outer retinal layer thickness (μm) *in the central 0-3° of the retina, with a significance threshold of p = 0.035, uncorrected for multiple comparisons, overlaid on the MNI152 standard brain.*

4.4.4 Cortical thickness is reduced within V1 in STGD1

Participants with STGD1 had thinner grey matter in V1 than control participants, indicated by a significant effect of group in a 2-way ANOVA ($F(1, 288) = 8.373$, $p = 0.004$) (figure 48). Cortical thickness changes across eccentricity in V1, indicated by a significant effect of position ($F(8, 288) = 6.295$, $p < 0.001$) (figure 48). However, there is no relationship between V1 eccentricity and group, indicated by a non-significant interaction between them ($F(8, 288) = 0.33$, $p = 0.954$), therefore there is not a significant difference of cortical thinning between eccentric positions in STGD1 as the hypothesis predicted.

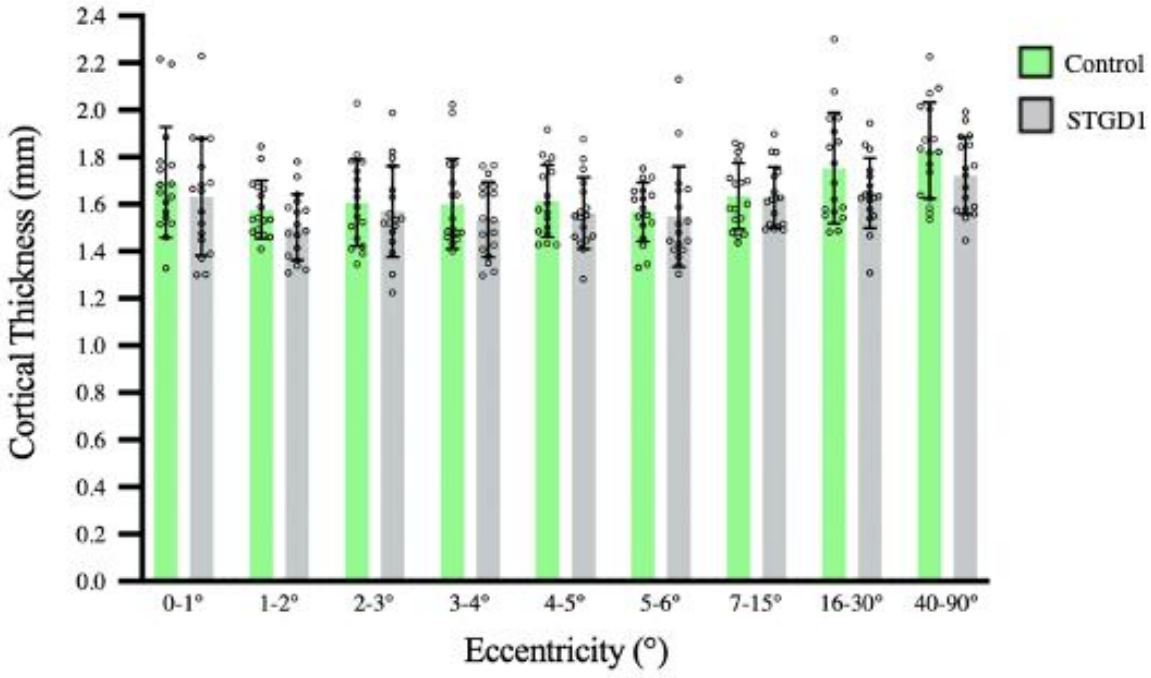


Figure 48: Primary visual cortex (V1) (left and right hemispheres averaged) cortical thickness (mm) values between controls with healthy vision (green) and STGD1 (grey) across the represented

eccentric positions (°) of the visual field. Individual data points are shown with circles (black) and error bars show standard deviation. All eccentricity comparisons of cortical thickness between STGD1 and controls were non-significant (p > 0.05).

4.4.5 Cortical thickness does not correlate with outer retinal layer thickness

As the disease severity varies in the STGD1 group, the cortical thickness was correlated with two types of vision loss regressors. The first was retinal structure, calculated as the overall thickness of the outer retinal layer (μm) (0 - 8°) from OCT. To investigate the effect of vision loss on cortical thickness a t-test was conducted for each eccentricity of the represented visual field with the outer retinal layer and cortical thickness in V1. The amount of thickness at the with outer retinal layer was not significantly correlated with cortical thickness in 0 - 2 ° (r (16) =- 0.01, p = 0.995), 2 - 4° (r (16) = -0.01, p = 0.997), 4 - 6° (r (16) = 0.25, p = 0.341) of the represented visual field (figure 49).

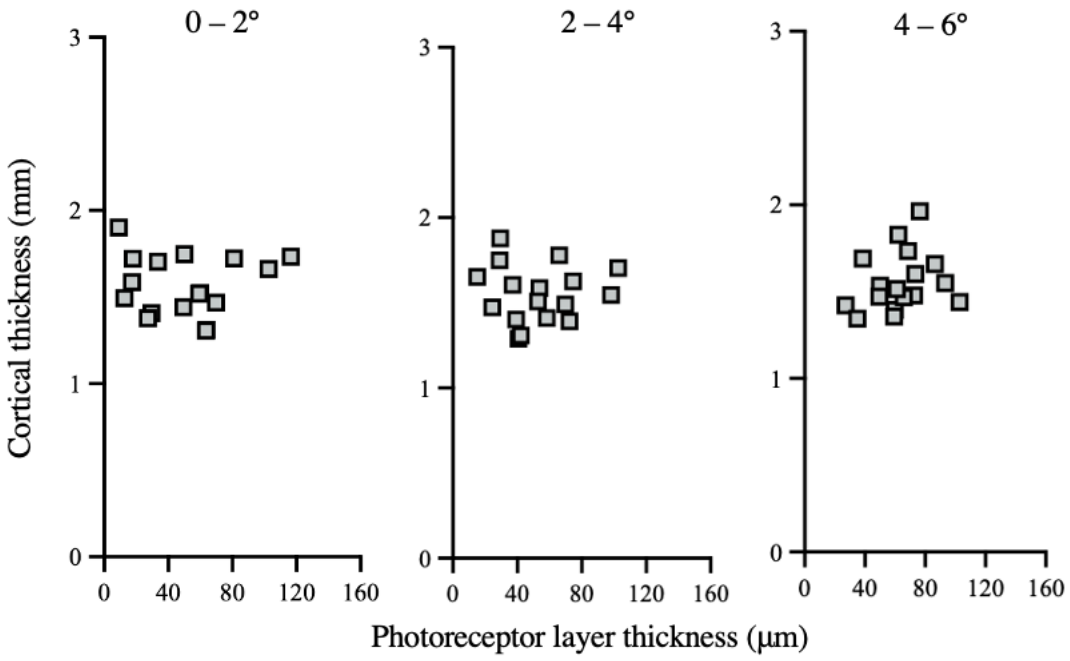


*Figure 49: Cortical thickness (mm) from 0 - 6° of the represented visual field in V1 correlated with the structural measure of vision loss, the outer retinal layer thickness (*μm*) averaged over the 0 - 8° of the retina. Individual data points from STGD1 patients (grey squares).*

A whole brain analysis of cortical thickness correlated with outer retinal layer thickness (µm) showed a significant cluster ($p < 0.05$) in the left hemisphere. This cluster is along the inferior visual cortex and shows where decreased cortical thickness correlates with decreased retinal thickness (figure 50).



Figure 50: Freesurfer whole-brain vertex-wise analysis of clusters showing significant cortical thickening with increased outer retinal layer thickness (µm), overlaid on the fsaverage brain. Statistical map displaying increased cortical thickness correlating with a thicker outer retinal layer (µm) (yellow - red) (demeaned) with the significance threshold set at $p < 0.05$. Colour bar shows logarithmic scale of p values (- log^{10}).

4.4.6 Cortical thickness does not correlate with retinal sensitivity

The cortical thickness analysis was repeated with the second measure of vision loss. Retinal function, calculated by the overall retinal sensitivity (dB) measured from microperimetry. To investigate the effect of vision loss on cortical thickness a t-test was conducted for each eccentricity of the represented visual field in the retinal sensitivity and cortical thickness in V1. The retinal sensitivity (dB) was not significantly correlated with cortical thickness in 1 - 3 ° ($r(16) = -0.12$, $p = 0.642$), 3 - 5° ($r(16) = -0.136$, $p = 0.601$), 5 - 9° ($r(16) = 0.11$, $p = 0.669$) of the represented visual field (figure 51).

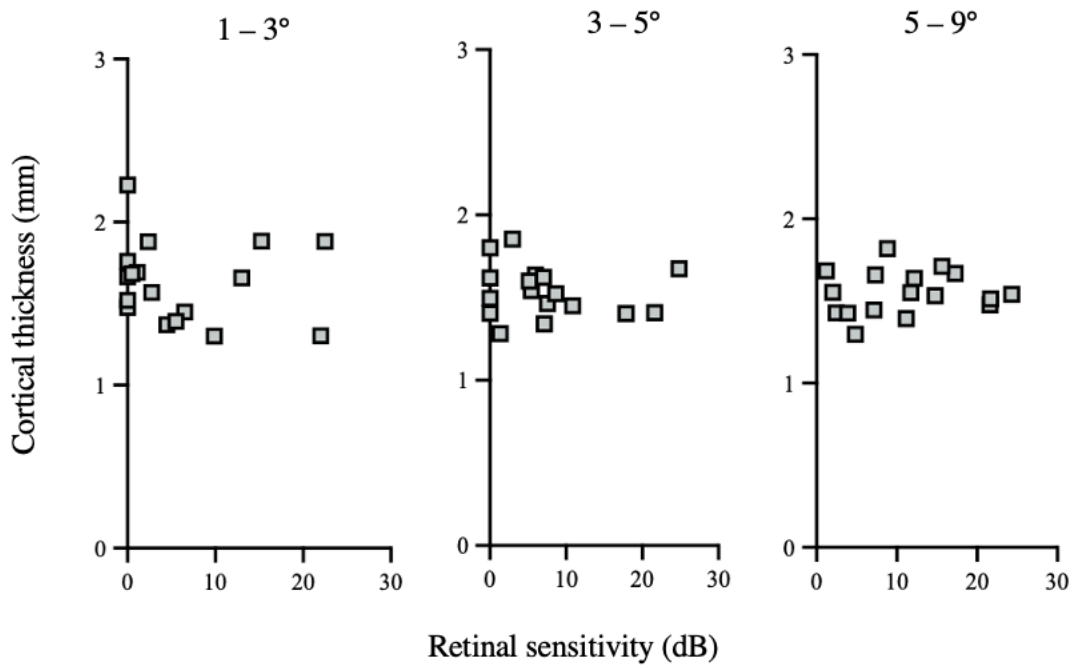


Figure 51: Cortical thickness (mm) from 0 - 9° of the represented visual field in V1 correlated with the functional measure of vision loss, retinal sensitivity (dB) averaged over 0 - 9°. Individual data points from STGD1 patients (grey squares).

Whole brain analysis of cortical thickness shows no specific region of change along the calcarine even when correlated with functional vision loss. Cluster-wise correction was applied but no clusters passed the significance threshold of $p < 0.05$, despite the observation of significant photoreceptor loss in the central retinae of patients with STGD1.

4.5 Discussion

4.5.1 STGD1 have a thinner retina than controls

To summarise, there was an extreme reduction in the outer retinal layer thickness in STGD1 compared to controls and this difference was the most severe in the central retinae. Given the toxic build-up of lipofuscin with secondary photoreceptor loss in STGD1 disease, it is unsurprising that STGD1 patients had thinner outer retinal layers, particularly in the central retina, as the damage is generally localised to the macula in STGD.

The inner retinal layers consist of the ganglion, bipolar layers (nerve fibre layers) and the nuclear layers. There was an increase in thickness in the central 2° of the inner retinae in STGD1, but a significant reduction in thickness elsewhere (2 - 8°). The thinning in the STGD1 inner retina may be due to the knock-on effect of lack of input from the photoreceptor layers. The central inner retinal layer was thicker in STGD1 and this is presumed to be due to inflammation from the build-up of lipofuscin (Reich et al., 2021), however OCT is unable to distinguish between loss in the inner retinal layer and inflammation.

4.5.2 Grey matter density does not change in STGD1

Even in a relatively large cohort of patients with STGD1 leading to significant visual loss, no difference in grey matter density was detected. If there is a difference in the grey matter density between STGD1 and controls, then an apparent difference in cortical structure is subtle. These results do not support those that found reductions in grey matter volume in patients with central vision loss from STGD1 (Olivo et al., 2015) and macular degeneration (Plank et al., 2011). Differences in VBM measures do not distinguish between increased gyrification, misregistration of images and cortical structure differences in the grey matter, this may be why the results in the STGD1 cohort did not replicate previous research.

4.5.3 Cortical thickness decreases within V1 in STGD1

Cortical thickness was used as a more sensitive method to measure changes in cortical structure between STGD1 and controls. V1 is significantly thinner in STGD1 compared to sighted controls, suggesting the loss of input from degeneration at the retina causes neuronal loss within V1. These findings replicate those found in cohorts with macular degeneration, where thinning is found within V1 after vision loss (Burge et al., 2016; Hanson et al., 2019). However, cortical thickness was not significantly different within the projected region of vision loss within V1 (posterior V1), as has been previously found in cohorts with macular degeneration (Burge et al., 2016; Hanson et al., 2019). Cortical thickness was correlated with disease severity as a greater amount of loss should have a larger impact on cortical structure. Cortical thickness was found to correlate with outer retinal layer

thickness within the inferior visual cortex. This replicates the findings in cohorts with glaucoma where retinal loss correlates with reductions in cortical structure (Yu et al., 2013) (Wang et al., 2020). These correlations were not significant when compared between eccentricities of the visual field within V1. The differences in cortical structure are subtle and may have been affected by including a range of disease severities, where those with milder loss may have diluted the cortical changes from patients with more severe loss. These results do not reflect the retinal results, where the outer retinal layer was thinner at the central retinae

4.5.4 Limitations and future directions

The STGD1 patients had a range of disease severities which may have affected the ability to detect cortical changes. Those with milder loss and therefore less cortical degeneration, may have diluted the cortical changes from patients with more severe loss. This may explain why reductions in the region of projected loss in V1 have been found in cohorts with macular degeneration (Burge et al., 2016; Hanson et al., 2019) but were not found in this study. The patients in the Burge et al (2016) and Hanson et al (2019) had larger scotoma sizes and longer disease durations than the STGD1 cohort investigated in this thesis. Future research could investigate the rate of the cortical thinning by comparing disease duration with grey matter thickness.

A limitation of using 3T MRI is the low spatial resolution of $1mm^3$, which does not allow differentiation between the different layers of the grey matter. Vision loss may cause degeneration to a specific layer of V1 which is unable to be detected using the spatial resolution in this study. Histology and microscopy have a much higher resolution (µm) than MRI (mm). The 'BigBrain' atlas has bridged between histology and neuroimaging, by creating a 3D histological atlas of 20µm resolution (Wagstyl et al., 2020). If this atlas could be replicated on a large group of participants, then a high-resolution laminar map for V1 in standard space could be created. The patients and controls then could be registered to this standard space of laminar ROIs to give a measure of any changes in the different laminar layers between groups. Another alternative is to image at a higher field strength

to increase the spatial resolution, such as at 7T MRI which can enable imaging of the individual grey matter layers.

4.5.5 Chapter Conclusion

To summarise, the work presented in this chapter shows that STGD1 causes degeneration in the retina, with a thinning of the outer retinal layer, predominantly affecting the central retina. STGD1 have cortical thinning within V1, however this difference is subtle and not found to differ across eccentricities of the projected visual field. These results indicate that degeneration in the retina causing a loss of visual input to V1, may cause neuronal degeneration which is reflected by cortical thinning within V1. Future research should investigate the rate of this thinning, and with higher resolution imaging it may be possible to identify subtle grey matter changes.

5 Functional connectivity

Functional Connectivity Changes in the Visual System between Stargardt patients and Controls

5.1 Abstract

Resting state fMRI provides a measure of functional connectivity strength between cortical regions. The effect a loss of visual input has on cortical connectivity in patients with STGD1 has yet to be comprehensively understood. In this chapter I investigated how connectivity strength changes within the visual cortex and between the visual cortex and the rest of the brain in STGD1 compared to controls. As the STGD1 patient cohort had a range of disease severities these were expected to have varying impacts on cortical function.

Using dual regression, I found that functional connectivity was reduced within the medial visual resting state network in STGD1 compared to controls. This region of decreased connectivity was localised within the lateral occipital complex which is responsible for object recognition and therefore requires high acuity vision. Using a seed-based analysis I found that functional connectivity was reduced from posterior regions of V1 to the medial frontal cortex, but no different in anterior regions of V1 reflecting the location of vision loss. The medial frontal cortex is involved in top-down modulation of visual attention to V1. Disease severity was found to correlate with functional connectivity between the posterior V1 and to areas involved in the relaying of visual information (LGN) and visual motion perception (hMT+).

These results show that a loss of high acuity vision in STGD1 causes a reduction in functional connectivity to areas involved in object recognition and visual attention. Therefore, this should be considered in conjunction with therapies that aim to restore function at the retina, as the reduced connectivity to the visual cortex may limit the ability of the brain to process the restored input.

5. 2 Introduction

As mentioned in the introductory chapter, a focal region of loss at the retina can be functionally mapped in the visual cortex, and this region is referred to as the LPZ (Baseler et al., 2011; Ritter et al., 2019; Silson et al., 2018). Due to the topographic representation of the visual field throughout the visual system, photoreceptor degeneration starting in the central retina, results in a loss of the central visual field that can be mapped to the posterior section of V1 (Baseler et al., 2011).

There is inconsistency in the literature as to whether a loss of visual input in adulthood causes a decrease or increase in functional connectivity measured by rs-fMRI. In patient groups with peripheral loss from glaucoma, reduced functional connectivity was found between V1 and V2 (Li et al., 2017). They found increased functional connectivity from V1 to the right inferior parietal lobule and basal ganglia (Li et al., 2017). Whereas decreased connectivity has been found from V1 to the fusiform gyrus, bilateral cuneus, left pre-cuneus in a cohort with glaucoma (Wu et al., 2020). These results suggest that functional connectivity reduces between regions within the visual cortex, whilst connectivity changes between the visual cortex and regions in the remaining brain is unclear. In a patient group with RP, who also have peripheral loss, decreased connectivity has been found between the calcarine and the post central gyrus and SPL (Huang et al., 2019). These results were also found to correlate with disease severity (Huang et al., 2019), where a greater loss at the retina causes a larger decrease in fucntional connecitivty.

There is limited research investigating how a loss of central vision from retinal disease affects functional connectivity in the cortex. As mentioned in the introductory chapter, there is one study investigating functional connectivity in a patient cohort with STGD1 (12 STGD1, 14 controls) (Sabbah et al., 2017). They found increased connectivity from the EVC to the cuneus, intraparietal sulcus and decreased connectivity to the central anterior cingulate cortex and the middle temporal gyri, but these results did not correlate with disease severity (Sabbah et al., 2017). These variable results may have been due to the ROIs used as they contained regions outside of V1 and were fairly small in size. Overall, the research investigating functional connectivity changes after a loss of visual

input are not consistent. Both increases and decreases in functional connectivity have been found within the visual cortex and between visual regions and the remaining cortex after vision loss. Therefore, the work presented in this chapter aims to clear up these inconsistencies by using a larger sample size and an ROI definition of posterior and anterior V1. Whether functional connectivity changes after vision loss from IRDs is important to clarify as treatments that aim to restore vision at the level of the retina may be limited by the cortex. If functional connectivity in the visual cortex has decreased and then it may not be able to properly process the restored input. Alternatively, it may serve as a biomarker for indicating patients most likely to benefit from retinal treatment.

5.2.1 Rationale

Degeneration at the retina creating a focal loss within the visual field causes a reduced input into the visual system. This loss of input should reflect a reduction in cortical function in the regions that process that input. As V1 contains a topographic organisation of the visual field, focal loss at the central retina will project to the LPZ at the posterior V1, which represents the central part of the visual field. In this chapter, rs-fMRI is used to investigate if there are differences between STGD1 and controls in functional connectivity both within the RSNs and between visual ROIs connectivity with the rest of the cortex.

Hypothesis 1: Functional connectivity will be decreased within the visual RSNs in STGD1 compared to controls. These regions of decreased connectivity will be particularly localised in the ventral visual stream (FFA, LOC, hV4) as they are involved in processing high acuity vision, which is affected in STGD1.

Hypothesis 2: The LGN will show decreased connectivity to the remaining cortex in STGD1 compared to controls.

Hypothesis 3: Functional connectivity will be reduced from posterior regions of V1 to the remaining cortex, but no different in anterior regions of V1 reflecting the location of vision loss.

Hypothesis 4: Functional connectivity strength between regions in the visual cortex will vary with disease severity in STGD1, where a greater loss at the retina will correlate with decreased functional connectivity.

5.3 Methods

5.3.1 Participants

The work in this chapter includes 16 participants with STGD1 (8 females, 8 males, mean age 36.8 ± 16 SD) and 16 comparison controls with healthy eyes and normal vision (7 females, 9 males, mean age 39.7 ± 14.7 SD). 17 controls and 17 STGD1 took part in the MRI scan session, however one STGD1 patient left the scan session early and therefore resting state data was not acquired. Therefore, the matching control was subsequently removed from the analysis.

5.3.2 Functional Magnetic Resonance Imaging acquisition

One run of fMRI which lasted 10 minutes was acquired with a gradient echo planar imaging (EPI) sequence with the following parameters, TR = 1355ms, TE = 32.4ms, 72 interleaved slices, orientated axially, flip angle = 70°, MB4, resolution = 2mm^3. In order to compensate for field inhomogeneity a B_0 field map was acquired TR= 482 ms, TE_1= 4.92 ms, TE_2 = 7.38 ms, resolution = 2 mm^3.

5.3.2.1 Stimulus presentation

A black screen was generated in MATLAB (v 8.3, Mathworks Inc., Natick, MA, USA) using Psychtoolbox (v3.0, https://psychtoolbox.org) and displayed on a LCD BOLDscreen (Cambridge Research Systems) at the rear of the scanner bore (Brainard, 1997) (Pelli, 1997). The BOLDscreen measured 518 × 324 mm with a resolution of 1920 × 1200. The participant viewed the display through correction glasses (if applicable) and a mirror mounted on the head coil.

5.3.2.2 Eye Movements

The participants were instructed to keep their eyes open and maintain a central gaze on the screen. This paradigm was chosen because functional connectivity within the primary visual network is most reliable with eyes open, compared to eyes closed (Patriat et al., 2013). Eye tracking was used to monitor the participants eyes throughout the scan to ensure they stayed awake. Eye tracking data was recorded using an EyeLink 1000 eye tracker (SR Research Ltd) but watched throughout the scan.

5.3.3 Rs-fMRI Analysis

5.3.3.1 Pre-processing

The individual rs-fMRI scans were pre-processed using the Probabilistic Independent Component Analysis (Beckmann and Smith, 2004) implemented in MELODIC (Multivariate Exploratory Linear Decomposition into Independent Components) version 3.15, part of FSL (FMRIB Software Library V6 (Analysis Group, FMRIB, Oxford, UK; http://www.fmrib.ox.ac.uk/fsl) (Woolrich et al., 2009). This involved motion correction using MCFLIRT, brain extraction using BET, FWHM highpass temporal filtering at 100s, voxel-wise demeaning and normalisation of the voxel-wise variance (Jenkinson et al., 2002) (Smith, 2002). Each individual rs-fMRI scan was spatially corrected for magnetic field inhomogeneities estimate by the B0 fieldmap and then registered to the high resolution T1w structural scan using FLIRT (Jenkinson et al., 2002; Jenkinson and Smith, 2001).

The pre-processed individual rs-fMRI data were whitened and projected into a 415-dimensional subspace using probabilistic PCA (Principal Component Analysis). The Laplace approximation to the Bayesian evidence of the model order was used to estimate the number of dimensions (Beckmann and Smith, 2004) (Minka, 2001). The whitened data were then decomposed into sets of vectors by optimising for non-Gaussian spatial source distributions using a fixed-point iteration technique (Hyvarinen, 1999). These sets of vectors described the signal variation across the spatial domain (maps), temporal domain (time-courses) and the subject domain. The estimated component maps were divided by the standard deviation of the residual noise, and then thresholded using a mixture model fitted to the histogram of intensity values (Beckmann and Smith, 2004).

ICA-denoising:

Identification of the ICA components between signal and noise was conducted using FIX (version 1.06) (Salimi-Khorshidi et al., 2014) (Griffanti et al., 2014). Noise components were classified into participant motion, cardiac artefacts, cerebrospinal fluid pulsation, scanner artefacts and low frequency drifts. The FIX classifier used the *WhII_MB6.RData* training dataset derived from the Whitehall Imaging Study (Griffanti et al., 2014). This training classifier was chosen as it closely resembles the acquisition parameters and pre-processing for the rs-fMRI data (MB6, resolution = $2mm^3$, session = 10 minutes, no spatial smoothing, 100s FWHM highpass temporal filtering). The classified components were checked manually with a conservative approach using the ICA noise component guidelines (Griffanti et al., 2017). Components were reclassified as signal unless they were clearly artefactual, to ensure components containing signal were not removed from the data. FIX was then re-applied to remove the noise components to create cleaned filtered functional data. The data was then spatially smoothed using a gaussian kernel of 4mm (FWHM) and registered to standard space using FNIRT (Jenkinson et al., 2002; Jenkinson and Smith, 2001). The individual rs-fMRI data from this process was subsequently input into the dual regression group analysis and the ROI connectivity analysis.

5.3.3.2 Dual Regression

The individual rs-fMRI data was input to group level MELODIC (version 3.15), part of FSL, where Probabilistic Independent Component Analysis was conducted at the group level. The data was projected into a 40-dimensional subspace using Principal Component Analysis. 40 dimensions were specified as this number of dimensions provided the highest spatial cross correlation of the RSNs of interest with previously described networks (Smith et al., 2009). Dual regression was used to generate subject-specific versions of the spatial maps and associated timeseries by regressing the group average set of spatial maps (Nickerson et al., 2017). The group-average is first regressed using multiple regression to create spatial regressors for each subject and these are concatenated into a subject specific 4D space-time dataset. This outputs a timeseries for each group-level spatial map per

subject. The timeseries are then regressed in multiple regression as temporal regressors, resulting in subject specific spatial maps of each RSN network. This was conducted by masking the subject-specific spatial maps within the group-mean RSN maps of interest and then using *randomise* permutation testing (5000 permutations) (FSL). Unmasked subject-specific spatial maps were also calculated to investigate if differences in connectivity occur outside the group-mean RSN maps. A paired t-test was used to determine regions of increased functional connectivity strength within the RSN's of interest between groups (controls vs STGD1). The three RSNs of interest within the visual cortex investigated are shown in figure 52. The resulting images were cluster-thresholded at $z > 3.1$ with a significance threshold of $p = 0.05$ (Worsley, 2001).

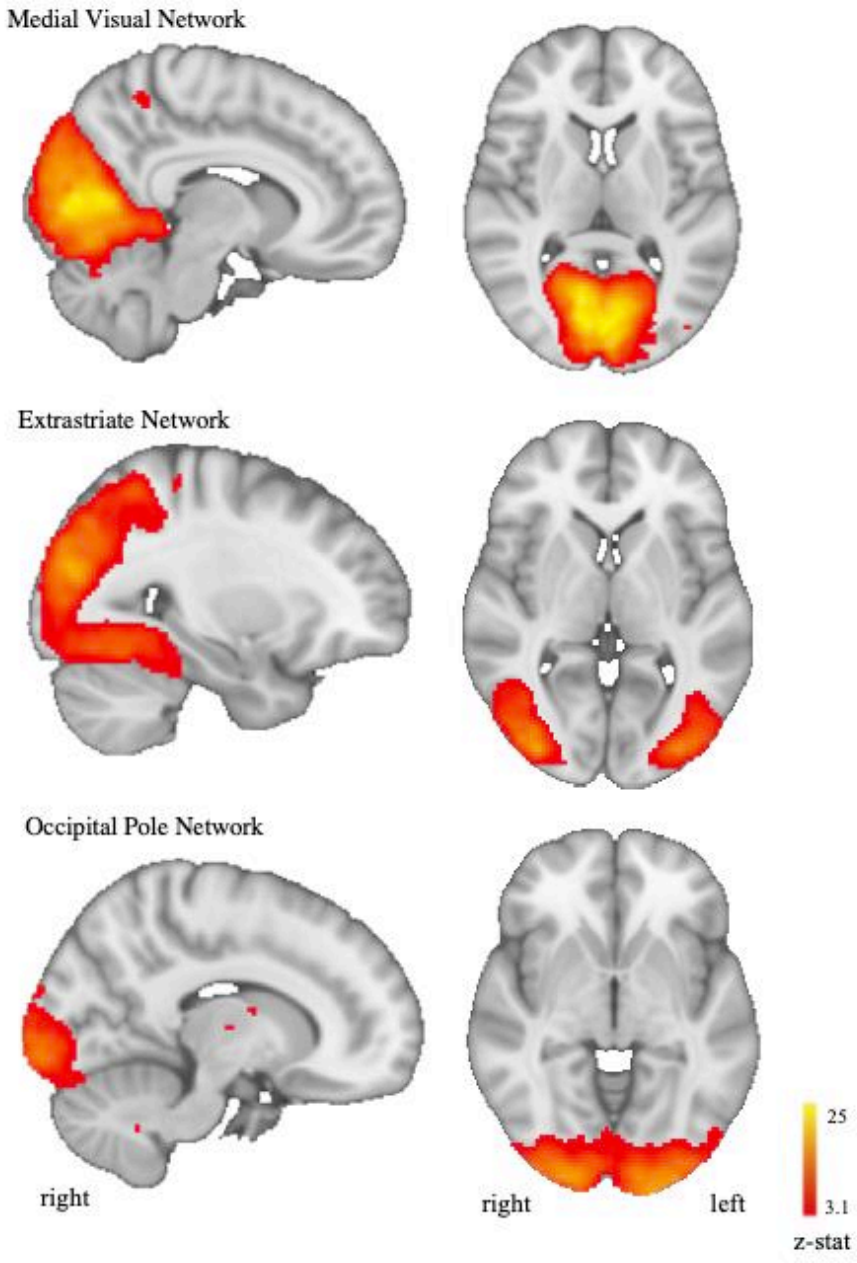


Figure 52: The three visual RSNs used in the dual regression analysis, overlaid on the MNI standard brain. Colour bar shows the cluster threshold of z > 3.1 at p = 0.05 (red - yellow).

5.3.3.3 Correlation with disease severity

To determine whether functional connectivity within the RSNs of interest related to disease severity, a correlation analysis was applied across all participants. Disease severity was calculated in two ways, firstly as a measure of functional loss using retinal sensitivity from microperimetry in chapter 3. Secondly, as a measure of structural loss using photoreceptor layer thickness calculated using OCT in

chapter 4. These values were demeaned and then input as regressors into a correlation analysis for the RSNs of interest and the seed-based connectivity analysis.

5.3.3.4 ROI connectivity to the whole brain

Seed-based connectivity was used to investigate time series correlation between ROIs in the visual system compared to the rest of the cortex. Time series data were extracted from the smoothed ICA-cleaned filtered functional data for each ROI per hemisphere using *fslmeants*. The mean timeseries for a specific ROI was then input as a regressor into individual-level FEAT analyses to find areas of correlated cortical activity. The individual maps of correlated activity were then input into a group-level analysis using FLAME (FMRIB's Local Analysis of Mixed Effects) (Beckmann et al., 2003; Woolrich et al., 2004) (Woolrich, 2008). A paired t-test was used to determine whether there was increased functional connectivity between the seed region and the rest of the cortex between groups (controls and STGD1). The resulting images were cluster-thresholded at $z > 3.1$ with a significance threshold of $p = 0.05$ (Worsley, 2001). This analysis was repeated for each ROI per hemisphere.

ROI localisation:

The bilateral LGN was defined from the Juelich atlas (Amunts et al., 2005) (Eickhoff et al., 2005) (Eickhoff et al., 2006) (orange in figure 53) which was generated using histological data from 10 individuals. A 20% threshold was applied to the bilateral LGN masks. Therefore, only voxels that contained the histological LGN from at least eight of the individuals were included, to give a more stringent definition of the ROI. The bilateral V4 (pink in figure 53) and hMT+ (yellow in figure 53) were defined in the same way as the LGN ROIs. V1 was defined from the standard Benson retinotopy atlas (Benson et al., 2014; Benson et al., 2012) generated in brainlife.io (Avesani et al., 2019). V1 was divided into posterior (0 - 6° of the visual field) (light green and blue in figure 53) and anterior sub-sections (6 - 90° of the visual field) (dark green and blue in figure 53). As the STGD1 groups vision loss was predominantly constrained to the macula region, the posterior sub-division was chosen to encapsulate a greater proportion of loss compared to the anterior V1.

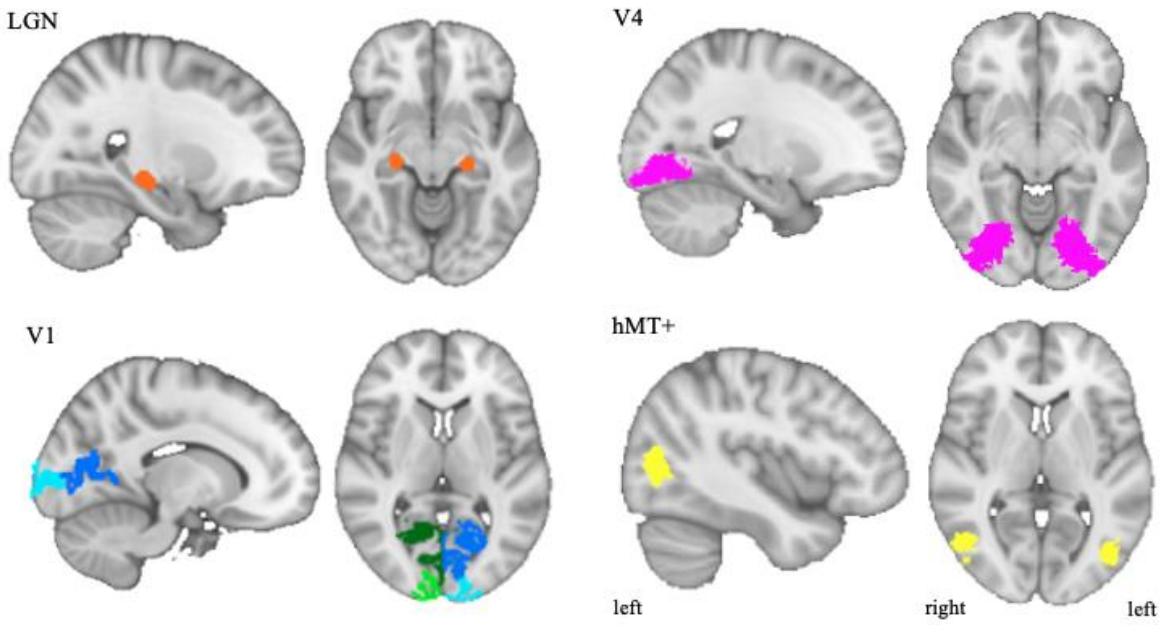


Figure 53: The ROIS used as seed regions for the connectivity analysis overlaid over the standard brain (MNI152). The bilateral LGN (orange), V4 (pink) and hMT+ (yellow) were defined by the Juelich histological atlas. The bilateral ROIs in V1 that respond to 0 - 6° of the visual field (light green = right posterior V1, light blue = left anterior V1) and 6 – 90° (dark green = right posterior V1, dark blue = left anterior V1) were defined by the functional retinotopy Benson atlas.

5.3.3.5 ROI connectivity within the visual cortex

To determine if the connectivity strength between regions of the visual cortex varied, the connectivity between the visual ROIs (LGN, V4 hMT+) and the anterior and posterior V1 were compared. The mean BOLD connectivity was calculated within specific ROIs (unilateral LGN, V4 hMT+) from the anterior and posterior V1 whole brain rs-functional connectivity maps at a subject-specific level (Sohn et al., 2015). Within each weighted ROI mask, *featquery* (FSL (Smith et al., 2004)) was used to calculate the mean parameter estimates. These are the estimates of how strongly the mean timeseries from the ROI fits the timeseries in the V1 connectivity maps at each voxel, they were then compared between groups for each unilateral ROI.

Correlation with disease severity

To determine whether changes in BOLD activity in any areas related to the amount of vision loss, a correlation analysis was carried out across all participants (from both the STGD1 and control groups). This higher-level analysis correlated BOLD signal with the amount of vision loss. Both structural and functional loss (from chapters 3 and 4) were input as a regressor, for all participants.

Statistical analysis for seed-based connectivity

Statistical analyses were performed using GraphPad Prism (version 9.0). Due to the range of disease severities in the STGD1 patient cohort, a larger amount of vision loss was expected to correlate with a decrease in functional connectivity. Therefore, Pearson's R was used to investigate if there were significant correlations between the extent of vision loss and the ROIs functional connectivity.

For all analyses described in this section, outlier detection was calculated using the robust regression and outlier removal (ROUT) method in GraphPad Prism (version 9.0) (Benjamini and Hochberg, 1995) (Benjamini and Yekutieli, 2001). This method is based on the false discovery rate (FDR) and considers both multiple comparisons and the distribution of p-values within the data (Motulsky and Brown, 2006). The FDR is chosen by the Q percentage which decides the distance from the predicted model that a point should be considered an outlier. Q = 1% was chosen for the results presented in this section, therefore > 1% of the statistically significant findings were false positives. Outliers are shown in the graphs shaded in orange but were removed from the subsequent statistical analyses.

5.5 Results

5.5.1 Functional connectivity decreases within the visual cortex in STGD1

The three visual RSNs derived from the group ICA decomposition were analysed with dual regression to understand if functional connectivity within the networks differed between groups. The medial visual network covers much of the occipital lobe, including V1. Figure 54 shows the mean medial visual network connectivity for controls (A) and STGD1 (B). Controls showed increased connectivity compared to STGD1 within the medial visual network (unmasked) (figure 54C) located within the

right inferior lateral occipital complex (LOC) defined by the Glasser atlas (Glasser et al., 2016) (black outline in figure 54). The region of increased connectivity within LOC was located outside the medial visual RSN which suggests this region is differently affected between STGD1 and controls, as the mean RSN was created from the averaged rs-fMRI connectivity across all participants. Results are reported with a significance threshold of $p < 0.05$ and corrected for multiple comparisons with threshold free cluster enhancement (TFCE) (figure 54C). The LOC is located within the ventral stream and responsible for object processing, this requires high acuity vision which is affected in STGD1.

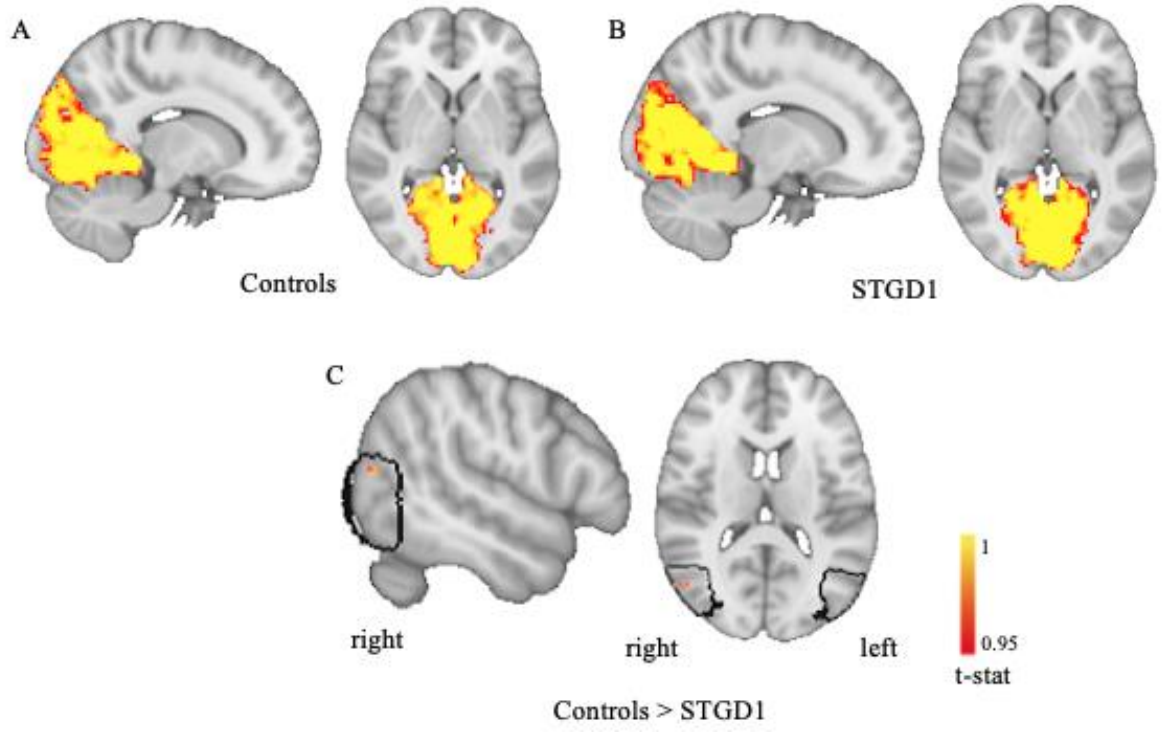


Figure 54: Mean connectivity within the medial visual network for controls (A) and STGD1 (B), overlaid on the MNI152 standard brain [137 71 80]. The region of increased functional connectivity in controls > STGD1 with a significance threshold of $p < 0.05$ (red - yellow), corrected for multiple comparisons with TFCE (C), localised within the inferior lateral occipital complex defined by the Glasser atlas (Glasser et al., 2016) (black outline).

The extrastriate network covers the extrastriate regions of the occipital lobe which visual areas localised in the ventral (V4, FFA, LOC) and dorsal streams (hMT+). Figure 55 shows the mean extrastriate network connectivity for controls (55A) and STGD1 (55B). Controls showed increased connectivity (figure 55C) within the extrastriate network and this was localised within the right inferior LOC defined by the Glasser atlas (Glasser et al., 2016) (black outline). These results were significant at p = 0.011 but were uncorrected for multiple comparisons.

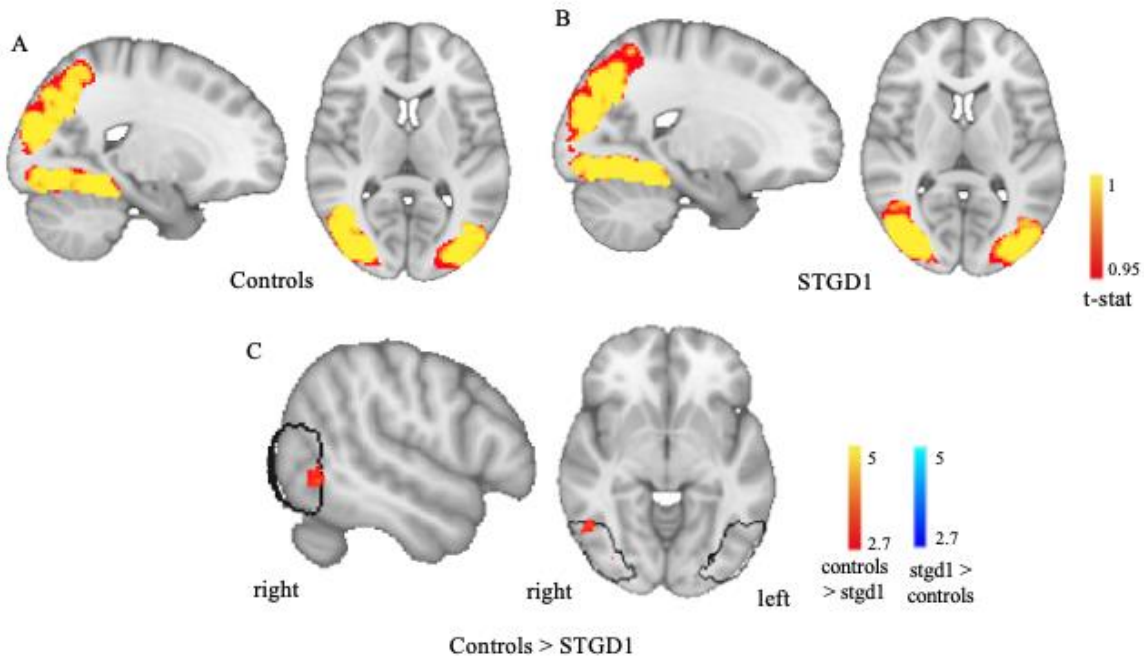


Figure 55: Mean connectivity within the extrastriate network for controls (A) and STGD1 (B), overlaid on the MNI152 standard brain [131, 65, 64]. Regions of increased functional connectivity in controls > STGD1 (red – yellow) a significance threshold of p = 0.011, uncorrected for multiple comparisons (C), localised within the inferior lateral occipital complex defined by the Glasser atlas (Glasser et al., 2016) (black outline).

The occipital pole visual network covers the posterior region of the occipital lobe, this includes the posterior V1 which processes the central representation of the visual field. Figure 56 shows the mean occipital pole network connectivity for controls (A) and STGD1 (B). Controls showed increased connectivity (figure 56 C) within the occipital pole visual network and this was localised within the

left inferior LOC defined by the Glasser atlas (Glasser et al., 2016) (black outline). These results were significant at p = 0.011 but were uncorrected for multiple comparisons.

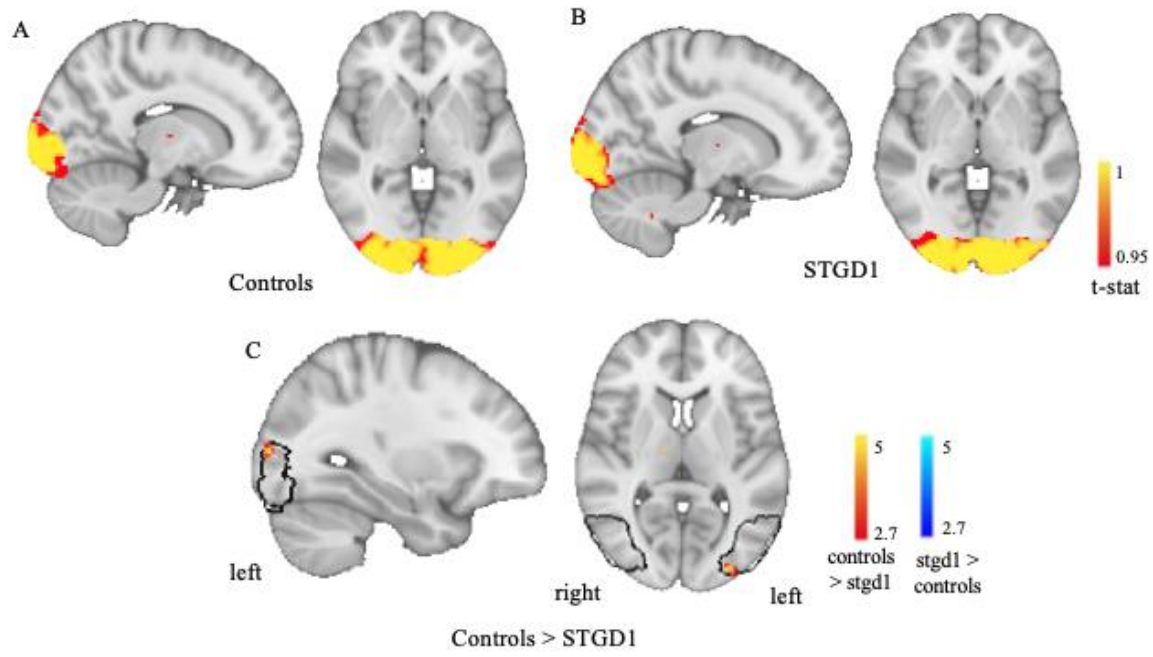


Figure 56: Mean connectivity within the occipital pole visual network for controls (A) and STGD1 (B), overlaid on the MNI152 standard brain [121, 39, 77]. Regions of increased functional connectivity in controls > STGD1 (red – yellow) with a significance threshold of p = 0.011, uncorrected for multiple comparisons (C), localised within the inferior lateral occipital complex defined by the Glasser atlas (Glasser et al., 2016) (black outline).

5.5.2 Functional connectivity within RSNs does not vary with disease severity

As the STGD1 patient cohort included a range of disease severities, these should have a varying impact on the functional connectivity within the visual RSNs. Retinal sensitivity (dB) provides a measure of functional loss at the retina. The mean retinal sensitivity for each participant (chapter 3) was input as a regressor into the dual regression analysis. When corrected for multiple comparisons and thresholded at $p < 0.05$ there was no significant effect of retinal sensitivity in the medial visual network and the occipital pole visual network. Photoreceptor layer thickness (μm) provides a measure of structural degeneration at the retina. The photoreceptor layer thickness from the central 0 – 3° of

the retinae (chapter 4) was input as a regressor for each participant into the dual regression analysis. When corrected for multiple comparisons and thresholded at $p < 0.05$ there was no significant effect of photoreceptor layer thickness in the medial visual network.

5.5.3 Functional connectivity from the LGN to the remaining cortex does not change in STGD1

The LGN receives visual information from the retina and relays this to the visual cortex. Therefore, a decrease in visual input should have a decrease in functional connectivity in the LGN. Figure 59 shows the mean correlated activity with the right LGN for controls (A) and STGD1 (B). Controls showed increased correlated connectivity particularly within them visual cortex for the left and right LGN (figure 59 C/D) significant at $p = 0.011$, but were uncorrected for multiple comparisons.

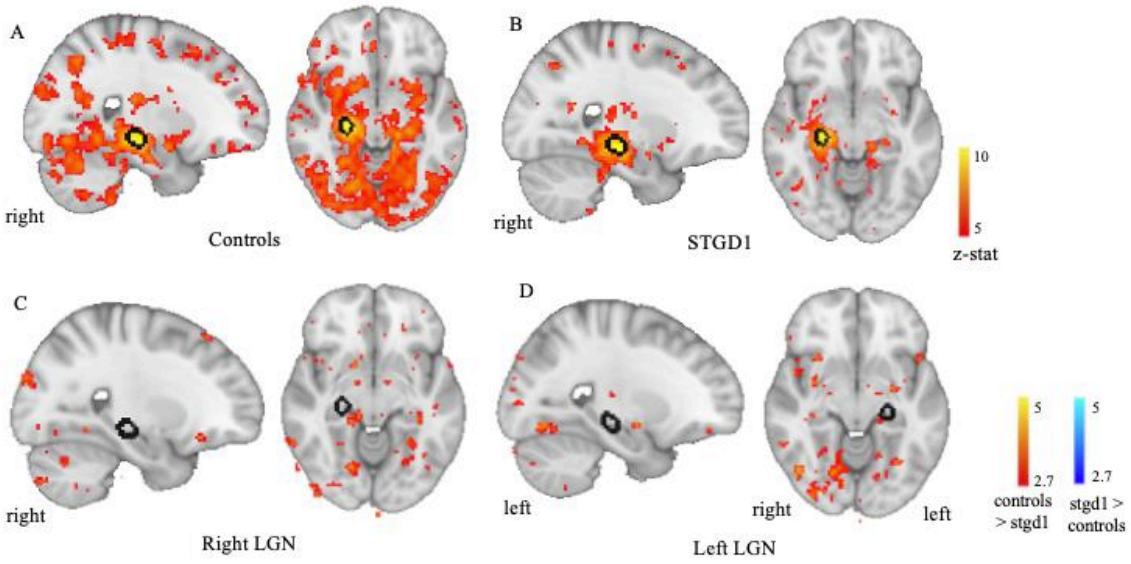


Figure 59: Mean correlated connectivity with the right LGN (black outline) for controls (A) and STGD1 (B) overlaid on the MNI152 standard brain [A – C: 64 103 63, D: 114 101 63]. Increased functional connectivity in controls > STGD1 (red-yellow) and STGD1 > controls (dark-light blue), with a significance threshold of p = 0.011, for the right (C) and left (D) LGN uncorrected for multiple comparisons.

5.5.4 Functional connectivity from V1 to the remaining cortex is reduced in STGD1

Due to the topographic organisation of V1, functional connectivity should be reduced to posterior V1, reflecting the location of vision loss in STGD1. In order to investigate this, V1 was split into central (0 - 6°) and peripheral (6 - 90°) representations of the visual field. Whole brain rs-functional connectivity maps for the individual V1 ROIs are shown for an example control and STGD1 in figure 60. The rs-functional connectivity maps were then calculated at the group level and are shown in figure 61. A larger amount of functional connectivity is shown in controls (A) compared to STGD1 (B) in the posterior V1 (0 – 6°) connectivity maps, whereas the connectivity is more similar between groups at the anterior V1 (6 – 90°). The posterior V1 is the location of projected loss in STGD1, and the group level maps suggest that a lack of input from the retina decreases the functional connectivity in the cortical region that processes that loss. In general, there is more connectivity in the anterior compared to the posterior V1 maps, but this is due to the anterior V1 ROI being larger than the posterior ROI.

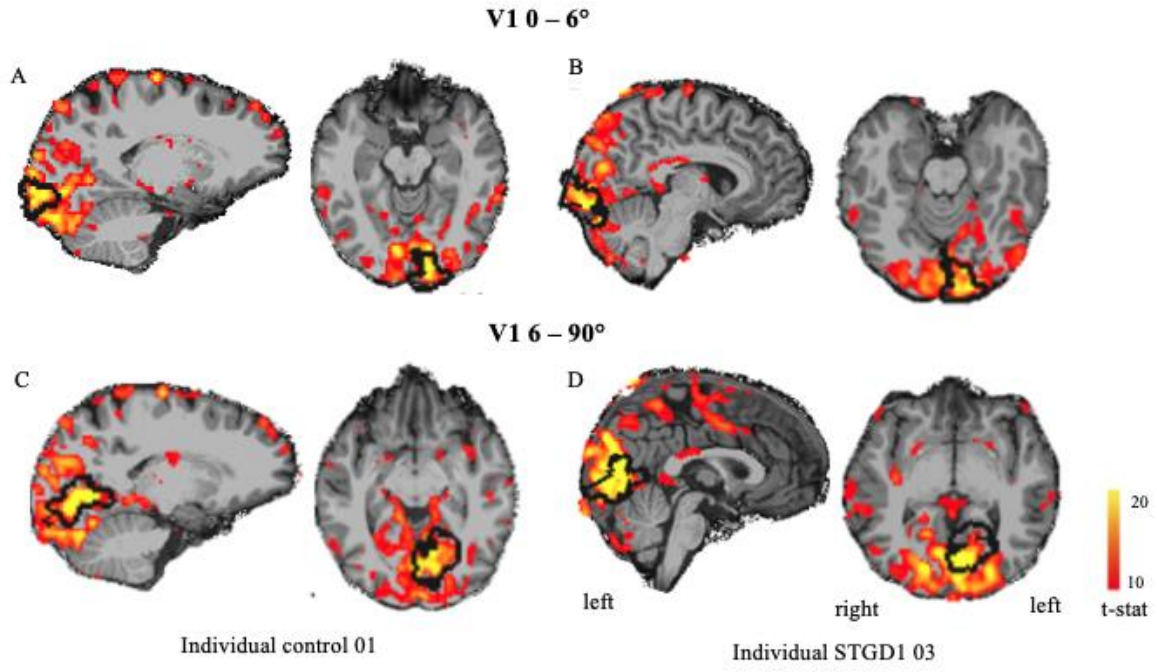


Figure 60: Mean correlated connectivity with the posterior (A/B) and anterior (C/D) V1 (black outline) from an example control (A/C) and STGD1 (B/D), overlaid on the individual T1w structural image. Colour bar shows t > 10 (red – yellow).

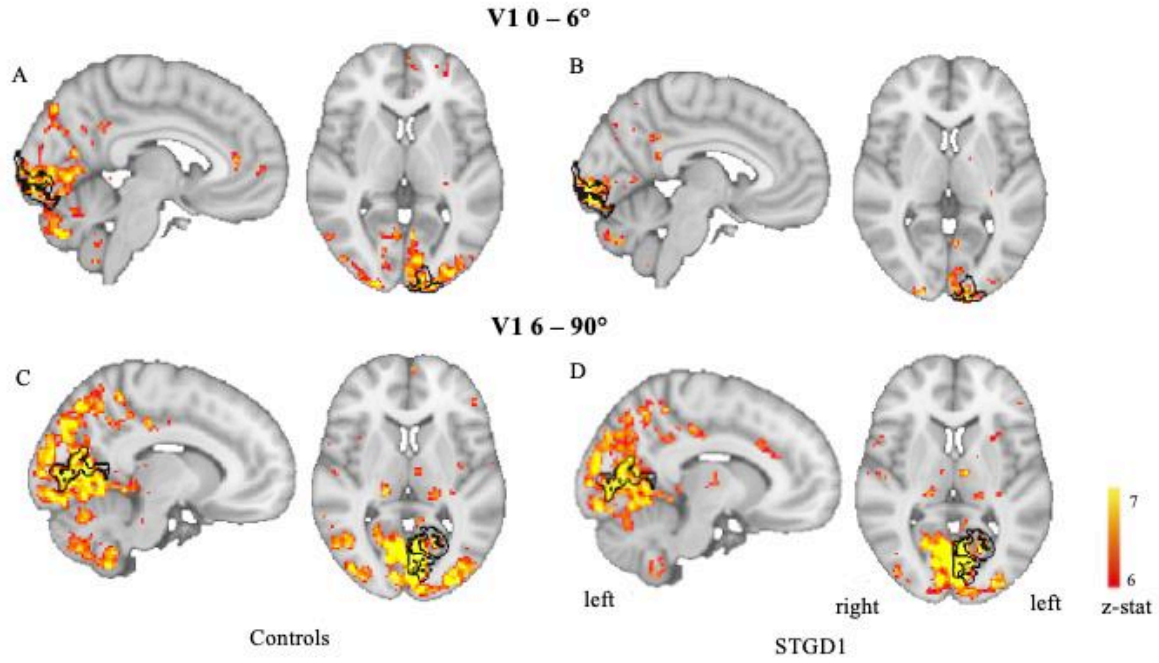


Figure 61: Mean correlated connectivity with the posterior (A/B) and anterior (C/D) V1 (black outline) from controls (A/C) and STGD1 (B/D) at the group level, overlaid on the MNI152 standard brain. Colour bar shows z > 6 (red – yellow).

Whole brain rs-connectivity comparisons between groups find a statistically significant correlation between the right posterior V1 and regions in the frontal cortex (figure 62 A) for controls > STGD1. Results are reported with a significance threshold of $p < 0.05$ and corrected for multiple comparisons with threshold free cluster enhancement (TFCE). These regions of increased connectivity in the frontal cortex were also found for the left posterior V1 (figure 62 B) ($p = 0.004$) however they were uncorrected for multiple comparisons. The region of correlated activity with the left posterior V1, was also within the medial frontal cortex, however it was below the threshold for significance. No frontal regions of correlated activity were found with the posterior V1 ROIs, even when uncorrected for multiple comparisons (figure 62 C/D).

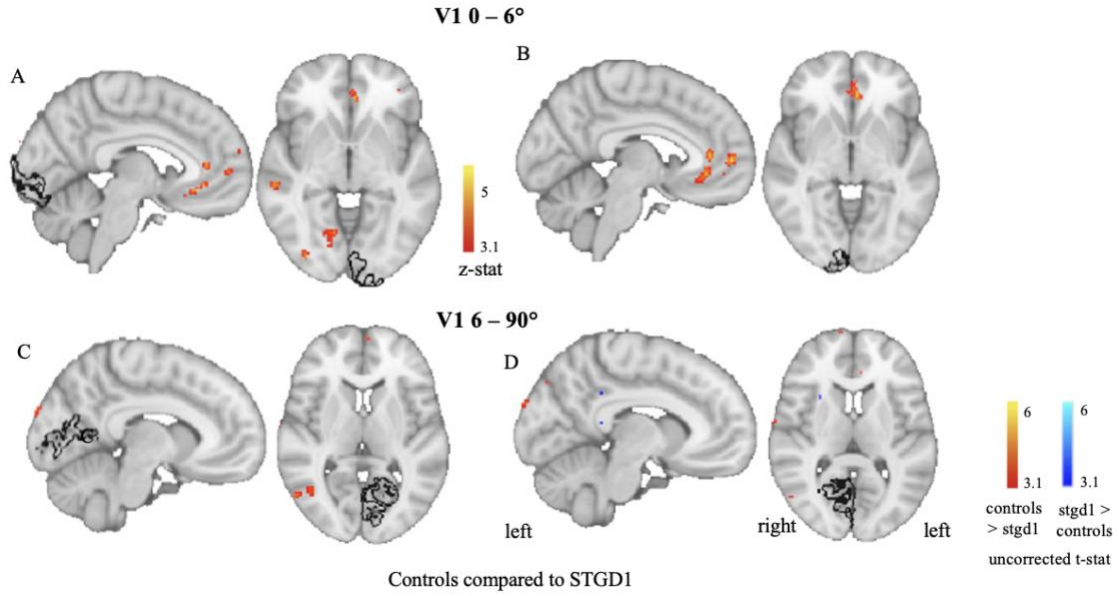


Figure 62: Correlated connectivity with the unilateral posterior (A/B) and anterior (C/D) V1 (purple mask) where controls > STGD1 overlaid on the MNI standard brain [A/B: 94 40 67, C: 94 51 84, D: 99 46 84]. Increased functional connectivity in controls > STGD1 significant for the right posterior V1 ($p < 0.05$, corrected) (A) and the left posterior V1 ($p = 0.004$, uncorrected) *(B). The colour bar shows regions of increased cortical connectivity for controls (red - yellow) and STGD1 (dark-light blue).*

To investigate whether V1 connectivity to the whole brain varies with disease severity, measures of vision loss were input as regressors into the GLM. Regions of increased connectivity to the frontal cortex were found for the left and right posterior V1 when correlated with increased retinal sensitivity (figure 62 B) ($p = 0.035$) however they were uncorrected for multiple comparisons. The region of increased connectivity with the frontal cortex was not present in the anterior V1 ROIs when correlated with retinal sensitivity, even when uncorrected for multiple comparisons with the same threshold. There was no significant relationship between functional connectivity when correlated with photoreceptor layer thickness, even when uncorrected for multiple comparisons.

5.5.5 Functional connectivity between visual areas correlates with disease severity

A loss of input to the visual cortex due to vision loss should reduce the functional connectivity between regions of the visual cortex. As there are a variety of disease severities in the STGD1 group, functional connectivity between ROIs should correlate with the amount of vision loss. The whole brain rs-functional connectivity maps for the V1 sub-sections were used to measure the mean connectivity in the visual areas of interest (unilateral LGN, V4 and hMT+).

To investigate the effect of photoreceptor layer thickness (0 -3 °) (μm) on functional connectivity Pearson's R correlation was conducted for each ROI connectivity to the posterior V1 (0 – 6°). and plotted against photoreceptor layer thickness (μm) (figure 63). This analysis was repeated to investigate the correlation between photoreceptor layer thickness (3 -8 °) (μm) and the anterior V1 (6 – 90°). Functional connectivity was significantly correlated with photoreceptor layer thickness for the connectivity between the posterior V1 (0 - 6°) connected to the right ($r(29) = .45$, $p = 0.012$) and left LGN ($r(29) = .38$, $p = 0.034$), right V4 ($r(30) = .51$, $p = 0.003$) and right ($r(30) = .57$, $p = 0.001$) and left ($r(22) = .47$, $p = 0.022$) hMT+, but not significantly correlated for the left V4 ($r(30) = .26$, $p = 0.150$). In comparison functional connectivity was only significantly correlated with photoreceptor layer thickness for the connectivity between the anterior V1 (6 - 90°) connected to the right ($r(22) = .47$, $p = 0.022$) hMT+, but not significantly correlated for the right ($r(30) = .47$, $p = 0.022$) and left LGN ($r(28) = .17$, $p = 0.355$), right V4 ($r(29) = .34$, $p = 0.006$) and left V4 ($r(29) = .05$, $p = 0.799$ and left ($r(30) = .18$, $p = 0.033$) hMT+. These results suggest that functional connectivity between the posterior V1 and both the LGN and hMT+ decreases with a reduction in photoreceptor layer thickness. This reduction was not present bilaterally between the anterior V1 and the ROIs, suggesting the reduction in V1 connectivity is linked to where the loss at the retina is projected to.

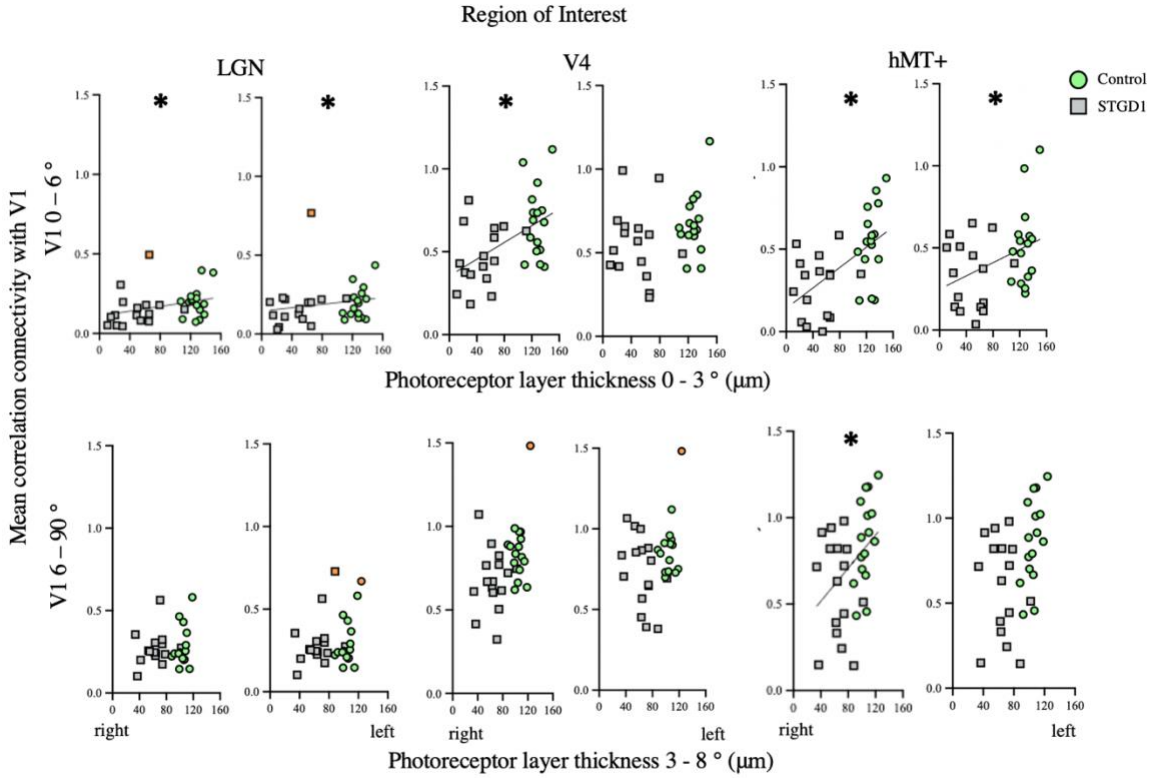


Figure 63: Functional connectivity between ROIs (LGN, V4, hMT+) and sub-regions of V1 plotted against photoreceptor layer thickness (µm). Individual data points for controls (green circles) and STGD1 (grey squares) are plotted with lines of best fit and asterisks to represent significance. Graphs include outliers (orange) removed from the statistical analysis.

This analysis was repeated to investigate the correlation between retinal sensitivity (0 – 3 dB) on functional connectivity Pearson's R correlation was conducted for each ROI connectivity to the posterior V1 (0 – 6°) and plotted against retinal sensitivity (dB) (figure 64). This analysis was repeated to investigate the correlation between retinal sensitivity (3 – 9 dB) and the anterior V1 (6 – 90°). Functional connectivity was significantly correlated with retinal sensitivity for the connectivity between the posterior V1 (0 -6°) connected to the right LGN ($r(29) = .36$, $p = 0.045$), V4 ($r(30) = .53$, $p = 0.002$) and hMT+ ($r(30) = .51$, $p = 0.003$) but not significantly correlated for the left LGN ($r(29) = .33$, $p = 0.07$), V4 ($r(30) = .24$, $p = 0.018$) and hMT+ ($r(30) = .34$, $p = 0.060$). Functional connectivity was only significantly correlated with retinal sensitivity (0 – 3 dB) for the connectivity between the anterior V1 (6 - 90°) connected to the right V4 ($r(29) = .43$, $p = 0.002$), but not

significantly correlated for the right (r (30) = .16, p = 0.374) and left LGN (r (28) = .005, p = 0.981), left V4 (r (29) = .14, p = 0.441) , right (r (30) = .33, p = 0.063) and left hMT+ (r (30) = .20, p = 0.272). As these results were not significant bilaterally, they do not suggest that functional connectivity correlates with retinal sensitivity.

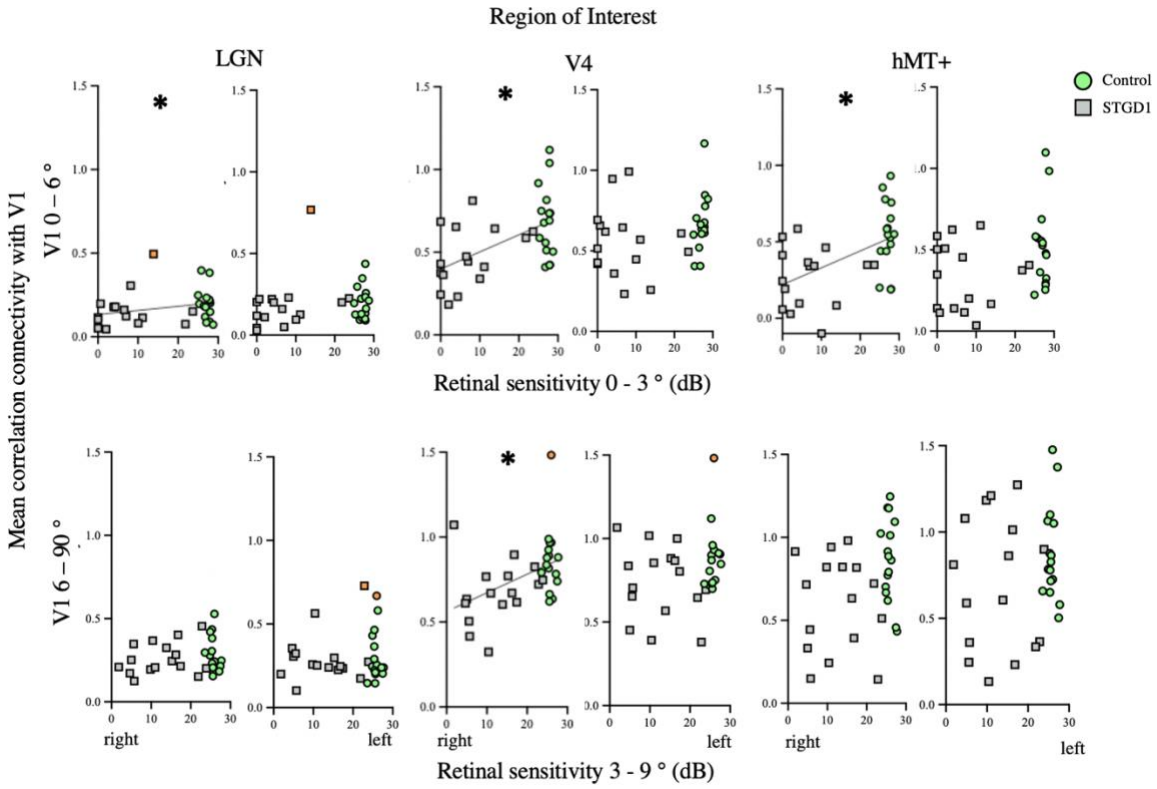


Figure 64: Functional connectivity between ROIs (LGN, V4, hMT+) and sub regions of V1 plotted against retinal sensitivity (dB). Individual data points for controls (green circles) and STGD1 (grey squares) are plotted with lines of best fit and asterisks to represent significance. Graphs include outliers (orange) removed from the statistical analysis.

5.6 Discussion

5.6.1 Functional connectivity decreases within the visual cortex in STGD1

I found significantly decreased functional connectivity within the medial visual RSN in STGD1 compared to controls. This region of increased connectivity was localised within the right LOC, which is part of the ventral stream and responsible for object processing (Malach et al., 1995) (Grill-

Spector, 2003). The visual loss in STGD1 is localised to the central visual field which is responsible for high acuity vision, and this is needed for object recognition. Therefore, the increase in functional connectivity to the LOC for controls compared to STGD1 may reflect the loss of high acuity vision in STGD1. High acuity vision is also needed for face recognition; however, no changes in functional connectivity were found within the FFA. The region of increased functional connectivity to the LOC was located outside the mean RSN map. This was located at the edge of the network so this may be due to this area being recruited in this visual network for controls with healthy vision but not for STGD1 due to their vision loss. Increased functional connectivity was found in the other RSN visual networks (lateral visual and occipital pole) between controls compared to STGD1when uncorrected for multiple comparisons. These regions of decreased connectivity within the RSNs were also localised within the LOC. These results are similar to those found in glaucoma which found reduced functional connectivity within the visual cortex after vision loss (Li et al., 2017). These findings are inconsistent with those from Sabbah et al (2017) who found an increase in functional connectivity to the LOC in STGD1, however this may have been due to differences in ROI sizes.

5.6.2 Posterior V1 connectivity to the frontal pole and the medial frontal cortex decreases in STGD1

V1 was divided into posterior (0 – 6°) and anterior (6 – 90°) subsections to target the region of visual loss in STGD1 (posterior V1). I found significantly decreased functional connectivity between the right posterior V1 to the frontal pole and the medial frontal cortex in STGD1 compared to controls. These results suggest that the lack of input to the posterior V1 in STGD1 reduces the functional connectivity from V1 to the frontal cortex, as the reduction in connectivity is not present in the anterior V1 where the seeing parts of the retina are projected in STGD1. Connections between V1 to the frontal pole and the medial frontal cortex are associated with top-down modulation of visual attention to the visual cortex (Paneri and Gregoriou, 2017) (Sims et al., 2021). As there is a reduced input into the posterior V1 this would require reduced attentional modulation from the medial frontal cortex. This reduction in frontal connectivity is also present in the left posterior V1 when uncorrected for multiple comparisons. This decrease in functional connectivity did not appear in the bilateral anterior V1 even at the liberal statistical significance thresholds. These findings demonstrate how the

region of projected focal loss causes a decrease in functional connectivity to the frontal cortex. These results are inconsistent with those from Sabbah et al (2017) who found an increase in functional connectivity from the visual cortex to the medial frontal gyrus in RP, however this may be due to the paper using an ROI location too posterior to encapsulate the projected loss in RP.

5.6.3 Posterior V1 connectivity to the LGN and hMT+ correlates with disease severity

In order to investigate how functional connectivity between visual regions varies with disease severity, I compared connectivity between the posterior and anterior V1 ROIs with the unilateral LGN, V4 and hMT+ and correlated these with measures of loss. I found that the posterior V1 connectivity to both the LGN and hMT+ was significantly correlated with photoreceptor thickness and this was present bilaterally. The LGN is part of the visual pathway which receives information from the retinal ganglion cells, it then relays this through the optic radiations to V1, which sends feedback connections (Cudeiro and Sillito, 2006). Therefore, a reduction in photoreceptor layer thickness would mean less input to the LGN and subsequently the visual cortex. hMT+ is involved in processing global motion (Kaderali et al., 2015), however motion detection and discrimination does not require high acuity vision. However, vision loss in STGD1 would still cause a disruption to motion perception due to the scotoma in the visual field, and therefore this would cause reduced connectivity in hMT+. These significant correlations were not present bilaterally for the anterior V1 where the seeing part of the retina is projected to in STGD1. This dissociation between connectivity with the posterior and anterior V1 shows that the changes in connectivity may reflect the reduced input from vision loss in STGD1.

5.6.4 Limitations and future directions

The experiment presented in this chapter used a larger sample size for the STGD1 group (n = 16) than previous research (n = 12) by Sabbah et al (2017), and therefore is more sensitive to detect differences between groups. A key limitation is that even with this larger sample size, the disease severities widely varied within the STGD1 patient cohort. The patients with mild severities categorised by smaller scotomas may have diluted the cortical differences in the relatively large posterior V1 ROI.

Participants with thicker photoreceptor layers show increased functional connectivity within the cortex, shown by the functional connectivity plotted against disease severity figures (figures 63/64). Therefore, this could have been investigated further by splitting the V1 ROI into smaller subsections, like the ones in the previous chapter (chapter 4) which would have better encapsulated the projected vision loss in the patients with milder disease severities.

In section 5.5.5 differences in connectivity strength were found between subsections of V1 and visual ROIs. Future research could investigate this further at a brain-wide level using network modelling in FSLNets (Smith et al., 2013). This would create a functional connectivity matrix to investigate how connectivity differs across the whole brain in STGD1 compared to controls. These results show that functional connectivity varies with disease severity, these changes in connectivity may limit treatments that aim to restore function at the retina, particularly at more severe disease severities. Therefore, future research should investigate the required time frame to implement treatments in order to maximally improve vision.

5.6.5 Chapter conclusion

In conclusion, the work presented in this chapter shows a decrease in functional connectivity after vision loss from STGD1. These decreases in functional connectivity were found in areas associated with object processing (LOC) and visual attention modulation (medial frontal cortex). Decreased functional connectivity was found to correlate with disease severity between the region of projected loss in V1 to areas involved in the relaying of visual information (LGN) and visual motion perception (hMT+). These results should be considered in conjunction with therapies that aim to restore vision at the level of the retina, as the visual cortex may not be functioning adequately to process that restored input.

6 Neurochemical validation

6.1 Abstract

Magnetic Resonance Spectroscopy Imaging (MRSI) is an advanced imaging technique which allows an *in vivo* measurement of neurochemical concentrations in the cortex at a higher spatial resolution compared to single-voxel MRS. Therefore, this allows neurochemical concentrations to be compared across multiple regions of the cortex.

The density weighted concentric ring trajectory (DW-CRT) k-space sampling acquisition method (DW-CRT MRSI) can acquire high resolution MRSI data at 3T, however, the only neuroscience applications papers published have acquired the slab centrally at A/P alignment over the motor cortex (Steel et al., 2018). For this study we tilted the acquisition slab to be parallel to the calcarine sulcus and then placed the slab posteriorly, as close to the back of the brain as possible, to gain maximal coverage of the visual cortex. As this is the first experimental study to investigate the occipital lobe with this technique, this chapter aims to validate the new placement of the acquisition slab to compare whether the methodology yields biologically plausible measurements.

I found that the neuro-metabolite concentrations within the grey and white matter within the occipital lobe are comparable to those across the motor cortex found in Steel et al (2018). Glutamate, *myo*-Ins and NAA show the expected concentration correlation with grey matter fraction. The results show that the closer the acquisition slab is placed towards the dura, the more susceptible the slab is to lipid contamination, which particularly affects reliable measurement of GABA concentrations. These results should be considered in future experiments that aim to acquire measures of GABA concentrations in regions near the edges of the brain. Future experiments that aim to measure the posterior visual cortex, could reduce the lateral slab width so it can be positioned further back in the brain and changing the slab acquisition direction.

6.2 Introduction

6.2.1 Single Voxel Magnetic Resonance Spectroscopy

Proton Magnetic Resonance Spectroscopy (^{1}H-MRS) can measure a multitude of neurometabolite concentrations *in vivo* in the human cortex (figure 65). The spectrum can provide a quantification of neuro-metabolite levels in the cortex and with these measures can provide an insight into neuronal and glial cell integrity. The neurometabolites of interest to this project are NAA (yellow arrow figure 65), *myo*-inositol (*myo*-Ins) (orange arrow), glutamate (blue arrow) and GABA (pink arrow). Each ^{1}H-MRS voxel contains thousands of neurons and therefore provides a global measurement of the neuro-metabolite concentrations across tissue compartments (WM, GM, CSF), rather than a measurement of neurotransmitter levels in each individual neuron. ^{1}H-MRS acquires data within a single voxel, which typically covers a substantial amount of the cortex (1 – 8 cm^3) (Spurny et al., 2019). Due to the low spatial resolution, this makes it difficult to differentiate which region of the cortex the neuro-metabolite concentrations are being measured within. Therefore, if the hypothesis is related to the neuro-metabolite concentrations within a specific ROI, these concentrations will be diluted by those in the surrounding tissue within that voxel, therefore making the results less reliable. If only one voxel can be positioned per acquisition, studies requiring more than one voxel, acquire the data sequentially. Therefore, the noise within the acquired data will be different per acquisition, meaning that the data may be more susceptible to noise, such as from participant motion.

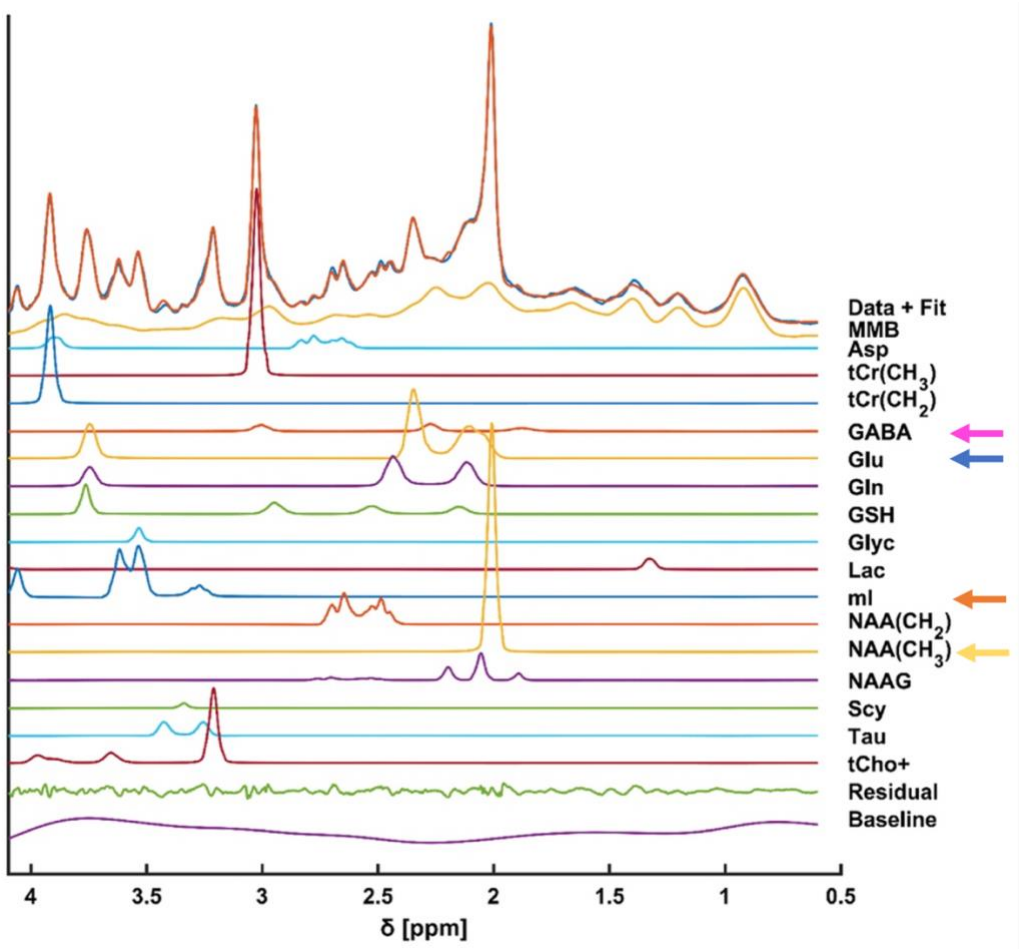


Figure 65: Output from a single ^{1}H-MRS voxel, showing the raw data, fit, baseline and residuals. The individual metabolite spectra (ppm) used in chapter 7 are represented with coloured arrows, myo-Ins (orange), glutamate (blue), NAA (yellow) and GABA (pink). Figure edited from (Murali-Manohar et al., 2020).

6.2.2 Magnetic resonance spectroscopy imaging

Magnetic Resonance Spectroscopy Imaging (MRSI) acquires multiple voxels in one acquisition, which addresses the low spatial resolution of ^{1}H-MRS. This higher spatial resolution therefore allows comparisons of neurochemical concentrations between different cortical areas. MRSI has shown that neurometabolite concentrations reflect the physiology of the differing tissue compositions across the cortex. The neurochemical concentrations such as NAA, have been found to vary across grey and white matter, reflecting the proportion of neuronal axons or cell bodies that are contained within them (Steel et al., 2018) (figure 66).

Currently the only neuroscience applications paper published with the density weighted concentric ring trajectory (DW-CRT) k-space sampling acquisition method (DW-CRT MRSI) sequence have acquired the slab centrally at A/P alignment over the motor cortex (Steel et al., 2018) (figure 66). As the experiments presented in this thesis relate to the visual system, the slab position was modified to maximally cover the visual cortex. The acquisition slab was tilted to be parallel to the calcarine sulcus and then positioned posteriorly rather than centrally in the brain. As there are currently no published studies using the DW-CRT MRSI sequence from (Steel et al., 2018) within the visual cortex we were unsure how this new placement will affect the validity of the neurochemical measures. This chapter aims to validate the reliability of these results by investigating the spatial variance of the voxels and comparing the findings with the results from Steel et al (2018) in controls with a healthy visual system.

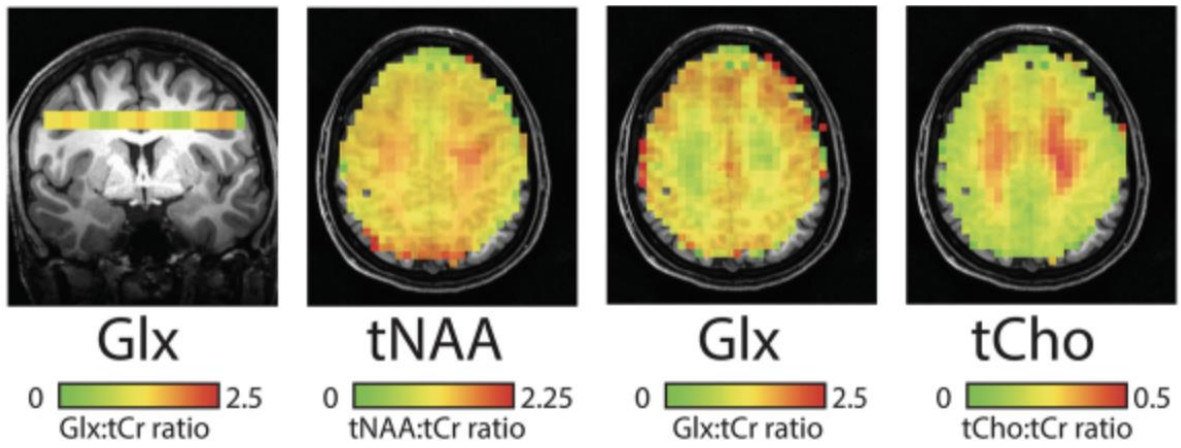


Figure 66: MRSI slab showing the acquisition coverage of the current A/P central alignment in a participant with a healthy cortex. Neurochemical concentration. maps of relative Glx (glutamate + glutamine), NAA and choline show distributions across the cortex. Colour map shows where relative neurochemical concentrations are lower (green) to higher (red) in the cortex.). Figure from (Steel et al., 2018).

6.2.3 Neurochemicals of interest

The following experimental chapter (chapter 7) contains the results for the neurochemical concentrations in the visual cortex between STGD1 and controls. These results provide an insight into whether neuronal degeneration or reorganisation is occurring in the adult human visual cortex after a loss of input from STGD1. The neurometabolites GABA, NAA, *myo*-Ins and glutamate were investigated as markers for neuronal reorganisation or degeneration, where GABA levels were used to infer neuronal inhibition as a marker for reorganisation and glutamate levels to infer cortical function. NAA is used as a marker neuronal loss and *myo*-Ins for glial-cell proliferation.

In MRS NAA(CH_2) resonates at the highest peak out of all the metabolites (after removal of the water peak) at 2.0080 parts per million (ppm) (yellow in figure 65) (Govindaraju et al., 2000). *Myo*-Ins resonant peaks are between 3.2690 – 4.0538 ppm (orange in figure 65) (Govindaraju et al., 2000). Glutamate's resonant peaks are between 2.0375 (blue in figure 65) and 3.7433 ppm and GABA's are between 1.8890 - 3.0128 ppm (pink in figure 65) (Govindaraju et al., 2000). NAA, *myo*-Ins and glutamate are present in a relatively high concentration (NAA 7.9 – 16.6 micro mol/g; *myo*-Ins 3.8 – 8.1 micro mol/g; glutamate 6.0 -12.5 micro mol/g) which makes quantification of these neurometabolites more accurate, compared to GABA (1.3 – 1.9 micro mol/g) which is present at an order of magnitude lower (Govindaraju et al., 2000). Additionally, the GABA resonant peaks of the spectrum overlap with other neurometabolite peaks and are easily contaminated by lipids. Concentrations of GABA and glutamate are higher in the GM compared to the WM (Jensen et al., 2005) (Goryawala et al., 2016), whereas NAA and *myo*-Ins concentrations are the opposite, with a decrease in GM compared to WM (Schuff et al., 2001) (Haris et al., 2011).

6.3 Measures of spectral quality

Currently the standards on how to reliably evaluate spectral quality are debated, with a variety of methods used throughout the literature that quantify spectral quality and threshold for data exclusion. The quality of spectra can be affected by many aspects, such as lipid contamination, head motion and the quality of shimming. There is a consensus for papers to include the minimum reporting guidelines

which are spectral linewidth, SNR and Cramér-Rao lower bound (CRLB) (Lin et al.), and I will discuss these below.

6.3.1 Spectral linewidth

Spectral resolution has a large effect on both the reliability of metabolite quantification and the separation of overlapping metabolite spectral peaks (Kreis et al.). The resonance linewidth is used to infer spectral resolution, and this is measured with the FWHM of the resonance peak. This can be determined at different time points either in pre-scan shimming, acquisition or in the analysis pipeline. Lower FWHM infers that the peaks are more spread out in the spectrum and therefore the metabolites will overlap less. This means that the metabolites can be more readily distinguished from one another, particularly important for low concentration metabolites or metabolites that overlap with other metabolite peaks in the spectrum. For the study described in this thesis the FWHM was determined in the pre-scan shimming and therefore could be improved by re-shimming if the FWHM was too high.

6.3.2 Signal-to-noise

MRS data is made up of two main components, the first is the inherent signal of the true metabolite concentrations, the intensity of this signal is represented as the signal peak in the frequency dimension (FD). The second component is noise which arises from thermal variations from the person and the scanner hardware, this noise adds varying fluctuations to the recorded data. The SNR is used to assess data quality and is affected by the size of the voxel of interest (VOI) and the number of averaged acquisitions. SNR can be calculated as signal per one standard deviation (SD) of noise (Kreis et al.).

Metabolite quantities vary across grey matter (GM), white matter (WM) and cerebrospinal fluid (CSF). Within each voxel the concentrations of these vary, therefore the tissue fractions need to be controlled for by normalising the metabolite concentrations. The study presented in this thesis uses GM fraction correction to account for metabolite differences across cortical tissue.

6.3.3 Cramér-Rao lower bounds

Cramér-Rao lower bounds (CRLB) are one of the standard measures of uncertainty in data quality in MRS. They are used to infer the quality of the model fitting and measured as the lower bound of the fit error (variance), which is a specific percentage away from the standard deviation. These can be expressed as a percentage of the estimated concentration, with values > 20% - 50% CRLB being excluded from the analysis (Kreis, 2016). However, these should be interpreted with caution as other aspects could affect these values, such as acquiring data from a patient population where we predict the concentrations of some neurochemicals would be reduced. This would in turn increase the CRLB values and therefore bias the amount of data excluded from the patient population. CRLB should be interpreted with the other measures described in this section, plus visual inspection of the spectrum before values are excluded.

6.3.4 Coefficients of variance

In MRS(I) typical protocols acquire multiple repeats of the same acquisition and these are then averaged together to create the final output spectrum. These scans can also be analysed individually and then compared to measure reproducibility between acquisitions, and this is called the coefficients of variance (CVs) (Langer et al., 2007; Terpstra et al., 2016). Reporting CVs are valuable as they add extra information about the reliability of the method over different acquisitions.

6.3.5 Importance of avoiding contamination

Some metabolites are more susceptible to contamination than others due to their concentration and where they sit on the spectrum. Metabolites with lower concentrations, with peaks on the right side of the spectrum are the most susceptible to contamination in MRS and therefore can be more difficult to gain an accurate concentration measurement. The dura is the outermost layer of the meninges located underneath the skull (figure 67); its function is to act as a barrier to protect the brain. The dura is made from connective tissues which contains a high quantity of lipids. The GABA spectra is particularly susceptible to lipid contamination as some of the lipid spectral peaks overlap at around 4 ppm (Tkac et al., 2021). Lipid signals pose challenges in metabolite estimation, if the metabolites of interest are on the right side of the spectrum, then lipid contamination should be avoided by placing

the slab within the brain boundary (figure 67). GABA was a neurometabolite of interest for this thesis and therefore the slab was placed as to avoid dura. If there was patient motion then occasionally dura entered the acquisition space and contamination of the spectrum occurred, so the GABA spectrum was unable to be accurately measured (figure 67).

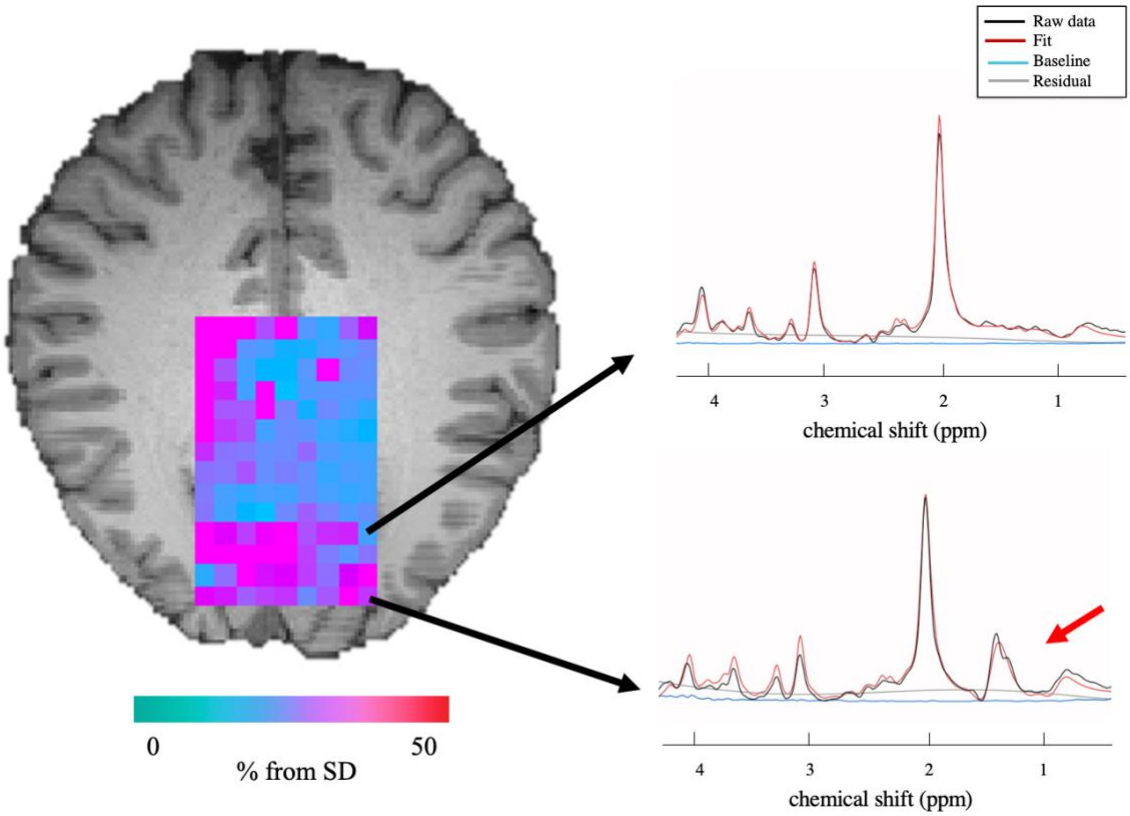


Figure 67: Chemical shift spectra from two voxels in the visual cortex, shown with a GABA CRLB map overlaid over an individual participant's brain. The spectra show the raw data (black) the model fit (red), the baseline (blue) and the residual (grey). The top spectrum shows an uncontaminated spectrum and is able to model the neurochemicals accurately, whereas the bottom spectrum shows lipid contamination from a voxel located near dura (red arrow).

6.3.6 Metabolite reference

In MRS, the signal intensity is proportional to individual neuro-metabolite concentrations, however this is indistinguishable from a variety of other variables, such as metabolite relaxation rates and RF

coil sensitivity (Minati et al, 2010). Therefore, a reference metabolite is used to distinguish the contribution of the metabolite of interest to the overall spectra (Ford and Crewther, 2016). There are three main choices of reference metabolites, and these are explained below.

Creatine and phosphocreatine:

A common reference used in the literature is the ratio of phosphocreatine and creatine (PCr+Cr) as these metabolites are stable and in high concentrations in the brain. In patient populations, where loss is predicted, creatine may also vary alongside the metabolite of interest, and therefore using it as a reference for a patient group may not be accurate. If there is noise in the signal, then creatine will also be affected as it is acquired in the same spectra as the metabolite of interest.

All metabolites:

An alternative to referencing to one individual metabolite like PCr + Cr, is to reference against an average of all metabolites acquired from the sequence. This is beneficial as it normalises to all potential quality differences in the spectra rather than being affected if part of the spectra is contaminated. This is worthwhile to use in control populations but again has limitations in patient populations with neuronal loss, as all metabolites may be reduced.

Water:

The water reference can be acquired separately to the MRS data acquisition, and this is unaffected by the intrinsic issues described above, as this reference is independent of the normalisation method used. The water reference is used to calculate the absolute concentration of metabolites and is displayed in institutional units (I.U.) but requires additional correction for tissue relaxation effects. If the water signal is collected separately, it is independent of the signal and the subsequent noise artefacts within the MRS data. Therefore, the water signal can be compared to the MRS data to help identify noise and artefactual components and subsequently remove them. However, the DW-CRT MRSI sequence has the water signal interleaved in the acquisition and not separately acquired therefore is not possible to use water as a reference that is acquired separately to the MRSI data. The

DW-CRT MRSI sequence used in the experiments described in this thesis acquires the water and metabolite signal simultaneously (Steel et al., 2018).

6.4 Methods

6.4.1 Participants

The work in this chapter displays the results from two controls (1 female aged 44, 1 male aged 51) with healthy visual systems and normal vision.

6.4.2 Magnetic Resonance Spectroscopy Imaging

Acquisition:

The DW-CRT MRSI sequence described in Steel et al (2018) was used to localise and acquire the MRSI data using the following acquisition parameters (FOV= 240 × 240 × 10mm, voxel size = 5 × 5 × 10mm, TE = 32ms, TR = 1350ms, semi-LASER localisation = 145mm x 120mm x 10mm.) Gradient echo shimming (GRESHIM) was used for B_0 shimming. The MRSI slab was manually placed using the T1-weighted image as a reference and positioned parallel to the calcarine sulcus, with an axial orientation under 45°. The data acquisition area was limited due to the constraints of the MRSI slab placement. The slab position was placed posteriorly to overlap with the foveal representations of the visual field, as this is where the region of projected loss is located in STGD1. The slab was positioned to avoid non-brain tissue due to macromolecular contamination within the right-hand side of the MR spectrum (3.5+ ppm). If the participants had uneven calcarine sulci locations, where one hemisphere was higher than the other, then the slab was shifted laterally in the axial view to maximally cover the calcarine sulcus in a single hemisphere. If the full width half maximum (FWHM) was > 20 Hz, then the shimming was repeated until the FWHM fell below 20 Hz. Three runs of MRSI were acquired over the acquisition slab (126 voxels of 5 x 5 x 10mm). A blank screen was shown for the MRSI scan and participants were instructed to look centrally at the screen and were monitored to ensure compliance.

Analysis:

The MRSI analysis was conducted with the FSL_MRS analysis toolbox (Clarke et al., 2021), this included pre-processing with the command *fsl_mrs_proc*. Pre-processing included coil combination, spectral registration, nuisance peak removal, residual water removal and eddy current correction. Fitting was performed using the command *fsl_mrsi* which uses linear combination (LC) modelling, an algorithm that takes basis spectra (simulated metabolite spins to that specific pulse sequence) and fits them to each voxel independently. Tissue volume fractions for each voxel were calculated with the command *mrsi_segment* for the participants T1w structural scan. Fitting was then re-analysed with the grey matter fraction from *mrsi_segment*. The outputs from both the fitting with and without grey matter fraction correction were used in the subsequent analyses. The T1-w image had brain extraction applied and was registered to standard space. Figure 68 shows the slab reconstruction of 126 voxels in individual structural space and a spectrum from an individual voxel on the right.

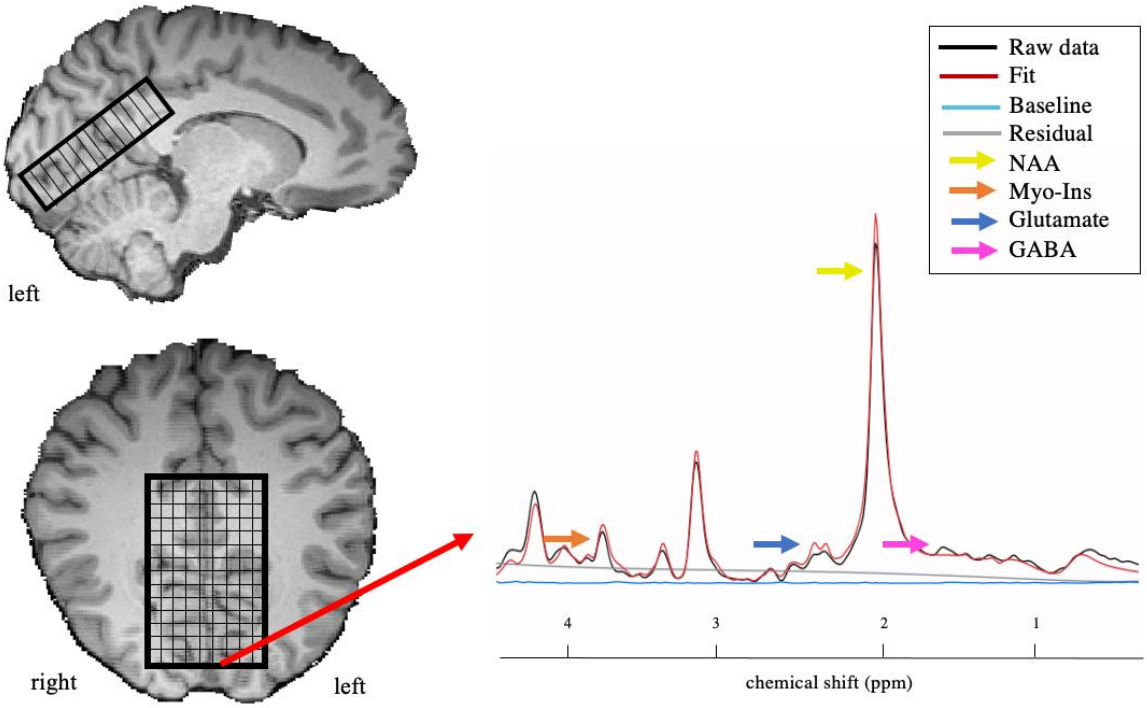


Figure 68: A MRSI slab overlaid on a participants T1w structural image. The corresponding spectrum from one voxel included in the analysis. The spectrum is an average of three acquisitions analysed by FSL_MRS, showing the raw data (black), fit (red), baseline (blue) and residuals (grey).

Metabolite peaks used in Chapter 7 are represented with arrows, myo-Ins (orange), glutamate (blue), NAA (yellow) and GABA (pink).

6.4.3 Measure of spectral quality

The posterior slab used here is not as homogenous as the one used in Steel et al (2018) because the position is more affected by artefacts at the edges of the brain. The analysis therefore requires further investigations to ensure the neurochemical concentrations are accurately measured for the new position. Spectral quality from two controls was assessed to determine whether the neurochemical measurements are biologically plausible and comparable to those found in Steel et al (2018).

6.4.4 Statistical Analysis for validation

Metabolite maps were thresholded for CRLB and SNR in the *fslmaths* command within FSL. Statistical analyses were performed using GraphPad Prism (version 9.0). Grey matter fraction (%) was plotted against metabolite concentrations relative to total creatine for all voxels that passed the thresholds for two control subjects. Pearson's R was used to investigate if there were significant correlations between the neurochemical concentrations grey matter fraction. Therefore, a Pearson's R correlation, was conducted to compared neurochemicals with GM fraction.

For all analyses described in this chapter, outliers of (+/-) 2.7 standard deviations from the mean were removed and results were considered statistically significant at $p < 0.05$.

6.5 Measures of Spectral Quality

6.5.1 Cramér-Rao Lower Bounds

The metabolites were compared against the PCr + Cr reference metabolite as this is most commonly reported in the literature. As neurochemical concentrations change in disease states, and these are predicted to change in patients with STGD1, the CRLB standard deviations for variance were chosen with liberal thresholds (SNR 40%, CRLB 20% for NAA, *myo*-Ins and glutamate and 50% for GABA). The spatial maps show how the CRLB is higher towards the posterior and left lateral edges

of the slab (figure 69). This is due to contamination from both the sequence acquisition and an increased amount of noise in the edge voxels, the voxels that surpassed the SNR and CRLB thresholds were removed from the subsequent analyses. Both the placement (to avoid dura) and increased posterior contamination has implications on the amount of the visual cortex that can be accurately measured.

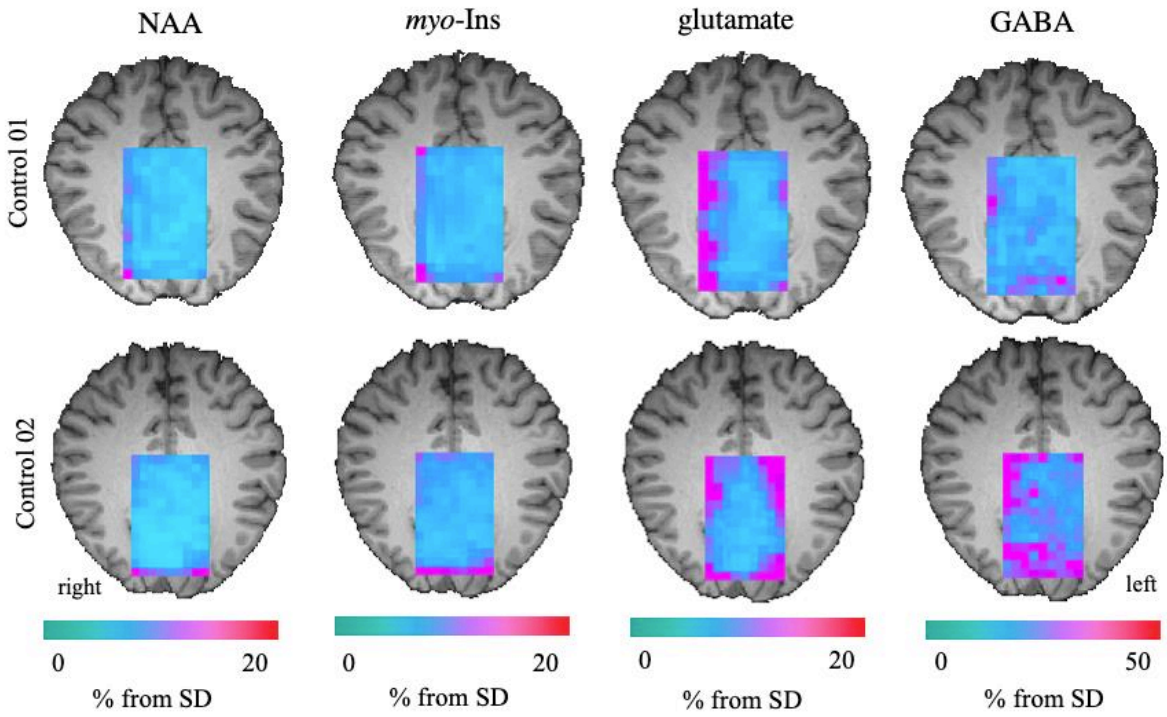


Figure 69: Spatial maps of Cramér-Rao Lower Bounds (CRLB) for NAA, myo-Ins, glutamate, and GABA from two controls overlaid on individual structural space, showing how CRLB deviates from the standard deviation, green (low CRLB) to red (high CRLB).

6.5.2 Grey matter fractions

6.5.2.1 Glutamate

Glutamate concentrations are higher in the grey matter and therefore should increase as the grey matter fraction increases and this is shown in figure 70. The relative glutamate concentration ratio (Glu:tCr) uncorrected for tissue segmentations were significantly correlated with grey matter fraction

(%) for control 01 (r (109) = .44, p < 0.001) and control 02 (r (103) = .67, p < 0.001). This concentration distribution replicates the findings presented in Steel et al (2018) (right on figure 70), where Glx:tCr is positively associated with grey matter fraction.

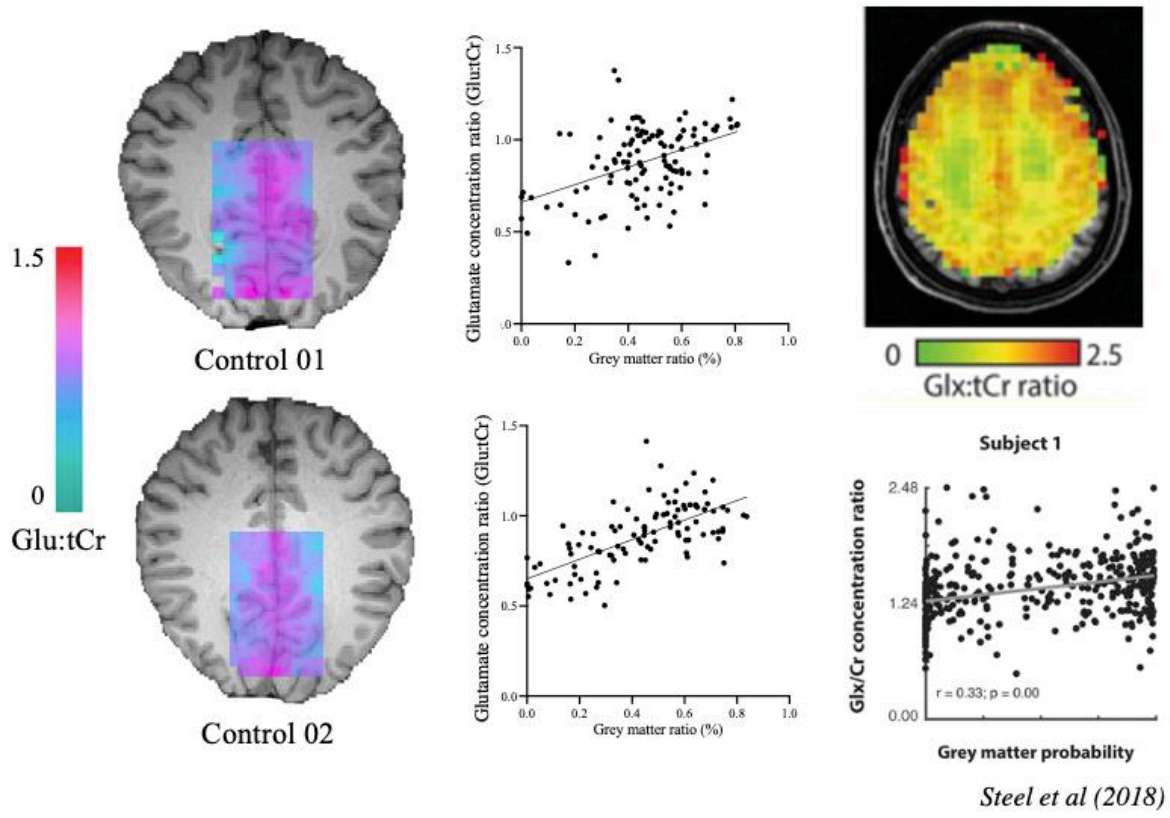


Figure 70: Glutamate ratios (Glu:tCr) (thresholded by 20 CRLB) increase in the grey matter compared to the white matter. The images on the left show how the concentration changes over a spatial map in two controls, the graph shows each voxel plotted against grey matter ratio (%) and the relative glutamate concentration ratio (Glu:tCr) with a line of best fit showing the significant correlation. The right image shows the MRSI results found by Steel et al (2018), where Glx:tCr positively correlates with grey matter ratio.

6.5.2.2 N-Acetylaspartate

NAA concentrations are lower in the grey matter and therefore should decrease as the grey matter fraction increases and this is shown in figure 71. The relative NAA concentration ratio (NAA:tCr) uncorrected for tissue segmentations were significantly inversely correlated with grey matter fraction

(%) for control 01 (r (95) = -.31, p = 0.002) and control 02 (r (91) = -.25, p = 0.017). This concentration distribution replicates the findings presented in Steel et al (2018) (right on figure 71), where tNAA concentrations are higher in the white matter.

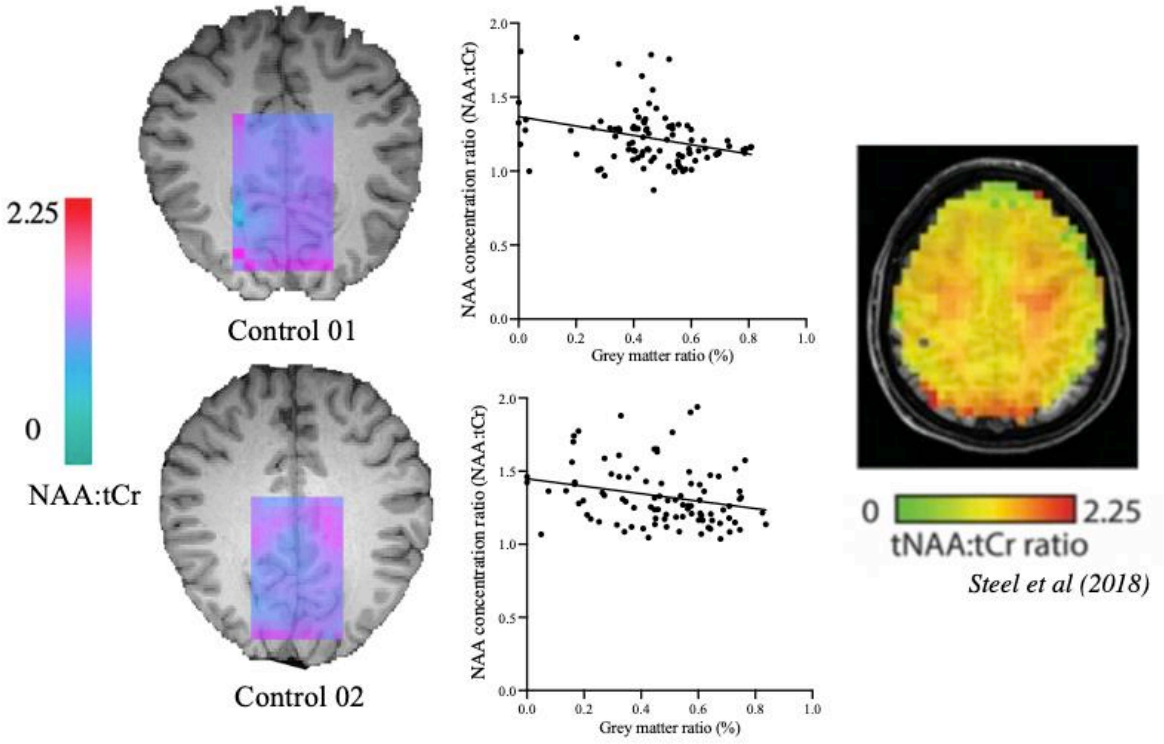


Figure 71: NAA concentrations (thresholded by 20 CRLB) increase in the white matter compared to the grey matter. The images on the left show how the concentration changes over a spatial map in two controls, the graph shows each voxel plotted against grey matter ratio (%) and the relative NAA concentration ratio (NAA:tCr) with a line of best fit showing the significant correlation. The right image shows the tNAA:tCr results found by Steel et al (2018), where tNAA concentrations are higher in the white matter.

6.5.2.3 Myo-Inositol

Myo-Ins concentrations are lower in the grey matter and therefore should decrease as the grey matter fraction increases and this is shown in figure 72. The relative *myo*-Ins concentration ratio (*myo*-Ins:tCr) uncorrected for tissue segmentations were significantly inversely correlated with grey matter

fraction (%) for control 01 (r (97) = -.71, p < 0.001) and control 02 (r (101) = -.57, p < 0.0101). This concentration distribution replicates the findings presented in Steel et al (2018) (right on figure 72) where *myo*-Ins concentrations are higher in the white matter.

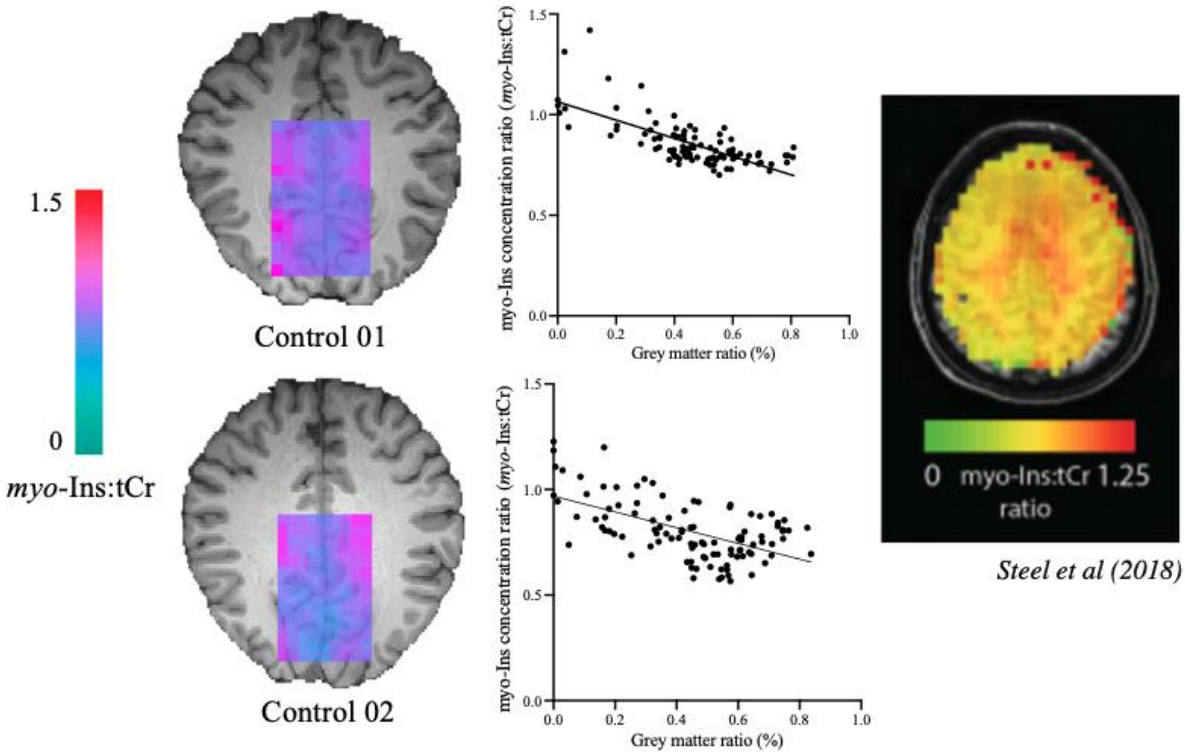


Figure 72: Myo-Inositol concentrations (thresholded by 20 CRLB) increase in the white matter compared to the grey matter. The images on the left show how the concentration changes over a spatial map in two controls, the graph shows each voxel plotted against grey matter ratio (%) and relative myo-Ins concentration ratio (myo-Ins:tCr) with a line of best fit showing the significant correlation. The right image shows the myo-Ins:tCr results found by Steel et al (2018), where myo-Ins concentrations are higher in the white matter.

6.5.2.4 Gamma-Aminobutyric Acid

GABA concentrations are higher in the grey matter and would be expected to increase as the grey matter fraction increases, however this is not the case as shown in figure 73. The relative GABA concentration ration (GABA:tCRr) uncorrected for tissue segmentations were significantly inversely

correlated with grey matter fraction (%) for control 01 (r (116) = -.27, p = 00.004) and control 02 (r (103) = -.32, p < 0.001). In the GABA:tCr map of control 02 (figure 73) the posterior edge voxels (red arrow) show a higher concentration of GABA:tCr, which does not follow the grey/white matter tissue distributions.

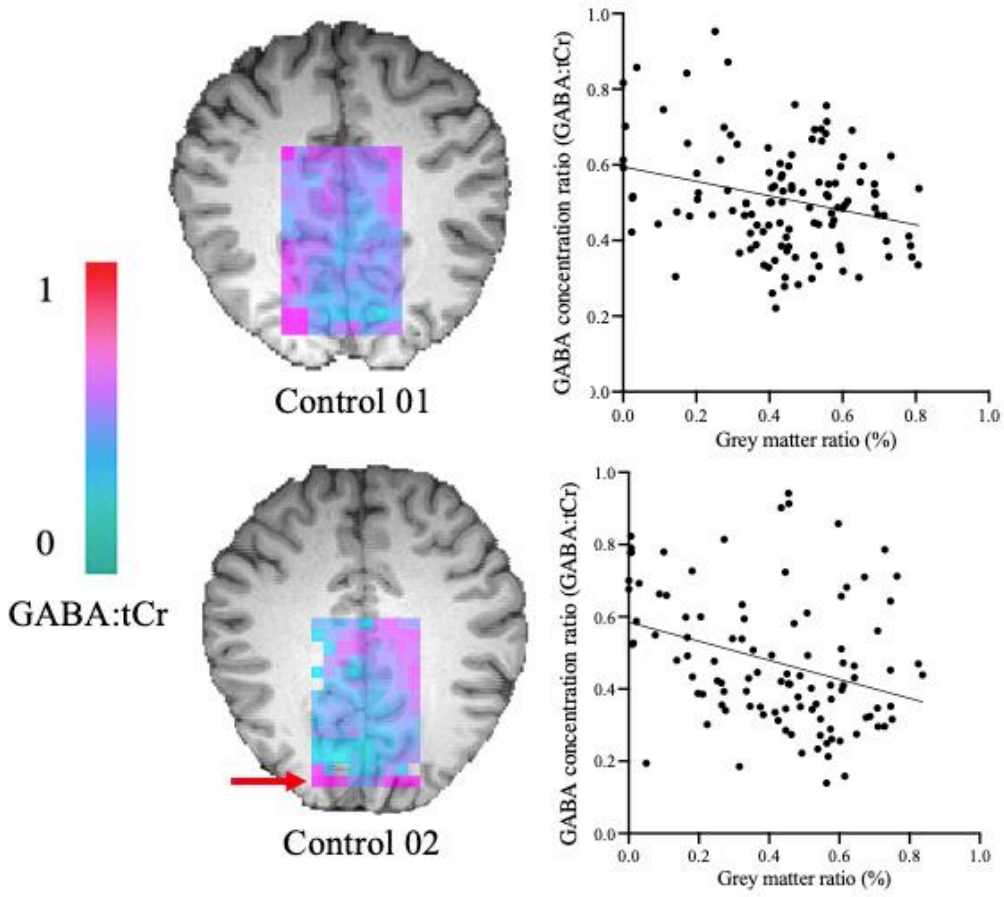


Figure 73: GABA concentrations (thresholded by 50 CRLB) decrease in the grey matter compared to the white matter. The images on the left show how the concentration changes over a spatial map in two controls, the graph shows each voxel plotted against grey matter ratio (%) and the relative GABA concentration ration (GABA:tCRr) with a line of best fit showing the significant correlation. The red arrow shows the posterior edge voxels that have lipid contamination.

6.6 Discussion

6.6.1 Spectral quality of occipital slab placement

I have shown that using the occipital position for the MRSI acquisition slab, reliable measurements of neuro-metabolites were able to be detected. CRLB were used to infer spectral quality by measuring the variance across the slab. I found that the lateral edge on the right hemisphere and the posterior edge of the slab did not accurately model the chemical shift spectra for all neuro-metabolites measured and this was a particular issue for GABA and glutamate. This is due to the direction of the acquisition of the slab which introduces noise into the signal acquired.

Neurochemicals with relatively strong signals (NAA, glutamate, *myo*-Ins) could be measured reliably in the visual cortex. NAA, *myo*-Ins and glutamate concentrations show the predicted correlation compared to grey matter fraction (Schuff et al., 2001) (Haris et al., 2011) (Goryawala et al., 2016); but GABA shows the opposite trend. GABA is ~2× higher in concentration within the GM compared to the WM (Jensen et al., 2005), therefore this difference in findings may be because it is unclear what the DWCRT-MRSI signal is measuring. As stated in the introductory chapter, MRS is thought to provide a measurement of the pool of GABA in extra-cellular space rather than a measure of intracellular metabolic activity (Stagg et al 2011a). Therefore, further research is needed to understand the GABA signal MRS is measuring and why this is higher in the WM.

Detection of GABA requires a higher CRLB threshold of (<50%) as it is present at lower quantities in the brain and therefore has a lower signal when measured by MRS. GABA was unable to be measured in the Steel et al (2018) paper due to the slab acquisition including the dura. The GABA peaks are towards the right of the chemical shift spectrum and are easily contaminated by macromolecules. The posterior edge voxels were unable to detect GABA concentrations due to contamination, as the signal measured GABA + macromolecules. Further modelling of macromolecules could be investigated to distinguish GABA from GABA+ macromolecule concentrations within the signal.

6.6.2 Limitations and future directions

This is the first study to investigate the visual cortex using DWCRT-MRSI. To achieve this, the MRSI slab was angled over the calcarine sulcus where the posterior edge was positioned as to avoid dura which creates contamination of the spectra. The right and posterior edge on the MRSI slab do not pass the signal-to-noise thresholds chosen due to inherent noise from the signal acquisition. This could be improved in the future by changing the slab acquisition to the opposite direction and therefore the row of posterior voxels over the calcarine would be less contaminated. If the slab was acquired at a voxel width thinner on both lateral edges, this could mean the slab could have been moved further posteriorly to encapsulate more of the central representation of the visual field, which is where the vision loss is represented in this patient group.

6.6.3 Chapter Conclusion

To summarise, the work presented in this chapter shows that neurochemicals with relatively strong signals (NAA, glutamate, *myo*-Ins) could be measured reliably in the visual cortex. Detection of GABA was more susceptible to contamination particularly in the edge voxels. GABA is more susceptible to macromolecule contamination; therefore, care should be taken when placing the slab to as avoid dura if GABA is a neurometabolite of interest. Future experiments that aim to measure the posterior visual cortex, could reduce the lateral slab width so it can be positioned further back in the brain and changing the slab acquisition direction.

7 Neurochemical

Neurochemical Changes in the Visual Cortex between Stargardt patients compared to Controls

7.1 Abstract

The topographic organisation of the primary visual cortex (V1) means that a focal region of vision loss due to damage at the retina is projected into a localised region of the visual cortex. A loss of visual input very early in life leads to a remarkable capacity for reorganisation in the visual cortex (Watkins et al., 2013), however whether this also occurs in adulthood is unclear. Literature regarding non-human primate models of vision loss suggests cortical degeneration occurs after vision loss in adulthood (Wu et al., 2013). There are only a few papers using single voxel magnetic resonance spectroscopy (MRS) in humans with vision loss, however this data is over a decade old (Bernabeu et al., 2009; Boucard et al., 2009). Therefore, currently very little is known about how the human visual cortex responds to a loss of input in adulthood. For this study, Magnetic Resonance Spectroscopy Imaging (MRSI) was used to measure neurochemical concentrations *in vivo* across the cortex at a high resolution. MRSI was used to quantify changes in the visual cortex after a partial loss of visual input in the patient group with STGD1 compared to controls with a healthy visual system.

There were differences in the concentration of neurochemicals that are markers for cortical degeneration and cortical function in the STGD1 visual cortex. Specifically, there was a significant elevation in myo-inositol (a marker for glial cell proliferation) concentration within V1 in STGD1 compared to controls. Reductions in glutamate levels were found within V1 in STGD1, additionally there were significant pairwise differences in glutamate levels within the region of projected visual field loss in STGD1. This reduction in glutamate levels, reflects a reduction in cortical function which may be from neuronal degeneration. The STGD1 patients had a range of disease severities and therefore a range of vision loss. If vision loss in adulthood causes cortical degeneration, then greater vision loss should correlate with a larger change in neurochemical concentrations. Indeed,

concentrations of myo-inositol, NAA and glutamate all correlated with the extent of vision loss, particularly at the lower eccentricities of the represented visual field in V1, which is where the loss is projected in STGD1. We found no significant changes in GABA, however as explained in the previous chapter, GABA was difficult to measure due to macromolecule contamination. Therefore, these results may be a measure of noise and therefore are unable to indicate if reorganisation occurs in the visual cortex when vision loss begins after the critical period. Our novel findings demonstrate, a considerable change in neurochemical concentrations after vision loss in adulthood. These results should be considered alongside treatments that aim to restore loss at the retina in adulthood, as the cortex may be unable to process the restored visual input due to degeneration.

7.2 Introduction

The cortex is an interconnected circuit of neurons and supporting glial cells, the neurons communicate with each other through action potentials and chemical signalling. Measures of neurochemistry can provide a valuable insight into neuronal and glial cell function, within a specific region of the cortex. In humans, Magnetic Resonance Spectroscopy (MRS) is a non-invasive technique that can measure neurochemical concentrations *in vivo*.

Glutamate levels are involved in cortical plasticity and GABA is fundamental in modulating cortical inhibitory plasticity by regulating membrane potential (Griffen and Maffei, 2014). Glutamate levels measured with MRSI do not relate directly to neuronal plasticity, as glutamate-related plasticity is generally reflected in changes in the density and sensitivity of receptors, and therefore undetectable by MRSI (Stagg, 2014). In human MRS studies, GABA levels are predominantly used as a measure of plasticity. Indications of lower GABA levels have been found in the visual cortex of individuals with vision loss in infancy, however the results from these studies were highly variable (Weaver et al., 2013). These results suggest a change in GABA in the visual cortex follows visual loss, however at the time of these studies the techniques to measure GABA were not as sensitive as the techniques used now, therefore these results should be interpreted with caution. As stated in the introductory chapter, MRS is thought to provide a measure of the extracellular concentration of GABA (Stagg et al 2011 a, b, c). Therefore, a measured increase in GABA concentrations is thought to reflect tonic inhibitory activity that affects local neuronal excitability (Stagg et al, 2011 a, b, c). Neuronal death may also push GABA into the extracellular space; therefore, when interpreting GABA results from MRS they should be considered in conjunction with concentrations of the other neurochemicals.

NAA levels are an accepted marker for neuronal health or dysfunction (Rigotti et al., 2007). High levels of NAA represent neuronal integrity, whilst lower levels are a marker for neuronal loss. As explained in the introductory chapter, non-human primate models of vision loss in adulthood have found markers for cortical degeneration in the visual cortex, rather than functional reorganisation (Horton and Hocking, 1998). As non-human primates share a similar visual system to humans, similar

degeneration processes would be expected to occur in the adult human visual cortex after vision loss. In human populations with vision loss ^{1}H-MRS has been used to measure if neuronal degeneration is occurring, however the studies have found inconsistent results (Boucard et al., 2009). This could be due to the large voxel size used, which does not optimally cover the LPZ from these visual disorders. An increase in *myo*-Ins is linked to damage to myelin and glial cell proliferation (Haris et al., 2011). Therefore, an increase in glial cell number is a sign of cortical degeneration. It has been found to be elevated in the visual cortex after vision loss (Bernabeu et al., 2009) (Weaver et al., 2013), however the majority of the patients in these studies had vision loss before the critical period. Therefore, currently very little is known about how the human visual cortex responds to a loss of input in adulthood.

7.2.1 Rationale

As V1 contains a topographic organisation of the visual field, focal loss at the central retina will project to the posterior part of V1, as it represents the central part of the visual field. In this chapter MRSI was used to investigate if there are changes in the neurochemical concentrations in V1 due to vision loss in patients with STGD1.

Hypothesis 1: NAA, a marker for neuronal degeneration, will be reduced in posterior regions of V1 compared to controls, but no different in anterior regions reflecting the location of vision loss.

Hypothesis 2: *Myo*-Ins, a marker for glial cell proliferation, will be elevated in posterior regions V1 compared to controls, but no different in anterior regions reflecting the location of vision loss.

Hypothesis 3: Glutamate levels are linked to neuronal activity, where a decrease should reflect a decrease in neuronal function. Glutamate will be reduced in posterior regions of V1 compared to controls, but no different in anterior regions reflecting the location of vision loss.

Hypothesis 4: After a loss of sensory input, there will be initial changes in chemical signalling towards lower inhibition, controlled by a decrease in inhibitory GABA activity. GABA will be reduced in posterior regions of the occipital lobe compared to controls, but no different in anterior regions reflecting the location of vision loss.

Hypothesis 5: Neuro-metabolite concentrations should correlate with disease severity, as those with a larger amount of vision loss should show a larger change in neuro-metabolite concentrations.

7.3 Methods

7.3.1 Participants

The work in this chapter includes 15 participants with STGD1 (7 females, 8 males, mean age 34.0 ± 15.1 SD) and 14 comparison controls with healthy eyes and normal vision (6 females, 8 males, mean age 38.7 ± 14.6 SD). Four participants (1 STGD1, 3 controls) were excluded from the subsequent analyses due to issues with slab reconstruction (one participant) or spectrum contamination (three participants).

7.3.2 MRSI acquisition

The density weighted concentric ring trajectory (DW-CRT) k-space sampling acquisition method (DWCRT-MRSI) described in Steel et al (2018) was used to acquire the MRSI data, the same acquisition parameters were used as those described in chapter 6. The DWCRT-MRSI slab (5x5x10mm) was placed to optimally cover the calcarine sulcus whilst avoiding the edges of the brain. As previously mentioned in chapter 6, the dura contains lipids, and part of the lipid spectra overlaps with the GABA peaks. If dura is included in the slab acquisition, then this interferes with the measurement of GABA as it creates lipid contamination in the spectra. Therefore, the slab was placed with at least $5mm^3$ (1 voxel size) from the edge of the brain, medially along the calcarine sulcus. An average of the individual slab placements that were used in this chapter is shown in figure 74.

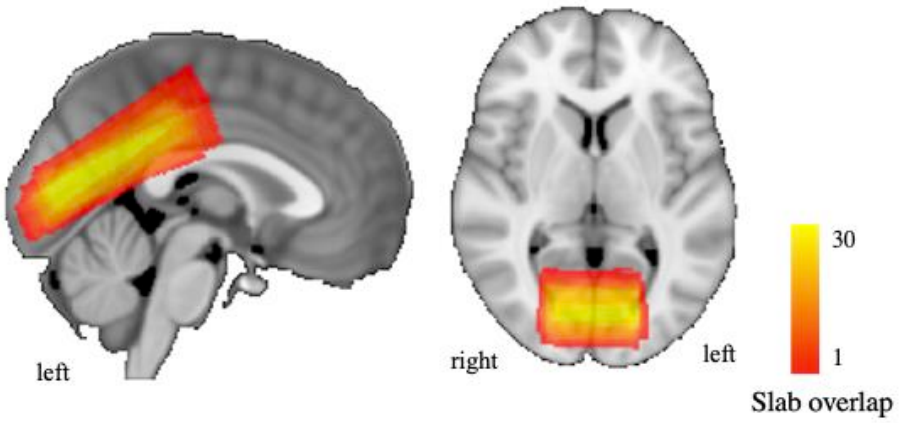


Figure 74: Average DWCRT-MRSI *slab placement (red - yellow) over the calcarine sulcus for the 30 controls and STGD1 patients who were included in the analysis, overlaid over the MNI152 brain.*

7.3.3 Analysis

The MRSI analysis described in chapter 6 was applied to this data, where the neurometabolite concentrations were referenced against total creatine (PCr+Cr), corrected for grey matter fraction, and had CRLB thresholds applied (20% for NAA, myo-Ins, glutamate and 50% for GABA). The slab voxels were allocated to each of the visual field eccentricity ROIs of V1 from the Benson atlas used in Chapter 4 (figure 75) (Benson et al., 2012). The V1 peripheral ROIs were each separated by a few degrees (4 – 6°, 7 – 15°, 16° - 30° and 40° - 90°) to ensure the representations were not completely overlapping. The DWCRT-MRSI slab was constrained within the separate V1 ROIs (figure 75). This meant that neurochemical concentrations in V1 were compared to areas within and outside the LPZ in STGD1. Only 2° - 90° of the represented visual field in V1 was located within the slab. The ROI for 0° - 2° of the visual field and part of the 2 - 4 ° V1 ROIs were outside the DWCRT-MRSI slab limits.

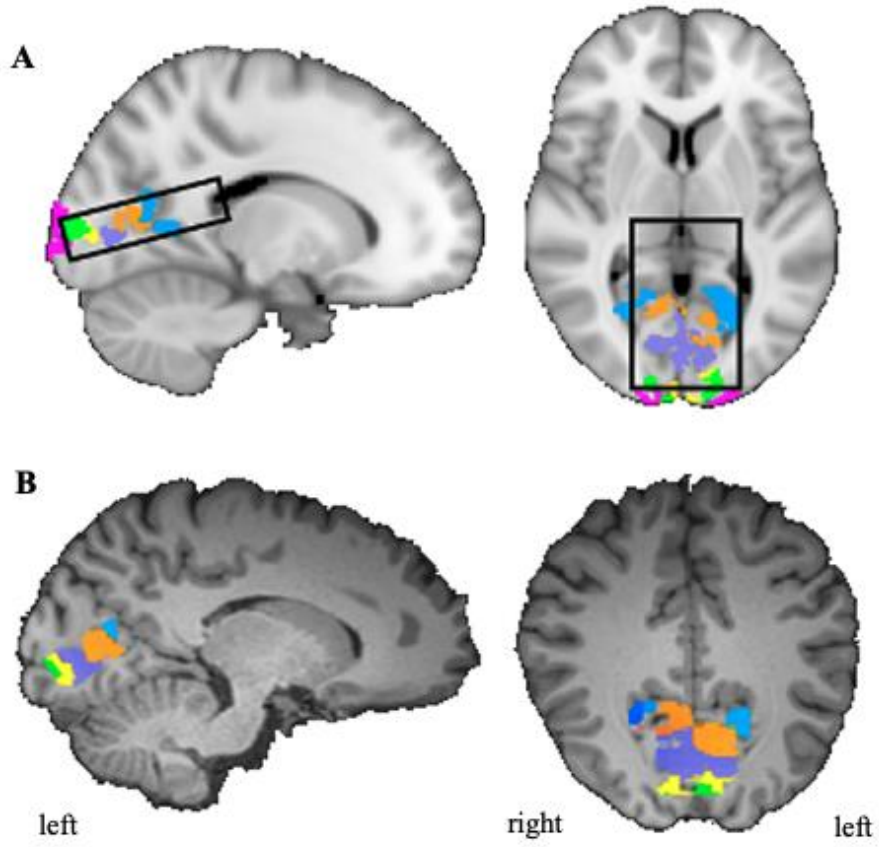


Figure 75: A) Regions of interest along V1 that respond to 0 - 90° of the visual field (0 - 2° = hot pink, 2 - 4°= green, 4 - 6° = yellow, 7 - 15° = purple, 16 - 30° = orange, 40 - 90° = blue) eccentricity generated from functional retinotopy in the Benson atlas, used to measure metabolites. Black rectangle shows the DWCRT-MRSI slab overlaid to maximally cover V1 whilst avoiding the edge of the brain, overlaid over the standard brain (MNI152). B) DWCRT-MRSI voxels constrained within the regions of interest along V1 that respond to 2 - 90° of the visual field (2 - 4°= green, 4 - 6° = yellow, 7 - 15° = purple, 16 - 30° = orange, 40 - 90° = blue) overlaid over the individual T1w image.

7.3.3.1 Correction for grey matter fractions

As stated in the previous chapter - NAA, *myo*-Ins and glutamate show the predicted trend in concentration compared to grey matter fraction, however GABA shows the opposite, and this could be due to the modelling of macromolecules as the signal may be measuring GABA+ macromolecules concentrations, therefore we are not confident in our method to quantify GABA. Therefore, this

analysis can accurately measure NAA and *myo*-Ins and Glu, but GABA concentrations should be interpreted with caution.

7.3.3.2 Statistical Analysis

Metabolite maps were thresholded for CRLB and SNR using the *fslmaths* command within FSL. Statistical analyses were performed using GraphPad Prism (version 9.0). Non-parametric t-tests were used to calculate if there was a difference between groups in the overall concentrations of the chosen neurochemicals in V1. The non-parametric statistical tests were used due to the small population sample size. A Two-way ANOVA was performed with main effects of group (STGD1 v control) and eccentricity to determine differences in neurometabolite concentrations. Tukey post-hoc analysis was used to investigate whether there was a statistically significant difference in neurochemical concentrations between groups within the individual eccentricities of the represented visual field in V1. For all analyses described in this chapter, outliers of (+/-) 2.7 standard deviations from the mean were removed and results were considered statistically significant if they were less than $p < 0.05$.

Due to the range of disease severities in the STGD1 patient cohort, the neurochemical concentrations were expected to vary with disease severity. Therefore, Pearson's R was used to investigate if there were significant correlations between the neurochemical concentrations and extent of vision loss in the individual V1 ROIs. These results were corrected for multiple comparisons using Bonferroni type adjustment, as three comparisons were made, the level of significance was chosen at $p < 0.017$.

7.4 Results

7.4.1 N-Acetylaspartate concentrations do not change within V1 in STGD1

NAA is a marker for neuronal cell health, therefore a decrease in NAA would reflect neuronal damage. A lack of visual input from photoreceptor loss could cause degeneration of the V1 neurons that would be reflected in a decrease in NAA. Collapsed across V1, the relative NAA concentration ratio (NAA:tCr) was not significantly different in the STGD1 group (1.319 +/- 0.11) compared to controls (1.222 +/- 0.36): $t(28) = 1.03$, $p = 00.313$ (figure 76) implying there is not a large difference

in NAA:tCr concentrations in V1. When investigated by eccentricity, there was a significant effect of eccentricity ($F(4, 115) = 53.26$, $p < 0.001$) (figure 76) but no significant effect of group or the interaction between them. Therefore, there is a non-significant difference in the in NAA:tCr concentrations of the eccentric positions in V1 between STGD1 and controls, this goes against the predicted hypothesis of a significant decrease in NAA:tCr.

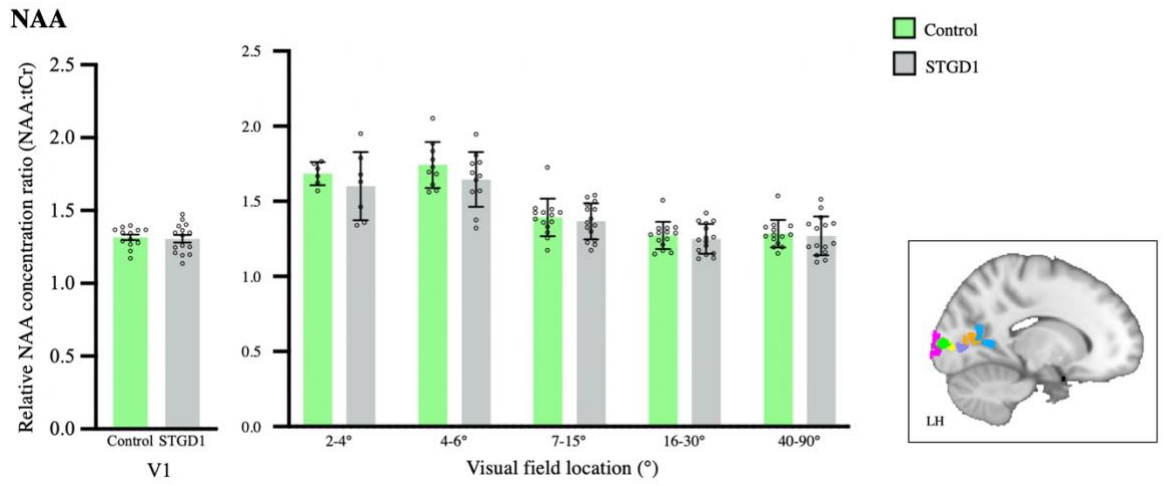


Figure 76: Primary visual cortex (V1) (left and right hemispheres averaged) NAA:tCr *concentrations between controls with healthy vision (green) and STGD1 (grey) across V1 (left) and the represented eccentric positions (°) of the visual field (right). Individual data points are shown with circles (black) and error bars show standard deviation. There was a non-significant effect of both group and eccentricity. Regions of interest along V1 of the left hemisphere that respond to 0 - 90° of the visual field (0 - 2° = hot pink, 2 - 4°= green, 4 - 6° = yellow, 7 - 15° = purple, 16 - 30° = orange, 40 - 90° = blue) eccentricity generated from functional retinotopy in the Benson atlas, used to measure metabolites, overlaid over the standard brain (MNI152). Bars show significance at $p \leq 0.05$ (*), $p \leq 0.01$ (**) or $p \leq 0.001$ (***) or non-significance of $p > 0.05$ (ns).*

7.4.2 Myo-inositol concentrations increase within V1 in STGD1

Myo-Ins is a marker for glial cell proliferation, therefore an increase in *myo*-Ins would reflect an increase in glial cell number. A lack of visual input from photoreceptor loss should cause

degeneration of the V1 neurons that should cause an increase in supporting glial cells reflected in an increase in *myo*-Ins. Collapsed across V1, the relative *myo*-Ins concentration ratio (*myo*-Ins:tCr) was significantly higher in the STGD1 group (0.87 +/- 0.05) compared to controls (0.81 +/- 0.06): t (28) = 2.69, p < 00.012 (figure 77). When investigated by eccentricity, there was a significant effect of group (F(1, 118) =13.77, p = 0.0003 and eccentricity (F(4, 118) = 7.06, p < 0.001) but no significant interaction (figure 77). Thus, the *myo*-Ins:tCr concentration did not show STGD1-specific reduction according to eccentricity. These findings support the hypothesis that levels of *myo*-Ins:tCr are elevated in V1 after vision loss.

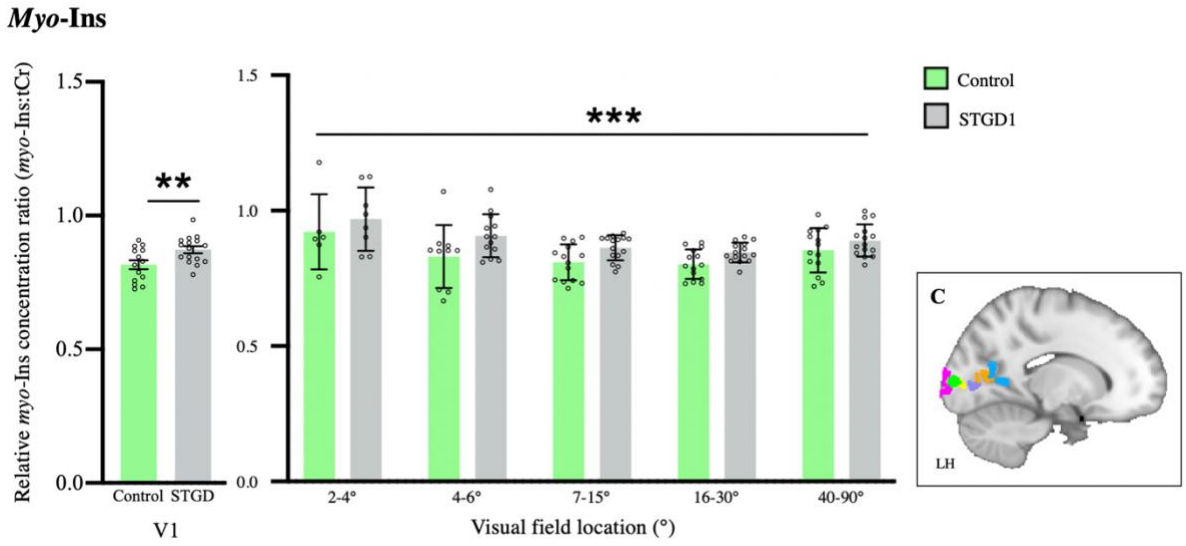


Figure 77: Primary visual cortex (V1) (left and right hemispheres averaged) myo-Ins:tCr *concentrations between controls with healthy vision (green) and STGD1 (grey) across V1 (left) and the represented eccentric positions (°) of the visual field (right). Individual data points are shown with circles (black) and error bars show standard deviation. There was a significant effect of both group and eccentricity but the pairwise comparisons were not significant. Regions of interest along V1 used to measure metabolites, colour coded as figure 76 overlaid over the standard brain (MNI152). Bars show significance at p ≤ 0.05 (*), p ≤ 0.01 (**) or p ≤ 0.001 (***) or non-significance of p > 0.05 (ns).*

7.4.3 Glutamate concentrations decrease within V1 in STGD1

Glutamate is a marker for neuronal function, therefore a decrease in glutamate would reflect a decrease in neuronal activity. A lack of visual input from photoreceptor loss should cause a reduction in activation within V1 that would be reflected in a decrease in glutamate. Collapsed across V1, the relative glutamate concentration ratio (Glu:tCr) was not significantly different in the STGD1 group (0.95 +/- 0.08) compared to controls (0.97 +/- 0.07): t (28) = 0.64, p < 0.529 (figure 78). When investigated by eccentricity, there was a significant effect of group: F(1, 119) =8.58, p = 0.004, eccentricity F(4, 119) = 22.79, p < 0.001 (figure 78), and a significant interaction between them: F(4, 115) = 4.13, p = 0.004 (figure 78). When investigated at eccentric positions, I found significant pairwise differences at 2 - 4° (p = 0.0353) and 4 - 6° (p = 0.0154) of the represented visual field, where STGD1 have significantly lower glutamate levels than controls. The lower eccentricities of the projected visual field re the region of projected loss in STGD1 and therefore this may reflect the reduced functional input to V1. Thus, Glu:tCr concentration did show STGD1-specific reduction according to eccentricity. These findings support the hypothesis that levels of Glu:tCr decrease in V1 after vision loss.

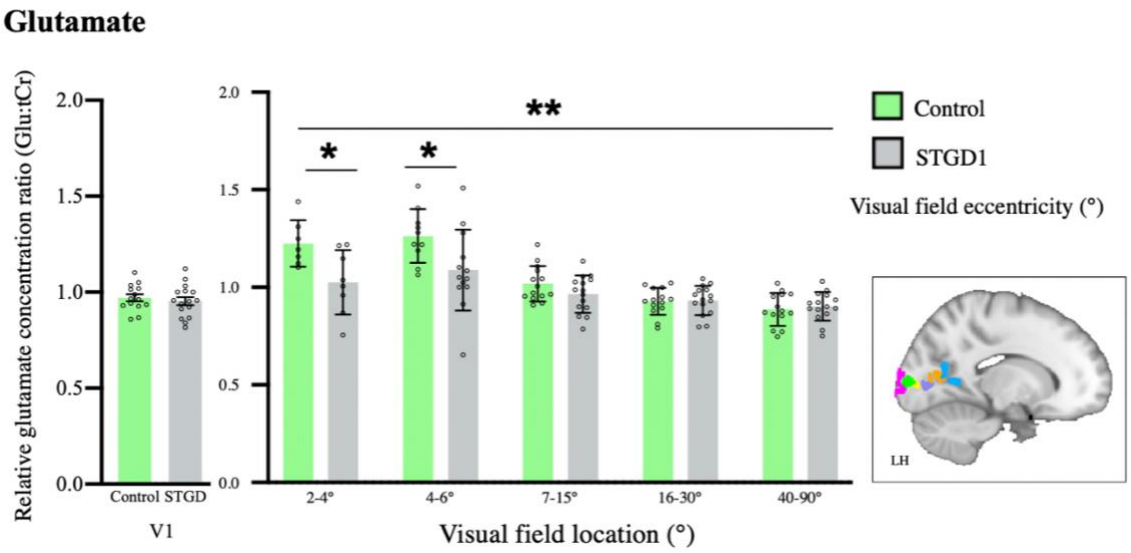


Figure 78: Primary visual cortex (V1) (left and right hemispheres averaged) Glu:tCr *concentrations between controls with healthy vision (green) and STGD1 (grey) across V1 (left) and the represented*

eccentric positions (°) of the visual field (right). Individual data points are shown with circles (black) and error bars show standard deviation. There was a significant effect of both group and eccentricity but the pairwise comparisons were not significant. Regions of interest along V1 used to measure metabolites, colour coded as figure 76, overlaid over the standard brain (MNI152). Bars show significance at p ≤ 0.05 (*), p ≤ 0.01 (**) or p ≤ 0.001 (***) or non-significance of p > 0.05 (ns).

7.4.4 GABA concentrations do not change within V1 in STGD1

A lack of visual input from photoreceptor loss should cause an initial change in chemical signalling towards lower inhibition in V1 which would be reflected in a decrease in GABA. Collapsed across V1, the relative GABA concentration ratio (GABA:tCr) was not significantly different in the STGD1 group (0.41 +/- 0.08) compared to controls (0.42 +/- 0.09): t (28) = 0.54, p < 0.593 (figure 79). When investigated by eccentricity, there was a non-significant effect of group: F(4, 104) =2.82, p = 0.096, eccentricity F(4, 104) = 1.34, p = 0.260 or the interaction between them F(4, 104) = 0.69, p = 0.259 (figure 79). There were not significantly different when specific eccentricity positions were compared between groups. These findings do not support the hypothesis that levels of GABA:tCr decrease in V1 after vision loss.

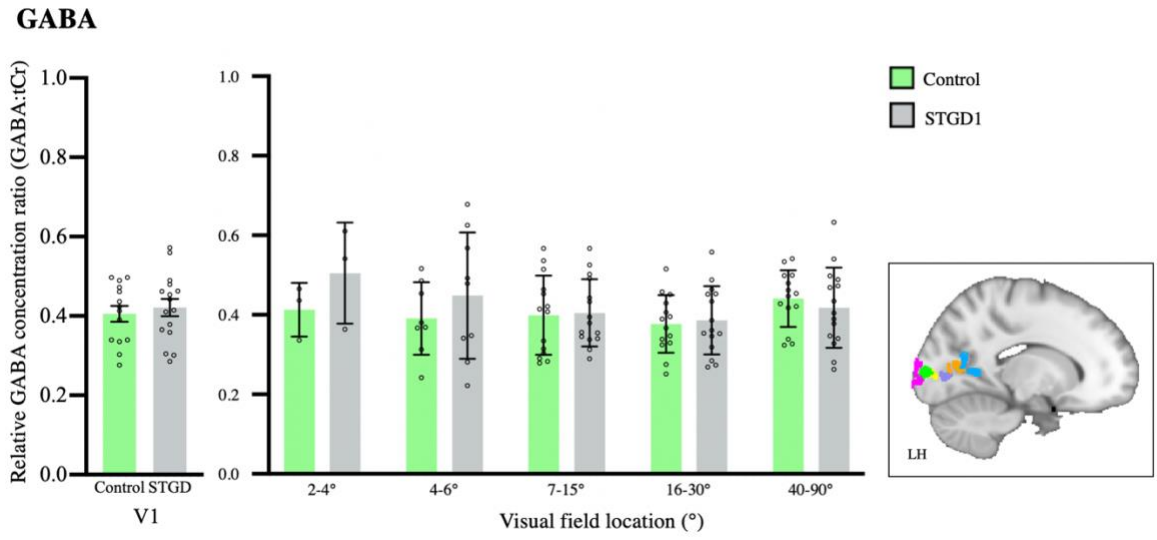


Figure 79: Primary visual cortex (V1) (left and right hemispheres averaged) GABA:tCr *concentrations between controls with healthy vision (green) and STGD1 (grey) across V1 (left) and the represented eccentric positions (°) of the visual field (right). Individual data points are shown*

with circles (black) and error bars show standard deviation. All eccentricity comparisons between STGD1 and controls were non-significant. Regions of interest along V1 used to measure metabolites, colour coded as figure 76 overlaid over the standard brain (MNI152). Bars show significance at p ≤ 0.05 (*), p ≤ 0.01 (**) or p ≤ 0.001 (***) or non-significance of p > 0.05 (ns).

7.4.5 Neurochemical markers for cortical degeneration correlate with disease severity

As there is a range of disease severity in the STGD1 group, the neurochemical concentrations would be expected to vary with disease severity. Therefore, the individual V1 visual field locations were correlated with two different measures of vision loss to investigate if the extent of disease severity and therefore vision loss relates to a larger difference in neurochemical concentrations compared to controls.

Neurometabolite concentrations vary with the amount of functional vision loss

Retinal sensitivity provides an indication of the participants functional visual ability and is calculated by the responsiveness of the retina to light (dB) (1 - 9°) using microperimetry (Chapter 3). Both the microperimetry response and neurometabolite concentrations were divided into three different visual field eccentricities, small, medium, and large. The exact retinal sensitivity locations and the visual field eccentricities are not completely overlapping as the retinal sensitivities were measured every 2° and only the central 9° of the visual field was measured.

For *myo*-Ins:tCr, the concentration was significantly correlated with retinal sensitivity at the small eccentricity ($r(7) = -0.81$, $p = 0.001$)) but not medium ($r(12) = -0.49$, $p = 0.088$) or and large ($r(14) = -0.42$, $p = 0.116$ (figure 80B). These findings support the hypotheses that *myo*-Ins increases with a larger amount of vision loss.

For NAA:tCr, the concentration was significantly correlated with retinal sensitivity at the small eccentricity ($r(6) = 0.78$, $p = 0.036$) but not medium ($r(10) = -0.07$, $p = 0.833$) or large ($r(14) = 0.09$,

p = 0.741) (figure 80B). These findings support the hypotheses that NAA decreases with a larger amount of vision loss.

For Glu:tCr, the concentration was significantly correlated with retinal sensitivity at the medium eccentricity (r (7) =-0. 36, p = 0.375) but not the small (r (12) = 0.35, p = 0.233) or large (r (28) = 0.17, p =0.523) (figure 80B). These findings support the hypotheses that glutamate decreases with a larger amount of vision loss.

GABA:tCr concentrations were not significantly correlated with retinal sensitivity at medium (r (9) = -0.50, p = 0.136) or large (r (15) = -0.37, p =0.157) (figure 80 D). For GABA, the small eccentricity only had 4 participants data that passed the CRLB thresholds, so these were treated as noise and excluded from the analysis. These findings do not support the hypotheses that NAA, glutamate, or GABA concentrations change with a larger amount of vision loss in the central representations of the visual field.

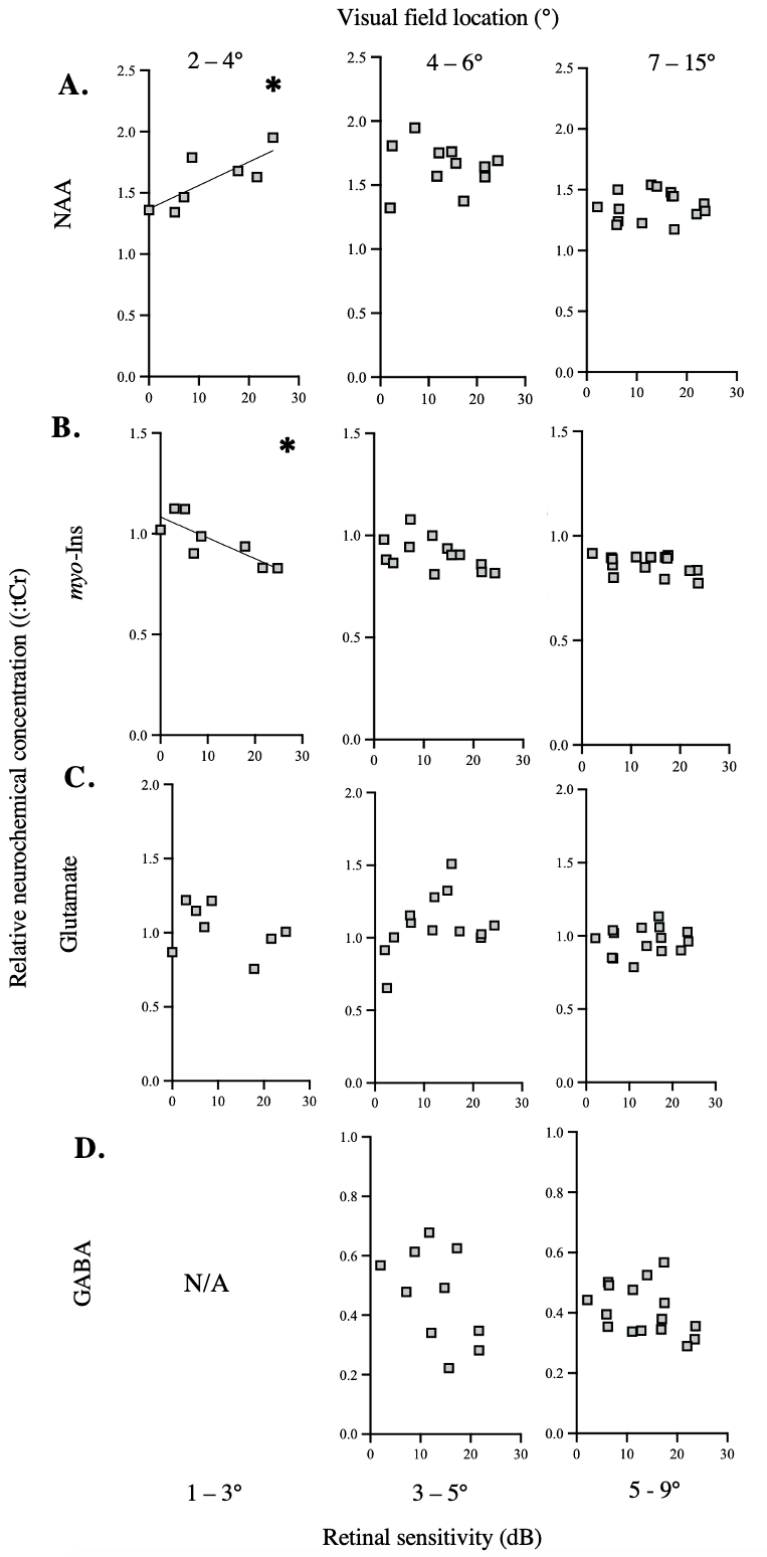


Figure 80: Retinal sensitivity (dB) 1 – 9° corelated with neurochemical concentrations (NAA (A), myo-Ins (B), glutamate (C), GABA (D)) (:tCr) from 2 - 15° of the represented visual field in V1. Individual data points from STGD1 patients (grey squares) are shown and lines of best fit show the correlations and an asterisk represent significance.

Neurometabolite concentrations vary with amount of structural vision loss

Photoreceptor layer thickness (μm) provides an indication of the amount of structural degeneration in the retina and is measured using OCT (Chapter 4). Both the photoreceptor layer thickness and neurometabolite concentrations were divided into three different visual field eccentricities, small, medium, and large.

For NAA:tCr, the concentration was significantly correlated with photoreceptor layer thickness at the small eccentricity ($r(5) = 0.85$, $p = 0.033$) but not the medium ($r(9) = 0.17$, $p = 0.634$) or large ($r(14) = 0.09$, $p = 0.749$) (figure 81A). These findings support the hypotheses that NAA decreases with a larger amount of vision loss, particularly in the central representations of the visual field. These findings are consistent with the correlates with retinal sensitivity as a measure for disease severity.

For *myo*-Ins:tCr, the concentration was significantly correlated with photoreceptor layer thickness at the medium eccentricity ($r(11) = -0.59$, $p = 0.040$) and large ($r(14) = -0.53$, $p = 0.044$), but not the small ($r(7) = -0.346$, $p = 0.400$) (figure 81B). These findings support the hypotheses that *myo*-Ins increases with a larger amount of vision loss, particularly in the central representations of the visual field. These findings are consistent with the correlates with retinal sensitivity as a measure for disease severity.

Glu:tCr and GABA:tCr concentrations were not significantly correlated with photoreceptor layer thickness at small eccentricity (Glu:tCr; ($r(7) = -0.01$, $p = 0.973$) medium (Glu:tCr; ($r(11) = -0.09$, $p = 0.758$), GABA:tCr ($r(7) = -0.16$, $p = 0.704$)) or large (Glu:tCr; ($r(14) = 0.12$, $p = 0.668$), GABA:tCr ($r(14) = 0.02$, $p = 0.933$) (figure 81 A, B, C, D). For GABA, the small eccentricity only had 4 participants data that passed the CRLB thresholds, so this was removed from the analysis. These findings do not support the hypotheses that NAA, glutamate, or GABA concentrations change with a larger amount of vision loss in the central representations of the visual field.

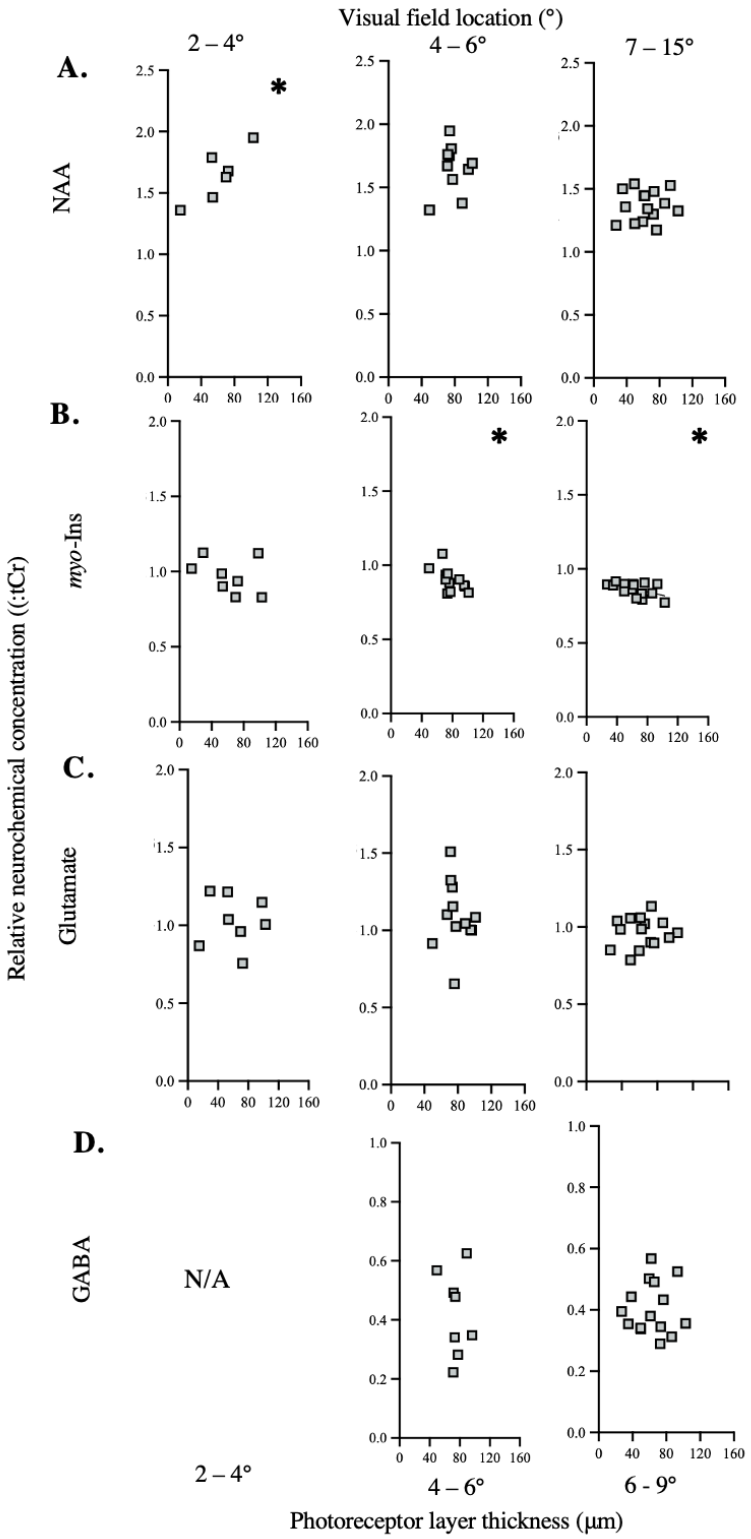


Figure 81: Photoreceptor layer thickness (µm) (2 - 9°) corelated with neurochemical concentrations (NAA (A), myo-Ins (B), glutamate (C), GABA (D)) (:tCr) from 2 - 15° of the represented visual field in V1. Individual data points from STGD1 patients (grey squares) are shown and lines of best fit show the correlations and an asterisk represent significance.

7.5 Discussion

This chapter provides the first evidence for changes in neurochemistry within V1 as a result of vision loss from STGD1. M*yo*-Ins, which reflects glial cell proliferation shows a significant difference between groups and also correlates with disease severity. Similarly, glutamate which is a marker for neuronal function is significantly decreased within V1 in STGD1 compared to controls and even showed significant pairwise differences in the region of projected visual field loss in STGD1. Whereas, NAA, which is a marker for neuronal integrity does not show differences between groups but correlated with the amount of vision loss. GABA, which is a marker for neuronal reorganisation does not show changes between groups, but this metabolite was difficult to measure due to macromolecule contamination.

7.5.1 Myo-inositol levels are elevated within V1 in STGD1

The literature on neurochemical changes after vision loss has thus far provided conflicting results (Bernabeu et al., 2009; Boucard et al., 2009). The work presented here uses the DWCRT-MRSI technique which has a higher spatial resolution than the ^{1}H-MRS previously used and has shown specific regional changes within V1 in neuro-metabolites that are markers for cortical degeneration.

Myo-Ins, which is a marker for glial cell health, was significantly higher within V1 between STGD1 patients compared to controls. There was a slight but non-significant increase in *myo*-Ins across all eccentricities of the represented visual field. When correlated with vision loss (both structural and functional) *myo*-Ins showed the predicted significant correlation with the amount of vision loss and the concentrations at the representation of the visual field between STGD1 and controls. Participants with a lower retinal sensitivity and therefore larger amount of vision loss had higher *myo*-Ins levels, suggesting a larger amount of cortical degeneration across the whole of V1, and particularly higher in the represented part of the vision loss in V1. These results replicate the findings of an increase in *myo*-Ins concentration in the visual cortex in a group of patients with vision loss before and after the critical period (Bernabeu et al., 2009). Therefore, the *myo*-Ins concentrations measured may reflect an

increase in glial cell proliferation, which occurs in response to neuronal degeneration in V1. This large increase in *myo*-Ins across V1 may reflect an increase in gliosis which occurs before other markers of neuronal degeneration in the visual cortex after a loss of input.

7.5.2 NAA levels correlate with disease severity in STGD1

NAA, which is a marker for neuronal loss, was not significantly different between STGD1 and controls. This reflects the inconsistent results found previously in the literature in neurochemical changes after vision loss concentrations (Boucard et al., 2009; Zhang et al., 2013). NAA is present at high concentrations in the cortex, therefore specific NAA reductions related to neuronal degeneration may be diluted by the global NAA levels. NAA concentrations correlated with the amount of vision loss at the central representation of the visual field. This may reflect specific neuronal degeneration at the region of projected loss in STGD1.

7.5.3 Reduced glutamate levels within V1 in STGD1

These experimental results show evidence for degeneration in the adult human visual cortex after vision loss from retinal disease. The results from glutamate as a measure of neuronal activity also strengthen the hypotheses that *myo*-Ins results are representing cortical degeneration. There was a significant decrease in glutamate within V1, and there were significant pairwise differences in glutamate levels within the region of projected visual field loss in STGD1. This reduction in glutamate levels, reflects a reduction in cortical function (Ip et al, 2017), due to the loss of input in STGD1.

7.5.4 GABA levels do not change within V1 in STGD1 compared to controls

These experimental results do not show evidence for reorganisation in the adult human visual cortex after vision loss from retinal disease. The results from GABA as a measure of neuronal inhibition do not show a significant difference between STGD1 patients and controls. There was a slight but non-significant increase in GABA particularly at the eccentricities of the represented visual field in V1, however the data points are widely variable. GABA is present in very low quantities in the brain and

its spectral peaks overlap with metabolites with much higher concentrations in the cortex. GABA is difficult to measure shown by the amount of data points, particularly at posterior regions of V1 that did not pass the thresholds for data quality, therefore firm conclusions cannot be generated without further corrections for macromolecule contamination within the data. The large variability in GABA concentrations are in line with the results found in the visual cortex of participants with anophthalmia (Coullon et al., 2015).

7.5.5 Limitations and future directions

This is the first study to position the DWCRT-MRSI slab over the calcarine to investigate the effects of vision loss. The left and posterior edge on the DWCRT-MRSI slabs did not pass the thresholds for data quality due to inherent noise from the signal acquisition. This could be improved in the future by flipping the slab acquisition to the opposite direction, therefore the row of posterior voxels over the calcarine would avoid the acquisition contamination as the opposite edge (which is not of interest to the hypotheses) would be acquired first and therefore be contaminated instead. If the slab was acquired at a voxel width thinner laterally on either side, this would have meant we could have pushed the slab further posterior to encapsulate more of the central representation of the visual field, which is where the vision loss is represented in this patient group. Three of the participants' contaminated spectra were from motion, therefore a way to correct for motion in the pre-processing could improve the quality of the spectra to increase the amount of useable data for statistical comparisons. Metabolite concentrations vary between the GM, WM and CSF. Therefore, future analysis should include GM as a co-variate of no interest in order to control for the ratio of tissue contained within each voxel.

Retinal degeneration is progressive in STGD1, and this project plans to measure the longitudinal effect of how an increase in vision loss affects the visual cortex. Therapies that aim to restore retinal function could use DWCRT-MRSI to investigate how V1 responds neurochemically to the restored input over time. This would provide a valuable insight into the individual differences that affect visual recovery, and these results could be used to inform therapies in order to optimally recover visual function. Therefore, the longitudinal study can investigate how vision loss affects the amount of

degeneration in the visual cortex and could provide a measure of the rate of neuronal degeneration that occurs from a loss of visual input.

7.5.6 Chapter Conclusion

To summarise, the work presented in this chapter shows a change in neurochemical concentrations in the visual cortex after vision loss. The findings that *myo*-Ins concentrations are elevated in V1 after vision loss shows a strong indication that degeneration is occurring after a loss of input in adulthood. Both *myo*-Ins and NAA were found to correlate with the amount of visual loss in the central visual field represented in V1. This demonstrates that a larger amount of vision loss in adulthood causes an increase in degeneration of the visual cortex. This has vital implications for therapies that aim to restore vision at the retina, as cortical degeneration should be considered when investigating how to optimally restore visual function.

8 General discussion

Measuring degeneration and the capacity for reorganisation in the adult human visual cortex

This chapter reviews the major findings of the work presented in this thesis. I first discuss the implications of these findings in relation to the literature that investigates how vision loss affects the visual cortex. Second, I explain the general limitations of the work presented here. Third, I discuss the possible directions for future research to develop on these findings. Finally, I summarise the main conclusions found from the work presented in this thesis.

8.1 Thesis overview

This thesis contributes to the current understanding of how the brain changes after a loss of sensory input to the visual system. I investigated the changes across the visual system after vision loss from the inherited retinal degeneration, STGD1, and then compared these results to controls with healthy vision. Several methods were used to investigate functional and structural changes at the retinae, along with measures of behavioural performance. The visual cortex was investigated with measures of structure, function, and neurochemistry to measure degeneration and understand the capacity for reorganisation after a loss of visual input. Retinal function was correlated with the MRI measures to investigate how disease severity impacts on brain structure, function, and neurochemistry.

In the first experimental chapter (Chapter 3) I quantified the visual function of STGD1 participants compared to controls with a healthy visual system. I did this using measures of retinal sensitivity, visual acuity, contrast sensitivity and colour vision. As predicted, the loss of cones in STGD1 reduces high acuity vision shown by reductions in visual acuity and contrast sensitivity. I found that the STGD1 participants had deficits across all three axes of colour space. This deficit was not specific to L-/ M-cones (red/green) compared to S-cones (blue) which has been found previously (Vandenbroucke et al., 2015). The STGD1 participants had scotomas larger than 0.34°, causing photoreceptor loss outside the S-cone free central fovea, therefore this would affect all three axes of colour space. Retinal sensitivity was used as a measure for disease severity, and I found that reduced retinal sensitivity correlated with reduced visual acuity, contrast sensitivity and colour vision.

In the second experimental chapter (Chapter 4), I quantified the structural loss at the retina and investigated if there were reductions in grey matter within the visual cortex in STGD1 compared to controls. As expected, STGD1 had an extreme reduction in photoreceptor layer thickness, and this was most severe at the central retinae. Even in a relatively large cohort of patients with STGD1 leading to significant visual loss, it was not possible to detect a difference in grey matter volume within the visual cortex. This did not replicate previous research in patients with STGD1 where reductions in GM volume in the visual cortex were found (Olivo et al., 2015). I found that STGD1

had significantly thinner grey matter within V1 compared to controls, suggesting the lack of visual input causes neuronal loss within V1. This supports findings from previous research that found cortical thinning within V1 in cohorts with macular degeneration (Burge et al., 2016; Hanson et al., 2019). However, there were no significant differences at a pairwise comparison between eccentricities of the visual field, which was expected as the central regions process the projected loss from STGD1. Focal thinning of posterior V1 was not found in the STGD1 group, which may be due to the range of disease severities, which made it difficult to detect a focal change at central representations of the visual field.

In the third experimental chapter (Chapter 5), I investigated functional changes within the visual cortex in STGD1. I found significantly reduced functional connectivity localised within the LOC which is responsible for object processing. The visual loss in STGD1 is localised to the central visual field which is responsible for high acuity vision, and this is needed for object recognition. These results are similar to those found in glaucoma which found reduced functional connectivity within the visual cortex after vision loss (Li et al., 2017). I found significantly decreased functional connectivity between the posterior V1 to the medial frontal cortex in STGD1 compared to controls. Connections between V1 and the medial frontal cortex are associated with visual attention modulation (Sims et al., 2021). As there is a reduced input into the posterior V1 this would require reduced attentional modulation from the medial frontal cortex. I found that the posterior V1 (region of projected loss) connectivity to both the LGN and hMT+ was significantly correlated with photoreceptor thickness and this was present bilaterally. This was not found with the anterior V1 (region of projected seeing field) and this dissociation between connectivity with the posterior and anterior V1 shows that the changes in connectivity may reflect the reduced input from vision loss in STGD1.

The final experimental chapter (Chapter 7), I investigated neurochemical differences within V1 in STGD1. I found a specific elevation in *myo*-Ins levels within V1 in STGD1 compared to controls, which reflects glial cell proliferation. Elevated *myo*-Ins levels were also found to correlate with disease severity at central representations of the visual field in V1. These results are in line with

previous research that found elevated myo-Ins levels after vision loss (Bernabeu et al., 2009; Weaver et al., 2013). I found that glutamate levels were significantly reduced in V1 in STGD1, particularly in the region of projected loss, compared to controls, which reflects a reduction in neuronal function due to the lack of input from vision loss. I did not find any changes in GABA levels; however, GABA was difficult to measure due to macromolecule contamination and is discussed further in section 8.3.

8.2 Summary of key findings

The work presented in this thesis demonstrates the effects of vision loss on the adult visual cortex. In particular it highlights how a loss of visual input impacts upon brain structure, function and neurochemistry. Overall, it appears that degeneration occurs in the visual cortex after a loss of visual input from STGD1. The findings from cortical structure show reduced cortical thickness within V1 in STGD1, reflecting a loss of neuronal bodies within the grey matter. However, this was not reflected in the neurometabolite measure of NAA, which is a marker for neuronal loss. NAA levels were not significantly different within V1 between STGD1 and controls, which may be due to the high concentration of global NAA within the cortex, which would dilute the specific NAA reductions related to neuronal degeneration. Elevated *myo*-Ins levels, which are a marker for glial cell proliferation were found within V1 in STGD1. This suggests that there is an increase in glial cells that are there to repair the degenerating neurons within V1 from a loss of visual input in STGD1.

8.2.1 Understanding cortical degeneration in the adult human visual cortex after vision loss

Neuronal degeneration should cause a decrease in neuronal activation, and this can be measured via functional connectivity. Decreased functional connectivity between V1 and the LOC was found in STGD1 compared to controls. As the LOC processes object recognition this requires high acuity vision which is reduced in STGD1 from degeneration of the central retina. Connectivity from the region of projected loss (posterior V1) to the frontal cortex is reduced in STGD1, suggesting a reduction in attentional modulation to the central part of the visual field. Decreased connectivity from posterior V1 to other visual areas (hMT+ and LGN) were found to correlate with disease severity, where a larger loss at the retina showed a greater reduction in connectivity strength. These results

suggest that neuronal degeneration occurs at the region of projected loss within V1, and this causes a reduction in cortical function. Glutamate, which is a marker for neuronal function, was decreased within V1 in STGD1, specifically in the region of projected loss, compared to controls. This suggests a lack of functional activation within V1 due to a lack of input from vision loss in STGD1.

8.2.2 Understanding the capacity for reorganisation in the adult human visual cortex after vision loss

The capacity for cortical reorganisation was measured via functional connectivity, glutamate, and GABA concentrations. If cortical reorganisation were to occur after vision loss, then functional connectivity and glutamate levels should increase reflecting an increase in neuronal connections. However, as previously stated functional connectivity and glutamate levels were found to decrease, reflecting a reduction in neuronal function, which may be due to cortical degeneration. GABA levels which are considered a marker for neuronal inhibition, should be reduced in the visual cortex if cortical reorganisation were to occur. No change in GABA levels were found between STGD1 and controls however, GABA levels were difficult to measure due to macromolecule contamination, which was largely in the area of the projected loss in STGD1. Therefore, these results suggest that there is a limited capacity for reorganisation in the visual cortex after vision loss but require further investigation when the measurements for GABA are more precise.

8.3 General limitations

The experiments described in this thesis are the first to show regional changes that reflect neuronal degeneration within V1 after vision loss from STGD1. This project had a relatively substantial sample size of 34 participations (17 STGD1, 17 controls) which is larger than previous studies investigating the visual cortex in STGD1 (Sabbah et al, 2017). However, for the neurochemical chapter this was reduced to n = 30 as data from 4 participants were unusable. This was largely due to participant motion, therefore if there was a way to correct for head motion within the MRSI analysis this should have increased the amount of useable data within that chapter.

The participants with STGD1 had a range of disease severities which allowed correlations between the amount of vision loss and measures of cortical structure, function, and neurochemistry. However, the participants with milder loss may have diluted the specific cortical changes from the participants with more severe vision loss and this may have been why regional changes were not found between groups at lower eccentricities of the projected visual field. STGD1 has a low prevalence within the population, and we had a strict inclusion criteria (bilateral loss to central 20° of retina, 3T MRI safe). This limited the number of participants we were able to recruit and therefore we were unable to only include patients with greater disease severities.

The cortical thickness and resting state techniques are well studied; and have standardised analysis pipelines, therefore, I am confident with the inferences made within these chapters. Cortical thickness was measured with T1w data at $1mm^3$ resolution which allows a measure of grey matter width but not a measurement of the specific layers within the grey matter. Therefore, it is unclear if the reduction in grey matter thickness within V1 reflects a reduction in neuronal bodies or glial cells and if this reduction is to the feedforward or feedback connections from the remaining cortex. Functional connectivity was measured using the BOLD signal at rest. The BOLD signal is a measure of regional changes in blood flow which are coupled to neuronal activity. The changes to blood flow are measured in seconds, compared to neuronal activation which occurs in milliseconds. Therefore, the changes in functional connectivity presented in chapter 5 are not directly linked to a reduction in neuronal activation caused by neuronal degeneration.

The research presented in this thesis is the first to use the DWCRT-MRSI acquisition positioned over the visual cortex. As explained in chapter 6 this caused macromolecule contamination to the spectra, which particularly affected the quantification of GABA. As this technique is relatively new, the inferences made should be interpreted with more caution. Voxels on the right and posterior edges of the MRSI slab did not pass the thresholds for data quality, due to inherent noise from the signal acquisition. The posterior edge of the slab overlapped with the projected vision loss in STGD1, therefore this region had fewer data points included in the analysis as many were removed due to

noise. This meant that the comparisons between groups at lower eccentricities of V1 had fewer data points, making the results less reliable. Therefore, it is unclear whether GABA concentrations decrease in the region of projected loss in STGD1.

8.4 Future research directions and open questions

Do these cortical changes vary with disease length?

The data presented in this thesis is part of a longitudinal study to investigate how loss affects the visual cortex over time. The within subject comparisons will be used as baseline measurements to compare to a two year follow up in the same cohort. The changes in cortical structure, function and neurochemistry presented in this thesis, were found to vary with disease severity. However, these may be differently affected in disease length and should be considered when restoring vision at the eye. The length of time since the onset of loss may have a larger effect on the visual cortex, as a longer disease duration would give the neurons more time to degenerate or reorganise. The age of disease onset is included in Table 1 and therefore this could be used to correlate with cortical structure, function, and neurochemistry to investigate whether this affects the amount of change within the cortex. The longitudinal follow up can provide a measure of the rate of degeneration at the retina and how this compares to the structural, functional, and neurochemical changes within the cortex. This would provide a measure for the optimal time frame for restoration at the retina that would still be able to be processed by the visual cortex.

Do these changes relate to inherited retinal degenerations that cause peripheral visual field loss?

The research presented in this thesis shows changes within V1 that reflect cortical degeneration after loss to the central visual field from STGD1. The data presented in this thesis is part of a larger cross-sectional study which included a group of participants with vision loss from choroideremia. Choroideremia is an inherited retinal degeneration that causes photoreceptor loss to the outer retina, this degeneration predominantly affects the rods. This degeneration of rods causes a loss to the peripheral visual field which is projected to the anterior section of V1. Measures of cortical structure, function and neurochemistry will be compared between STGD1 and choroideremia participants to

investigate whether the focal loss from the retina causes specific changes between the anterior and posterior V1. This would show if localised degeneration at the retina caused specific regional changes within the visual cortex.

Can the critical period be reopened in adulthood within the visual cortex?

The closing of the critical period limits the brain's ability to adapt to a change of input later in life. The findings from functional connectivity, and the glutamate and GABA results suggest that after vision loss in adulthood the visual cortex is less able to reorganise, shown by the reduction in functional connectivity, reduced glutamate levels and stable GABA levels within V1. If function is restored at the retina, the visual cortex would need to be able to process this restored input, therefore a mechanism to reopen the critical period and allow cortical reorganisation to occur would be needed. In adult rats with amblyopia, administration of fluoxetine has been found to reinduce ocular dominance plasticity (Maya-Vetencourt et al., 2008). They found that patching the healthy eye while the rat was administered with fluoxetine improved the visual acuity in the amblyopic eye. This suggests that fluoxetine can boost the capacity for reorganisation within the visual cortex in adulthood. Brain stimulation using transcranial direct current stimulation (tDCS) has been shown to reduce GABA levels and accelerate GABA-ergic plasticity on a visual training task (Karlafis et al, preprint). This shows that tDCS could be used to reduce GABA levels and therefore inhibition in the visual cortex in order to learn a new task. Therefore, this demonstrates that brain stimulation or GABA-ergic drugs could be used to reduce inhibition in the cortex, promoting plasticity for the visual cortex to process a restored input from the retina.

8.5 Final conclusions

To conclude this thesis demonstrates the effects of a loss of sensory input on the visual system by investigating degeneration and the capacity for reorganisation within the adult visual cortex. The loss of photoreceptors in STGD1 causes a loss to the central visual field which reduces high acuity and colour vision. Reductions in functional connectivity, cortical thinning, elevated *myo*-Ins levels reflecting glial cell proliferation and reduced glutamate levels were found within V1. These are all

markers for cortical degeneration, whereas markers for reorganisation (increased functional connectivity, increased glutamate, and decreased GABA) were not found; therefore, I conclude that after a loss of visual input in adulthood, the visual cortex degenerates and has less of a capacity for reorganisation.

References

Al-Bahadly, I & Bernt, R. (2010). LED-based color sensing system. Sens. Transducers J. 114.

Al-Khuzaei, S., S. Broadgate, C. R. Foster, M. Shah, J. Yu, S. M. Downes, and S. Halford, 2021a, An Overview of the Genetics of ABCA4 Retinopathies, an Evolving Story: Genes, v. 12.

Al-Khuzaei, S., M. Shah, C. R. Foster, J. Yu, S. Broadgate, S. Halford, and S. M. Downes, 2021b, The role of multimodal imaging and vision function testing in ABCA4-related retinopathies and their relevance to future therapeutic interventions: Therapeutic Advances in Ophthalmology, v. 13.

Alahmadi, B. O., A. A. Omari, M. F. Abalem, C. Andrews, D. Schlegel, K. H. Branham, N. W. Khan, A. Fahim, and T. Jayasundera, 2018, Contrast sensitivity deficits in patients with mutation-proven inherited retinal degenerations: Bmc Ophthalmology, v. 18.

Altman, L. K., 1997, Naked to the bone - Medical imaging in the twentieth century - Kevles,BH: New York Times Book Review, p. 31-31.

Alvarez, I., A. J. Parker, and H. Bridge, 2019, Normative cerebral cortical thickness for human visual areas: Neuroimage, v. 201.

Amunts, K., O. Kedo, M. Kindler, P. Pieperhoff, H. Mohlberg, N. J. Shah, U. Habel, F. Schneider, and K. Zilles, 2005, Cytoarchitectonic mapping of the human amygdala, hippocampal region and entorhinal cortex: intersubject variability and probability maps: Anatomy and Embryology, v. 210, p. 343-352.

Andersson, Jenkinson, M. & Smith, S. Non-linear registration, aka Spatial normalisation. Report No. TR07JA2, (2007).

Avesani, P., B. McPherson, S. Hayashi, C. F. Caiafa, R. Henschel, E. Garyfallidis, L. Kitchell, D. Bullock, A. Patterson, E. Olivetti, O. Sporns, A. J. Saykin, L. Wang, I. Dinov, D. Hancock, B. Caron, Y. M. Qian, and F. Pestilli, 2019, The open diffusion data derivatives, brain data upcycling via integrated publishing of derivatives and reproducible open cloud services: Scientific Data, v. 6.

Barrett, K E, et al. Ganong's Review of Medical Physiology. Twenty-fifth edition. New York: McGraw Hill Education, 2016.

Baseler, H. A., A. A. Brewer, L. T. Sharpe, A. B. Morland, H. Jagle, and B. A. Wandell, 2002, Reorganization of human cortical maps caused by inherited photoreceptor abnormalities: Nature Neuroscience, v. 5, p. 364-370.

Baseler, H. A., A. Gouws, K. V. Haak, C. Racey, M. D. Crossland, A. Tufail, G. S. Rubin, F. W. Cornelissen, and A. B. Morland, 2011, Large-scale remapping of visual cortex is absent in adult humans with macular degeneration: Nature Neuroscience, v. 14, p. 649-U148.

Bavik, C., S. H. Henry, Y. Zhang, K. Mitts, T. McGinn, E. Budzynski, A. Pashko, K. L. Lieu, S. Zhong, B. Blumberg, V. Kuksa, M. Orme, I. Scott, A. Fawzi, and R. Kubota, 2015, Visual Cycle Modulation as an Approach toward Preservation of Retinal Integrity: Plos One, v. 10.

Beckmann, C. F., M. Jenkinson, and S. M. Smith, 2003, General multilevel linear modeling for group analysis in FMRI: Neuroimage, v. 20, p. 1052-1063.

Beckmann, C. F., and S. A. Smith, 2004, Probabilistic independent component analysis for functional magnetic resonance imaging: Ieee Transactions on Medical Imaging, v. 23, p. 137-152.

Benjamini, Y., and Y. Hochberg, 1995, CONTROLLING THE FALSE DISCOVERY RATE - A PRACTICAL AND POWERFUL APPROACH TO MULTIPLE TESTING: Journal of the Royal Statistical Society Series B-Statistical Methodology, v. 57, p. 289-300.

Benjamini, Y., and D. Yekutieli, 2001, The control of the false discovery rate in multiple testing under dependency: Annals of Statistics, v. 29, p. 1165-1188.

Benke, T. A., A. Luthi, J. T. R. Isaac, and G. L. Collingridge, 1998, Modulation of AMPA receptor unitary conductance by synaptic activity: Nature, v. 393, p. 793-797.

Benson, N. C., O. H. Butt, D. H. Brainard, and G. K. Aguirre, 2014, Correction of Distortion in Flattened Representations of the Cortical Surface Allows Prediction of V1-V3 Functional Organization from Anatomy: Plos Computational Biology, v. 10.

Benson, N. C., O. H. Butt, R. Datta, P. D. Radoeva, D. H. Brainard, and G. K. Aguirre, 2012, The Retinotopic Organization of Striate Cortex Is Well Predicted by Surface Topology: Current Biology, v. 22, p. 2081-2085.

Bernabeu, A., A. Alfaro, M. Garcia, and E. Fernandez, 2009, Proton magnetic resonance spectroscopy (H-1-MRS) reveals the presence of elevated myo-inositol in the occipital cortex of blind subjects: Neuroimage, v. 47, p. 1172-1176.

Bettler, B., K. Kaupmann, J. Mosbacher, and M. Gassmann, 2004, Molecular structure and physiological functions of GABA(B) receptors: Physiological Reviews, v. 84, p. 835-867.

Binley, K., P. Widdowson, J. Loader, M. Kelleher, S. Iqball, G. Ferrige, J. de Belin, M. Carlucci, D. Angell-Manning, F. Hurst, S. Ellis, J. Miskin, A. Fernandes, P. Wong, R. Allikmets, C. Bergstrom, T. Aaberg, J. Yan, J. Kong, P. Gouras, A. Prefontaine, M. Vezina, M. Bussieres, S. Naylor, and K. A. Mitrophanous, 2013, Transduction of Photoreceptors With Equine Infectious Anemia Virus Lentiviral Vectors: Safety and Biodistribution of StarGen for Stargardt Disease: Investigative Ophthalmology & Visual Science, v. 54, p. 4061-4071.

Boucard, C. C., A. T. Hernowo, R. P. Maguire, N. M. Jansonius, J. Roerdink, J. M. M. Hooymans, and F. W. Cornelissen, 2009, Changes in cortical grey matter density associated with long-standing retinal visual field defects: Brain, v. 132, p. 1898-1906.

Boumezbeur, F., G. F. Mason, R. A. de Graaf, K. L. Behar, G. W. Cline, G. I. Shulman, D. L. Rothman, and K. F. Petersen, 2010, Altered brain mitochondrial metabolism in healthy aging as assessed

by in vivo magnetic resonance spectroscopy: Journal of Cerebral Blood Flow and Metabolism, v. 30, p. 211-221.

Brainard, D. H., 1997, The psychophysics toolbox: Spatial Vision, v. 10, p. 433-436.

Bridge, H., A. Cowey, N. Ragge, and K. Watkins, 2009, Imaging studies in congenital anophthalmia reveal preservation of brain architecture in 'visual' cortex: Brain, v. 132, p. 3467-3480.

Bridge, H., E. A. H. von dem Hagen, G. Davies, C. Chambers, A. Gouws, M. Hoffmann, and A. B. Morland, 2014, Changes in brain morphology in albinism reflect reduced visual acuity: Cortex, v. 56, p. 64-72.

Burge, W. K., J. C. Griffis, R. Nenert, A. Elkhetali, D. K. DeCarlo, L. W. V. Hoef, L. A. Ross, and K. M. Visscher, 2016, Cortical thickness in human V1 associated with central vision loss: Scientific Reports, v. 6.

Cai, C., J. G. Light, and J. T. Handa, 2017, Quantifying the rate of ellipsoid zone loss in Stargardt disease: Investigative Ophthalmology & Visual Science, v. 58.

Campbell, F. W., 1990, probing the human visual-system - a citation-classic commentary on application of fourier-analysis to the visibility of gratings by Campbell, F.W., and Robson,J.G.: Current Contents/Agriculture Biology & Environmental Sciences, p. 16-16.

Cecil, K. M., 2013, Proton Magnetic Resonance Spectroscopy Technique for the Neuroradiologist: Neuroimaging Clinics of North America, v. 23, p. 381-+.

Cinciute, S., 2019, Translating the hemodynamic response: why focused interdisciplinary integration should matter for the future of functional neuroimaging: Peerj, v. 7.

Clarke, W. T., C. J. Stagg, and S. Jbabdi, 2021, FSL-MRS: An end-to-end spectroscopy analysis package: Magnetic Resonance in Medicine, v. 85, p. 2950-2964.

Coullon, G. S. L., U. E. Emir, I. Fine, K. E. Watkins, and H. Bridge, 2015, Neurochemical changes in the pericalcarine cortex in congenital blindness attributable to bilateral anophthalmia: Journal of Neurophysiology, v. 114, p. 1725-1733.

Cudeiro, J., and A. M. Sillito, 2006, Looking back: corticothalamic feedback and early visual processing: Trends in Neurosciences, v. 29, p. 298-306.

Curcio, C. A., K. A. Allen, K. R. Sloan, C. L. Lerea, J. B. Hurley, I. B. Klock, and A. H. Milam, 1991, Distribution and morphology of human cone photoreceptors stained with anti-blue opsin: Journal of Comparative Neurology, v. 312, p. 610-624.

Dale, A. M., B. Fischl, and M. I. Sereno, 1999, Cortical surface-based analysis - I. Segmentation and surface reconstruction: Neuroimage, v. 9, p. 179-194.

Dan, H. D., F. Q. Zhou, X. Huang, Y. Q. Xing, and Y. Shen, 2019, Altered intra- and inter-regional functional connectivity of the visual cortex in individuals with peripheral vision loss due to retinitis pigmentosa: Vision Research, v. 159, p. 68-75.

Douaud, G., S. Smith, M. Jenkinson, T. Behrens, H. Johansen-Berg, J. Vickers, S. James, N. Voets, K. Watkins, P. M. Matthews, and A. James, 2007, Anatomically related grey and white matter abnormalities in adolescent-onset schizophrenia: Brain, v. 130, p. 2375-2386.

Dougherty, R. F., V. M. Koch, A. A. Brewer, B. Fischer, J. Modersitzki, and B. A. Wandell, 2003, Visual field representations and locations of visual areas V1/2/3 in human visual cortex: Journal of Vision, v. 3, p. 586-598.

Dyke, K., S. E. Pepes, C. Chen, S. Kim, H. P. Sigurdsson, A. Draper, M. Husain, P. Nachev, P. A. Gowland, P. G. Morris, and S. R. Jackson, 2017, Comparing GABA-dependent physiological measures of inhibition with proton magnetic resonance spectroscopy measurement of GABA using ultra-high-field MRI: Neuroimage, v. 152, p. 360-370.

E.R. Kandel, J.H. Schwartz and T.M. Jessell. Principles of Neural Science. New York: McGraw-Hill. 2000

Eickhoff, S. B., S. Heim, K. Zilles, and K. Amunts, 2006, Testing anatomically specified hypotheses in functional imaging using cytoarchitectonic maps: Neuroimage, v. 32, p. 570-582.

Eickhoff, S. B., K. E. Stephan, H. Mohlberg, C. Grefkes, G. R. Fink, K. Amunts, and K. Zilles, 2005, A new SPM toolbox for combining probabilistic cytoarchitectonic maps and functional imaging data: Neuroimage, v. 25, p. 1325-1335.

Ferreira, S., A. C. Pereira, B. Quendera, A. Reis, E. D. Silva, and M. Castelo-Branco, 2017, Primary visual cortical remapping in patients with inherited peripheral retinal degeneration: Neuroimage-Clinical, v. 13, p. 428-438.

Fischl, B., and A. M. Dale, 2000, Measuring the thickness of the human cerebral cortex from magnetic resonance images: Proceedings of the National Academy of Sciences of the United States of America, v. 97, p. 11050-11055.

Fishman, G. A., E. M. Stone, S. Grover, D. J. Derlacki, H. L. Haines, and R. R. Hockey, 1999, Variation of clinical expression in patients with Stargardt dystrophy and sequence variations in the ABCR gene: Archives of Ophthalmology, v. 117, p. 504-510.

Fjell, A. M., H. Grydeland, S. K. Krogsrud, I. Amlien, D. A. Rohani, L. Ferschmann, A. B. Storsve, C. K. Tamnes, R. Sala-Llonch, P. Due-Tonnessen, A. Bjornerudar, A. E. Solsnes, A. K. Haberg, J. Skranes, H. Bartsch, C. H. Chen, W. K. Thompson, M. S. Panizzon, W. S. Kremen, A. M. Dale, and K. B. Walhovd, 2015, Development and aging of cortical thickness correspond to genetic organization patterns: Proceedings of the National Academy of Sciences of the United States of America, v. 112, p. 15462-15467.

Ford, T. C., and D. P. Crewther, 2016, A Comprehensive Review of the H-1-MRS Metabolite Spectrum in Autism Spectrum Disorder: Frontiers in Molecular Neuroscience, v. 9.

Francis, P. J., 2006, Genetics of inherited retinal disease: Journal of the Royal Society of Medicine, v. 99, p. 189-191.

Frangou, P., M. Correia, and Z. Kourtzi, 2018, GABA, not BOLD, reveals dissociable learning-dependent plasticity mechanisms in the human brain: Elife, v. 7.

Fricker, M., A. M. Tolkovsky, V. Borutaite, M. Coleman, and G. C. Brown, 2018, NEURONAL CELL DEATH: Physiological Reviews, v. 98, p. 813-880.

Ganguly, K., A. F. Schinder, S. T. Wong, and M. Poo, 2001, GABA itself promotes the developmental switch of neuronal GABAergic responses from excitation to inhibition: Cell, v. 105, p. 521-532.

Glasser, M. F., T. S. Coalson, E. C. Robinson, C. D. Hacker, J. Harwell, E. Yacoub, K. Ugurbil, J. Andersson, C. F. Beckmann, M. Jenkinson, S. M. Smith, and D. C. Van Essen, 2016, A multi-modal parcellation of human cerebral cortex: Nature, v. 536, p. 171-+.

Gomes, N. L., V. C. Greenstein, J. N. Carlson, S. H. Tsang, R. T. Smith, R. E. Carr, D. C. Hood, and S. Chang, 2009, A Comparison of Fundus Autofluorescence and Retinal Structure in Patients with Stargardt Disease: Investigative Ophthalmology & Visual Science, v. 50, p. 3953-3959.

Good, C. D., I. S. Johnsrude, J. Ashburner, R. N. A. Henson, K. J. Friston, and R. S. J. Frackowiak, 2001, A voxel-based morphometric study of ageing in 465 normal adult human brains: Neuroimage, v. 14, p. 21-36.

Goryawala, M. Z., S. Sheriff, and A. A. Maudsley, 2016, Regional distributions of brain glutamate and glutamine in normal subjects: Nmr in Biomedicine, v. 29, p. 1108-1116.

Govindaraju, V., K. Young, and A. A. Maudsley, 2000, Proton NMR chemical shifts and coupling constants for brain metabolites: Nmr in Biomedicine, v. 13, p. 129-153.

Griffanti, L., G. Douaud, J. Bijsterbosch, S. Evangelisti, F. Alfaro-Almagro, M. F. Glasser, E. P. Duff, S. Fitzgibbon, R. Westphal, D. Carone, C. F. Beckmann, and S. M. Smith, 2017, Hand classification of fMRI ICA noise components: Neuroimage, v. 154, p. 188-205.

Griffanti, L., G. Salimi-Khorshidi, C. F. Beckmann, E. J. Auerbach, G. Douaud, C. E. Sexton, E. Zsoldos, K. P. Ebmeier, N. Filippini, C. E. Mackay, S. Moeller, J. Q. Xu, E. Yacoub, G. Baselli, K. Ugurbil, K. L. Miller, and S. M. Smith, 2014, ICA-based artefact removal and accelerated fMRI acquisition for improved resting state network imaging: Neuroimage, v. 95, p. 232-247.

Griffen, T. C., and A. Maffei, 2014, GABAergic synapses: their plasticity and role in sensory cortex: Frontiers in Cellular Neuroscience, v. 8.

Grill-Spector, K., 2003, The neural basis of object perception (vol 13, pg 159, 2003): Current Opinion in Neurobiology, v. 13, p. 399-399.

Gusnard, D. A., and M. E. Raichle, 2001, Searching for a baseline: Functional imaging and the resting human brain: Nature Reviews Neuroscience, v. 2, p. 685-694.

Hallett, M., 2001, Plasticity of the human motor cortex and recovery from stroke: Brain Research Reviews, v. 36, p. 169-174.

Hanson, R. L. W., R. P. Gale, A. D. Gouws, A. Airody, M. T. W. Scott, F. Akthar, S. Waterson, M. T. Wells, A. J. Wright, K. Bell, E. Silson, H. A. Baseler, and A. B. Morland, 2019, Following the

Status of Visual Cortex Over Time in Patients With Macular Degeneration Reveals Atrophy of Visually Deprived Brain Regions: Investigative Ophthalmology & Visual Science, v. 60, p. 5045-5051.

Haris, M., K. J. Cai, A. Singh, H. Hariharan, and R. Reddy, 2011, In vivo mapping of brain myo-inositol: Neuroimage, v. 54, p. 2079-2085.

Hartline, H. K., 1938, The response of single optic nerve fibers of the vertebrate eye to illumination of the retina: American Journal of Physiology, v. 121, p. 400-415.

Hensch, T. K., 2005, Critical period plasticity in local cortical circuits: Nature Reviews Neuroscience, v. 6, p. 877-888.

Hernowo, A. T., D. Prins, H. A. Baseler, T. Plank, A. D. Gouws, J. M. M. Hooymans, A. B. Morland, M. W. Greenlee, and F. W. Cornelissen, 2014, Morphometric analyses of the visual pathways in macular degeneration: Cortex, v. 56, p. 99-110.

Hilbert, D. R., 1992, WHAT IS COLOR-VISION: Philosophical Studies, v. 68, p. 351-370.

Horton, J. C., and D. R. Hocking, 1998, Monocular core zones and binocular border strips in primate striate cortex revealed by the contrasting effects of enucleation, eyelid suture, and retinal laser lesions on cytochrome oxidase activity: Journal of Neuroscience, v. 18, p. 5433-5455.

Huang, X., H. D. Dan, F. Q. Zhou, Q. Q. Deng, and Y. Shen, 2019, Abnormal intrinsic functional network hubs and connectivity following peripheral visual loss because of inherited retinal degeneration: Neuroreport, v. 30, p. 295-304.

Huang, X., Y. Tong, C. X. Qi, Y. T. Xu, H. D. Dan, Q. Q. Deng, and Y. Shen, 2021, Mapping Regional Homogeneity and Functional Connectivity of the Visual Cortex in Resting-State fMRI: Jove-Journal of Visualized Experiments.

Hubel, D. H., and T. N. Wiesel, 1968, Receptive fields and functional architecture of monkey striate cortex: Journal of Physiology-London, v. 195, p. 215-&.

Hyvarinen, A., 1999, Fast and robust fixed-point algorithms for independent component analysis: Ieee Transactions on Neural Networks, v. 10, p. 626-634.

Ip, I. B., A. Berrington, A. T. Hess, A. J. Parker, U. E. Emir, and H. Bridge, 2017, Combined fMRI-MRS acquires simultaneous glutamate and BOLD-fMRI signals in the human brain: Neuroimage, v. 155, p. 113-119.

Issa, P. C., A. R. Barnard, P. Herrmann, I. Washington, and R. E. MacLaren, 2015, Rescue of the Stargardt phenotype in Abca4 knockout mice through inhibition of vitamin A dimerization: Proceedings of the National Academy of Sciences of the United States of America, v. 112, p. 8415-8420.

Jakel, S., and L. Dimou, 2017, Glial Cells and Their Function in the Adult Brain: A Journey through the History of Their Ablation: Frontiers in Cellular Neuroscience, v. 11.

Jenkinson, M., P. Bannister, M. Brady, and S. Smith, 2002, Improved optimization for the robust and accurate linear registration and motion correction of brain images: Neuroimage, v. 17, p. 825-841.

Jensen, J. E., B. D. Frederick, and P. F. Renshaw, 2005, Grey and white matter GABA level differences in the human brain using two-dimensional, J-resolved spectroscopic imaging: Nmr in Biomedicine, v. 18, p. 570-576.

Jolly, J. K., K. Junemann, H. Boagey, M. Nadsady, H. Bridge, and R. E. Maclaren, 2020, Validation of electronic visual acuity (EVA) measurement against standardised ETDRS charts in patients with visual field loss from inherited retinal degenerations: British Journal of Ophthalmology, v. 104, p. 924-931.

Josan, A. S., T. M. W. Buckley, L. J. Wood, J. K. Jolly, J. Cehajic-Kapetanovic, and R. E. MacLaren, 2021, Microperimetry Hill of Vision and Volumetric Measures of Retinal Sensitivity: Translational Vision Science & Technology, v. 10.

Kaderali, S., Y. J. Kim, A. Reynaud, and K. T. Mullen, 2015, The Role of Human Brain Area hMT plus in the Perception of Global Motion Investigated With Repetitive Transcranial Magnetic Stimulation (rTMS): Brain Stimulation, v. 8, p. 200-207.

Karlaftis, V. M ., Frangou, P., Higgins, C., Vidaurre. D., Ziminski, J. J., Stagg, C. J., Emir, U. E., Kourtzi, Z. Brain stimulation boosts perceptual learning by altering sensory GABAergic plasticity and functional connectivity. Preprint. Biorxiv (2021)

Karni, A., G. Meyer, P. Jezzard, M. M. Adams, R. Turner, and L. G. Ungerleider, 1995, Functional mri evidence for adult motor cortex plasticity during motor skill learning: Nature, v. 377, p. 155-158.

Kelber, A., 2018, Vision: Rods See in Bright Light: Current Biology, v. 28, p. R364-R366.

Kennedy, C. J., P. E. Rakoczy, and I. J. Constable, 1995, Lipofuscin of the retinal pigment epithelium: A review: Eye, v. 9, p. 763-771.

Kjellstrom, U., 2015, Reduced macular function in ABCA4 carriers: Molecular Vision, v. 21, p. 767-782.

Kong, X. R., S. K. West, R. W. Strauss, B. Munoz, A. V. Cideciyan, M. Michaelides, A. Ho, M. Ahmed, E. M. Schonbach, J. K. Cheetham, A. M. Ervin, and H. P. N. Scholl, 2017, Progression of Visual Acuity and Fundus Autofluorescence in Recent-Onset Stargardt Disease: ProgStar Study Report #4: Ophthalmology Retina, v. 1, p. 514-523.

Kreis, R., V. Boer, I. Y. Choi, C. Cudalbu, R. A. de Graaf, C. Gasparovic, A. Heerschap, M. Krssak, B. Lanz, A. A. Maudsley, M. Meyerspeer, J. Near, G. Oz, S. Posse, J. Slotboom, M. Terpstra, I. Tkac, M. Wilson, W. Bogner, and M. R. Experts working Grp Terminology, Terminology and concepts for the characterization of in vivo MR spectroscopy methods and MR spectra: Background and experts' consensus recommendations: Nmr in Biomedicine.

Langer, D. L., P. Rakaric, A. Kirilova, D. A. Jaffray, and A. Z. Damyanovich, 2007, Assessment of metabolite quantitation reproducibility in serial 3D-H-1-MR spectroscopic Imaging of human brain using sterelotactic repositioning: Magnetic Resonance in Medicine, v. 58, p. 666-673.

Larcombe, S. J., C. Kennard, J. O'Shea, and H. Bridge, 2019, No Effect of Anodal Transcranial Direct Current Stimulation (tDCS) Over hMT plus on Motion Perception Learning: Frontiers in Neuroscience, v. 12.

Lawlor, M., H. Danesh-Meyer, L. A. Levin, I. Davagnanam, E. De Vita, and G. T. Plant, 2018, Glaucoma and the brain: Trans-synaptic degeneration, structural change, and implications for neuroprotection: Survey of Ophthalmology, v. 63, p. 296-306.

Lewis, T. L., and D. Maurer, 2009, Effects of Early Pattern Deprivation on Visual Development: Optometry and Vision Science, v. 86, p. 640-646.

Li, S. H., P. Li, H. H. Gong, F. Jiang, D. Liu, F. Q. Cai, C. G. Pei, F. Q. Zhou, and X. J. Zeng, 2017, Intrinsic Functional Connectivity Alterations of the Primary Visual Cortex in Primary AngleClosure Glaucoma Patients before and after Surgery: A Resting-State fMRI Study: Plos One, v. 12.

Liew, G., M. Michaelides, and C. Bunce, 2014, A comparison of the causes of blindness certifications in England and Wales in working age adults (16-64 years), 1999-2000 with 2009-2010: Bmj Open, v. 4.

Lin, A. D., O. Andronesi, W. Bogner, I. Y. Choi, E. Coello, C. Cudalbu, C. Juchem, G. J. Kemp, R. Kreis, M. Krssak, P. Lee, A. A. Maudsley, M. Meyerspeer, V. Mlynarik, J. Near, G. Oz, A. L. Peek, N. A. Puts, E. M. Ratai, I. Tkac, P. G. Mullins, and S. Experts Working Grp Reporting, Minimum Reporting Standards for in vivo Magnetic Resonance Spectroscopy (MRSinMRS): Experts' consensus recommendations: Nmr in Biomedicine.

Logothetis, N. K., 2002, The neural basis of the blood-oxygen-level-dependent functional magnetic resonance imaging signal: Philosophical Transactions of the Royal Society B-Biological Sciences, v. 357, p. 1003-1037.

Logothetis, N. K., 2003, The underpinnings of the BOLD functional magnetic resonance imaging signal: Journal of Neuroscience, v. 23, p. 3963-3971.

Logothetis, N. K., J. Pauls, M. Augath, T. Trinath, and A. Oeltermann, 2001, Neurophysiological investigation of the basis of the fMRI signal: Nature, v. 412, p. 150-157.

Lunghi, C., U. E. Emir, M. C. Morrone, and H. Bridge, 2015, Short-Term Monocular Deprivation Alters GABA in the Adult Human Visual Cortex: Current Biology, v. 25, p. 1496-1501.

Macgillivray, T. J., E. Trucco, J. R. Cameron, B. Dhillon, J. G. Houston, and E. J. R. Van Beek, 2014, Retinal imaging as a source of biomarkers for diagnosis, characterization and prognosis of chronic illness or long-term conditions: British Journal of Radiology, v. 87.

Machado, A. R., A. C. Pereira, F. Ferreira, S. Ferreira, B. Quendera, E. Silva, and M. Castelo-Branco, 2017, Structure-function correlations in Retinitis Pigmentosa patients with partially preserved vision: a voxel-based morphometry study: Scientific Reports, v. 7, p. 10.

Malach, R., J. B. Reppas, R. R. Benson, K. K. Kwong, H. Jiang, W. A. Kennedy, P. J. Ledden, T. J. Brady, B. R. Rosen, and R. B. H. Tootell, 1995, OBJECT-RELATED ACTIVITY REVEALED BY FUNCTIONAL MAGNETIC-RESONANCE-IMAGING IN HUMAN OCCIPITAL CORTEX: Proceedings of the National Academy of Sciences of the United States of America, v. 92, p. 8135-8139.

Maunsell, J. H. R., and W. T. Newsome, 1987, VISUAL PROCESSING IN MONKEY EXTRASTRIATE CORTEX: Annual Review of Neuroscience, v. 10, p. 363-401.

Maurer, D., C. J. Mondloch, and T. L. Lewis, 2007, Effects of early visual deprivation on perceptual and cognitive development: From Action to Cognition, v. 164, p. 87-104.

Maya-Vetencourt, J. F., A. Sale, A. Viegi, L. Baroncelli, R. De Pasquale, O. F. O'Leary, E. Castren, and L. Maffei, 2008, The antidepressant fluoxetine restores plasticity in the adult visual cortex: Science, v. 320, p. 385-388.

McBain, V. A., J. Townend, and N. Lois, 2012, Progression of Retinal Pigment Epithelial Atrophy in Stargardt Disease: American Journal of Ophthalmology, v. 154, p. 146-154.

Melillo, P., A. Prinster, V. Di Iorio, G. Olivo, F. M. D'Alterio, S. Cocozza, A. Orrico, M. Quarantelli, F. Testa, A. Brunetti, and F. Simonelli, 2018, Visual Cortex Activation in Patients With Stargardt Disease: Investigative Ophthalmology & Visual Science, v. 59, p. 1503-1511.

Michaelides, M., D. M. Hunt, and A. T. Moore, 2003, The genetics of inherited macular dystrophies: Journal of Medical Genetics, v. 40, p. 641-650.

Minati, L., Aquino, D., Bruzzone, M. G., & Erbetta, A. (2010). Quantitation of normal metabolite concentrations in six brain regions by in-vivoH-MR spectroscopy. *Journal of medical physics*, *35*(3), 154–163.

Minka, T. P., 2001, Automatic choice of dimensionality for PCA: Advances in Neural Information Processing Systems 13, v. 13, p. 598-604.

Moffett, J. R., B. Ross, P. Arun, C. N. Madhavarao, and A. M. A. Namboodiri, 2007, N-acetylaspartate in the CNS: From neurodiagnostics to neurobiology: Progress in Neurobiology, v. 81, p. 89-131.

Molday, R. S., 2007, ATP-binding cassette transporter ABCA4: Molecular properties and role in vision and macular degeneration: Journal of Bioenergetics and Biomembranes, v. 39, p. 507-517.

Morawski, M., E. Kirilina, N. Scherf, C. Jager, K. Reimann, R. Trampel, F. Gavriilidis, S. Geyer, B. Biedermann, T. Arendt, and N. Weiskopf, 2018, Developing 3D microscopy with CLARITY on human brain tissue: Towards a tool for informing and validating MRI-based histology: Neuroimage, v. 182, p. 417-428.

Motulsky, H. J., and R. E. Brown, 2006, Detecting outliers when fitting data with nonlinear regression - a new method based on robust nonlinear regression and the false discovery rate: Bmc Bioinformatics, v. 7.

Nguyen, P. V., and N. H. Woo, 2003, Regulation of hippocampal synaptic plasticity by cyclic AMP-dependent protein kinases: Progress in Neurobiology, v. 71, p. 401-437.

Nickerson, L. D., S. M. Smith, D. Ongur, and C. F. Beckmann, 2017, Using Dual Regression to Investigate Network Shape and Amplitude in Functional Connectivity Analyses: Frontiers in Neuroscience, v. 11.

Noro, T., K. Namekata, A. Kimura, Y. Azuchi, N. Hashimoto, K. Moriya-Ito, Y. Komaki, C. Y. Lee, N. Okahara, X. L. Guo, C. Harada, E. Kim, T. Nakano, H. Tsuneoka, T. Inoue, E. Sasaki, H. Tokuno, and T. Harada, 2019, Normal tension glaucoma-like degeneration of the visual system in aged marmosets: Scientific Reports, v. 9.

Ogawa, S., D. W. Tank, R. Menon, J. M. Ellermann, S. G. Kim, H. Merkle, and K. Ugurbil, 1992, INTRINSIC SIGNAL CHANGES ACCOMPANYING SENSORY STIMULATION - FUNCTIONAL BRAIN MAPPING WITH MAGNETIC-RESONANCE-IMAGING: Proceedings of the National Academy of Sciences of the United States of America, v. 89, p. 5951-5955.

Olivo, G., P. Melillo, S. Cocozza, F. M. D'Alterio, A. Prinster, F. Testa, A. Brunetti, F. Simonelli, and M. Quarantelli, 2015, Cerebral Involvement in Stargardt's Disease: A VBM and TBSS Study: Investigative Ophthalmology & Visual Science, v. 56, p. 7388-7397.

Paneri, S., and G. G. Gregoriou, 2017, Top-Down Control of Visual Attention by the Prefrontal Cortex. Functional Specialization and Long-Range Interactions: Frontiers in Neuroscience, v. 11.

Pantano, P., J. C. Baron, P. Lebrungrandie, N. Duquesnoy, M. G. Bousser, and D. Comar, 1984, REGIONAL CEREBRAL BLOOD-FLOW AND OXYGEN-CONSUMPTION IN HUMAN AGING: Stroke, v. 15, p. 635-641.

Papermaster, D. S., B. G. Schneider, M. A. Zorn, and J. P. Kraehenbuhl, 1978, IMMUNOCYTOCHEMICAL LOCALIZATION OF A LARGE INTRINSIC MEMBRANE-PROTEIN TO INCISURES AND MARGINS OF FROG ROD OUTER SEGMENT DISKS: Journal of Cell Biology, v. 78, p. 415-425.

Park, P., J. Georgiou, T. M. Sanderson, K. H. Ko, H. Kang, J. I. Kim, C. A. Bradley, Z. A. Bortolotto, M. Zhuo, B. K. Kaang, and G. L. Collingridge, 2021, PKA drives an increase in AMPA receptor unitary conductance during LTP in the hippocampus: Nature Communications, v. 12.

Patriat, R., E. K. Molloy, T. B. Meier, G. R. Kirk, V. A. Nair, M. E. Meyerand, V. Prabhakaran, and R. M. Birn, 2013, The effect of resting condition on resting-state fMRI reliability and consistency: A comparison between resting with eyes open, closed, and fixated: Neuroimage, v. 78, p. 463-473.

Pelli, D. G., 1997, The VideoToolbox software for visual psychophysics: Transforming numbers into movies: Spatial Vision, v. 10, p. 437-442.

Petroff, O. A. C., 2002, GABA and glutamate in the human brain: Neuroscientist, v. 8, p. 562-573.

Plank, T., J. Frolo, S. Brandi-Ruhle, A. B. Renner, K. Hufendiek, H. Helbig, and M. W. Greenlee, 2011, Gray matter alterations in visual cortex of patients with loss of central vision due to hereditary retinal dystrophies: Neuroimage, v. 56, p. 1556-1565.

Polyak, S. L. (1972). The Retina, Chicago, 1941. *University of Chicago Press. Potts, AM, Hodges, D.*

Poizner, H., U. Bellugi, and E. S. Klima, 1990, BIOLOGICAL FOUNDATIONS OF LANGUAGE - CLUES FROM SIGN LANGUAGE: Annual Review of Neuroscience, v. 13, p. 283-307.

Putnam, C. M., 2017, Clinical imaging of macular pigment optical density and spatial distribution: Clinical and Experimental Optometry, v. 100, p. 333-340.

Raichle, M. E., A. M. MacLeod, A. Z. Snyder, W. J. Powers, D. A. Gusnard, and G. L. Shulman, 2001, A default mode of brain function: Proceedings of the National Academy of Sciences of the United States of America, v. 98, p. 676-682.

Reh, T. A., 2016, Photoreceptor Transplantation in Late Stage Retinal Degeneration: Investigative Ophthalmology & Visual Science, v. 57.

Reich, M., J. Lubke, L. Joachimsen, J. Stifter, S. Kuchlin, D. Bohringer, C. Lange, and W. A. Lagreze, 2021, Thinner temporal peripapillary retinal nerve fibre layer in Stargardt disease detected by optical coherence tomography: Graefes Archive for Clinical and Experimental Ophthalmology, v. 259, p. 1521-1528.

Ribeiro, J., C. A. Procyk, E. L. West, M. O'Hara-Wright, M. F. Martins, M. M. Khorasani, A. Hare, M. Basche, M. Fernando, D. Goh, N. Jumbo, M. Rizzi, K. Powell, M. Tariq, M. Michaelides, J. W. B. Bainbridge, A. J. Smith, R. A. Pearson, A. Gonzalez-Cordero, and R. R. Ali, 2021, Restoration of visual function in advanced disease after transplantation of purified human pluripotent stem cell-derived cone photoreceptors: Cell Reports, v. 35.

Rigotti, D. J., M. Inglese, J. S. Babb, M. Rovaris, B. Benedetti, M. Filippi, R. I. Grossman, and O. Gonen, 2007, Serial whole-brain N-acetylaspartate concentration in healthy young adults: American Journal of Neuroradiology, v. 28, p. 1650-1651.

Ritter, M., A. Hummer, A. A. Ledolter, G. E. Holder, C. Windischberger, and U. M. Schmidt-Erfurth, 2019, Correspondence between retinotopic cortical mapping and conventional functional and morphological assessment of retinal disease: British Journal of Ophthalmology, v. 103, p. 208-215.

Sabbah, N., C. N. Authie, N. Sanda, S. Mohand-Said, J. A. Sahel, A. B. Safran, C. Habas, and A. Amedi, 2016, Increased functional connectivity between language and visually deprived areas in late and partial blindness: Neuroimage, v. 136, p. 162-173.

Sabbah, N., N. Sanda, C. N. Authie, S. Mohand-Said, J. A. Sahel, C. Habas, A. Amedi, and A. B. Safran, 2017, Reorganization of early visual cortex functional connectivity following selective peripheral and central visual loss: Scientific Reports, v. 7.

Salimi-Khorshidi, G., G. Douaud, C. F. Beckmann, M. F. Glasser, L. Griffanti, and S. M. Smith, 2014, Automatic denoising of functional MM data: Combining independent component analysis and hierarchical fusion of classifiers: Neuroimage, v. 90, p. 449-468.

Schuff, N., F. Ezekiel, A. C. Gamst, D. L. Amend, A. A. Capizzano, A. A. Maudsley, and M. W. Weiner, 2001, Region and tissue differences of metabolites in normally aged brain using multislice 1H magnetic resonance spectroscopic imaging: Magnetic Resonance in Medicine, v. 45, p. 899-907.

Sejnowski, T. J., P. S. Churchland, and J. A. Movshon, 2014, Putting big data to good use in neuroscience: Nature Neuroscience, v. 17, p. 1440-1441.

Shannon, R. J., S. van der Heide, E. L. Carter, I. Jalloh, D. K. Menon, P. J. Hutchinson, and K. L. H. Carpenter, 2016, Extracellular N-Acetylaspartate in Human Traumatic Brain Injury: Journal of Neurotrauma, v. 33, p. 319-329.

Shao, Y. B., G. A. Keliris, A. Papanikolaou, M. D. Fischer, D. Zobor, H. Jagle, N. K. Logothetis, and S. M. Smirnakis, 2013, Visual cortex organisation in a macaque monkey with macular degeneration: European Journal of Neuroscience, v. 38, p. 3456-3464.

Shi, S. H., Y. Hayashi, R. S. Petralia, S. H. Zaman, R. J. Wenthold, K. Svoboda, and R. Malinow, 1999, Rapid spine delivery and redistribution of AMPA receptors after synaptic NMDA receptor activation: Science, v. 284, p. 1811-1816.

Silson, E. H., T. S. Aleman, A. Willett, L. W. Serrano, D. J. Pearson, A. M. Rauschecker, A. M. Maguire, C. I. Baker, J. Bennett, and M. Ashtari, 2018, Comparing Clinical Perimetry and Population Receptive Field Measures in Patients with Choroideremia: Investigative Ophthalmology & Visual Science, v. 59, p. 3249-3258.

Sims, S. A., P. Demirayak, S. Cedotal, and K. M. Visscher, 2021, Frontal cortical regions associated with attention connect more strongly to central than peripheral V1: Neuroimage, v. 238.

Simunovic, M. P., and A. T. Moore, 1998, The cone dystrophies: Eye, v. 12, p. 553-565.

Simunovic, M. P., M. Votruba, B. C. Regan, and J. D. Mollon, 1998, Colour discrimination ellipses in patients with dominant optic atrophy: Vision Research, v. 38, p. 3413-3419.

Smith, S. M., P. T. Fox, K. L. Miller, D. C. Glahn, P. M. Fox, C. E. Mackay, N. Filippini, K. E. Watkins, R. Toro, A. R. Laird, and C. F. Beckmann, 2009, Correspondence of the brain's functional architecture during activation and rest: Proceedings of the National Academy of Sciences of the United States of America, v. 106, p. 13040-13045.

Smith, S. M., M. Jenkinson, M. W. Woolrich, C. F. Beckmann, T. E. J. Behrens, H. Johansen-Berg, P. R. Bannister, M. De Luca, I. Drobnjak, D. E. Flitney, R. K. Niazy, J. Saunders, J. Vickers, Y.

Y. Zhang, N. De Stefano, J. M. Brady, and P. M. Matthews, 2004, Advances in functional and structural MR image analysis and implementation as FSL: Neuroimage, v. 23, p. S208-S219.

Smith, S. M., D. Vidaurre, C. F. Beckmann, M. F. Glasser, M. Jenkinson, K. L. Miller, T. E. Nichols, E. C. Robinson, G. Salimi-Khorshidi, M. W. Woolrich, D. M. Barch, K. Ugurbil, and D. C. Van Essen, 2013, Functional connectomics from resting-state fMRI: Trends in Cognitive Sciences, v. 17, p. 666-682.

Sohn, W. S., K. Yoo, Y. B. Lee, S. W. Seo, D. L. Na, and Y. Jeong, 2015, Influence of ROI selection on resting state functional connectivity: an individualized approach for resting state fMRI analysis: Frontiers in Neuroscience, v. 9.

Stagg, C. J., 2014, Magnetic Resonance Spectroscopy as a tool to study the role of GABA in motor-cortical plasticity: Neuroimage, v. 86, p. 19-27.

Stagg, C. J., V. Bachtiar, and H. Johansen-Berg, 2011a, The Role of GABA in Human Motor Learning: Current Biology, v. 21, p. 480-484.

Stagg, C. J., S. Bestmann, A. O. Constantinescu, L. M. Moreno, C. Allman, R. Mekle, M. Woolrich, J. Near, H. Johansen-Berg, and J. C. Rothwell, 2011b, Relationship between physiological measures of excitability and levels of glutamate and GABA in the human motor cortex: Journal of Physiology-London, v. 589, p. 5845-5855.

Stagg C.J., Bachtiar V., Johansen-Berg H. 2011c. What are we measuring with GABA magnetic resonance spectroscopy? *Commun. Integr. Biol.* 2011;4:573–575.

Starace, V., M. Battista, M. Brambati, M. Pederzolli, C. Vigano, A. Arrigo, M. V. Cicinelli, F. Bandello, and M. B. Parodi, 2021, Genotypic and phenotypic factors influencing the rate of progression in ABCA-4-related Stargardt disease: Expert Review of Ophthalmology, v. 16, p. 67-79.

Steel, A., M. Chiew, P. Jezzard, N. L. Voets, P. Plaha, M. A. Thomas, C. J. Stagg, and U. E. Emir, 2018, Metabolite-cycled density-weighted concentric rings k-space trajectory (DW-CRT) enables high-resolution 1 H magnetic resonance spectroscopic imaging at 3-Tesla: Scientific Reports, v. 8.

Takado, Y., N. Sato, Y. Kanbe, M. Tomiyasu, L. J. Xin, J. Near, K. Yoshikawa, N. Sahara, T. Higashi, T. Suhara, M. Higuchi, and T. Obata, 2019, Association between Brain and Plasma Glutamine Levels in Healthy Young Subjects Investigated by MRS and LC/MS: Nutrients, v. 11.

Taylor, M. J., E. R. Tiangga, R. N. Mhuircheartaigh, and P. J. Cowen, 2012, Lack of effect of ketamine on cortical glutamate and glutamine in healthy volunteers: a proton magnetic resonance spectroscopy study: Journal of Psychopharmacology, v. 26, p. 733-737.

Terpstra, M., I. Cheong, T. Lyu, D. K. Deelchand, U. E. Emir, P. Bednarik, L. E. Eberly, and G. Oz, 2016, Test-Retest Reproducibility of Neurochemical Profiles with Short-Echo, Single-Voxel MR Spectroscopy at 3T and 7T: Magnetic Resonance in Medicine, v. 76, p. 1083-1091.

Testa, F., S. Rossi, A. Sodi, I. Passerini, V. Di Iorio, M. Della Corte, S. Banfi, E. M. Surace, U. Menchini, A. Auricchio, and F. Simonelli, 2012, Correlation between Photoreceptor Layer

Integrity and Visual Function in Patients with Stargardt Disease: Implications for Gene Therapy: Investigative Ophthalmology & Visual Science, v. 53, p. 4409-4415.

Testa F, Melillo P, Di Iorio V, Orrico A, Attanasio M, Rossi S, Simonelli F. Macular function and morphologic features in juvenile stargardt disease: longitudinal study. Ophthalmology. 2014 Dec;121(12):2399-405. Epub 2014 Aug 2. PMID: 25097154; PMCID: PMC4252720.

Tkac, I., D. Deelchand, W. Dreher, H. Hetherington, R. Kreis, C. Kumaragamage, M. Povazan, D. M. Spielman, B. Strasser, and R. A. de Graaf, 2021, Water and lipid suppression techniques for advanced H-1 MRS and MRSI of the human brain: Experts' consensus recommendations: Nmr in Biomedicine, v. 34.

Tognarelli, J. M., M. Dawood, M. I. F. Shariff, V. P. B. Grover, M. M. E. Crossey, I. J. Cox, S. D. Taylor-Robinson, and M. J. W. McPhail, 2015, Magnetic Resonance Spectroscopy: Principles and Techniques: Lessons for Clinicians: Journal of Clinical and Experimental Hepatology, v. 5, p. 320-328.

Vandenbroucke, T., R. Buyl, J. De Zaeytijd, M. Bauwens, A. Uvijls, E. De Baere, and B. P. Leroy, 2015, Colour Vision in Stargardt Disease: Ophthalmic Research, v. 54, p. 181-194.

Vithlani, M., M. Terunuma, and S. J. Moss, 2011, THE DYNAMIC MODULATION OF GABA(A) RECEPTOR TRAFFICKING AND ITS ROLE IN REGULATING THE PLASTICITY OF INHIBITORY SYNAPSES: Physiological Reviews, v. 91, p. 1009-1022.

Wagstyl, K., S. Larocque, G. Cucurull, C. Lepage, J. P. Cohen, S. Bludau, N. Palomero-Gallagher, L. B. Lewis, T. Funck, H. Spitzer, T. Dickscheid, P. C. Fletcher, A. Romero, K. Zilles, K. Amunts, Y. Bengio, and A. C. Evans, 2020, BigBrain 3D atlas of cortical layers: Cortical and laminar thickness gradients diverge in sensory and motor cortices: Plos Biology, v. 18.

Wandell, B. A., S. O. Dumoulin, and A. A. Brewer, 2007, Visual field maps in human cortex: Neuron, v. 56, p. 366-383.

Wang, Y., X. Wang, J. Zhou, J. F. Qiu, T. Q. Yan, Y. Z. Xie, L. Li, and W. Z. Lu, 2020, Brain morphological alterations of cerebral cortex and subcortical nuclei in high-tension glaucoma brain and its associations with intraocular pressure: Neuroradiology, v. 62, p. 495-502.

Watkins, K. E., T. J. Shakespeare, M. C. O'Donoghue, I. Alexander, N. Ragge, A. Cowey, and H. Bridge, 2013, Early Auditory Processing in Area V5/MT+ of the Congenitally Blind Brain: Journal of Neuroscience, v. 33, p. 18242-18246.

Weaver, K. E., T. L. Richards, M. Saenz, H. Petropoulos, and I. Fine, 2013, NEUROCHEMICAL CHANGES WITHIN HUMAN EARLY BLIND OCCIPITAL CORTEX: Neuroscience, v. 252, p. 222-233.

Weber, A. J., H. Chen, W. C. Hubbard, and P. L. Kaufman, 2000, Experimental glaucoma and cell size, density, and number in the primate lateral geniculate nucleus: Investigative Ophthalmology & Visual Science, v. 41, p. 1370-1379.

Weng, J., N. L. Mata, S. M. Azarian, R. T. Tzekov, D. G. Birch, and G. H. Travis, 1999, Insights into the function of Rim protein in photoreceptors and etiology of Stargardt's disease from the phenotype in abcr knockout mice: Cell, v. 98, p. 13-23.

West, E. L., J. Ribeiro, and R. R. Ali, 2020, Development of Stem Cell Therapies for Retinal Degeneration: Cold Spring Harbor Perspectives in Biology, v. 12.

Westeneng-van Haaften, S. C., C. J. F. Boon, F. P. M. Cremers, L. H. Hoefsloot, A. I. den Hollander, and C. B. Hoyng, 2012, Clinical and Genetic Characteristics of Late-onset Stargardt's Disease: Ophthalmology, v. 119, p. 1199-1210.

Woolrich, M., 2008, Robust group analysis using outlier inference: Neuroimage, v. 41, p. 286-301.

Woolrich, M. W., T. E. J. Behrens, C. F. Beckmann, M. Jenkinson, and S. M. Smith, 2004, Multilevel linear modelling for FMRI group analysis using Bayesian inference: Neuroimage, v. 21, p. 1732-1747.

Woolrich, M. W., S. Jbabdi, B. Patenaude, M. Chappell, S. Makni, T. Behrens, C. Beckmann, M. Jenkinson, and S. M. Smith, 2009, Bayesian analysis of neuroimaging data in FSL: Neuroimage, v. 45, p. S173-S186.

Worsley, K.J Statistical analysis of activation images. Ch 14, in Functional MRI: An Introduction to Methods, eds. P. Jezzard, P.M. Matthews and S.M. Smith. OUP, 2001

Wu, L. J., Z. H. Tang, X. H. Sun, X. Y. Feng, W. Qian, J. Wang, and L. X. Jin, 2013, Metabolic Changes in the Visual Cortex of Binocular Blindness Macaque Monkeys: A Proton Magnetic Resonance Spectroscopy Study: Plos One, v. 8.

Wu, Y. Y., S. F. Wang, P. W. Zhu, Q. Yuan, W. Q. Shi, Q. Lin, B. Li, Y. L. Min, Q. Zhou, and Y. Shao, 2020, Altered Intrinsic Functional Connectivity of the Primary Visual Cortex in Patients with Neovascular Glaucoma: A Resting-State Functional Magnetic Resonance Imaging Study: Neuropsychiatric Disease and Treatment, v. 16, p. 25-33.

Yang, S. N., Y. G. Tang, and R. S. Zucker, 1999, Selective induction of LTP and LTD by postsynaptic Ca2+ , elevation: Journal of Neurophysiology, v. 81, p. 781-787.

You, M., Rong, R., Zeng, Z., Xia, X., & Ji, D. (2021). Transneuronal degeneration in the brain during glaucoma. *Frontiers in Aging Neuroscience*, *13*, 157

Yu, L. H., B. Xie, X. T. Yin, M. L. Liang, A. C. Evans, J. Wang, and C. Dai, 2013, Reduced Cortical Thickness in Primary Open-Angle Glaucoma and Its Relationship to the Retinal Nerve Fiber Layer Thickness: Plos One, v. 8.

Zhang, Y., X. Y. Chen, G. Wen, G. J. Wu, and X. L. Zhang, 2013, Proton Magnetic Resonance Spectroscopy (H-1-MRS) Reveals Geniculocalcarine and Striate Area Degeneration in Primary Glaucoma: Plos One, v. 8.

Zhou, Y., and N. C. Danbolt, 2014, Glutamate as a neurotransmitter in the healthy brain: Journal of Neural Transmission, v. 121, p. 799-817.

Zikou, A. K., G. Kitsos, L. C. Tzarouchi, L. Astrakas, G. A. Alexiou, and M. I. Argyropoulou, 2012, Voxel-Based Morphometry and Diffusion Tensor Imaging of the Optic Pathway in Primary Open-Angle Glaucoma: A Preliminary Study: American Journal of Neuroradiology, v. 33, p. 128-134.